Università degli Studi di Palermo

AREA RICERCA E TRASFERIMENTO TECNOLOGICO
SETTORE DOTTORATI E CONTRATTI PER LA RICERCA
U. O. DOTTORATI DI RICERCA

Dottorato di Ricerca in Scienze Molecolari e Biomolecolari

Dipartimento Scienze e Tecnologie Biologiche Chimiche e Farmaceutiche (STEBICEF)

Settore Scientifico Disciplinare SSD CHEM-08/A

Polysaccharide-based injectable/printable hydrogels as therapeutic systems for drug delivery and regenerative medicine

IL DOTTORE

GIUSEPPE BARBERI

IL COORDINATORE

GIOVANNA PITARRESI

IL TUTOR

GIOVANNA PITARRESI

IL CO TUTOR

CALOGERO FIORICA

CICLO XXXVII

ANNO CONSEGUIMENTO TITOLO 2024

Index

1. Introduction

1.1 Hydrogels

Hydrogels could be defined as semi-solid pharmaceutical preparations where the dispersed phase, of colloidal size, creates a three-dimensional network that retains the aqueous liquid dispersing phase. The dispersed phase can be either inorganic or organic, but it must be capable of establishing intermolecular bonds with other particles or macromolecules within the dispersed phase, creating a three-dimensional network that can incorporate water, thereby forming a high-viscosity system[1,2].

However, most hydrogels are based on three-dimensional hydrophilic polymer networks that contain water or aqueous media, such as physiological fluids[3,4].

Thanks to their interesting properties and high versatility, hydrogels are, today, exploited in various fields: they are particularly well-suited for applications in tissue engineering and regenerative medicine[5–9], as carriers for drug delivery[10–13], as sensors and actuators[14,15], in wearable electronics[16], in catalysis[17], for solar water purification[18] and as supercapacitors[3,19].

1.2 Hydrogels for biomedical applications

Hydrogels have been explored and used in various biomedical applications thanks to their advantageous physicochemical, biological, and structural properties. In detail, they have been employed as 3D models of different diseases[20,21], for pathogenesis study or high-throughput drug screening, but, additionally, for cancer therapy[22,23] and for tissue regeneration (bone, cartilage, skin, heart, nerve, skeletal muscle)[5,8,9,24–27], also through cell encapsulation[28,29], and as drug carriers for controlled and sustainable release[2,10,30–32] (Figure 1).

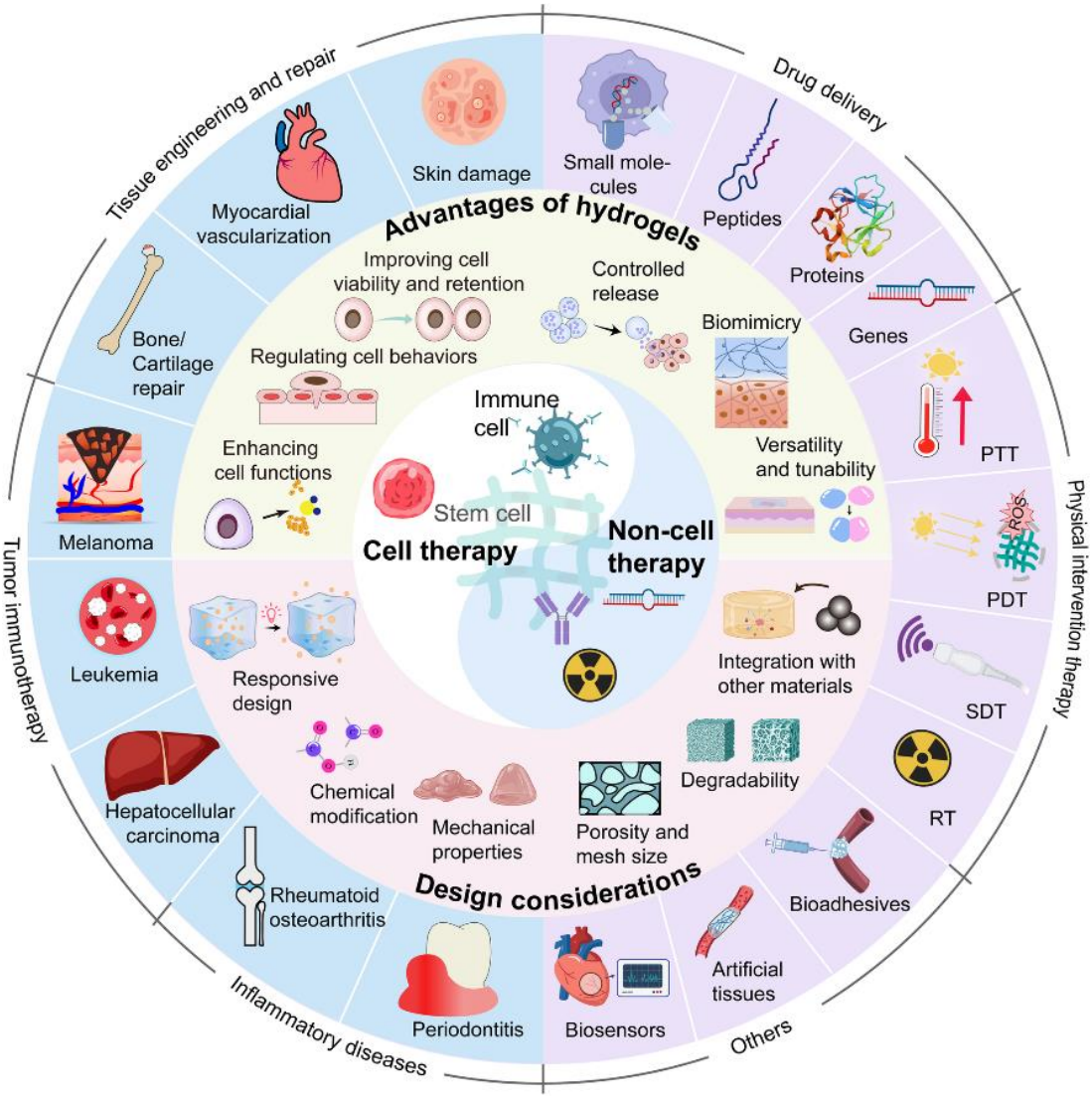

Figure 1. Schematic overview of the applications of hydrogels in the biomedical field and of their properties and advantages[33].

The success of hydrogels in the biomedical field is mainly related to their ability to mimic the extracellular matrix (ECM) of various tissues. In particular, this similarity is due to different aspects, like their porous structure, which could promote cell adhesion and proliferation, their composition, since they can be formulated with ECM-like materials (mainly composed of collagen, glycosaminoglycans, growth factors and tissue-specific components), such as polysaccharides, proteins and nanomaterials, and their high-water content, which creates an environment similar to that of native tissues. This is an important feature because it underlies the interaction of the cells (encapsulated into the hydrogel or

present in the tissue) with the system, enabling cell proliferation, activation of differentiation mechanisms and cell communication, potentially leading to regeneration of damaged tissue[33,34].

A key consideration in the use of hydrogels in the biomedical field is related to their physicochemical, viscoelastic, and mechanical properties. First of all, since hydrogels may be implanted or injected into the human body, biocompatibility is paramount. This means they should perform their function without inducing toxicity in the host tissue: specifically, the polymer biomaterials that constitute the hydrogels, along with their degradation products, must be non-toxic. Furthermore, the gelation process and preparation techniques should be non-cytotoxic: it is essential to remove any unreacted monomers or initiators that could cause adverse effects. Also, the hydrogels should not elicit any immunological response[35–37].

Another important feature of hydrogels is biodegradability and bioresorbability. The latter, in particular, refers to the ability of the system not only to degrade but also to be absorbed by the organism, through physiological processes; indeed, generally, natural biomaterials and their derivatives, such as polysaccharides and polypeptides, contain chemical bonds that can be broken by physiological processes, thus making these polymers generally biodegradable and bioabsorbable[35,38,39]. In addition, controlled degradation within the human body is essential so that the system does not remain indefinitely at the site of injury but can be gradually removed and replaced by new tissue. For this reason, the rate of degradation should ideally be customizable during the design phase according to the application required, to make it as close as possible to the rate of new tissue formation[40].

Researchers demonstrated that another hydrogels' essential parameter that should be taken into account is their swelling ratio; this is a measure of their ability to absorb and retain water or other fluids and it is typically defined as the ratio of the weight or the volume of the swollen hydrogel (including the absorbed fluid) to respectively the weight or the volume of

the dry hydrogel. In this sense, the swelling ratio provides valuable information on the expansion capacity of hydrogel and its overall water absorption capacities, which are crucial for some biomedical applications such as drug delivery, tissue engineering and, most importantly, wound healing[35,41,42].

A further aspect to be emphasized concerns the porosity and pore size of hydrogels. Since these features affect the diffusion of nutrients and oxygen necessary for cell survival and proliferation, but also influence drug release, they need to be accurately regulated[43,44]. In general, the required porosity depends on the application: for example, for bone tissue regeneration is usually requested a minimum pore size of 100 μm, with an optimal range of 200 to 350 μm[40]. Furthermore, some studies highlighted that multi-scale porous systems, combining micro- and macroporosity, offer more advantages for cell attachment and colonization than purely macroporous systems, while a homogeneous pore size and distribution is desirable for drug delivery system to better control release profile[45,46]. However, the correlation between porosity and mechanical properties needs to be considered; indeed, increased porosity can reduce the mechanical strength of the hydrogel, so a suitable balance between these two parameters should be pursued[47,48].

Lastly, also the mechanical and viscoelastic properties of the hydrogel must be taken into account as they have to match those of the natural tissue being treated. Hydrogels designed for regenerative medicine should have rheological and mechanical properties similar to those of the target tissue to withstand the physical stresses encountered under normal conditions, which means they should show appropriate strength, stiffness, and surface characteristics necessary for tissue formation. In this sense, hydrogels are highly versatile systems, because they can be engineered to exhibit a wide range of rheological and mechanical properties, from very soft and flexible to more rigid and robust, depending on the specific application[49–51].

1.3 Physical and chemical hydrogels classification

Hydrogels can be classified according to different criteria. Firstly, based on the type of interactions among the dispersed phase, they can be divided into physical or chemical hydrogels[52,53] (Figure 2). The first ones are composed of reversible non-covalent bonds such as hydrogen bonds, Van der Waals forces, ionic bonds, and hydrophobic interactions. Although these bonds are, individually, quite weak, collectively they contribute to a stable structure: hence, they are referred to as cooperative bonds[54–56]. In physical hydrogels, stimuli such as temperature can induce gelation. For example, in thermoresponsive hydrogels, a temperature change can cause the reorganization of the dispersed phase, the establishment of new weak bonds and the subsequent formation of a new three-dimensional network, modifying the properties of the system[57,58].

These hydrogels offer a lot of advantages for clinical applications, such as the absence of potentially toxic chemical crosslinkers, ease of preparation and handling through simple procedures, and reversible gelation in response to mild environmental stimuli. Polysaccharides-based hydrogels are, usually, belong to this group, because of the presence of a large number of hydrogen bonds or electrostatic interactions inside their network. Such hydrogels are potentially applicable in the regeneration of small defects (e.g. wound healing, alveolar and cranial bone lesions) and as injectable systems[52,54]. Given all these positive aspects, the development of these hydrogels has received increasing interest for tissue engineering applications; however, the weak nature of these interactions prevents the system from meeting the mechanical properties required for certain applications.

On the other hand, covalent bonds between polymer chains provide a more stable network in chemical hydrogels. These linkages are usually produced via reactions that result in disulfide bridges, Schiff bases (such as imines, oximes, and hydrazones), or other covalent connections like those formed via click chemistry, involving either the use of molecular

agents or electromagnetic waves. Indeed, a variety of crosslinking approaches, such as the creation of covalent bonds between functionalized polymer chains, crosslinking with small molecules, photo-crosslinking, and enzymatic crosslinking, is frequently used to produce chemical hydrogels[52,59,60].

Compared to physical systems, these are more robust and stiffer due to the covalent character of their network, which makes them appropriate, for instance, for use in hard tissues like bone[61,62]. They, also, differ from physical hydrogels, in that they have a better load-bearing capacity, less deformation under stress, and increased stability, which makes them perfect for applications where mechanical robustness is crucial[63].

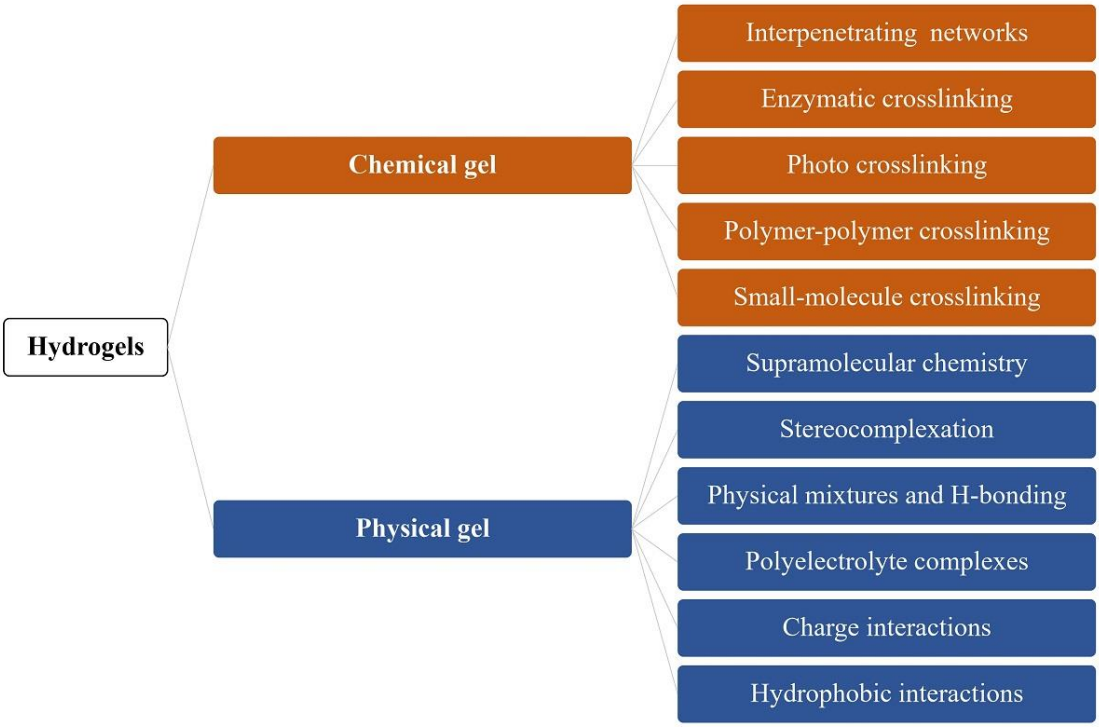

Figure 2. Schematic illustration of interactions within physical and chemical hydrogels[64].

1.4 Stimuli-responsive hydrogels classification

Hydrogels can also be classified based on their responsiveness to different stimuli, such as biological (e.g. enzymes), chemical (ionic strength, pH, presence of glucose or other molecules) and physical stimuli (temperature, light, electric field, magnetic field, pressure

and ultrasound radiation)[65] (Figure 3). The temperature-, pH- and light-sensitive hydrogels will be discussed below.

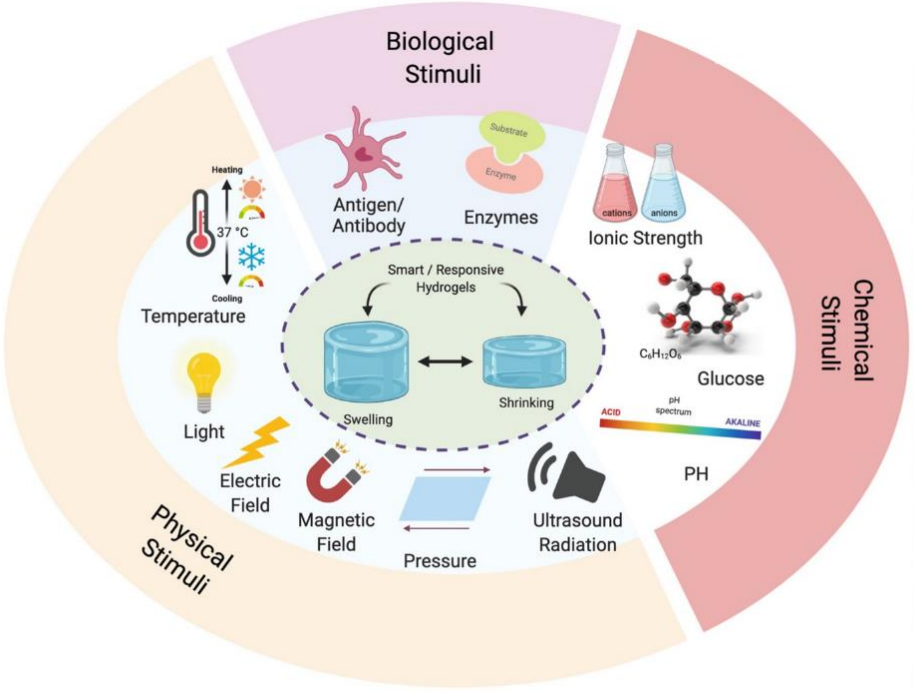

Figure 3. Schematic illustration of different smart/stimuli-responsive hydrogels employed for biomedical applications[65].

1.4.1 Temperature-responsive hydrogels

Temperature-sensitive hydrogels change their properties by varying the environmental temperature because they contain polymers with both hydrophilic and hydrophobic groups, whose interactions are influenced by temperature[66].

One of the most extensively studied temperature-responsive hydrogels is poly(N-isopropyl acrylamide) (pNIPAM)-based one. pNIPAM hydrogels are particularly interesting since they exhibit a lower critical solution temperature (LCST) around 32-33°C[67]: this means that below this temperature, they are hydrophilic and swollen, while above the LCST, they become more hydrophobic and contract into a condensed state, due to a coil-to-globule change that involves the release of water molecules bound to the polymer's isopropyl side

groups, leading to increased intra- and intermolecular hydrophobic interactions[68,69] (Figure 4). This value of LCST is particularly useful because allows it to easily operate at environmental temperature, but at the same time, enables the creation of stable systems when pNIPAM-based hydrogels are administrated into the human body[33]. For this reason, thanks to its advantageous properties, this biomaterial has been exploited to functionalize polymer backbones like chitosan, gelatin, hyaluronic acid, and dextran and create, in this way, novel derivatives for temperature-responsive hydrogels for regenerative medicine[70–72].

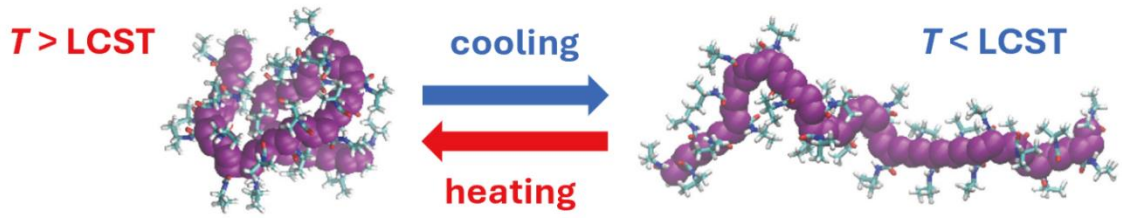

Figure 4. Schematic temperature-induced transition for pNIPAM[67].

Another class of temperature-responsive injectable hydrogels, widely used for cell delivery, includes block copolymers made of polyethylene glycol (PEG), polypropylene glycol (PPG), polylactic acid (PLA), poly(lactic-co-glycolic) acid (PLGA), polycaprolactone (PCL), like PEG-PPG-PEG, PLGA-PEG-PLGA, PEG-PLA-PEG, PCL-PEG-PCL, and PEG-PCL-PEG. These copolymers consist of hydrophobic and hydrophilic blocks; consequently, at low temperatures, the amphiphilic polymer chains assemble into micelles and bridged micelles, while as the temperature reaches the LCST, the exposure of more hydrophobic segments increases the hydrophobicity, leading to the micellar aggregation and the hydrogel's formation[70,73,74].

1.4.2 pH-responsive hydrogels

pH-responsive hydrogels, on the other hand, modify their structure, morphology and properties in response to changes in environmental pH[75]. This responsiveness is particularly useful because of the presence of various pH values in different parts of the human body: 7.35-7.45 in most tissues, 4.0-6.0 on the skin, around 5 in inflamed or infected sites, and 6.0-7.0 in solid tumours[35].

To produce pH-responsive materials, the main strategy is the incorporation of functional groups into the hydrogel polymer backbone, undergoing protonation or deprotonation in response to pH changes: in this way, a *sol-gel* transition (and vice versa) could occur, affecting the hydrogel's stiffness, permeability, and ability to release active substances or drugs. This kind of hydrogel is particularly promising for targeted drug delivery and tissue engineering applications, where controlled response to physiological or pathophysiological pH variations is crucial[76,77].

1.4.3 Light-responsive hydrogels

Light-responsive hydrogels incorporate materials with photo-responsive moieties, known as chromophores, which absorb or respond to specific wavelengths of light and convert optical signals into chemical ones resulting in isomerization, rearrangement, dimerization, chain cleavage reactions or photo-crosslinking[78].

The energy and wavelength of light are critical factors for these hydrogels' applications. Indeed, ultraviolet (UV) light, thanks to its short wavelength and high energy, allows for rapid responsiveness but is limited in its ability to penetrate biological tissues, restricting its use to superficial applications; conversely, visible or infrared light, which can penetrate deeper into tissues, offers a promising alternative for more extensive biomedical applications[79,80].

Among light-responsive hydrogels, photo-crosslinkable systems have gained significant interest and a wide application[81]. These systems, when irradiated in the presence of photoinitiators (eosin Y, lithium phenyl-2,4,6-trimethylbenzoylphosphinate (LAP), Irgacure-2959), crosslink prepolymers containing photoreactive moieties like thiol-ene, acrylate, or methacrylate groups, leading to gelation or increasing system's stiffness[82–84]. This mechanism offers several advantages, including an efficient curing rate, mild reaction conditions without the need for organic solvents or heating, low cytotoxicity, and precise spatiotemporal control[85,86]. Moreover, by regulating crosslinking degree, it is possible to modulate the physicochemical, viscoelastic, and mechanical properties of hydrogels: this is a great advantage when designing new therapeutic systems for advanced applications in tissue engineering, drug delivery, and other areas where precise control over material properties is essential.

1.5 Preformed and injectable hydrogels classification

Hydrogels can also be classified considering their application method in two different classes. The traditional method requires directly applying preformed hydrogels to the damaged area, while the innovative strategy involves the injection of the gelling system in the lesion site[2]. The first approach can be advantageous in cases where surgery is necessary, although it has certain limitations, particularly related to the hydrogel's ability to optimally conform to the shape of the lesion, resulting in reduced retention of the system on the wound site and then, diminishing its regenerative potential. Moreover, if the application requires surgical procedures, it can lead to longer hospitalization and recovery times, increased post-operative pain, and the risk of bacterial infections[87–89].

The alternative strategy involves the use of injectable hydrogels, which, thanks to their viscoelastic nature, allow for an efficient filling of target sites even with irregular geometries.

Injectable hydrogels can be classified into two main types considering the injectability mechanism: in situ forming hydrogels and shear-thinning hydrogels[90–92].

In situ forming hydrogels, due to chemical and physical crosslinking mechanisms, mediated by click chemistry, enzymatic crosslinking, light-induced crosslinking, the formation of dynamic covalent bonds, or induced by stimuli present at the administration site, such as temperature, ionic strength or pH, undergo gelation directly at this site, throughout a *sol-gel* transition[93–95].

On the other side, shear-thinning hydrogels, also known as shear-responsive hydrogels, are in a gel state before of the injection, but exhibit a reversible *gel-sol* transition mediated by the stress applied during the administration, due to the presence of reversible bonds like electrostatic interactions, hydrogen bonds, guest-host interactions or dynamic covalent bonds (e.g. Schiff base, hydrazone bonds, Boronate-diol complexation, thiol–disulfide exchange bonds, coordination bonds). Specifically, this means that these hydrogels (existing initially in gel state) show a *gel-sol* transition when high shear stresses are applied, such as during the injection but return to the starting gel state once the stress is removed (after the administration), quickly recovering their initial viscoelastic properties and preventing, in this way, the material's flow into surrounding tissues[96–98].

1.5.1 Shear-thinning injectable hydrogels' properties

Going into more detail, shear-thinning injectable hydrogels should possess some viscoelastic properties that allow them to be easily injected into the lesion site, while quickly recovering their original viscoelastic properties after the injection[90]. This implies that, generally, injectable hydrogels should exhibit pseudoplastic and self-healing behaviour. Pseudoplasticity, or shear-thinning, refers to the decrease in viscosity of a fluid, as the shear rate increases. From a molecular point of view, this behaviour is mainly related to the alignment and disentanglement of polymer chains under shear stress: when a shear force is

applied, the polymer chains align in the direction of flow, reducing internal bonds and resistance and decreasing viscosity, while, since this alignment is reversible when the shear force is removed, the polymer chains return to their original and more entangled state, allowing the hydrogel to go back to its higher starting viscosity (Figure 5)[92]. This is a fascinating feature since it enables easy administration of hydrogels while at the same time maintaining in situ the system. However, viscosity influence also mechanical properties, which are essential for the biomedical aim of the developed biomaterial: in this sense, achieving the right balance between injectability and mechanical strength is a key challenge; indeed, hydrogels must be sufficiently fluid under shear to be easily injected but, at the same time, they should provide adequate mechanical support once in place[99–101].

Regarding self-healing behaviour, this is deeply connected with shear-thinning properties and refers to the hydrogels' intrinsic ability to autonomously repair structural damage or restore their original viscoelastic properties after being damaged, without the need for external intervention or manual repair processes[102]. Both properties, self-healing and shear-thinning behaviour, are the result of the dynamic nature of the physical or chemical bonds that create the hydrogel network, which can break and repair reversibly as a result of various types of mechanical damage[92,103].

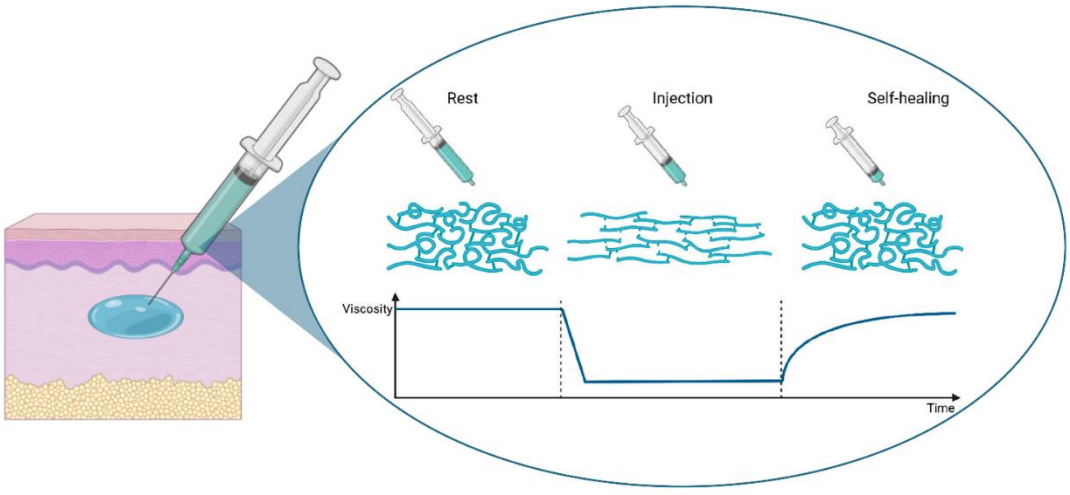

Figure 5. Schematic behaviour of shear-thinning injectable hydrogels[92].

Before treating the nature of bonds that confer injectable properties, it is important to discuss the viscoelastic properties and investigate the rheological parameters of these hydrogels, since they need to be carefully controlled to develop new systems. Firstly, it is essential to balance elastic and viscous moduli, and, thus, the elastic and plastic response of the hydrogel, in order to regulate its viscoelastic properties. In detail, the elastic or storage modulus (G'), describes the hydrogel's ability to store and recover elastic energy and refers to its solid-like behaviour and elastic response. Actually, a high G' indicates a stiff material, which is essential for applications that require considerable mechanical resistance (e.g. bone), ensuring that the hydrogel maintains its shape and provides mechanical support after gelation. The viscous or loss modulus (G''), on the other hand, measures the hydrogel's ability to dissipate energy as flow, and thus, its liquid-like behaviour and more plastic response. In this sense, a high G'' suggests great fluidity and less rigidity, which can be advantageous for hydrogels that need to adapt to dynamic conditions within the body. Balancing carefully G' and G'' is extremely important for producing hydrogels that are both injectable and stable in their final form[92,104].

Additionally, the viscosity of injectable hydrogels affects their injectability and then, their administration. In particular, hydrogels with appropriate viscosity can be easily injected into target sites without clogging the needle or requiring excessive force, while a higher or lower viscosity could respectively make injection difficult as well as determine pain during the administration or cause an excessive flow of the gelled system, resulting in low retention of the system in administration site[105].

Another important parameter, considered the threshold stress at which a hydrogel transitions from a solid-like to a more fluid-like state, is the yield stress, which precisely refers to the minimum stress required by the hydrogel to start flow. This property is the one that most regulates that the hydrogel remains stable and does not flow under low-stress conditions

while still being injectable and, at the same time, it's a key parameter to manage easy handling and administration. Specifically, a hydrogel with too high yield stress may be difficult to inject, requiring excessive force and potentially causing discomfort in the patient; meanwhile, a hydrogel with too low value of yield stress might not hold its shape after injection, leading to suboptimal placement and reduced efficacy. Thus, yield stress is a fundamental property that influences the injectability, stability, and overall functionality of injectable hydrogels[106,107].

In summary, the viscoelastic properties of injectable hydrogels are decisive factors in controlling their performance and efficacy in biomedical applications. By optimizing these properties, it would be possible to develop hydrogels that are not only easy to inject (the first key aspect for the patient's compliance), but also effective in supporting tissue regeneration, delivering drugs and enhancing healing processes.

1.5.2 Chemical and physical bonds in injectable hydrogels

As often mentioned, injectable hydrogels owe their properties to dynamic and reversible bonds, both physical and chemical, which make them suitable for biomedical applications (Figure 6)[108].

Noncovalent or physical interactions are the main linkages within the hydrogels' network and represent a key feature in the design of injectable systems due to their reversibility and compatibility with aqueous environments. Although they are individually quite weak, their cumulative effect (there is a huge amount of them in a hydrogel) can lead to robust gelation and self-healing properties. Several noncovalent strategies have been explored (electrostatic and metal coordination interactions, hydrophobic and hydrogen bonds) depending on the chemical nature of the polymer backbone[92,109].

Electrostatic interactions between oppositely charged chemical groups commonly involve harnessing the intrinsic attractive forces between anionic and cationic polymers or

incorporating an ionic monomer, such as negatively charged citrate, to crosslink a cationic polymer like chitosan[110].

Additionally, natural polymers, like proteins, which are polyampholytes with both anionic and cationic groups distributed along their backbone, can establish electrostatic interactions with other macromolecules of the same biomaterial[111]. The same result has been obtained with synthetic zwitterionic polymers, which are synthesized by copolymerizing anionic and cationic building blocks[112,113]. Even if electrostatic interactions could be extremely strong, they are highly sensitive to the ionic strength and pH of their environment. Indeed, high ionic strength can shield these electrostatic forces, while variations in pH can alter the net charge of the polymers, reducing, thus, their effectiveness and compromising the hydrogel's formation and stability[110,114].

Hydrophobic interactions, driven by the tendency of nonpolar groups to minimize contact with water, play a critical role in biological processes like protein folding and are often exploited for hydrogel formation, even if, considering their high-water content cannot be considered among the main gelation causes. With this in mind, hydrogels that use these interactions are formulated by incorporating hydrophilic biomaterial, whose backbone was functionalized with hydrophobic moieties, such as alkyl chains or peptides[115,116]. Within this class, there are also host–guest interactions which involve cyclodextrin motifs that, with their hydrophobic cavities, can form reversible complexes with hydrophobic guest molecules like adamantane, facilitating the self-assembly of the hydrogels[117,118].

Among hydrophobic bonds, π-π stacking involves interactions between aromatic systems, where attractions are due to the overlap of electron clouds in the aromatic rings[35,119]. Liang et al. exploited this kind of interaction to produce injectable composite hydrogels as suitable drug delivery systems for wound healing involving hyaluronic acid-graft-dopamine and reduced graphene oxide coated with polydopamine[120].

Regarding hydrogen bonds, they are particularly prominent in polysaccharides-based hydrogels such as those composed of hyaluronic acid, chitosan, alginate, gellan gum, and xanthan gum, due to the high density of hydroxyl groups present in their polymer backbones[95,111,121–123].

Metal–ligand coordination interactions (often classified as covalent interactions) are established through chelation between ligands and metal ions. The strength of these bonds varies depending on the specific ligand–ion pair since it is influenced by the ion charge, the number of ligands and the physicochemical properties of these chemical species. For instance, mussel-inspired self-healing hydrogels often use catechol–Fe^{3+} coordination to enhance their properties, bisphosphonate-containing compounds like alendronate could bind calcium to support bone regeneration or, also, biopolymers such as alginate and carrageenan form hydrogels with Ca^{2+} ions too[23,92,124–126].

Regarding covalent interactions, it is necessary to remember that chemical crosslinking has traditionally been used for hydrogel formation even if in the form of static interactions, which often lacked the necessary reversibility for creating self-healing injectable hydrogels. As a result, dynamic covalent interactions like Schiff base reactions, Diels–Alder reactions, boronate-diol complexation, and disulfide bonds, have gained significant attention lately[92].

Schiff base reactions refer to the formation of reversible imine or hydrazone bonds between a nucleophilic group (such as an amine or hydrazine) and the electrophilic carbon of aldehydes or ketones[127–131]. Indeed, a common application of Schiff base chemistry is the reaction between aldehyde-functionalized polymers and amine-containing biomaterial, as in systems made of such as gelatine and oxidized hyaluronic acid[132] or chitosan crosslinked with aldehyde-functionalized dextran[133].

Similar to the previous, acylhydrazone bonds are often exploited for the same purpose. In this case, these bonds are formed between aldehyde or ketone groups (like the previous example) and imine groups derived from acylhydrazine[134].

Diels–Alder reactions, that involve a diene and a dienophile, are often used by exploiting polymers functionalized with maleimide groups (dienophile) and furan groups (diene)[135,136]. The reversibility of these bonds depends on their ability to undergo a retro Diels–Alder reaction, although this reversibility typically requires elevated temperatures, limiting their use for certain biomedical applications[137]. However, some recent examples suggested the possibility of obtaining this reversibility at room temperature, using fulvene-modified dextran and dichloromaleic-acid-modified PEG as hydrogel's components[138].

Boronate-diol complexation involves ester bond formation between boronic acids and hydroxyl groups, mainly diols, resulting particularly useful in the presence of catechol functionalized biomaterial[35,139,140]. Shi et al. developed a hydrogel composed of phenylboronic acid, hyaluronic acid, and polyvinyl alcohol, demonstrating that its self-healing mechanism is based on boronate-diol complexation[141].

Thiol–disulfide exchange reactions, on the other hand, take advantage of the dynamic nature of disulfide bonds in the presence of nucleophilic thiols under neutral or alkaline conditions, allowing a reversible crosslinking. During this reaction, a thiolate anion attacks a disulfide bond, generating a new disulfide bond and releasing a new thiolate[142–144]. Thiolation of polymer building blocks can be achieved by introducing thiol groups into polymer chains or by reducing disulfide bonds in proteins as demonstrated by Zhang et al.[35,145]. Here, using hydrogen peroxide on a bovine serum albumin dispersion, known for its high disulfide bond content, they activated the hydrogel's self-healing mechanism by cleaving disulfide bonds within individual albumin molecules, leading, thus, formation of free sulfhydryl groups, which then interacted with other albumin molecules to form new disulfide bonds. As a result,

the hydrogel exhibited rapid self-healing properties and showed promise as an injectable system, highlighting its potential for use in regenerative medicine and tissue engineering[145].

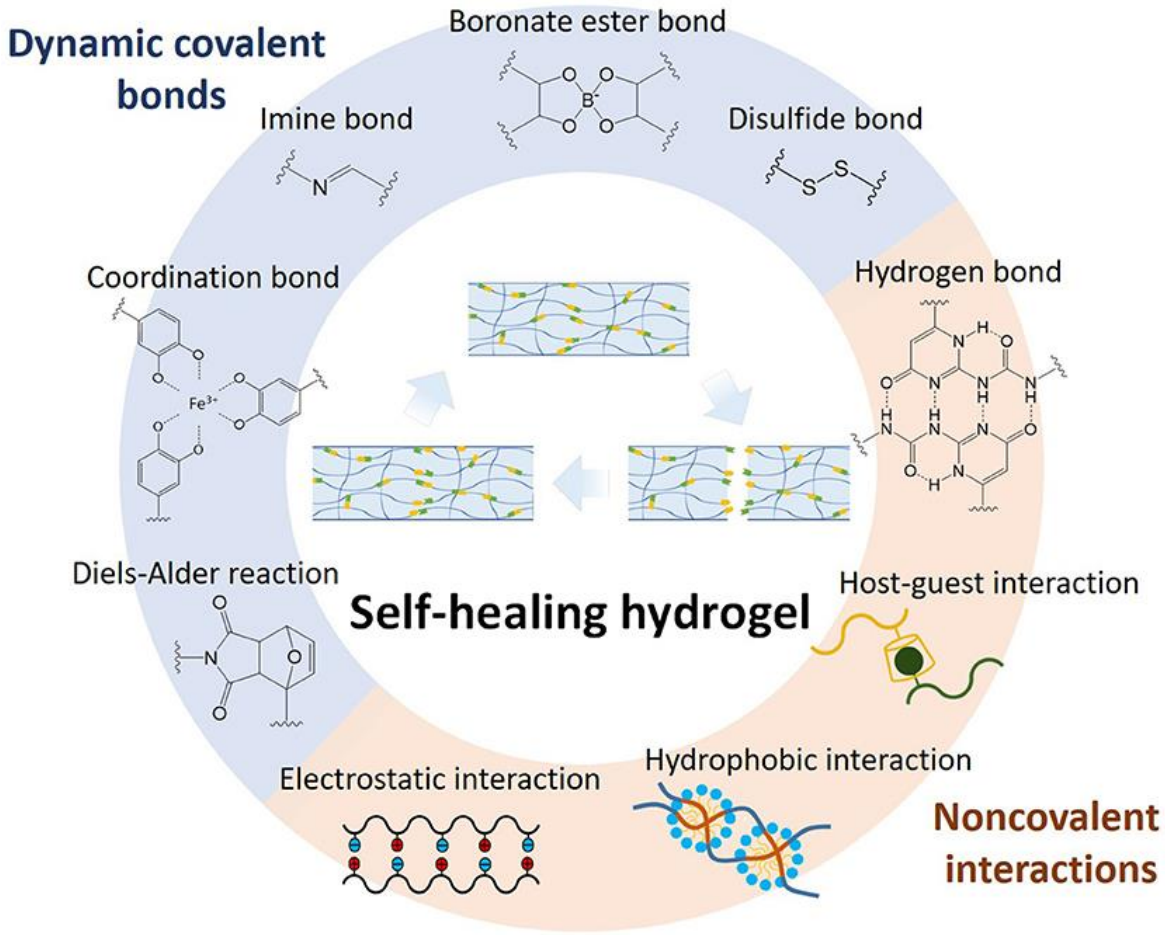

Figure 6. Overview of common noncovalent and covalent chemical interactions used for the design of self-healing and shear-thinning injectable hydrogels[121].

Even though each type of reversible bond possesses its advantages, the development of injectable hydrogels increasingly integrates various dynamic interaction approaches. This can be obtained either by employing different interaction types within a single polymer network (dual-crosslinked hydrogels)[146], between two different biomaterials (double-crosslinked hydrogels)[62], or, also, by combining two different and independently crosslinked polymer networks (double-network hydrogels)[147]. As already highlighted,

although noncovalent interactions are valuable, they are often weak and sensitive to environmental factors such as pH and ionic strength. As a result, researchers frequently combine multiple noncovalent interactions or merge dynamic covalent interactions with noncovalent bonds to enhance performance[148–151].

From this point of view, double-network and double-crosslinked hydrogels represent a significant innovation in injectable hydrogel technology. Specifically, the first ones consist of two interpenetrating polymer networks with different crosslinking mechanisms and different functions in the hydrogel formation. The second ones, on the other hand, usually exploit a double-crosslinking process between the biomaterials composing the hydrogels, thus, creating a three-dimensional network. In both cases, the mechanical and viscoelastic properties of these systems are derived from the combined effects of both networks/crosslinking: one of them is formed by weaker, often noncovalent crosslinks, facilitating injection and rapid self-healing, while the other one consists of "stronger" (often covalent) bonds, that confer additional mechanical support[92]. Furthermore, static covalent bonds, although generally not used in self-healing injectable hydrogels due to their irreversibility, can be leveraged to improve hydrogels' stability when introduced post-injection, such as through photo-crosslinking, stabilizing the material in situ (Figure 7)[152–154].

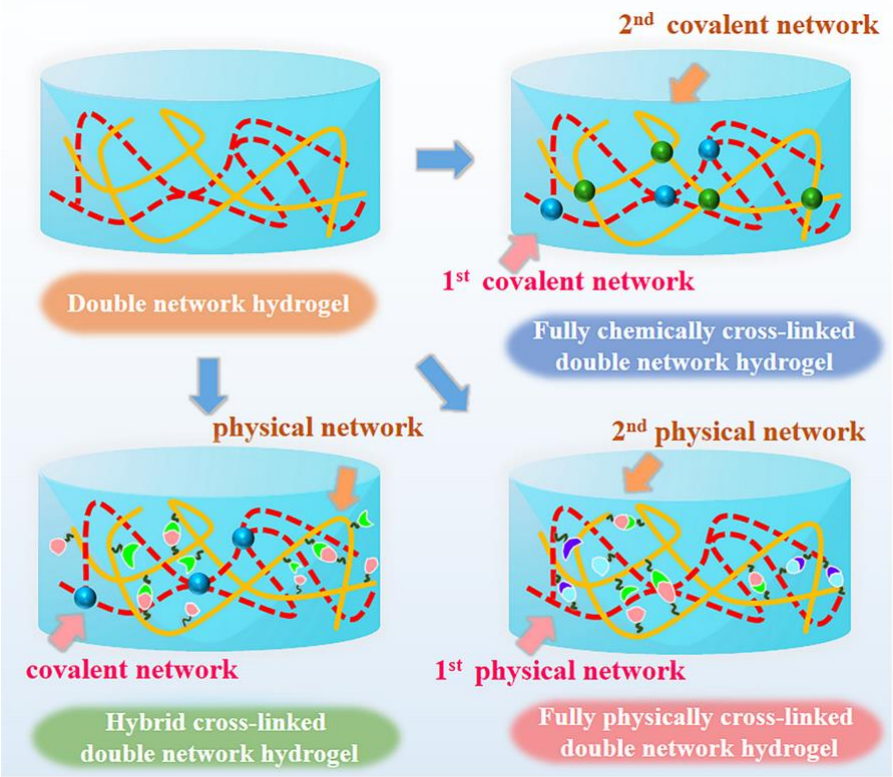

Figure 7. Different combinations of physical and chemical networks in double-network and double-crosslinked hydrogels[155].

In synthesis, by integrating both dynamic and covalent networks, these hydrogels not only achieve self-healing and shear-thinning properties but also exhibit excellent shape retention after injection or extrusion[156]. Dynamic linkages, indeed, facilitate easy injection and recovery from deformation, while irreversible covalent bonds improve shape stability, as well as mechanical and viscoelastic properties[157–159]. Consequently, double-crosslinked hydrogels are particularly well-suited for 3D printing since reversible dynamic crosslinking enhances printability and toughness, and irreversible crosslinking provides structural reinforcement after printing[159].

1.6 3D printable hydrogels

3D printing, also known as additive manufacturing, is a production technology that allows the creation of 3D structures by depositing successive layers of material, starting from a

digital model, generally obtained using computer-aided design (CAD) software; this is then converted into precise instructions for the 3D printer, that through layer-by-layer deposition of materials (plastic, resin, metal, or even biocompatible substances), can create complex and customized designs[160]. In this sense, 3D printing is an advanced biofabrication technique capable of fine control over morphological and structural properties of created structures, and of remarkable geometric accuracy at both the macro and, mainly, microscale levels[161].

Regarding its application in the biomedical field, 3D printing is revolutionizing regenerative medicine since it is possible to create highly personalized and complex biological structures. In this context, 3D printing and, especially, 3D bioprinting can fabricate tissue-like structures that can deeply mimic the architecture and function of human organs, by precisely controlling the geometry, porosity and composition of these structures[162].

One of the most significant advantages of 3D printing in the biomedical field concerns the possibility of its application in personalised medicine since it can create patient-specific implants (Figure 8)[161,163]. In particular, 3D printers can produce highly accurate structures that perfectly match the patient's lesion, by using their medical imaging data, allowing, thanks to this level of customization, a better integration in the lesion site, reducing the risk of rejection and improving overall outcomes. It is in this sense that 3D printing shows great potential for personalized healthcare, offering the possibility to treat conditions that currently have limited or no effective therapies[164,165].

3D printing methods include inkjet printing, extrusion-based printing, laser-assisted printing, stereolithography, and VAT polymerization[160].

Extrusion-based 3D printing is the most used 3D printing technique thanks to its different advantages, like efficiency, adaptability and the possibility to work with a wide range of materials. In this process, inks are extruded through a micronozzle or an extrusion head,

controlled by mechanisms like an endless screw, pneumatic pressure, or a mechanical piston[166]. The creation of 3D structures, regulated by CAD file (like for the other 3D printing techniques) is obtained by the ink deposition layer-by-layer throughout the print-head movement in x y z directions. Different parameters (nozzle diameter, number of print-head, type of materials) can be controlled, providing the creation of advanced structures with various types of layers with different composition and function[167].

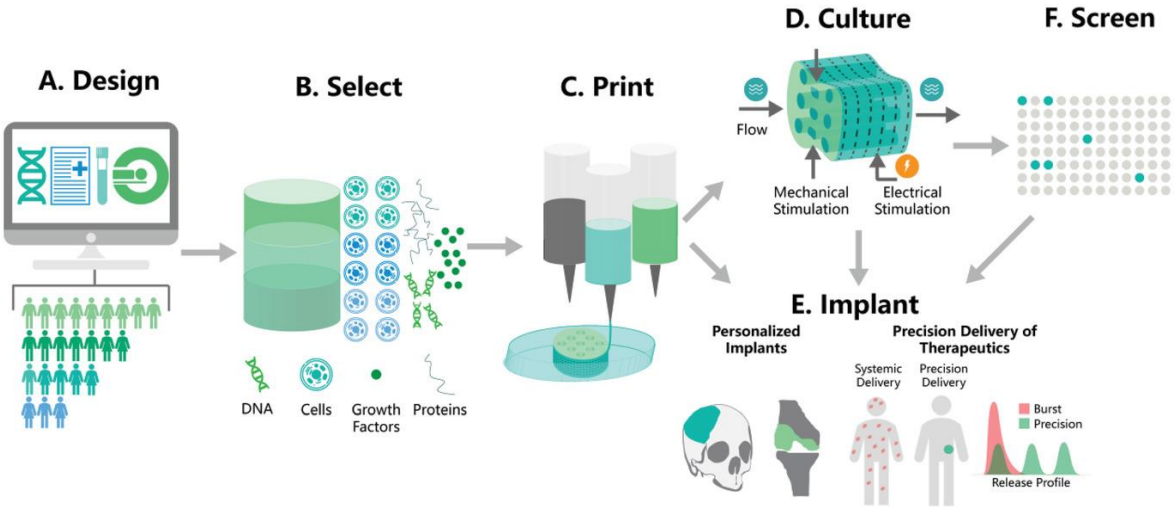

Figure 8. 3D printing for precision medicine[168].

Inside the extrusion-based 3D printing, hydrogel-based extrusion has been generating increasing interest across various biomedical fields (oral and topical/transdermal drug delivery, tissue engineering and regenerative medicine (Figure 9)), because of the numerous advantages derived from the use of hydrogels[163,169–171]. Indeed, as already discussed in detail, they can replicate the intricate tissue microenvironments; at the same time, they also allow to operate at or near room temperature, which represents an advantage for materials that are sensitive to high temperatures and if the ink (bioink) contains cells[161,163,172,173].

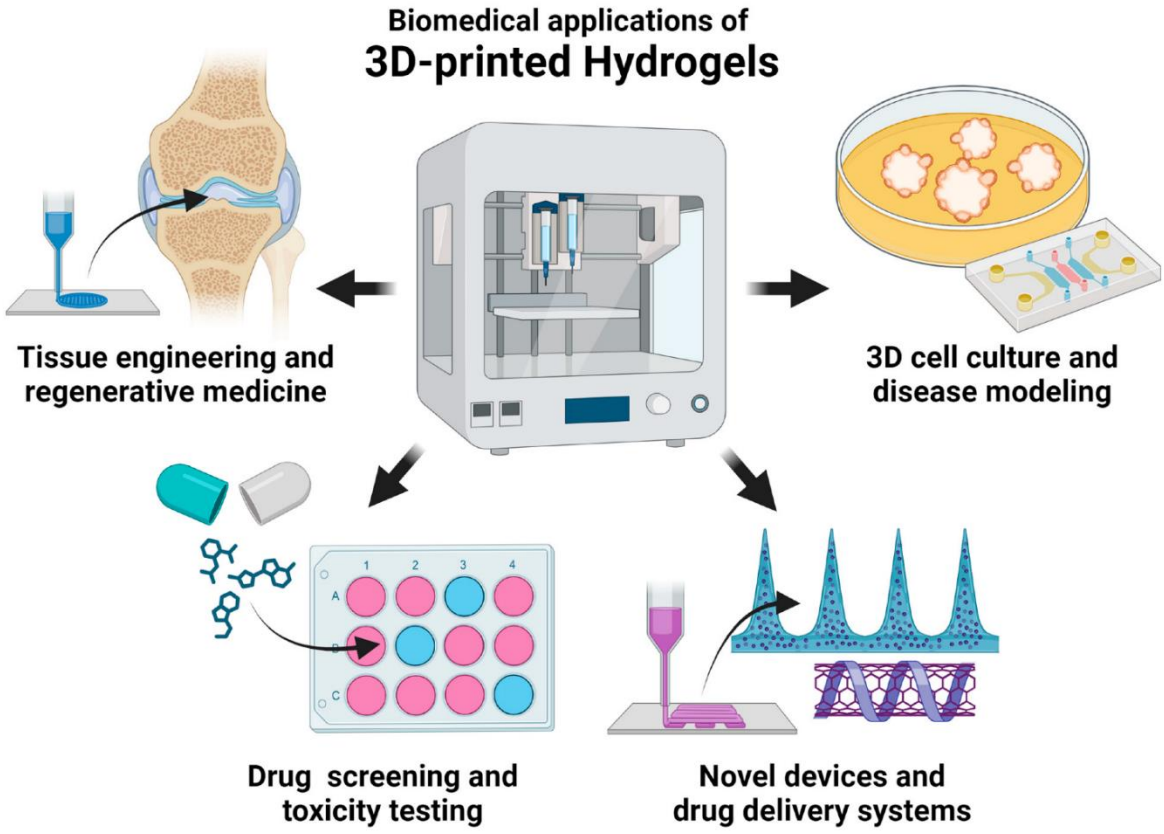

Figure 9. Current biomedical applications of 3D-printed hydrogels[174].

The main component of this technique is the ink, even if it is, at the same time, one of the most limiting factors because of the lack of a wide availability of such materials. This is why, the development of new inks is a continuous challenge: developing and optimizing printable ink materials, indeed, is essential to obtain the desired physicochemical, mechanical, rheological and biological properties[175–177].

An ideal ink for extrusion-based 3D printing should satisfy different primary criteria: relatively high viscosity, pronounced shear-thinning behaviour, and a rapid crosslinking process after printing, to be easily extruded and maintain the original shape. Most hydrogels lack self-supporting properties, necessitating a secondary crosslinking immediately after printing, to stabilize the structure[178]. From this point of view, injectable hydrogels, as described previously, could be considered an interesting perspective in extrusion-based 3D

printing as inks, with double-crosslinking hydrogels that appear as ideal candidates[159,179].

Given these premises and considering that the main feature of inks is their ability to be continuously extruded from the needle during printing, several parameters need to be taken into account to predict extrusion performance. In this sense, the rheological parameters highlighted so far (viscosity, shear-thinning behaviour, viscoelastic moduli, yield stress, gelation rate) need to be deeply controlled for 3D printing application[180].

Firstly, the ink's extrudability is mainly determined by its shear-thinning properties. Indeed, if a hydrogel ink has sufficient shear-thinning behaviour, it will be printed with good shape retention[181,182]. Furthermore, for the ink to flow, it must reach a critical stress level, defined by the yield stress: the higher this value, the greater the pressure required to overcome the intermolecular bonds in the crosslinked network[183,184]. Additionally, to ensure optimal printability, the gelation time of the hydrogel should be minimized as much as possible. For this reason, injectable hydrogels, because of their pseudoplastic behaviour, appear as optimal candidates as inks[161].

Another key physicochemical factor influencing the suitability of hydrogels for 3D printing is their viscosity. While higher viscosity can technically improve printing accuracy enhancing the extrusion of stable layers that could prevent the entire printed construct from collapsing, it also could cause nozzle clogging and non-continuous filament extrusion during the printing process. On the other side, low viscosity can minimize nozzle clogging during printing but can result in poor printing accuracy and shape fidelity retention[183]. Moreover, the viscosity of the ink also affects the porosity of the printed scaffolds, influencing, thus, the mechanical, pharmaceutical and biological properties of the printed structures[161]. Furthermore, an increase in viscosity, requiring an increase in the extrusion shear stress, can

also influence cell viability and consequent biological performance (for bioink which encapsulates cells), or drug retention capabilities[185].

Therefore, it is essential to evaluate the viscoelastic moduli, G' and G''. While for the injectable hydrogels, only their single values were discussed, in this section it is necessary to focus also on their ratio of G'' to G', known as the loss tangent (tan δ), which determines the main viscoelastic response of the ink. In particular, if the tan δ is too high, the ink is more in a liquid state and may collapse after printing, while, if it is too low, the extrusion may be not continuous. To achieve a construct with good resolution and mechanical strength, and, thus, good printability, the ink should show both high viscosity and an appropriate G'' to G' ratio[161,183].

Injectable hydrogels usually respect these parameters: this is why they are suitable to be exploited as inks. Furthermore, injectable double-crosslinkable hydrogels could represent interesting candidates for 3D printing, because their double-crosslinking mechanisms allow respectively easy extrusion and good shape maintenance: the reversible dynamic crosslinks are used as the energy dissipation mechanism to improve the printability as described before, while the second, often irreversible, crosslinking can be used to reinforce the structure after printing[156,159].

For example, Jafari et al. designed double-crosslinked hydrogels using marine poly- and oligosaccharides for wound healing. In detail, they exploited both enzymatically mediated crosslinking via glucose oxidize/horseradish peroxidase and phenolated polyelectrolyte complex between positively charged chito-oligosaccharides and phenolated chitosan with negatively charged phenolated alginate. In this way, they developed injectable and printable hydrogels, with antioxidant and antibacterial activities, which enhanced *in vivo* wound healing in a rat model[186].

Osi et al. designed a new bioink based on methylacrylated chitosan and gelatin doped with hydroxyapatite nanoparticles with a thermo/photo-crosslinking strategy. Specifically, the thermal gelation of methylacrylated gelatin was used to improve the viscosity of methylacrylated chitosan inks and stabilize the 3D-printed structures before photo-crosslinking. In this manner, a long-term stable structure able to promote cell attachment and growth was obtained, appearing as a prospective material for tissue engineering[187].

In another study, Wang et al. developed a double-network/double-crosslinked hydrogel with significantly enhanced mechanical strength, self-healing, and shear-thinning properties. Thanks to the dynamic hydrazone crosslinking (oxidized and adipic acid dihydrazide-modified hyaluronic acid) and photo-crosslinking (due to the presence of gelatin methacrylate), this double-network hydrogel represents a promising material for 3D printing in tissue engineering[188].

In order to establish if the printing process is successful and, therefore, evaluate the printing quality, different parameters can be taken into account. As often highlighted, an important aspect that should be considered in 3D printing is the printability of inks. Literally, this refers to the ability of a material to be used in a layer-by-layer system to create a 3D structure according to a computer-defined design[185,189]. However, at the same time, several definitions of printability refer to different parameters of the inks (rheological properties, gelation mechanisms (crosslinking)) and of the printing process (printing rate, printing pressure, printing temperature, construct design, nozzle geometry). There are also some equations that allow to describe printability quantitatively[190–192]:

$$Pr = \frac{\pi}{4} \times \frac{1}{C} = \frac{L^2}{16A} \quad (1)$$

where C is the circularity of an enclosed area ($C = \frac{4\pi A}{L^2}$), while L stands for perimeter and A for area (Figure 10A).

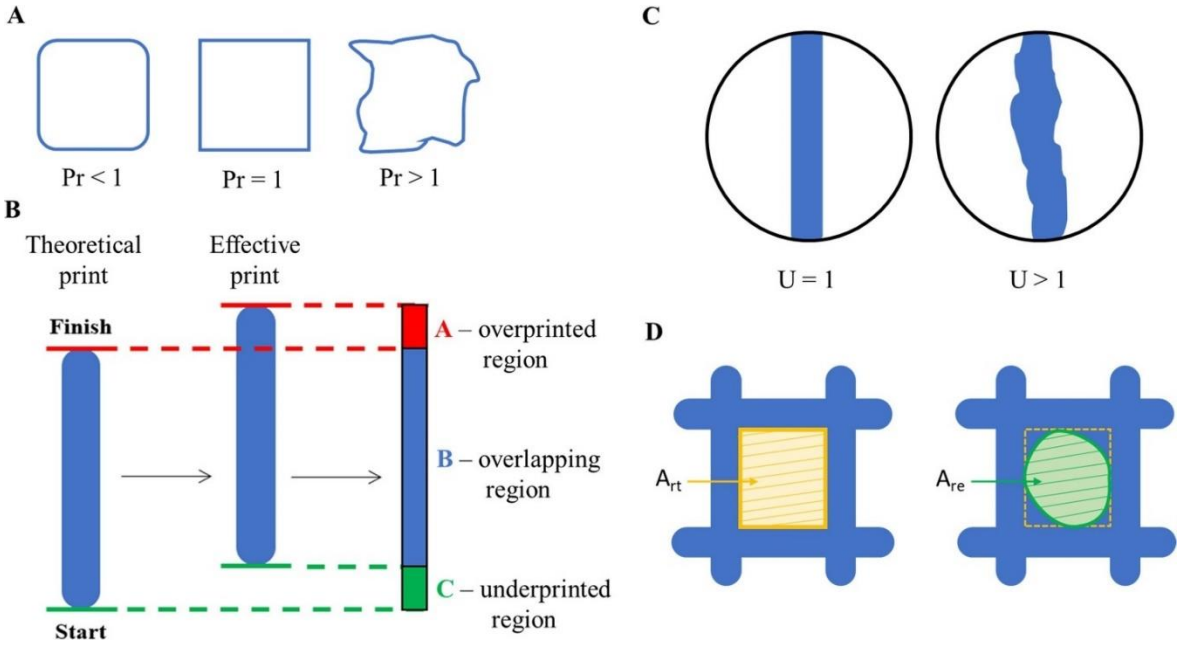

Figure 10. Graphical printing quality evaluation referred to the equations used in recent research. Application of the printability formula developed by Ouyang et al.[192], (Pr = 1 refers to a properly gelled, Pr < 1 corresponds to under-gelled, and Pr > 1 means over-gelled ink) (A). Representation of the L' index suggested by Kang et al.[193](B). Illustration of a nonuniform (U > 1) and a uniform strand filament (U = 1)[190](C). Schematic representation of printing fidelity proposed by He et al.[194], in which ratios closer to 0 depict enhanced printing fidelity(D)[185].

Furthermore, another term that is often used for this evaluation is "printing accuracy" which normally describes how similar the printed construct is to the CAD model in terms of geometry and spatial resolution. The printing accuracy is defined as the degree to which printed constructs match their intended size, shape, and location when applying determined printing parameters[195]. For Webb and Doyle, printing accuracy depends on the geometry of printed structures and the printing pressure[196]. Indeed, an increase in shear rate due to a decrease in nozzle diameter or an increase in printing pressure could affect negatively printing accuracy. To maximise the latter, Webb and Doyle considered the new Parameter Optimization Index (POI), determined by the following equation:

$$POI = Accuracy \times \frac{1}{DG \times p} = \frac{1}{tline \times DG \times p} \quad (2)$$

where *DG* represents the nozzle gauge, *p* is the pressure and *tline* corresponds to line thickness.

In another study, Kang et al.[193] evaluated printing accuracy utilizing another equation, where it was taken into account the layer thickness considering its length, width, and height. Printing accuracy was evaluated by length index L':

$$L' = \frac{C}{(A+B+C)} \quad (3)$$

where A is the average underprinted, B is the overlapping and C is the overprinted length of the printed construct (Figure 10B).

Another parameter that is often used for the description of printing success is printing or shape fidelity, which refers to the shape maintenance ability after extrusion. According to Gillispie et al.[195], printing fidelity can be analysed by measuring the size of printed filaments and evaluating phenomena like filament collapse and height maintenance. In particular, different parameters, correlated to the printed structure, could be considered: filament circularity, pore geometry and optical visual grid. To do that, Soltan et al.[190] defined uniformity factor with the following equation (Figure 10C):

$$U = \frac{lenght\ of\ the\ printed\ strand}{(lenght\ of\ theoretical\ stright\ strand)} \quad (4)$$

He et al.[194], on the other hand, used another equation to refers to printing fidelity:

$$\varphi = \frac{(A_{rt} - A_{re})}{A_{rt}} \quad (5)$$

where A_{rt} is the theoretical area of a lattice and A_{re} is the experimental area of the lattice (Figure 10D).

Lastly, extrudability is another concept derived from printability, it is macroscopically evaluable and refers to the capability to obtain suitable extrusion. A good extrudability is essential for further printing quality[185]. A filament drop test could be carried out to determine, macroscopically, the extrusion-related parameters of the ink. This is a test of static extrusion that gives information about the gelation status and homogeneity of the ink, and, consequently, about its extrudability[194].

Specifically, inks are generally classified as under-gelled, if a droplet forms at the nozzle tip, properly gelled if a continuous filament is extruded, or over-gelled if an irregular, curvy and non-uniform filament is formed. Only a continuous filament could be, theoretically, well printed. For under-gelled inks, the viscosity is too low, leading to the extrusion of droplets instead of a filament and the printed structure could collapse during the printing process itself. Regarding the over-gelled inks, the printed structure would show irregular pores and low fidelity to the digital model[185,190–192].

In synthesis, the printing quality, which could be expressed with different parameters, depends on many aspects mainly related to the hydrogel ink itself like polymer concentrations, molecular weight or water content but also to the printing process. Indeed, the temperature, nozzle diameter, printing speed, extrusion pressure, and flow speed could also influence the printing quality[180,194].

1.7 Biomaterials for injectable and printable hydrogels

After examining and evaluating the properties of injectable hydrogels, as well as their potential use as inks for 3D printing, it is important to highlight their composition and, thus, the most used biomaterials for biomedical applications.

As widely described, hydrogels are formulations where the dispersed phase creates a three-dimensional network that retains the aqueous liquid dispersing phase. This dispersed phase has colloidal size and can be organic or inorganic, although organic macromolecules like

polymers (natural, synthetic, or semi-synthetic) are the most exploited biomaterials[3,4]. Among all of them, natural polymers are preferred over synthetic ones due to their higher biocompatibility, biodegradability, and low toxicity. Regarding their source, they are generally isolated from plants or algae (alginate and cellulose), animals (elastin, collagen, and chitosan), and bacteria (xanthan gum or gellan gum), while, about their chemical nature, most of them are proteins and polysaccharides[90,197]. Proteins like collagen, gelatin and elastin are employed for the presence of domains that cells can bind (cell adhesion properties) and for their ability to promote tissue regeneration[93,132,198,199]; polysaccharides such as hyaluronic acid, alginate, chitosan, gellan and xanthan gum, on the other hand, are utilized for their capability to mimic the native ECM and for they easy functionalization that allow modifying their physicochemical properties, making them very versatile[95,111,121–123,200–202].

Compared to natural ones, synthetic biomaterials generally show more definite and repeatable physicochemical, and therefore mechanical properties, thanks to the fact that reaction conditions can be finely controlled during synthetic processes. PEGs, for instance, easily synthesisable with precise control on the desired molecular weight, are valued for low toxicity and low immunogenicity, and, thus, for their biocompatibility. In general, synthetic polymers can be customized to obtain a wide range of mechanical and chemical properties, making them extremely versatile[203,204].

In summary, while natural hydrogels show higher biocompatibility and similarity to the ECM, synthetic hydrogels offer greater customization and control of material properties. With this in mind, to combine the advantages of both biomaterials' classes, the ideal choice is the use of semi-synthetic polymers, which are usually obtained through the chemical functionalisation of the natural polymer backbone.

Regarding the chemical nature of the most used natural polymers, it is important to make some clarifications and highlight the different advantages related to protein and polysaccharides in hydrogels' preparation.

Protein and peptide-based hydrogels, since they are often components of the ECM, show high biocompatibility, minimal immune response and interesting biological properties in terms of cell interaction capabilities[205]. Common proteins, exploited in hydrogels' formulation, include gelatin, fibrin, elastin and serum albumin, which undergo gelation generally through non-covalent interactions. However, these hydrogels often show some limitations, like low mechanical properties, and more laborious preparation since proteins are particularly delicate to handle (unfolded proteins are required for protein-based hydrogels), needing to be combined with other polymers[202,206].

Polysaccharides, instead, are mainly derived from animals, plants, algae, and microorganisms. Thanks to their good biocompatibility, biodegradability and low toxicity, but also to their self-healing and shear-thinning behaviour (due to the dynamic covalent and non-covalent interactions within their molecular structure) they are extensively used for biomedical applications[207,208]. Polysaccharide-based hydrogels are particularly exploited as drug carriers due to their strong affinity for mucosal layers (e.g. in the gastrointestinal tract), and their ability to stabilize encapsulated drugs allowing controlled release[207]. However, traditional polysaccharide-based hydrogels composed of one single component present some limitations, like poor mechanical strength (Figure 11). Despite these challenges, both polysaccharide-based and protein/peptide-based hydrogels are promising for biomedical applications, especially after chemical modifications that allow to overcome their single disadvantages and improve their properties[202,209].

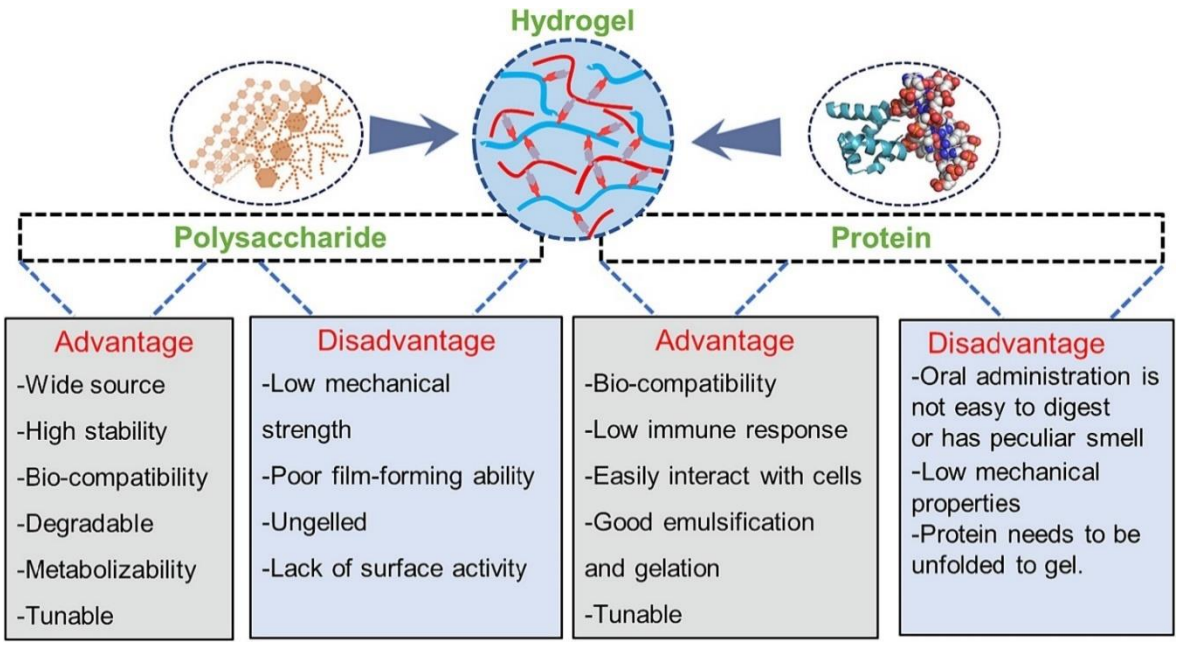

Figure 11. Summary of the main advantages and disadvantages of polysaccharide-based hydrogels and protein/peptide-based hydrogels[202].

Below there are some examples that highlight the remarkable applicability and versatility of some of the most used biomaterials.

Gelatin, a natural polymer derived from animal collagen's hydrolysis, has been often used for hydrogel formulation thanks to its temperature-induced gelation and its several biological properties, like biocompatibility, low antigenicity, biodegradability, and ability to promote cell growth and attachment. For these advantageous features, gelatin is utilized in various medical applications as a tissue engineering scaffold, supporting cell growth and tissue regeneration, for wound dressings, to create a conducive healing environment, in controlled drug delivery systems, and as a haemostatic agent during surgical procedures. As methacrylated gelatin, it is often exploited in 3D printing, stabilizing the printing constructs after extrusion by photo-crosslinking [82,132,210–212].

Chuang et al. designed a biofunctionalized hydrogel incorporating lyophilized platelet-rich fibrin (containing several growth factors), into a genipin-crosslinked gelatin/hyaluronic acid hydrogel to create an injectable material for segmental bone defect repair. The study

highlighted the advantages of this type of hydrogel as well as the benefits of biological properties linked to the use of this mix of growth factors, demonstrating the potential application of the developed system for bone tissue engineering[211].

Shih et al. fabricated 3D-printed biocompatible proangiogenic patches using a combination of living cells and biodegradable hydrogels. In detail, they formulated a bioink incapsulating endothelial cell in photo-crosslinked gelatin bioink and smooth muscle cells in polyurethane hydrogels. Implantation of 3D-bioprinted proangiogenic patches in a mouse model showed the formation of new microvessels, indicating the system's capability to induce angiogenesis for treating ischemic vascular diseases[212].

Alginate is a natural polysaccharide mainly extracted from marine brown algae, whose backbone is composed of β-D-mannuronic acid and α-L-guluronic acid connected by glycosidic bonds. Alginate-based hydrogels, whose formation is favoured by the presence of divalent ions, particularly calcium (Ca^{2+}), are widely used in drug delivery systems, in wound healing, but also in 3D printing as inks, where inotropic crosslinking can stabilize printed constructs [191,213,214].

Fang et al. developed an injectable hydrogel based on oxidized sodium alginate, gelatin and chondroitin sulfate for the minimally invasive treatment of osteochondral defects. The hydrogel possessed a double network based on hydrogen bonds and dynamic Schiff-base bonds, demonstrating impressive injectability and self-healing properties. Furthermore, it guided the controlled release of active components to the lesion site and promoted the formation of new tissue, providing interesting results for both articular cartilage and subchondral bone injuries[214].

Hyaluronic acid is a glycosaminoglycan, naturally present in human ECM, whose structure is composed alternately of D-glucuronic acid and N-acetyl-D-glucosamine. It is well-known for its strong hydrophilicity, due to its numerous carboxyl and hydroxyl groups, for its high

biocompatibility, biodegradability and low toxicity, which make it a valuable component in many cosmetic products and an interesting biomaterial for wound healing and drug delivery hydrogels[142,215–217].

For example, Duan et al. designed injectable hyaluronic acid-based hydrogels for diabetic wound healing. In particular, the latter was developed by incorporating platelet-rich plasma into dopamine-modified hyaluronic acid crosslinked through Fe^{3+}. In this way, the systems showed good injectability, tissue adhesiveness, rapid self-healing and anti-inflammatory and anti-oxidative properties. At the same time, the hydrogels demonstrated the capability to promote fibroblast proliferation and migration (thanks to the platelet-rich plasma) and antibacterial properties, proving, *in vivo*, a fine regulation for the microenvironment of the diabetic wounds and promoting their complete regeneration[216].

In another study, Wang et al. evaluated the application of a hyaluronic acid-based hydrogel for the preservation of cardiac functions after myocardial infarction. In detail, they developed an injectable hydrogel composed of hydrazide and phenylboric acid derivatives of hyaluronic acid and oxidized dextran, which showed a strong antioxidant effect *in vitro* and *in vivo* and the capability to protect cells from oxidative stress damage. Furthermore, it reduced fibrosis, promoted vascularization, and preserved cardiac functions over a long-term period, suggesting its potential use to preserve cardiac functions after infarction, but, at the same time, its application for the treatment of other types of inflammation-related diseases[217].

Chitosan, on the other hand, is a linear polysaccharide derived from chitin (extracted from crustacean exoskeletons), consisting of D-glucosamine and N-acetyl-D-glucosamine units. Chitosan is particularly known for the presence of free amino groups, which are protonated under neutral or acid conditions, enhancing, thus, its water solubility and bioadhesiveness (by electrostatic interactions with negatively charged mucosa surfaces), but, above all,

conferring it intrinsic antimicrobial and antifungal properties that are useful for the treatment of infected wounds[26,76,104,218–220].

Ding et al. designed injectable hydrogels based on salic acid chitosan and oxidized dextran incorporating also different amounts of plant-derived polyphenol tannic acid. The hydrogels, based on Schiff-base reaction, exhibited excellent self-healing and injectable properties, as well as, *in vitro* ROS scavenging and antibacterial activity, suggesting their potential in treating skin wounds in clinical practice[220].

All these examples highlight the potential of both injectable hydrogels and natural-derived biomaterials for this purpose. However, among polysaccharides, gellan gum and xanthan gum need to be carefully and thoroughly focused for their remarkable properties, which have significantly increased their use in the biomedical field.

1.7.1 Gellan gum

Gellan Gum (GG), a water-soluble linear anionic polysaccharide with high molecular weight, shows a wide range of applications in the chemical, pharmaceutical, cosmetic, and food industries due to its exceptional biocompatibility, biodegradability, low cytotoxicity, low cost and industrial reproducible production. Indeed, it is a highly versatile food additive used as a stabilizer, texturizer, film-forming and suspending agent. However, it is, also, extensively applied in the production of biomaterials for biomedical applications, thanks to some own peculiar features like temperature and ionic strength-sensitive gelation properties and adjustable physical and mechanical characteristics. It is an optimal starting material for the development of hydrogels for the controlled delivery and release of therapeutic agents, as well as a good material for regenerative medicine applications[221–223].

GG is an exopolysaccharide, produced by the bacterium group *Sphingomonas*, discovered in 1978 but approved by the FDA in 1992. The primary structure of this biomaterial consists of the repetition of tetramers formed by β-D-glucose, β-D-glucuronic acid, β-D-glucose, and

α-L-rhamnose, linked by α- and β-glycosidic bonds according to the following structure: [D-Glc(β-1,4)D-GlcA(β-1,4)D-Glc(β-1,4)L-Rha(α-1,3)]$_n$ (Figure 12)[224].

The secondary structure can be represented by a coaxial double helix where each chain twists three times on its vertical axis. The interactions between the two linear chains of the helix are due to the chemical groups of the repetitive units: specifically, the three β-1,4 glycosidic bonds allow for equatorial bonds, meaning they lie in the same plane as the ring; while the α-1,3 bond induces an orderly and repetitive rotation in the polymer's structure. This type of twist is not random but follows a regular and predictable pattern, influencing the 3D conformation of this polysaccharide and, thus, its properties[225].

The natural form of GG presents an L-glycerol substituent on the third carbon of the first monomer (D-Glc) of the repeating unit and an acetyl group on the anomeric carbon of the same residue, that, however, can be removed with a thermal treatment with alkali[226,227]. This leads to a classification of GG into two main types based on its acyl group content: high-acyl GG (haGG) and low-acyl GG (laGG) (Figure 12), which have different physicochemical properties and, consequently, give rise to aqueous dispersions and hydrogels with different viscoelastic behaviour[228]. The haGG forms soft and elastic hydrogels, while laGG produces brittle hydrogels. Additionally, haGG is remarkably stable and maintains its properties over a wide temperature range. Therefore, the choice between haGG or laGG depends on the specific application requirements[229].

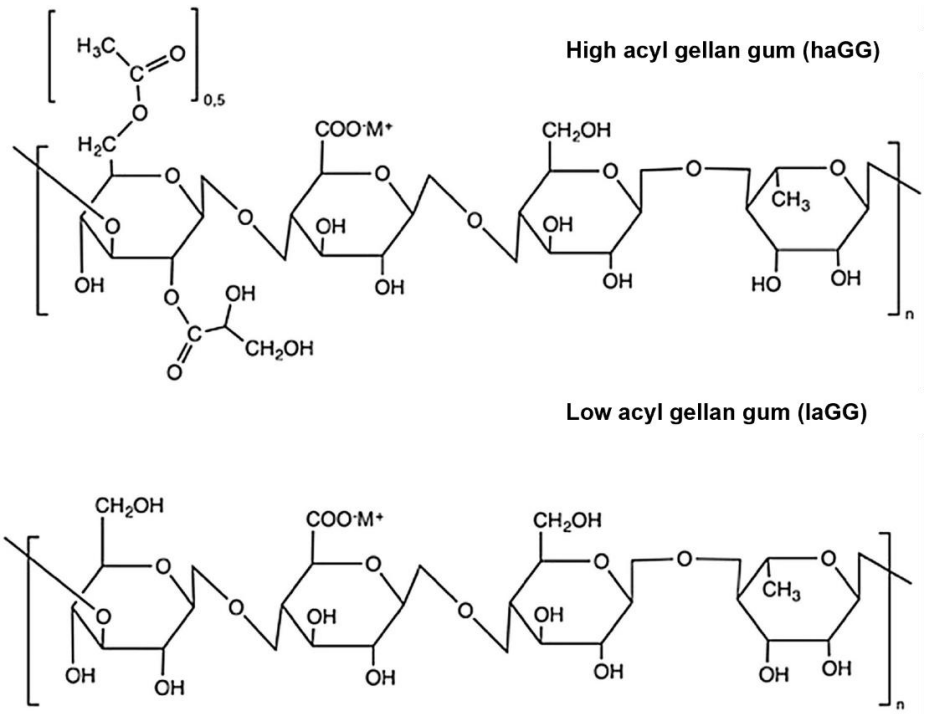

Figure 12. Chemical structure of high acyl gellan gum (haGG) and low acyl gellan gum (laGG)[224].

Regarding the gelation process of GG, its gelling properties are influenced by various factors, such as temperature, pH, polymer concentration, molecular weight, and the presence and type of cations in the solution[223]. One of the main gelation features of GG in its natural form is the physical and reversible gelation depending on temperature, which leads to physical hydrogels; indeed, when heated to temperatures equal to or higher than 90°C, a homogeneous liquid dispersion of GG is obtained. As the temperature decreases, there is a *sol-gel* transition that leads to the formation of GG physical hydrogels. In more detail, GG exhibits a thermotropic gelation process due to a random coil to double helix conformational transition. At 90°C, the GG polymer chains (in aqueous dispersion) are in a random coil state, while as the temperature decreases, the polymer chains undergo structural reorganization into double helix systems (coil to helix transition), followed by the formation of complex and ordered 3D network due to aggregation resulting in hydrogel's formation (thermo-induced *sol-gel* transition) (Figure 13)[224].

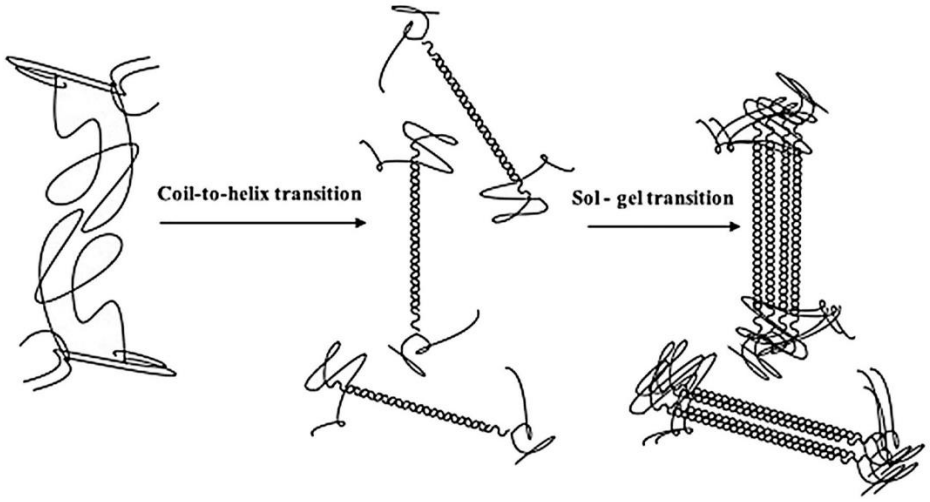

Figure 13. Coil-to-helix and *sol-gel* transition of gellan gum[224].

GG, also, shows an ionotropic gelation, which means that GG is ion-sensitive as its dispersions are sensitive to the presence of ions in the medium. Specifically, both monovalent and divalent cations can interact electrostatically with the carboxylate groups of D-glucuronic acid, inhibiting the repulsion between the polymer chains. This clearly leads to a greater degree of interaction between them, thus increasing the hydrogel's architectural strength. Moreover, divalent cations can form additional bonds between spatially close carboxylate groups, resulting in more intense ionotropic crosslinking than that given by monovalent cations[230].

Furthermore, since GG is an anionic polysaccharide due to the presence, in its backbone, of not completely protonated carboxylic groups (in physiological conditions), it is strongly influenced by pH too. Specifically, it has been observed that at pH values between 3 and 5, carboxylic groups will predominantly be in non-ionized form, minimizing repulsions between polymer chains and inducing stronger aggregation and greater structuring of the corresponding hydrogels. Additionally, the H^+ ion, like monovalent cations, exerts a shielding effect on the electrostatic repulsion between the ionized carboxylic groups, increasing aggregation of the different helices[231].

Despite these interesting properties, that led to the application of GG-based hydrogel in many fields, it is worth highlighting some disadvantages of the native form of the polysaccharide. For example, the gelation temperature is incompatible with most cell encapsulation strategies, GG hydrogels are unstable due to cations exchange in physiological media (the higher concentration of Na^+ compared to Ca^{2+} results in the substitution of Ca^{2+} with Na^+, which weakens the hydrogels and leads to premature degradation *in vivo*) and is free of specific attachment sites for anchorage-dependent cells. However, different strategies have been developed to reduce the gelation temperature of GG and improve the processability of its dispersions and the stability of its hydrogels[224].

Strategies for reducing GG molecular weight through ultrasound, alkaline or oxidizing solutions result in a suitable decrease in molecular weight and thus gelation temperature, overcoming the aforementioned disadvantages. Furthermore, reducing molecular weight often allows GG derivatives to be dispersed in saline solutions (e.g., phosphate buffer) due to lower ionic strength sensitivity, making formulations easier to handle and prepare, even in cell therapy[226,232,233].

Moreover, GG can be functionalized in various ways, depending on the application for which the hydrogels are intended (Figure 14). For instance, degradation kinetics, rheological and biological characteristics, as well as tissue-specific properties, can be modified through grafting or copolymerization, achieving new and desired physicochemical properties. The latter depends on the degree and type of functionalization: carbodiimide amidation, esterification, and other chemical reactions have enabled the functionalization of hydroxyl and carboxyl groups of the repeating units with acrylates, methacrylates, thiol groups, amine, alkyl chains and other substituents[95,111,234–236].

Chemical structures of some GG derivatives	Chemical procedure
Functionalization of OH groups	
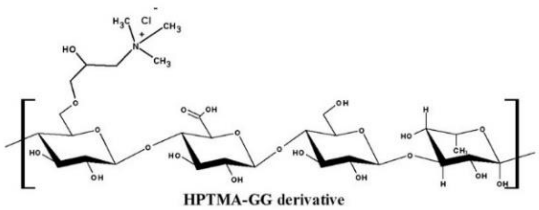 HPTMA-GG derivative	Functionalization of OH groups with the alkyl chloride of 2-hydroxypropyl-trimethyl ammonium (HPTMA) performed in water, under alkaline conditions.
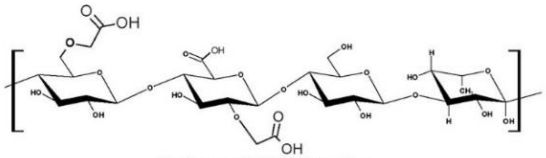 Carboxymethyl GG derivative	Treatment of gellan with sodium monochloroacetic acid under alkaline conditions
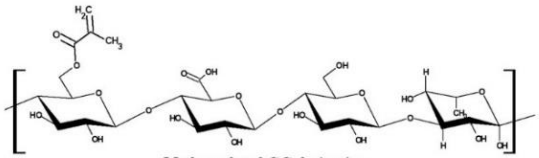 Methacrylated GG derivative	Gellan Gum in water with methacrylic anhydride at pH 8-9
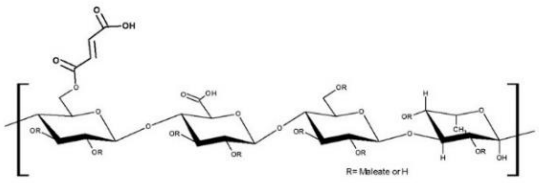 GG Maleate derivative	Gellan Gum dispersed in acetone With the addition of Maleic Anhydride
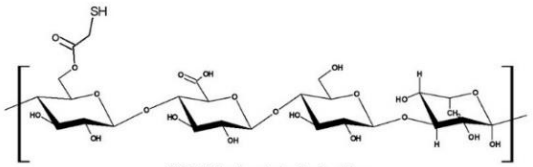 GG Thioglycolate derivative	Gellan Gum in acid solution 3 h at 80 ◦C under reflux conditions
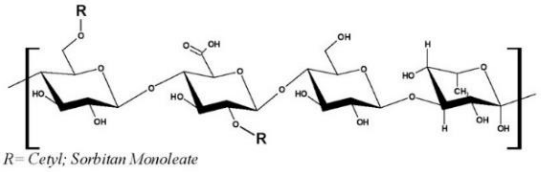 *R= Cetyl; Sorbitan Monoleate* Cetyl and sorbitan monoleate GG derivatives	Activation of OH groups performed in DMF with the addition of sodium hydride to obtain the GG alkoxide. Afterwards, reaction of the GG alkoxide with the alkyl chloride in DMF
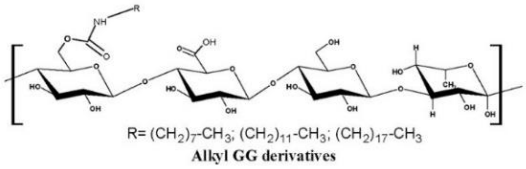 R= $(CH_2)_7$-CH_3; $(CH_2)_{11}$-CH_3; $(CH_2)_{17}$-CH_3 Alkyl GG derivatives	p-Nitrophenol mediated functionalization of OH groups with alkylamines performed in organic solvent
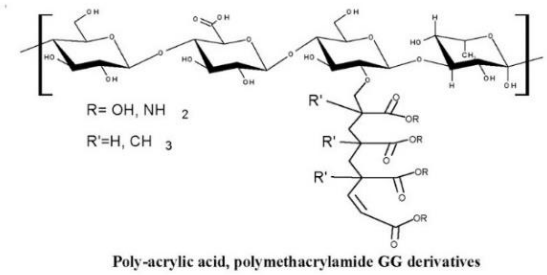 Poly-acrylic acid, polymethacrylamide GG derivatives	Microwave-promoted free radical initiation method performed in aqueous environment

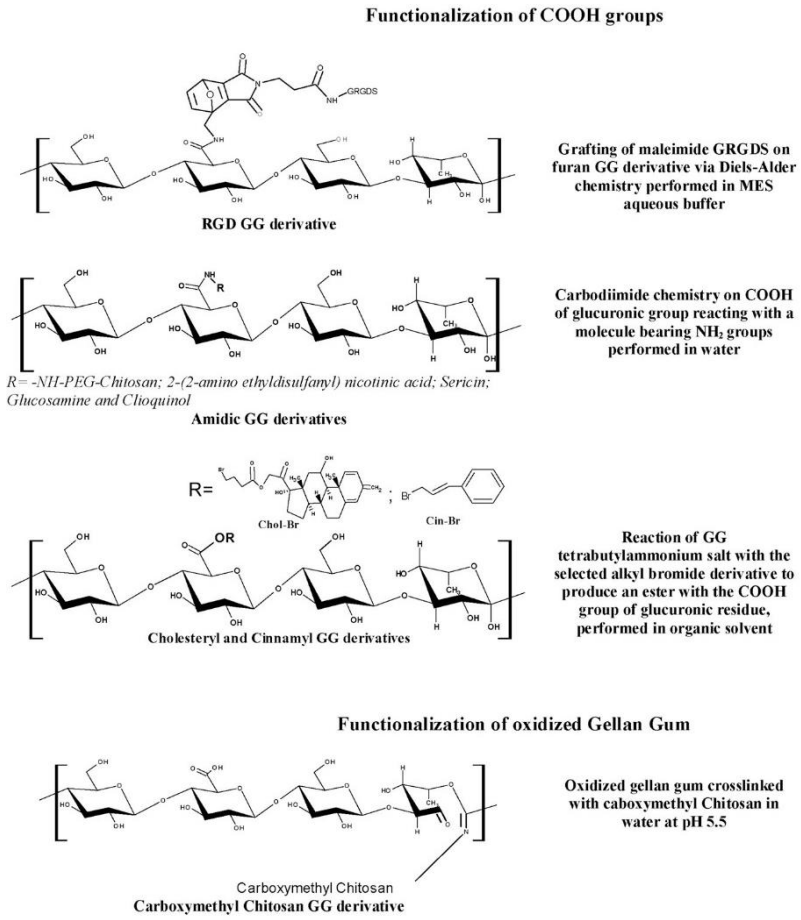

Figure 14. Chemical structures of some GG derivatives[224].

One of the main chemical modifications of GG is the methacrylation. This functionalization, introducing methacrylic groups into the GG backbone, allows photo-crosslinking of its hydrogels, increasing their *in vitro* and *in vivo* strength and stability, making it possible, also, their application in the regeneration of hard tissues, like bone and cartilage. Many researchers have studied this reaction, developing it with different approaches[234,237,238]. For example, Coutinho et al. developed methacrylated GG (GG-MA) hydrogels by reacting GG with varying amounts of methacrylic anhydride, creating hydrogels with two different degrees of methacrylation. Combining physical crosslinking methods (such as adding cations) with chemical crosslinking approaches (via photo-crosslinking) allowed the development of GG-MA hydrogels with highly adjustable physical and mechanical properties without compromising biocompatibility[237].

Additionally, Vieira et al. developed a methacrylated GG (GG-MA) through the reaction of GG with glycidyl methacrylate to formulate hydrogels to promote osteogenesis and allow dexamethasone release. GG-MA hydrogel undergoes an initial photo-induced crosslinking process followed by subsequent ionotropic crosslinking with calcium chloride, further improving its hydrolytic resistance and viscoelastic and mechanical properties[238].

These two different approaches, using a different chemical mechanism of functionalization, exploited both double physical and chemical crosslinking.

Jongprasitkul et al. exploited GG-MA for 3D printing for biomedical applications. In detail, they pre-crosslinked GG-MA dispersion with Ca^{2+} to confer suitable viscoelastic properties to obtain good extrudability. The 3D-printed constructs were further photo-crosslinked to stabilize their structure. In this way, the two-step crosslinking approach allowed to get hydrogel-inks with good printability for future biomedical applications[239].

Pitarresi et al. designed a hydrogel based on a low molecular weight alkyl derivative of GG containing tricalcium phosphate and hydroxyapatite nanoparticles as an injectable scaffold for bone tissue regeneration. The alkyl derivative functionalization occurred on the free hydroxyls of the polysaccharide, leaving the acid functions (carboxyl group) free and thus not altering the polymer's ionotropic properties. The amphiphilic nature of the obtained derivative, along with its thermotropic behaviour and ionotropic crosslinking characteristics, enabled the production of scaffolds that mimic bone tissues and can be used to release osteoinductive biomolecules[240].

Functionalization could also improve the biological properties of GG. This polymer, indeed, is characterized by the lack of cell adhesion sites, mainly attributed to the extreme hydrophilic nature of its hydrogels, which per se allows water molecules to bind to the polymer backbone, but also to the negative charge of the polymer that repulse cells, limiting the adsorption of cell-adhesive proteins before cell attachment[241]. To overcome this

feature, GG was often functionalized or used in combination with proteins and peptide sequences[242–244]. Alheib et al. developed injectable GG-based hydrogels for the delivery of skeletal muscle cells to treat localized muscular trauma. In particular, they functionalized GG with laminin-derived peptide to mimic the native muscular ECM, thus conferring the polysaccharide cell-friendly properties. In this way, it was possible to encapsulate muscle cells into the hydrogels, thus promoting myogenesis, neoinnervation and angiogenesis. The obtained results suggested that this type of approach could represent a reliable strategy for the regeneration of localized muscular trauma[244].

The results of all these studies indicate that the use of GG derivatives allows for overcoming some limitations of the native polymer, such as reduced physical stability, handling difficulty, high-temperature operating conditions and the lack of cell adhesion thus obtaining a biomaterial suitable for the desired applications. These properties make the described polymer ideal for biomedical applications.

From this point of view, as partially highlighted with the previous examples, GG is, often, used for the production of injectable hydrogels for drug delivery and regenerative medicine applications.

Chen et al., for example, formulated a new injectable, double-crosslinked and magnetic hydrogel for drug delivery and bone repair. The systems were prepared by Schiff-base reaction and ionic interactions between carboxymethyl chitosan and oxidized GG. Furthermore, magnetic hydroxyapatite/gelatin microspheres containing antibacterial drugs (tetracycline hydrochloride and silver sulfadiazine) and hydroxyapatite were incorporated into the hydrogels to improve their mechanical and biological properties and confer antimicrobial activity, with a controlled (magnetically) release of bactericidal substances. In this manner, the formulation could be a therapeutically effective platform for drug delivery and bone regeneration[245].

Choi et al. functionalized GG with β-cyclodextrin derivative to administrate dexamethasone by forming inclusion complexes. In this way, it was possible to formulate injectable hydrogel for the delivery of this anti-inflammatory drug and thus reduce the inflammatory response in cartilage tissues improving, at the same time, chondrogenesis[246].

Biscari et al. synthesized dopamine and PEG functionalized GG for the production of injectable hydrogels with radical scavenging activity and both specific and nonspecific antimicrobial properties. Specifically, the hydrogels were produced by mixing this derivative with colistin sulphate, thanks to the formation of electrostatic interactions. Also, polymeric GG-based microparticles, with polydopamine coating, were introduced into the system conferring simultaneously antioxidant and photothermal and, thus, non-specific antimicrobial properties. In this way, a synergistic antibacterial effect was possible by combining the photothermal effect with colistin's release. The obtained results demonstrated that the hydrogels could be interesting candidates for the treatment of infected wounds[247].

1.7.2 Xanthan gum

Xanthan gum (XG) is a natural biodegradable exopolysaccharide extracted from *Xanthomonas* microorganisms through a fermentation process[248,249]. It is a water-soluble polymer with high molecular weight (around 10^6 g/mol) composed of repetitive units consisting of a β-D-glucose backbone alternatively linked by β-1,4 bonds to trisaccharide side chains of β-D-mannopyranosyl-(1,4)-α-D-glucopyranosyl-(1,2)-β-D-mannopyranosyl-6-O-acetate. The ketal linkages connect pyruvic acid residues to about half of the terminal mannose residues. The amount of pyruvic acid is related to the fermentation process and the Xanthomonas strain used (Figure 15)[250,251].

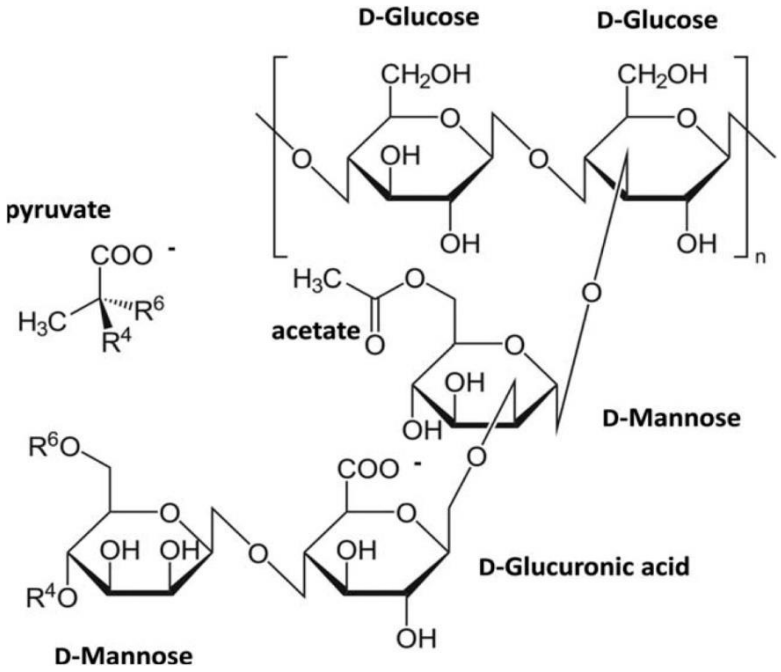

Figure 15. Primary structure of xanthan gum[252].

The secondary structure of XG is represented by a helix with a pitch of 4.7 nm and a diameter of 1.9 nm, which undergoes a thermally induced conformational transition from a helix to a spiral structure[253,254]. XG, easily dispersible in hot water, but also in cold water under intense agitation to avoid clumping, gives rise to viscous dispersions which behave as non-Newtonian fluids and exhibit highly pseudoplastic behaviour. Generally, the thermal stability of XG is far better than many other polysaccharides or water-soluble polymers, likely due to the ordered helical structure of XG protecting the molecules from depolymerization[255]. Thus, the viscosity of XG dispersions is only minimally affected by thermal treatment processes (e.g., sterilization) and is also not influenced by pH.

XG acts as a polyanion at pH levels higher than 4.5 due to the deprotonation of O-acetyl and pyruvyl residues[252]. For this reason, the viscoelastic properties of XG dispersion can be influenced by monovalent and divalent ions depending on their concentration. In detail, the viscosity could decrease because of the charge shielding effect on the electrostatic repulsion between carboxylate groups[256], but, from the other side, it may increase in the presence of divalent ions because of their crosslinking effect[248,257]. Regarding the latter, XG

chains can form physical networks with divalent cations by involving two disaccharide units in the main chain and O-acetyl and pyruvyl residues in the side chains, leading to intramolecular crosslinking and chain contraction[248].

A key factor that needs to be discussed refers to the rheological properties of XG dispersions since it is crucial for the development of injectable hydrogels. The viscosity of XG dispersions strongly depends on several factors, like ion concentration, polymer concentration or XG molecular weight. In particular, because of shear-thinning properties, at low shear rates, the viscosity of XG aqueous dispersions is higher than the viscosity when high shear rates are applied. Moreover, at low shear rates and in the absence of electrolytes, the viscosity increases linearly with the increase in XG concentration in the range of 0.3–2.0 g/L, but it decreases substantially when salt is added[258]. Furthermore, for XG concentrations above 2.0 g/L and in the presence of salt, the viscosity increases with increasing shear rate. These changes occur due to the variation in molecular conformation from an ordered state (helical molecular conformation) to a disordered state (extended conformation due to strong electrostatic repulsions between like charges) (Figure 16)[259]. Indeed, at lower concentrations below 2.0 g/L, the addition of salt neutralizes the ionic charge of the XG chains, resulting in a conformational change towards a helical structure, with a decrease in viscosity. However, at a higher polymer concentration (> 2.0 g/L), the addition of electrolyte causes a conformational change towards the more extended form, responsible for the increased viscosity[254].

Despite all the advantages of XG, one limitation, linked to its physicochemical properties, is its slow dissolution rate since it first needs to swell, after solvent penetration, and only then it can dissolve. This process can sometimes be excessively long (based on molecular weight and concentration of XG), to the point that it could be disadvantageous to use this biomaterial[260].

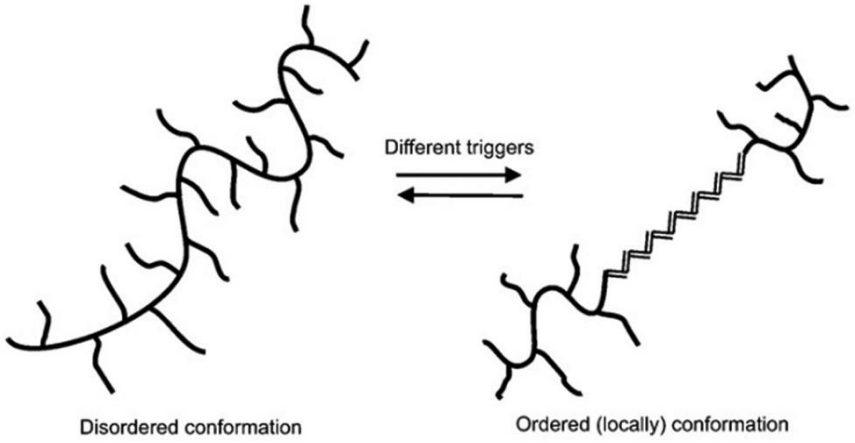

Figure 16. Schematic of conformational transition of xanthan gum chains in aqueous solution[261].

Concerning XG applications, due to its advantageous properties (absence of toxicity, biocompatibility, biodegradability, thermal stability), this biomaterial has been recognized as safe and approved by the US FDA for use as food additive without any application limit[262,263]. Furthermore, XG has, also, extensively been used in a wide range of applications such as food packaging, water-based paints, the petroleum industry, water treatments, oil recovery, toiletries, cosmetics, and drug delivery[264–267]. Regarding the latter application, due to its mucoadhesive properties, XG has found widespread application in the formulation of drug delivery systems for the localized release of drugs, ensuring they remain longer at the application site (buccal, topical, mucosal)[268–270].

XG has recently attracted great attention as a biomaterial for the preparation of hydrogels for tissue regeneration. However, it is often mixed with other materials or functionalized to improve some properties or better meet the application needs[254].

Indeed, XG possesses hydroxyl and carboxyl groups that can be modified through physical, chemical, chemo-enzymatic methods, or a combination of these approaches. Carboxymethylation is among the most common modifications of XG: in the presence of chemical agents such as monochloroacetic acid and sodium hydroxide, ether bonds are formed between the primary hydroxyl groups of the XG repeating units and

carboxymethylated molecules. The modification results in a reduction in the molecular weight of XG, an increase in hydrophilicity, and a reduction in the viscosity and elastic modulus of aqueous dispersions[271,272].

XG can also be functionalized through the esterification of the primary hydroxyl group, binding molecules of different natures and properties[273,274]. Another modification of the XG polymer backbone is oxidation, which partially converts glucopyranose units into aldehydes and creates additional functional sites for covalent crosslinking. Oxidized xanthan gum (XGox) can be obtained through oxidation mediated by sodium metaperiodate, which causes the cleavage of C–C bonds between (–CHOH) groups of the D-glucose units to form dialdehydes. Specifically, this method improves the reactivity of the polysaccharide and allows covalent interaction with polymers having amino or hydrazine groups, thus forming Schiff bases[264,275–278]. Kumar Sharma et al. formulated an injectable hydrogel based on oxidized XG (XGox) and 8-arm polyethylene glycol functionalized with hydrazine for controlled release of doxorubicin. Through the formation of hydrazone bonds, an injectable, self-healing system with optimal rheological properties was obtained for local anticancer treatment[278].

Namazi et al. exploited XGox for 3D printing through dynamic crosslinking with gelatin via Schiff base reaction. The developed hydrogel/inks showed suitable viscoelastic properties, good extrudability and shape maintenance making possible their future use for 3D printing applications[277].

In another study, Chen et al. designed double-crosslinked hydrogels using Schiff base reaction, but at the same time, adding one more crosslinking through UV irradiation. In detail, they utilized carboxymethyl chitosan and aldehyde/glycidyl methacrylate functionalized xanthan gum to develop a 3D-printed hydrogel for the treatment of tubular enterocutaneous fistulas. While the first dynamic network enhanced printability, the second

one (photo-crosslinking) conferred to the system enough high strength and effective resistance against corrosion by intestinal fluid and the high pressure of the intestinal cavity, and, lastly, excellent anti-digestive performance[276].

Double-network formation was exploited also by Zhang et al. to develop an injectable conductive hydrogel for cardiac regeneration after myocardial infarction. The system was composed of oxidized xanthan gum grafted with 3-aminophenyl boronic acid, gelatin and dopamine-grafted gelatin, which established imine and boronic ester bonds. By encapsulating polydopamine-rosmarinic acid nanoparticles and adding conductive polypyrrole-modified gelatin, the hydrogel showed anti-inflammatory and anti-fibrosis effects, good mechanical strength, conductive properties, restoring electrical signal transmission in the infarct area, inducing angiogenesis and promoting the expression of cardiac-specific markers to restore cardiac function[275]. These examples from the scientific literature highlight the possibility of exploiting XG and its derivatives both for injectable hydrogels production and 3D printing applications.

1.8 Biomedical applications of injectable hydrogels

The use of injectable hydrogels has greatly increased due to their versatile and highly tunable properties, as well as advances in biomaterial technologies. They are currently employed for several biomedical applications, including tissue engineering, drug delivery, wound healing, cellular encapsulation, disease modelling, immunomodulation, biosensors, and cosmetic fillers. Furthermore, as previously highlighted, they could be exploited, with some appropriate modifications, in 3D printing and bioprinting for the regeneration of damaged tissues, the creation of disease models for drug screening, and the development of new advanced drug delivery systems[2,33,279].

Injectable hydrogels exhibited excellent properties as carriers for topical and localized drug delivery. Various kinds of payloads, e.g. drugs, peptides, proteins, nanoparticles and genes,

can be loaded into a hydrogel matrix, by absorption and/or encapsulation method. Compared to systemic administration, topical injectable hydrogels are favourable for sustained or controlled release and, of course, to treat local wounds[76,120]. In this sense, incorporated drugs (both hydrophilic and hydrophobic molecules) can be released from the hydrogel matrix by various mechanisms: free diffusion and erosion of the matrix are usually the main ones. Furthermore, the release can be also influenced by external or internal stimuli (temperature, pH, glucose concentration, redox, enzymatic reactions, magnetic field and light irradiation) thanks to the incorporation of sensitive moieties in the polymer backbone. Thus, these drug delivery systems, are exploited for different purposes: treatment of inflammatory diseases, eradication of microbial infections, and cancers, tissue repair and regeneration through the delivery of growth, and chemoattracted factors[90].

As already mentioned, injectable hydrogels are, also, increasingly used in regenerative medicine for tissue regeneration due to their exceptional ability to mimic the natural 3D tissue environment. This capability makes possible cell encapsulation and the incorporation of bioactive molecules and nanostructures, rendering ideal candidates for promoting the regeneration of damaged tissues[2]. Furthermore, when combined with 3D printing technology, these hydrogels allow for precise control over morphological properties and, for 3D bioprinting, also on the cellular disposition, allowing too deep imitation of the physicochemical, mechanical and biological properties of the human tissues[93,98,123,161,171].

1.8.1 Use of injectable hydrogels for the treatment of local microbial infection

As drug delivery systems, injectable hydrogels are often applied for the delivery of antimicrobial agents to eradicate topical infections and, thus, support the regeneration of wounds or injuries[120,198,280,281].

The prevention and treatment of local infections caused by microbes like bacteria, viruses, mycetes and parasites, is a global health issue, mainly due to the low efficacy of current antimicrobial treatments and the rapid development of antibiotic resistance[282]. The main factors of increasing antibiotic resistance are the misuse and overuse of conventional antibiotics, coupled with a declining tendency for new antibiotic development against resistant microbes[283,284]. Consequently, there is an urgent need to develop innovative strategies to overcome this challenge[285,286].

To address this goal, several therapeutic approaches have been developed: new micro- and macromolecular antimicrobial agents, as well as natural extracts with antimicrobial properties and metallic nanoparticles, emerged as effective treatments[287–290]. However, despite their effectiveness, these materials show some limitations that restrict their therapeutic efficacy, such as low potency, limited bioavailability, lack of controlled release, high dosage requirements and potential toxicity[291].

In this scenario, hydrogels appear as attractive systems for the delivery of antimicrobial agents, allowing high efficacy, improved bioavailability, long-term effects and controlled/sustained release. Furthermore, their rheological properties allow for prolonged retention on the surface and controlled diffusion of bioactive molecules that may reduce the need for frequent administration, enhancing patient compliance[292].

In addition to the mentioned advantages, it is important to highlight that the use of hydrogels in the treatment of infected wounds offers significant benefits since they can absorb exudate from the wound, maintaining, at the same, time, a hydrated environment that facilitates physiological diffusion of nutrients and bioactive molecules. Moreover, injectable hydrogels can efficiently fill target sites with irregular shapes and guarantee perfect integration with surrounding tissues[293].

Several systems have been developed over the past few years to address this issue. These treatments are directed not only towards the mucous membranes of our body (vaginal, buccal) but are specially designed for the regeneration of chronic and infected skin wounds.

1.8.1.1 Injectable hydrogels in wound healing

The skin, composed of three layers (epidermis, dermis, and hypodermis), is the largest organ of the human body and represents the first defensive barrier of the organism against pathogens, UV radiation, chemicals and mechanical damage[294]. Following the formation of wounds, the skin can regenerate itself since it possesses self-repair capabilities: this is particularly true for acute injuries, which are usually healed within 8-12 weeks. However, if the regeneration process goes over 12 weeks or does not complete normally, the wound is considered chronic and needs an external intervention for a complete regeneration[295,296]. In general, wound healing is a complex process that can be ideally divided into four phases (haemostasis, inflammation, proliferation, and remodelling), which involves cells, proteins and enzymes, aiming to restore the morphological and functional properties of the damaged site[297]. However, several factors can influence this process, leading to a tardive or incomplete regeneration and, thus, to the formation of chronic wounds (Figure 17). They include pathological conditions such as diabetes, poor blood circulation, old age, weakened immune system, large-sized injuries, excessive oxidative stress and pro-inflammatory responses, or infections caused by resistant microorganisms such as bacteria (*Staphylococcus aureus*, *Streptococcus pyogenes*, *Pseudomonas aeruginosa*, *Escherichia coli*), mycetes (e.g. *Candida albicans*) or protozoa (e.g. *Leishmania*)[298–300].

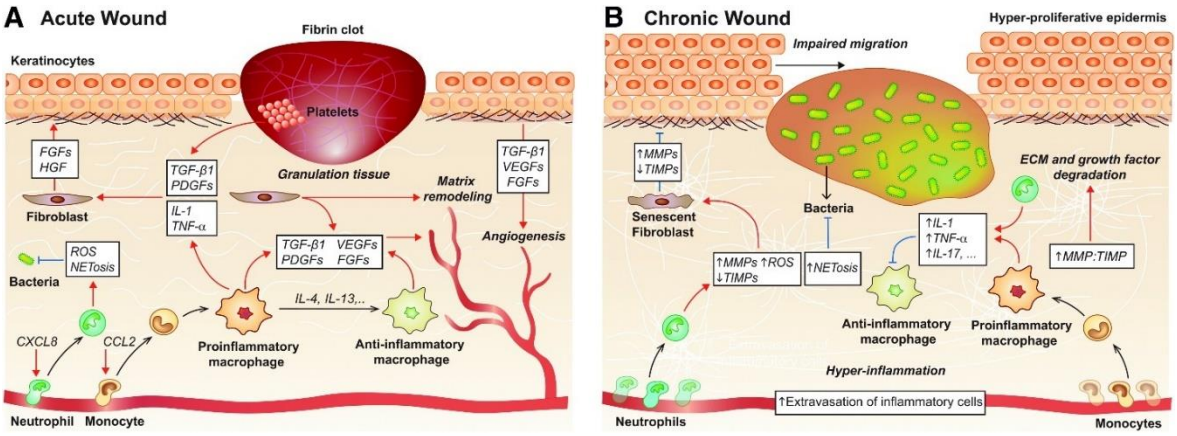

Figure 17. Overview of the physio-pathological mechanisms in acute and chronic wound healing[297].

In all these cases, innovative therapies are necessary: in this scenario, the use of injectable hydrogels and 3D printing systems plays a significant role. The latter, in particular, allows not only the previously mentioned advantages but also to modulate the architecture of the constructs for perfect adaptability to the lesion's shape, as well as to better control the release of pharmacological agents, thus playing a crucial role in personalized therapy.

For example, Bergonzi et al. developed printable antibacterial hydrogels based on chitosan and alginate, doped with silver sulfadiazine as a drug model, for wound healing. The study demonstrated the advantages of 3D printing since it was possible to obtain different drug release profiles and, consequently, antimicrobial potency from different 3D printed constructs, offering, thus, a key for the tailoring of drug administration as a function of the wound-healing stage. In this sense, 3D printing could apport significant advantages in personalized therapies[301].

In another study, Wang et al. exploited the advantages of 3D printing for wound regeneration using novel hydrogels with antibacterial and antioxidant properties composed of glycidyl methacrylate-modified carboxymethyl cellulose and ε-polylysine. Combining the good mechanical properties of carboxymethyl cellulose-derivative hydrogels with the strong

antibacterial properties of ε-polylysine, they obtain systems with a higher capability for commercial dressing and which were applicable in personalized medicine[302].

Tang et al., on the other hand, developed a ROS-responsive injectable hydrogel composed of ε-polylysine functionalized with caffeic acid and phenylboronic acid grafting hyaluronic acid, doped with a mixture of CaO_2@Cur-PDA consisting of calcium peroxide (CaO_2) coated with polydopamine (PDA) and curcumin (Cur). The release of caffeic acid-grafted ε-polylysine, O_2, curcumin, conferred to the system antibacterial, antioxidant and angiogenetic properties, allowing also to regulate macrophage polarization. In this way, it could be possible to accelerate the regeneration of diabetic-infected skin wounds[303].

Wei et al. designed an antimicrobial injectable hydrogel exploiting the photothermal properties of PDA. In detail, the hydrogel was composed of methacrylated gelatin and oxidized hyaluronic acid, incorporating also polydopamine nanoparticles; the latter, by means of its photothermal conversion under near-infrared light irradiation conferred to the hydrogel not-specific antimicrobial properties overcoming classic antibiotics limitations. In this way, thanks to its antioxidant potential too, the hydrogel appeared as a good candidate for the treatment of infected skin wounds[304].

As previously discussed, and also highlighted from the previous examples, the delivery of antimicrobial agents that are not only effective against various microbial strains (primarily bacteria) but also prevent the emergence of resistant microbial species is a crucial aspect. In recent years, new molecules extracted from animal and plant organisms[305,306], as well as metal nanoparticles[288,307], have gained significant attention.

In particular, metal nanoparticles represent an innovative approach for the treatment of microbial infections, given their non-specific action and the limited phenomena of bacterial resistance mechanisms[288]. Among them, silver, gold, and titanium-based nanosystems are the main ones. However, silver nanoparticles (AgNPs) have found wider application for their

remarkable antimicrobial activity against Gram-positive and Gram-negative bacteria, as well as against other microorganisms (viruses, mycetes, protozoa), and for their low tendency to induce bacterial resistance. Moreover, compared to other metals, silver is more active against the above-mentioned pathogens and is often more cost-effective[308].

During the last few years, several hypotheses have been proposed regarding their mechanism of action, and to date, it seems that their antimicrobial activity can be referred to different factors: reactive oxygen species (ROS) production, interaction with proteins and Ag^+ release. In detail, AgNPs can induce the production of ROS, which can, subsequently, interact with the bacterial proteins (e.g. plasma membrane proteins), altering their structure and function; they can directly interact with bacteria membranes, modifying their integrity, and, finally, they can, also, release Ag^+ ions, which interact with intracellular enzymes and proteins, affecting, in this way, essential biological function like cellular respiration and transmembrane transport (Figure 18)[288,307,309,310].

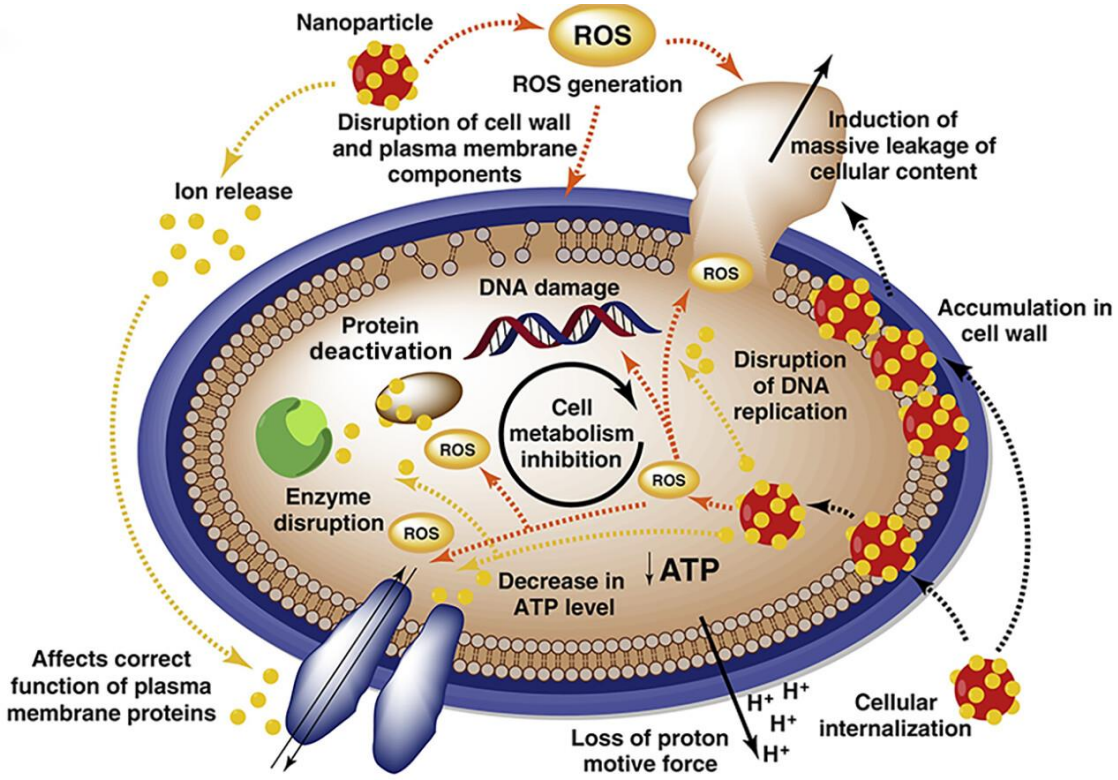

Figure 18. Principal antimicrobial mechanisms of metal nanoparticles[288,310].

AgNPs can be delivered through hydrogels by doping them during their formulation[311,312] or by in situ synthesis[313]. The latter is the most efficient approach as highlighted in different examples. Furthermore, several studies have highlighted the capability of polysaccharides as capping agents towards AgNPs[313–315].

Wang et al. developed an easy, reproducible, green and low-cost method for the production of AgNPs-containing hydrogels. This system was achieved by using cellulose nanofibrils containing carboxylated lignin as a reducing agent for Ag^+ ions and, also, as a stabilizer for AgNPs. This approach is particularly interesting because it allows nanocomposite gels to be obtained in a single production step[313].

Xiang et al. exploited tannic acid-reducing properties to in situ synthesize AgNPs. In detail, they developed a bioadhesive antibacterial hydrogel based on silk fibroin and tannic acid doped with AgNPs produced in situ during hydrogel formation, thanks to tannic acid. The hydrogel showed shear-thinning, self-healing, and wet tissue adhesion as well as an even distribution of AgNPs in the adhesive network and antibacterial activity, suggesting the potential application of the system as biological tissue adhesives and wound healing dressings[316].

On the other hand, Reithofer et al. reported an efficient synthesis of AgNPs by in situ reduction using only UV irradiation and no additional chemical-reducing agents. In particular, they formulated an innovative system based on ultrashort peptides which can self-assemble in water to form hydrogels, which were used as a matrix for in situ AgNPs synthesis[317].

Several studies demonstrated that AgNPs have significant toxic effects also against protozoa like *leishmania*, suggesting the application of an AgNPs-based system not only for the treatment of bacterial infections but also for protozoan lesions. Specifically, the activity of AgNPs results in promastigote (infective stage of *leishmania* parasites) death through ROS-

mediated apoptosis and loss of mitochondrial integrity, phosphatidylserine exposure and damage to promastigotes membrane[318,319]. Fanti et al. demonstrated that the treatment with AgNPs causes a significant reduction in infected macrophages, decreasing thus the number of amastigotes (intracellular forms of *leishmania*). In addition, these systems influenced the immunomodulatory capacity of infected macrophages, reducing the synthesis of mediators of inflammation that would otherwise aggravate leishmaniasis lesions[318].

1.8.2 Injectable hydrogels for bone tissue engineering

Bone is a specialized connective tissue with different biological functions, mainly constituted by osteoblasts, osteoclasts, osteocytes, and osteogenic cells. Osteoblasts are responsible for bone tissue formation through the production of several components of the bone ECM, like calcium phosphates in the form of hydroxyapatite (mineralization process), collagen I, proteoglycans, cell adhesion proteins (integrins, cadherins, osteopontin, bone sialoprotein, fibronectin) and osteocalcin and osteonectin (proteins involved in bone mineralization)[320].

Osteoclasts, multinucleated cells derived from monocytes, are engaged, in response to local stimuli, in bone resorption, an essential physiological process involved in maintaining blood physiological calcium levels. Osteocytes, instead, derived from osteoblasts that get trapped within the mineralized bone matrix, detect mechanical stresses, converting them into physiological responses and facilitating the physiological exchanges within the bone tissue. Osteogenic cells, finally, are mesenchymal stem cells crucial in bone tissue formation and maintenance, since they can differentiate into osteoblasts[321].

Bone regeneration, a complex self-healing process that starts in response to trauma, consists of different sequential phases: an inflammatory phase, a repair step (also divided into the hematoma organization phase and callus phase), and a remodelling step[322]. Even if the human body usually can regenerate bone injuries, this process is limited to small fractures

(less than 6 mm). In the presence of larger injuries or adverse physio-pathological conditions, such as osteoporosis, diabetes, or rheumatoid arthritis, bone repair could not lead to complete regeneration, needing external help[323].

Currently autografting is considered the gold standard, although its application is limited by various disadvantages, including the risk of infection, donor-site morbidity and poor integration with host tissues[323]. In this scenario, tissue engineering has emerged as one of the most effective strategies for bone regeneration[324].

Before describing its approaches, it is necessary to explain tissue engineering principles to better understand its application in bone regeneration. Tissue engineering is an interdisciplinary field which, combining principles of engineering and life sciences, is focused on the design, development and production of specific constructs in order to repair or enhance the function of damaged tissues after trauma or diseases[325]. To reach this goal, it relies on the production of bioengineered tissues, composed of implantable scaffolds, autologous cells (stem or differentiated cells), and bioactive molecules such as growth factors and/or drugs, whose combination allows the creation of three-dimensional structures that mimic the composition, architecture, and functions of natural tissues[326].

In particular, the scaffold is designed to mimic ECM and is designed to mimic its function, since, in this way, could promote cell growth and differentiation, and tissue functionality. On the other hand, the incorporation of bioactive molecules such as growth factors, peptides, or small molecules, can improve the effectiveness of the scaffold, since they can stimulate physiological biological functions. Finally, bioengineered tissues can also incorporate cells, increasing their similarity with the native ones. It is important to use directly progenitor cells derived from the patient because this practice guarantees faster tissue regeneration, better delivery of the cells to the damaged site and, above all, optimization of immunological properties, with a reduction of inflammation and immune response[327].

Among the strategies employed in tissue engineering, the development of hydrogels has garnered widespread interest and has demonstrated significant potential, especially in bone regeneration, for all the advantages described before. In this sense, indeed, injectable hydrogels are often used in bone tissue engineering as a filling material for irregular bone defects that are not subjected to large forces, like alveolar, maxillofacial and cranial bone fractures[328]. Furthermore, the similarity to the soft callus (a cartilage-like intermediate rich in collagen and glycosaminoglycans, formed before mineralization) could allow its use as a transient and intermediate structure for the subsequent formation of bone tissue[329,330].

Amiryaghoubi et al. formulated a thermosensitive injectable hydrogel based on pNIPAM, graphene oxide and chitosan for the proliferation and differentiation of human dental pulp stem cells to osteoblasts. The hydrogels thus prepared accelerated the expression of certain osteogenic genes as well as the ALP activity and also calcium deposition[331].

Chu et al. developed an injectable, self-healing hydrogel with remarkable bone regeneration properties. In particular, the system was formulated by exploiting a double-crosslinking between N-succinyl chitosan and oxidised hyaluronic acid loaded with exosomes derived from mesenchymal stem cells. The hydrogel showed good injectability and osteogenic, angiogenic and murine cranial defect regeneration properties[332].

Moreover, although bone is a hard tissue and many systems for its regeneration are made of metallic supports (such as titanium prostheses) or biomaterials with higher mechanical strength (e.g., polyesters), hydrogels or 3D-printed hydrogel-based systems possess suitable viscoelastic and mechanical properties to support the stresses to which small bone lesions, such as those in the mandible or cranium, are subjected[333].

On the other hand, 3D-printed hydrogel-based scaffolds could be an interesting alternative in bone tissue engineering, since as already described, it is possible to develop personalized

constructs tailored to individual requirements utilizing patient-specific medical imaging data. Moreover, 3D printing facilitates the fabrication of intricate geometric structures that are challenging to achieve using traditional manufacturing methods. In this way, it is possible to deeply regulate the mechanical and structural properties of implantable constructs[334].

Monavari et al. employed 3D printing for the fabrication of an osteogenic construct. They used alginate dialdehyde-gelatin hydrogel doped with bioactive mesoporous silica-calcium nanoparticles loaded with osteogenic phyto therapeutic drug. The 3D printed nanocomposite hydrogel showed promising potential for applications as bone defect osteogenesis filling materials, since increased proliferation, adhesion, and differentiation of osteoblasts as well as induced mineralization[335].

As highlighted by the examples provided, an ideal system for bone regeneration must also be osteoconductive, osteoinductive, and osteogenic. This means it should support cell colonization and proliferation (osteoconductive), as well as the cell migration differentiation and migration (osteoinductive), and the formation of new bone tissue (osteogenic)[336].

For this reason, the incorporation of biological or chemical factors such as ceramics, bioactive glass nanoparticles (sodium calcium phosphosilicate), and magnesium-based nanocomposites, mimicking bone natural properties, is essential. Calcium phosphate ceramics, in particular, present chemical similarities with human bone matrix, as observed in many studies, can induce bone formation in animals without the addition of any osteogenic biomolecules, since their intrinsic osteoinductive properties[320].

Hydroxyapatite (Hap, $Ca_{10}[PO_4]_6[OH]_2$) is the most commonly used calcium phosphate to produce coatings or thin films on the surface of prosthetic devices to accelerate bone healing after implantation[337]. This coating must be biocompatible, bioactive, and osteoconductive and should promote osseointegration, i.e., the anchoring of bone tissue around the implant without the formation of fibrous tissue at the bone-implant interface. However, recently,

synthetic Hap and its nanocomposites have been employed also in bone tissue engineering, thanks to their above-mentioned properties, but also because they can stimulate macrophages to secrete angiogenic and osteogenic growth factors[338].

Pan et al. incorporated nanoHap into a self-healing Schiff base-based hydrogel composed of N-carboxyethyl chitosan, oxidized hyaluronic acid and adipic acid dihydrazide for bone regeneration and alveolar ridge promotion. The study highlighted the presence of Hap-induced osteogenic differentiation and the formation of mineralized matrix, providing an excellent osteo-conductive and osteoinductive micro-environment that facilitated bone formation *in vivo* and, thus, accelerating alveolar ridge preservation in the aesthetic area[329].

Similarly to Hap, β-tricalcium phosphate (β-TCP), with a chemical formula of $Ca_3(PO_4)_2$ and a Ca/P ratio of 1.5, is often incorporated in bone healing hydrogels. Its use is linked not only to its excellent biocompatibility and osteoconductivity, as it promotes bone cell growth and new bone formation by providing a scaffold for cell adhesion and proliferation but also to the fact that its degradation releases calcium and phosphate ions, which can stimulate and enhance the healing process. Various studies in the literature reported its use and significant results when incorporated into different systems[339].

Zhuang et al. demonstrated the great advantages of the incorporation of β-TCP into a gelatin/sodium alginate hydrogel. The results showed that the presence of this bioceramic improved the osteogenic differentiation ability of bone marrow mesenchymal stem cells (BMSCs) affecting phosphorylation of ERK1/2 and BMP-2 signalling pathway, suggesting a positive role of β-TCP in bone regeneration[340].

At the same time, the incorporation of zinc-based compounds can further stimulate the regenerative process while also conferring antibacterial properties. In this regard, zinc oxide nanoparticles (ZnO NPs) contribute to the creation of wound regeneration systems due to

their non-toxic, antibacterial, anti-inflammatory, pro-regenerative, and antioxidant properties. These effects are linked to the reduction of pro-inflammatory cytokines and the increase of anti-inflammatory ones, inhibition of osteoclast activity and the stimulation of that of osteoblasts, inducing, thus, calcium and phosphate deposition, collagen synthesis, reducing oxidative stress and ensuring, in this way, a favourable environment for bone regeneration[341–343].

Tang et al. demonstrated the potential of ZnO NPs on osteoblast differentiation and inhibition of osteoclastic activity. Specifically, *in vitro* studies on MG-63 conducted with nanoparticles synthesized using extracts from the plant *S. baicalensis*, showed a remarkable ability to stimulate cell proliferation and differentiation, as well as the deposition of new bone matrix[341].

2. Aim of the work

In light of what has been discussed, it is evident the need to develop advanced therapeutic systems for tissue regeneration and the delivery of bioactive molecules and, thus, allow a suitable restoration of the morpho-functional characteristics of damaged tissues. Among the various strategies being scientifically investigated, hydrogels emerged as one of the most promising alternatives due to their high application versatility, ease of production, and numerous advantages[2]. The fine control over the physicochemical, biological, and viscoelastic properties, the ability to mimic the ECM of human tissues, the possibility to control the release of bioactive molecules, and the enormous potential to regulate cell adhesion, proliferation, differentiation, and function represent undisputed application advantages[33]. In addition, injectable hydrogels allow efficient filling of target sites even in the presence of lesions with irregular geometry, making better treatment and thus better healing of damaged tissues[90,92]. At the same time, the application of hydrogels in 3D printing enables the creation of highly personalized and complex biological structures, since it makes it possible to reproduce the shape of the lesion faithfully and, thus, fine control over the geometry, porosity, and composition of these structures, thus creating patient-specific implants[161,163].

In this context, the development of new biomaterials for the formulation of hydrogels is an ongoing challenge. In this sense, natural polymers, and especially polysaccharides, appear to be the most suitable starting biomaterials, given the numerous advantages already discussed. In detail, gellan gum and xanthan gum have shown considerable potential, such that they can be widely applied in the biomedical field[224,254].

At the same time, the formulation of hydrogels that simultaneously show good injectability or extrudability and good permanence at the site of the lesion is a considerable challenge in the technological formulation field. The use of multiple crosslinking strategies allows for an

innovative approach, both in the production of injectable hydrogels and in the development of new 3D printing inks. The presence of dynamic bonds (covalent or non-covalent) allows the system to be easily extruded, while the creation of further networks through successive crosslinking or the reinforcement of the same through changes in the polymer molecular structure allows the hydrogel to remain in situ or stabilize the 3D-printed construct[155].

With this in mind, in this thesis work, several injectable and/or printable hydrogels were designed and developed for drug delivery and/or regenerative medicine. In particular, these systems were designed for the local treatment of infected lesions and the regeneration of small bone defects. Therefore, the first objective was to design and synthesize new biomaterials that would make it possible to overcome the limitations of the starting polymers (GG and XG) and, above all, to formulate injectable and possibly also printable hydrogels with suitable physicochemical, biological, and viscoelastic properties that would meet the therapeutic needs of the lesion to be treated. At this stage, various synthetic strategies have been adopted to achieve the intended goal: carboxy- or hydroxy-functionalisation, methacrylation, and oxidation have been exploited.

In the second step, the obtained biomaterials have been used for the formulation of hydrogels with specific properties. In each case, the aim was to guarantee both injectability or extrudability as well as suitable permanence in situ. In this respect, the development of dual/double-crosslinked hydrogels was the main approach pursued. The produced systems were then doped with suitable active agents because of the proposed application: antimicrobial peptides and silver nanoparticles for the treatment of infected lesions, hydroxyapatite, β-tricalcium phosphate, and zinc oxide nanoparticles for the regeneration of bone lesions. Finally, the systems produced were studied to assess their physicochemical, viscoelastic, and biological/microbiological properties.

Specifically, in a first work, an injectable thermosensitive hydrogel was developed for the treatment of local candidiasis through the delivery of a recently discovered synthetic antifungal peptide. In detail, an XG/pNIPAM graft copolymer (named XG-pNIPAM) was synthesized and exploited for the formulation of a thermoresponsive hydrogel. Since pNIPAM exhibits an LCST around 32-33 °C[67], the ratio of the synthesis of this derivative was to obtain a biomaterial and, so, a hydrogel that could be easily injected in the lesion site but, once in contact with the human body, it could create a more stable network, thanks to a coil-to-globule transition, promoting its permanence in situ, which was also favoured by the mucoadhesive properties of XG. Furthermore, the incorporation of a recently designed peptide with antifungal activity allows to confer anti-candida properties to the hydrogels thanks to its controlled release. In addition to the synthesis of XG derivative and to the production of the hydrogel, physicochemical, rheological, and biological analyses were conducted; in this sense, the shear-thinning, mucoadhesive, and thermosensitive properties were explored as well as the hydrogel's stability in physiological fluids. At the same time, the drug release profile and antifungal activity were investigated, validating the prospective application of the hydrogel in managing mucosal and superficial candidiasis.

In another work, an amino derivative of gellan gum (GG-EDA)[122] was chosen as a starting polysaccharide for the production of antibacterial and antileishmanial injectable hydrogels. In detail, through functionalization with glycidyl trimethyl ammonium chloride (GTMAC), a novel cationic derivative of gellan gum (named GG-EDA-GTMAC) was synthesized and exploited to formulate injectable AgNPs nanocomposite hydrogels. The introduction of quaternary ammonium groups into the GG backbone could potentially confer to the hydrogel the capability to stabilize AgNPs[344,345] produced within the hydrogel itself through UV irradiation and thus, to obtain an injectable system for a suitable delivery of such broad-spectrum antimicrobial agents. Furthermore, since GG possesses ionotropic gelation, the

system could be a promising candidate for 3D printing applications, stabilizing the printed constructs with $CaCl_2$ solutions. With this in mind, after the synthesis of the new derivative, several hydrogels were prepared by mixing the aqueous dispersion of GG-EDA-GTMAC with different amounts of $AgNO_3$ solution. Silver reduction was conducted by irradiating the system with UV light to enable the in situ production of the metal nanoparticles, through a simple and reproducible method, and obtain injectable nanocomposite hydrogels with different amounts of AgNPs. The developed systems were further characterized by spectroscopic analyses to confirm quali-quantitatively the formation of AgNPs with the hydrogels. Moreover, degradation studies were conducted to investigate samples' stability in physiological fluids. The rheological characterization allowed to further investigate the injectability, self-healing behaviour, ionic strength and temperature sensitivity of all hydrogels. The preliminary printing tests evaluated the capability of the materials to be applied in extrusion-based 3D printing as inks. Lastly, *in vitro* cytocompatibility analysis and antimicrobial studies (against Gram-negative, Gram-positive bacteria and *Leishmania infantum* protozoan) were carried out to prove the possible application for the treatment of infected wounds.

After dealing with applications in wound healing, other works focused on bone regeneration and, in particular, on the healing of small bone defects.

In the first of these, double-crosslinked 3D-printed hydrogels were designed and developed by combining XGox and a methacrylate polyaspartylhydrazide (PAHy-MA), incorporating also hydroxyapatite nanoparticles. PAHy-MA, a novel synthetic biomaterial with a polyaminoacid-based structure, with its dual functionalization (both hydrazine and methacrylic groups), acts as a macromolecular crosslinker, allowing the spontaneous formation of dynamic bonds with XGox under physiological conditions and, at the same time, a controllable covalent crosslinking upon UV irradiation. In this way, hydrazone bonds'

formation and photo-crosslinking were exploited to confer the hydrogel respectively injectability and shape retention after printing. Different amounts of Hap were introduced into the hydrogel, to assess its influence on viscoelastic, printing and biological properties. For these reasons, rheological characterization took place to investigate viscoelastic, pseudoplastic and self-healing properties as well as the hydrogels' responsiveness to UV light. Printing tests allow to verify the printability of the hydrogels, evaluating the influence of the concentration of Hap. Lastly, cell differentiation experiments were carried out evaluating collagen I deposition, mineralization and the expression of characteristic osteogenic markers. Part of this work (printing and biological evaluation) was carried out during my time at the Polymat-Basque Center for Macromolecular Design and Engineering in Donostia - San Sebastian and in particular at the BioSmarTE Lab of Dr. Sandra Camarero-Espinosa.

Finally, in the last work, injectable gellan gum-based hydrogels were developed as bone fillers for small bone defects, like alveolar, maxillofacial and cranial ones.

This work aimed to design and develop injectable hydrogels that could be both injected and stabilized at the lesion site. To reach this goal, a low-molecular-weight methacrylate derivative of gellan gum was produced as a starting biomaterial by functionalising this polysaccharide by means of 2-amino-ethyl methacrylate (AEMA), obtaining GG-AEMA. In order to produce hydrogels with cell adhesion properties, methacrylated elastin (ELMA), obtained by functionalising a soluble fraction of bovine elastin with methacrylic anhydride, was covalently incorporated into the hydrogel network. The production of the hydrogels was carried out by exploiting the thermotropic properties of gellan gum, as well as the possibility of photo-crosslinking the obtained system and further stabilizing it by ionotropic crosslinking. The synthesized polymers were characterized by spectroscopic analysis and colourimetric assays, while the hydrogels obtained were investigated by rheological

analysis, to assess their viscoelastic properties, injectability, the strongness of the different types of crosslinking and their influence on the rheological properties.

At the same time, ZnO and β-TCP NPs were further incorporated to provide osteoinductive properties. The produced systems were characterized by physicochemical, rheological and biological analyses highlighting the potential of hydrogels for applications in bone tissue engineering. In particular, the stability of the systems in a physiological medium, the influence of concentration and type of particles on the rheological properties of the systems, the cytocompatibility of the produced samples as well as the adhesive capabilities provided by the presence of elastin were evaluated.

3. Results, discussion and conclusions

3.1 Developing xanthan gum-based hydrogel with thermosensitive and mucoadhesive properties for the treatment of local candidiasis

Candidiasis is generally caused by *Candida albicans*, an opportunistic fungus living in human mucous membranes and skin, whose excessive proliferation can cause severe infections in different parts of the body, like throat, mouth, genitals, skin, and sometimes in the whole organism[346,347]. The treatment of these infections could be often difficult, depending on their location and severity, due to the rise of drug-resistance phenomena and the formation of biofilm, leading to the inefficacy of traditional antifungal medications (triazoles, echinocandins, polyenes)[348–351].

However, natural and especially synthetic, antimicrobial peptides (AMPs) could be an interesting alternative to overcome the limitations of conventional treatments[352]. Currently, novel AMPs are being studied, thanks to protein engineering and peptide library screening technologies, to discover novel therapeutic molecules that could help the medical treatment of various diseases, especially infections[289,290,353]. In a recent study, a synthetic peptide (FHLVWRAGGTF, named AMP14d), with great antifungal and antibiofilm *in vitro* activity against *C. albicans*, was designed thanks to computer modelling and bioinformatic analysis, starting from a series of peptides discovered in hemocytes and hemolymph extracts from freshwater crayfish *Procambarus clarkia*, improving some physicochemical parameters (percentage of hydrophobic ratio, charge, Boman index)[354].

Given these considerations, this work has aimed to formulate an injectable hydrogel, potentially useful for the easy administration of the synthetic antifungal peptide for the treatment of local candidiasis[355]. To achieve this goal, a thermoresponsive and mucoadhesive injectable hydrogel was designed and developed starting from an XG/pNIPAM graft copolymer.

The easy preparation and administration on various mucosal or skin surfaces made the system an interesting platform for the delivery of a new anti-candida peptide. Furthermore, its high stability, tunable temperature-dependent viscoelastic properties and mucoadhesion behaviour highlighted its retention in the application site long enough to perform its intended function.

Lastly, the peptide's release profile coupled with its efficacy in inhibiting fungal growth validates the prospective application of the formulation in managing mucosal and superficial candidiasis.

3.1.1 Synthesis and characterization of XG-pNIPAM

The synthesis of the copolymer consisting of XG grafted with pendant pNIPAM moieties was carried out by pre-activating the terminal carboxylic group of pNIPAM and allowing its reaction with primary hydroxyl groups of XG (Figure 19A). In detail, the molar ratio between pNIPAM and XG repetitive units was fixed to 0.1 to obtain a derivative that maintained the viscoelastic and mucoadhesive properties of XG hydrogels while concurrently exhibiting the thermosensitive behaviour of pNIPAM. The functionalization of primary hydroxyl groups of the polysaccharide instead of the carboxylic ones was made to preserve the negative charge of XG related to its pendant trisaccharide chains since the latter play a key role in influencing the XG dispersibility in an aqueous media[248].

Furthermore, this synthesis approach allows the reaction in two simple steps without isolation of the intermediates, followed by purification through dialysis to remove all the unreacted species. In this sense, it does not need the previous activation of XG usually requested for free-radical grafting with pNIPAM as already reported elsewhere[356].

The characterization of the new derivative was conducted by FT-IR and ^{1}H-NMR. The FT-IR spectrum for XG-pNIPAM (Figure 19B) shows XG and pNIPAM characteristic transmittance peaks: in particular, it is possible to note, for XG, the O–H axial deformation

and the C–H (methyl and methylene groups) symmetric and asymmetric stretching vibrations respectively around 3280 cm^{-1} and 2850–2950 cm^{-1}[201,357], but, at the same time, for pNIPAM, its typical peaks at 1530 cm^{-1} (N–H bending) and 1630 cm^{-1} (C=O stretching)[358,359].

Furthermore, the success of the reaction and the derivative structure were also confirmed through ^{1}H-NMR spectroscopy. As shown in Figure 19C, comparing XG and XG-pNIPAM spectra, the derivative shows the typical peaks of both polymers[356,360–363].

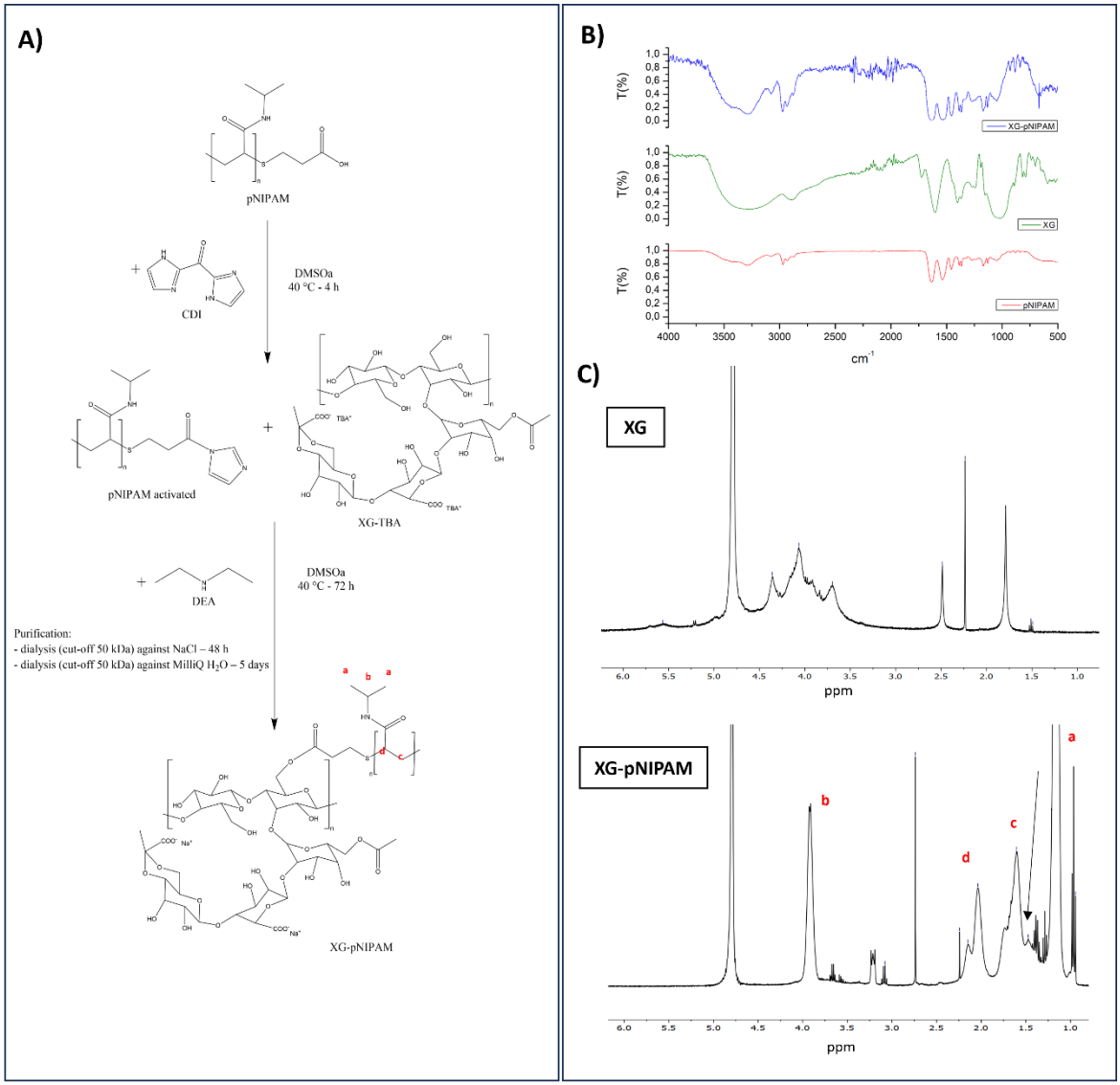

Figure 19. Scheme of synthesis of XG-pNIPAM (A); FT-IR spectra of XG-pNIPAM, XG, and pNIPAM (B); ^{1}H-NMR spectra of XG and XG-pNIPAM (C).

3.1.2 Production and characterization of XG-pNIPAM hydrogel

XG-pNIPAM hydrogels were formulated using a polymer concentration of 5% (w/v) in MilliQ water. This value of concentration was chosen because it allowed for relatively easy dispersion of XG-pNIPAM, producing a viscous system that can still flow upon vial tilting at room temperature, but not after heating the hydrogel to 37°C. Furthermore, when the system was heated to this temperature, a chromatic change from transparent to opalescent was observed, confirming the thermoresponsiveness of the obtained graft copolymer. Indeed, as already reported, in aqueous media, pNIPAM shows a conformational variation from a hydrated to a dehydrated form (highlighted by the obtainment of a milky solution) when the temperature is higher than the LCST (around 32 °C)[364]. As shown in Figure 20, the 5% w/v pNIPAM aqueous solution initially exhibits high fluidity and undergoes the distinctive temperature-induced transition when exposed to 37 °C while the unmodified XG aqueous dispersion (5% w/v) forms a structured hydrogel with limited macroscopic fluidity both at room temperature and at 37 °C and does not show any colour variation.

In this sense, the macroscopic behaviour of XG-pNIPAM dispersion confirms that grafting synthetic thermosensitive polymer chains onto the polysaccharide backbone confers interesting properties to the starting underivatized XG, enhancing its suitability as a starting material to produce advanced pharmaceutical hydrogels. The improved fluidity at room temperature improves its administration, while the capacity to structure at 37 °C makes it particularly advantageous for its prolonged retention in the administration site.

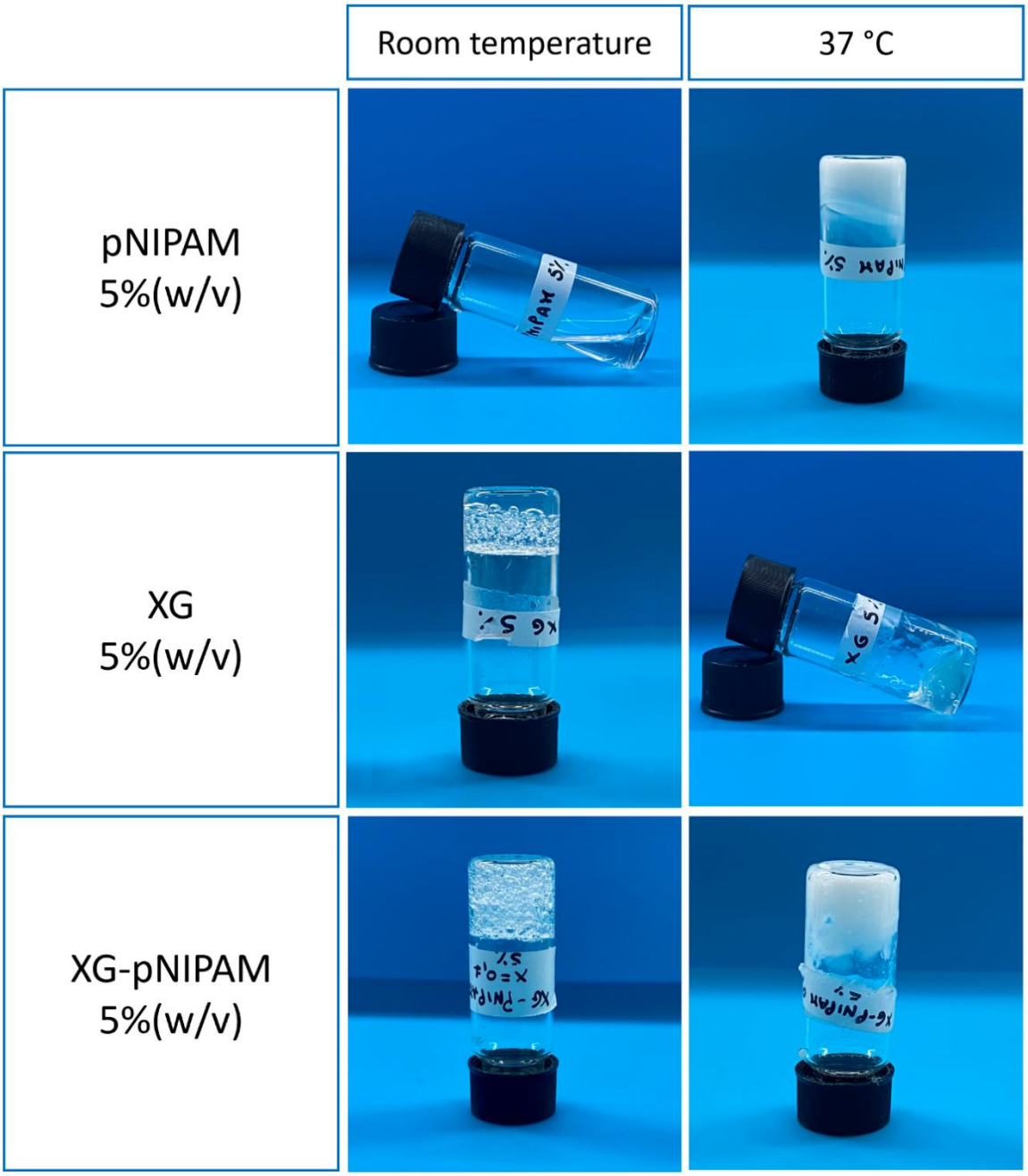

Figure 20. Macroscopically view of thermoreversibility of pNIPAM, XG and XG-pNIPAM hydrogels at room temperature (left) and at 37 °C (right).

Since a new antimicrobial peptide, AMP14d (FHLVWRAGGTF) was previously designed and synthesized starting from some natural peptides from *P. clarkia*, showing interesting anti-Candida activity and low toxicity towards human cells[354], a peptide-loaded hydrogel was formulated.

For the preparation of the AMP14d-loaded sample, the peptide was simply mixed with the aqueous dispersion of XG-pNIPAM at room temperature through mild shaking, highlighting the extraordinary versatility of the developed system in producing pharmaceutical hydrogels. The peptide concentration, however, was set above its Minimum Inhibitory Concentration (MIC, 31.2 µg/mL)[354], since the system was designed as a drug reservoir for controlled release.

The degradation studies of XG-pNIPAM hydrogels revealed a very low weight loss of approximately 9% after 24 h (Figure 21). This indicates that the hydrogel can withstand in infected sites long enough to perform its function. This result is in accordance with the expected stability profile for hydrogels intended for local administration, as they remain stable over a certain period between potential administrations.

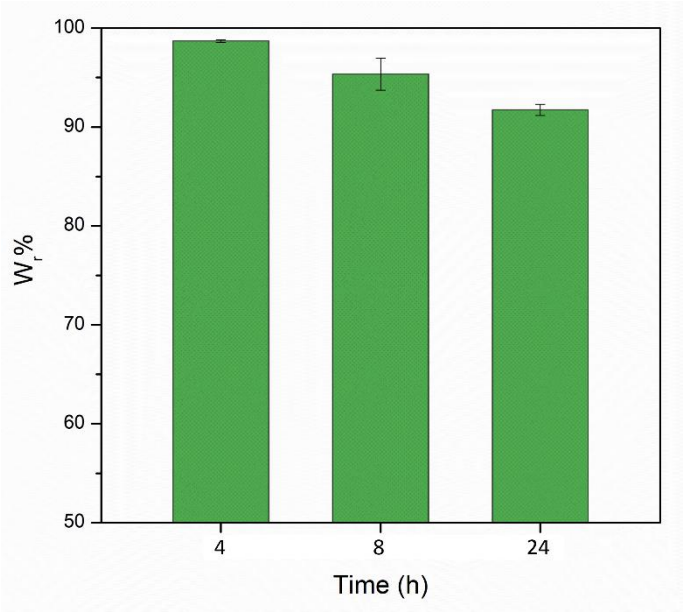

Figure 21. Degradation profile of XG-pNIPAM hydrogel after 24 h of incubation in DPBS.

Figure 22 macroscopically demonstrates the stability of the hydrogel over 24 h when applied to porcine skin tissue. As observed, the hydrogel (area within the red lines) remains attached to the skin surface for the entire investigation period even when the sample is completely

soaked in DPBS, showing, also, its representative chromatic change from transparent to opalescent when incubated at respectively at 25 °C and 37 °C, as described before.

Figure 22. Macroscopic stability of XG-pNIPAM hydrogel after 24 h of incubation in DPBS when adhered to porcine skin tissue.

3.1.3 Rheological characterization

The rheological characterization allowed to quantitatively confirm the macroscopic behaviour of the XG-pNIPAM hydrogel both at room temperature and at 35 °C. Oscillatory experiments were carried out to determine the viscoelastic properties of the system and highlight its gel state both under and above the LCST. In detail, as shown in Figure 23A, when low values of strain % were applied, the system exhibited a G' higher than the G'', which means it possesses a more pronounced elastic character and a solid-like behaviour, which is typical of physical hydrogels.

However, increasing the strain % (after the cross point,), G'' becomes higher than G', which indicates that formulation shows a more liquid-like behaviour. This is a remarkable result because it means the system is in a gel state before the administration at room temperature but still capable of being potentially injected or extruded, e.g. from a syringe or a commercial container. On the other hand, thermo-rheological experiments (Figure 23B) showed, as expected, an increase in viscoelastic moduli with temperature: in particular, at 30 °C there is a rapid increase of G' and G'' due to the presence of pNIPAM[364]. This test confirmed the

advantage of grafting pNIPAM into the XG backbone since the increase of G' and G'' could improve the stiffness of the formulation and, consequently, its permanence in situ. Flow sweep tests allowed to study the relationship between the viscosity of the hydrogel and the shear rate, evaluating if XG-pNIPAM hydrogel had shear-thinning properties. The test was carried out at both 25 °C and 35 °C to study the flow behaviour before and after the administration. In both cases (Figure 23C-D), the formulation showed a shear thinning behaviour, with higher values of viscosity at lower shear rate at 35 °C. This result, due to the capability of the molecular chains to align in the direction of the shear rate, reducing the viscosity of the dispersion is particularly interesting since suggests that the formulation could be easily extruded and administered to the application site.

Furthermore, this result confirms the influence of temperature on the viscoelastic properties (in this case viscosity) outlined in the previous test (thermo-rheological experiment) and the possibility that the formulation could remain on the administration surface.

All the obtained results confirmed the viscoelastic and pseudoplastic behaviour of XG-pNIPAM formulation, as well as its thermoresponsiveness, suggesting easy administration and good retention on administration sites.

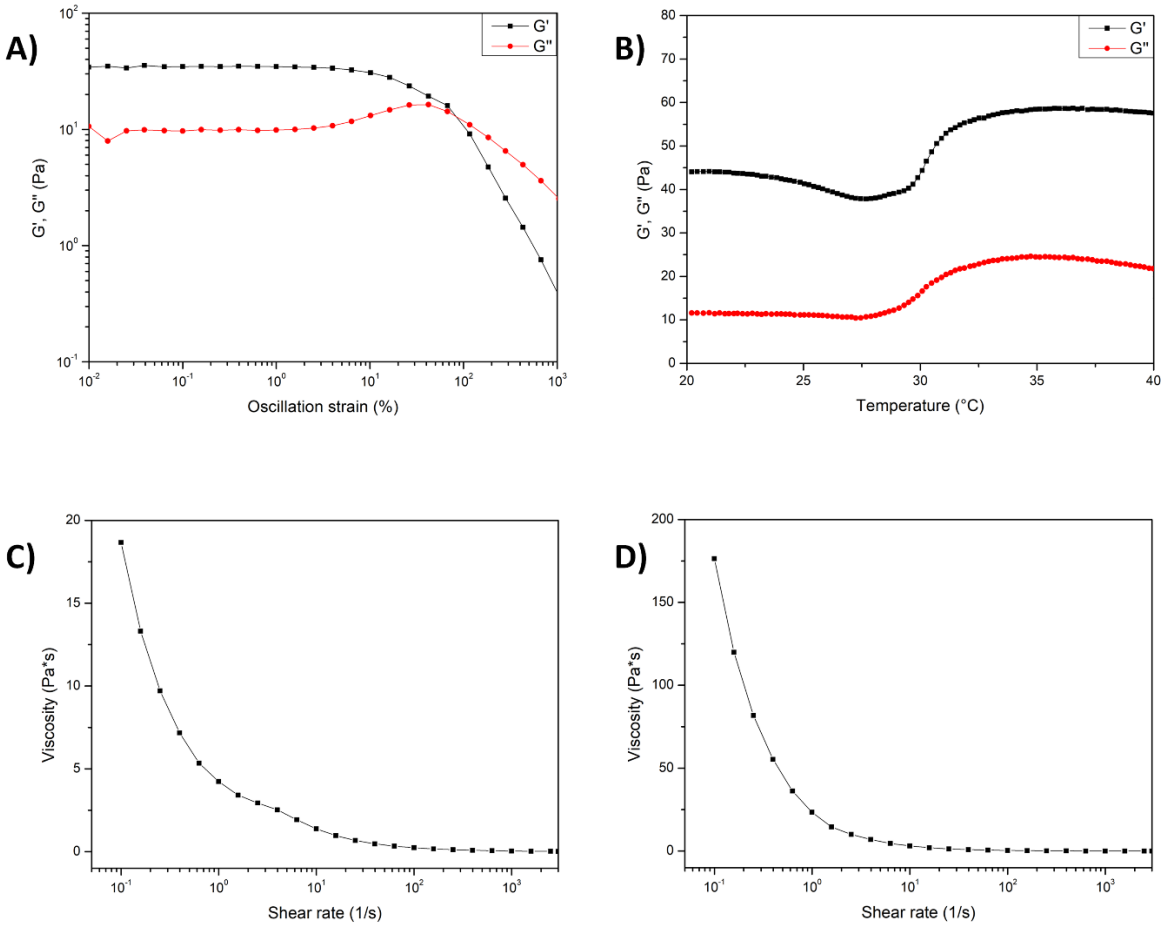

Figure 23. Rheological characterization of the XG-pNIPAM hydrogel. Results of oscillation amplitude tests (A), thermo-rheological experiments (B) and flow sweep tests at 25 °C (C) and 35 °C (D) for XG-pNIPAM hydrogel.

3.1.4 Mucoadhesive behaviour

XG usually shows good mucoadhesive properties, that are useful for its administration as a drug carrier, but also as a scaffold since they allow it to resist on mucosa surface. The evaluation of the mucoadhesive properties of the XG derivative was performed by measuring the force required to detach the formulations from a mucin film (mucoadhesion force). The analysis was performed focusing on the surface interactions between the formulation and a mucin film acting as a biological substrate. In this test, the force of detachment was recorded and the data obtained with and without mucin film were compared (Figure 24)[95]. The results showed a significantly higher increase of this force in the presence of mucin film,

indicating a positive interaction between the formulation and mucin. On the other hand, there was a small difference between XG-pNIPAM and XG dispersion, that may be attributed to the presence of pNIPAM, which, however, does not interfere so much in the interaction with the mucin film.

These results suggest that the interaction between the hydrogel and the mucin of the infected areas could enhance the retention of the formulation upon local application in the ocular, oral, or vaginal mucosa, thereby facilitating a prolonged and more effective treatment.

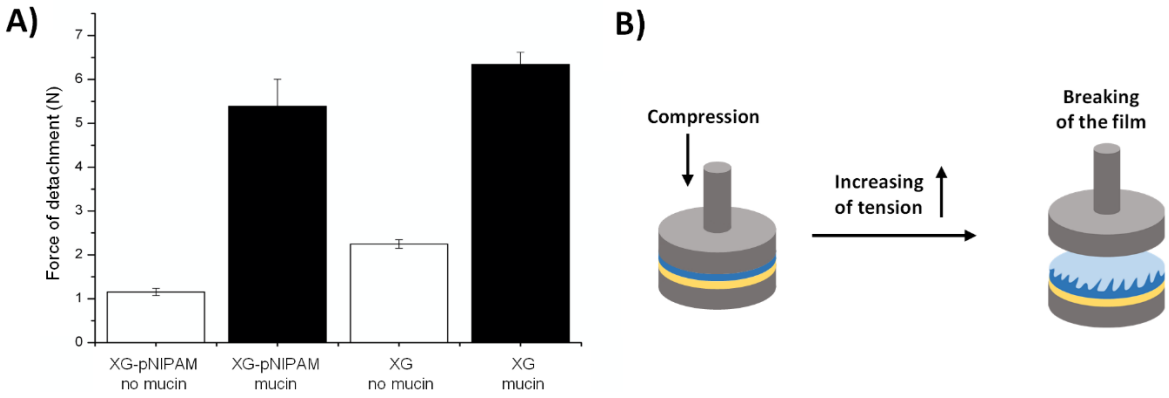

Figure 24. Results of the mucoadhesion test for XG-pNIPAM and XG with and without mucin film (A). Schematic representation of the mucoadhesion test (B).

3.1.5 *In vitro* cytocompatibility

NIH/3T3 cells were employed as a model to evaluate the cytocompatibility of the hydrogels. Both peptide-loaded and non-peptide-loaded hydrogels were studied, introducing them directly into the wells of the plate where the cells had been seeded 24 h earlier. Figure 25 shows the results of cell viability expressed in terms of both metabolic activity (MTS) and live/dead staining.

No cytotoxicity (cell viability above 80%) was detected by the analysis of the metabolic activity of cells cultured in the presence of the two hydrogels after 24 h of incubation, suggesting that both the biomaterial and the entire formulation were not cytotoxic (Figure

25A). The results were also confirmed through the live/dead staining, which allows a qualitative observation of viable (green) and non-viable (red) cells using different fluorescent probes. No dead cells were detected either in the absence nor in the presence of the peptide and, as it was possible to observe by comparing to the control, the cells have maintained their characteristic morphology (Figure 25B).

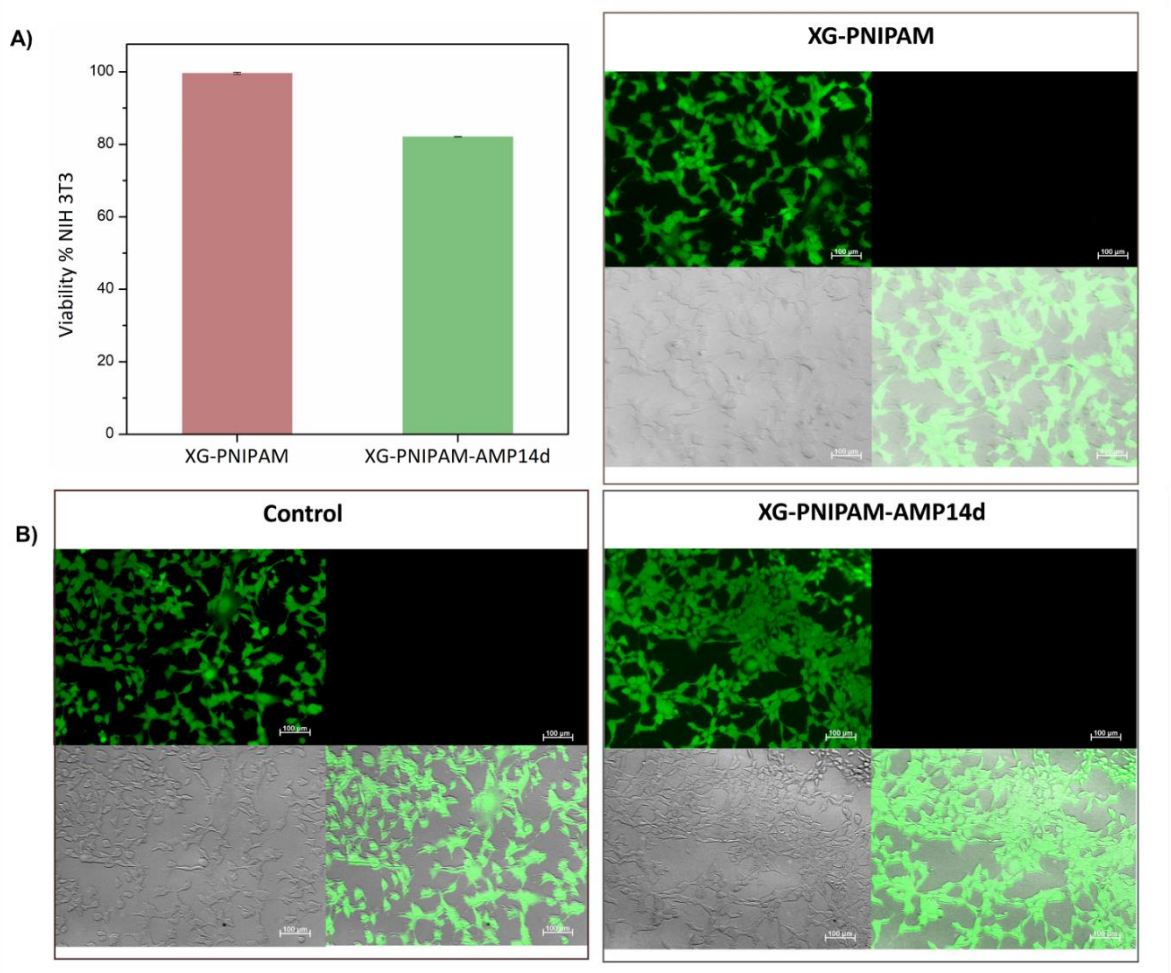

Figure 25. Cytocompatibility results for XG-pNIPAM and XG-pNIPAM-AMP14d hydrogels with NIH/3T3 cells (A). Live/dead staining of NIH/3T3 after incubation with XG-pNIPAM and XG-pNIPAM-AMP14d hydrogels (B). Scale bars are 100 µm.

3.1.6 Release study of AMP14d and *in vitro* antifungal activity of the hydrogel

As explained in the experimental section, the hydrogels were loaded with the AMP14d and then its release was studied in DPBS pH 7.4. The release graph of peptide 14d from the XG-

pNIPAM hydrogel studied up to 24 h shows an interesting profile (Figure 26A), with the gradual release of the peptide, approximately 90% within the first 24 h. The timing and magnitude of release could be attributed to specific characteristics of the hydrogel structure, such as temperature sensitivity, to the nature of the interactions between pNIPAM and the XG backbone and to the possible electrostatic interactions between the negative charges of XG-pNIPAM and the positive charges of AMP14d. All these parameters could influence and explain the release of the anti-Candida peptide.

Furthermore, since the hydrogel is stable over 24 h, the peptide release is not mainly due to the degradation of the system, supporting the hypothesis that diffusion is the predominant release mechanism. Anyway, these data indicate high efficiency in the process of peptide release from the hydrogel system, suggesting its potential use in the treatment of candidiasis.

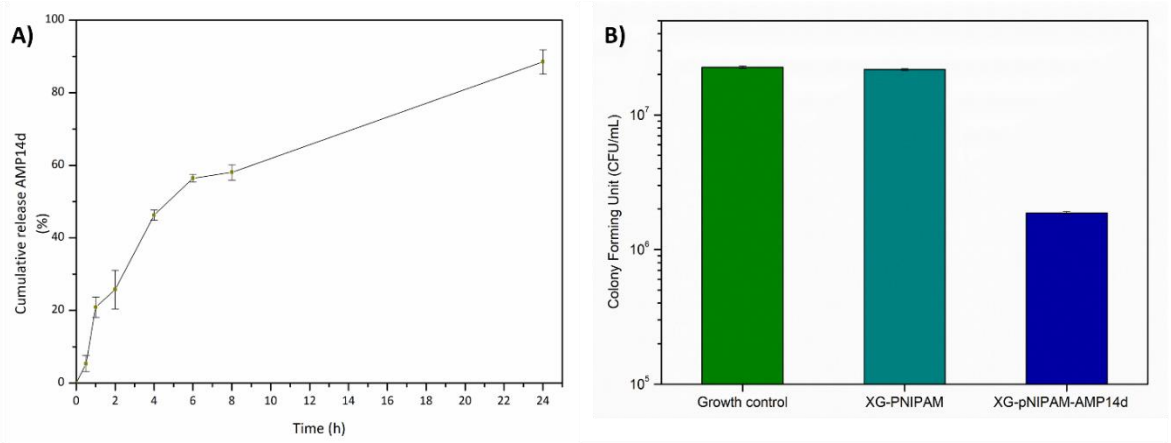

Figure 26. Release of AMP14d from XG-pNIPAM hydrogel. All data are shown as a mean value ± SD (n =3) (A). Antifungal activity of XG-pNIPAM-AMP14d hydrogels (viable cell count method) against *C. albicans* ATCC 10231 after 24 h incubation at 37 °C. Growth control) microorganisms without hydrogels. XG-PNIPAM) microorganisms incubated with XG-pNIPAM hydrogels without AMP14d (B).

Regarding the antimicrobial effect of the formulation, the inhibition of *C. albicans* planktonic growth in the presence of the XG-pNIPAM-AMP14d hydrogels after 24h of

incubation, was evaluated by the count of viable fungal cells. In particular, the hydrogel showed antifungal activity against planktonic strain: indeed, the fungal counts of *C. albicans*, incubated with XG-pNIPAM-AMP14d hydrogels for 24 h, was equal to 1.9×10^6, while the growth control fungal count was equal to 2.3×10^7 CFU/mL (Figure 26B). The incubation with non-peptide-loaded hydrogel did not affect the viability of *C. albicans*, while that with XG-pNIPAM-AMP14d hydrogel resulted in an efficient reduction in viable fungal cells, achieving a logarithmic reduction of 1.08.

The antifungal activity coupled with the release profile suggested a potential use of the developed hydrogel as a new alternative approach for local candidiasis treatment.

3.1.7 Conclusions

In this work, a novel thermoresponsive biomaterial was successfully synthesized by grafting pNIPAM onto the XG backbone. The resulting XG-pNIPAM hydrogel exhibited macroscopic thermoresponsiveness, transitioning from a more fluid state at room temperature to a more viscous gel state at 37 °C. Rheological characterization highlighted the viscoelastic properties of the XG-pNIPAM formulation, demonstrating its gel-like state at both room temperature and 37 °C and confirming, also, its thermoresponsive behaviour. Flow sweep tests demonstrated shear thinning behaviour at both temperatures, advantageous for easy administration. Importantly, the hydrogel displayed resistance to washout, enhancing its stability on potential application surfaces, as well as good mucoadhesive properties. Cytocompatibility studies using NIH/3T3 cells revealed good cell viability (>80%) for both peptide-loaded and non-peptide-loaded hydrogels, with live/dead staining showing no significant impact on cell morphology or viability. Employed as a carrier for the anti-Candida AMP14d, the formulation showcased a gradual peptide release, with approximately 90% released within the first 24 h. Lastly, antimicrobial studies, assayed *in vitro* against *C. albicans*, highlighted an effective logarithmic reduction of the pathogen

cultures in planktonic conditions which means an antifungal activity of XG-pNIPAM-AMP14d hydrogels according to the release profile of antimicrobial peptide.

In summary, the XG-pNIPAM hydrogel presented promising attributes for peptide delivery, combining thermoresponsiveness, efficient release, rheological versatility, and mucoadhesive characteristics, positioning it as a potential candidate for local biomedical and pharmaceutical applications and a new therapeutic approach alternative to conventional topical antifungal treatment.

3.2 3D-printed quaternized gellan gum-based hydrogels doped with in situ synthesized silver nanoparticles for the treatment of infected wounds

Infected skin wounds represent a serious health concern because of the risk of colonization by multi-drug-resistant bacteria and the subsequent long healing process[365]. At the same time, cutaneous lesions caused by parasites like *Leishmania* could be difficult to treat due to poor efficacy and compliance with conventional medications[300]. In this sense, developing smart biomedical systems with non-specific antimicrobial properties could be a promising strategy in wound healing[198]. Silver nanoparticles (AgNPs), with their broad-spectrum antimicrobial properties[366,367], could enhance the treatment of infected wounds.

For these reasons, in this work, a novel cationic derivative of gellan gum (named GG-EDA-GTMAC) was synthesized and exploited for the formulation of printable AgNPs nanocomposite hydrogels. It was demonstrated that AgNPs can be easily synthesized and stabilized within the hydrogels without the need for toxic reducing agents, thanks to the capping properties of the derivative. The rheological characterization highlighted good viscoelastic properties, injectability and self-healing, as well as confirmed ionic strength sensitivity of all hydrogels, suggesting also the suitability of the developed systems as printable materials, as further demonstrated. Indeed, thanks to the advantageous viscoelastic properties of the hydrogels and their strong ion sensitivity, it was possible to print the hydrogels and subsequently stabilise the printed constructs.

Lastly, *in vitro* biological studies proved cytocompatibility and strong antimicrobial activity against both Gram-negative and Gram-positive bacteria and *Leishmania infantum* protozoan, suggesting that the developed biomaterials and hydrogels could be exploited for easy synthesis and administration of AgNPs, making the systems promising candidates in infected wound healing.

3.2.1 Synthesis and characterization of GG-EDA-GTMAC

In order to produce injectable hydrogels with optimal antimicrobial activity and viscoelastic properties, GG-EDA was chosen as the starting polymer for further functionalization with GTMAC. The ability of GG-EDA to establish inter- and intramolecular electrostatic interactions capable of resulting in the formation of compact hydrogels has been extensively studied in a previous work[111]. On the other hand, the functionalization of this polymer with GTMAC allowed the introduction, into its backbone, of quaternary ammonium groups, i.e. permanent positive charges, potentially capable of stabilising the AgNPs[344,345] produced within the hydrogel, thus obtaining an injectable and printable system for a suitable delivery of such antimicrobial agents. For these reasons, GG-EDA was, first of all, synthesized according to the protocol reported by Tomasello et al.[122], using a molar ratio between bis(4-nitrophenyl)carbonate (4-NPBC) and GG repeating units of 0.5 and, subsequently, a 10-fold molar excess of ethylenediamine (EDA) (compared to 4-NPBC). The reaction was conducted in two steps without isolation of the intermediates. The product was obtained, after precipitation and washings in acetone and vacuum drying at room temperature, with a yield of 98 ± 1.5%. Afterwards, GG-EDA was functionalized with GTMAC, in the presence of diethylamine (DEA) as a catalyst, according to the scheme shown in Figure 27.

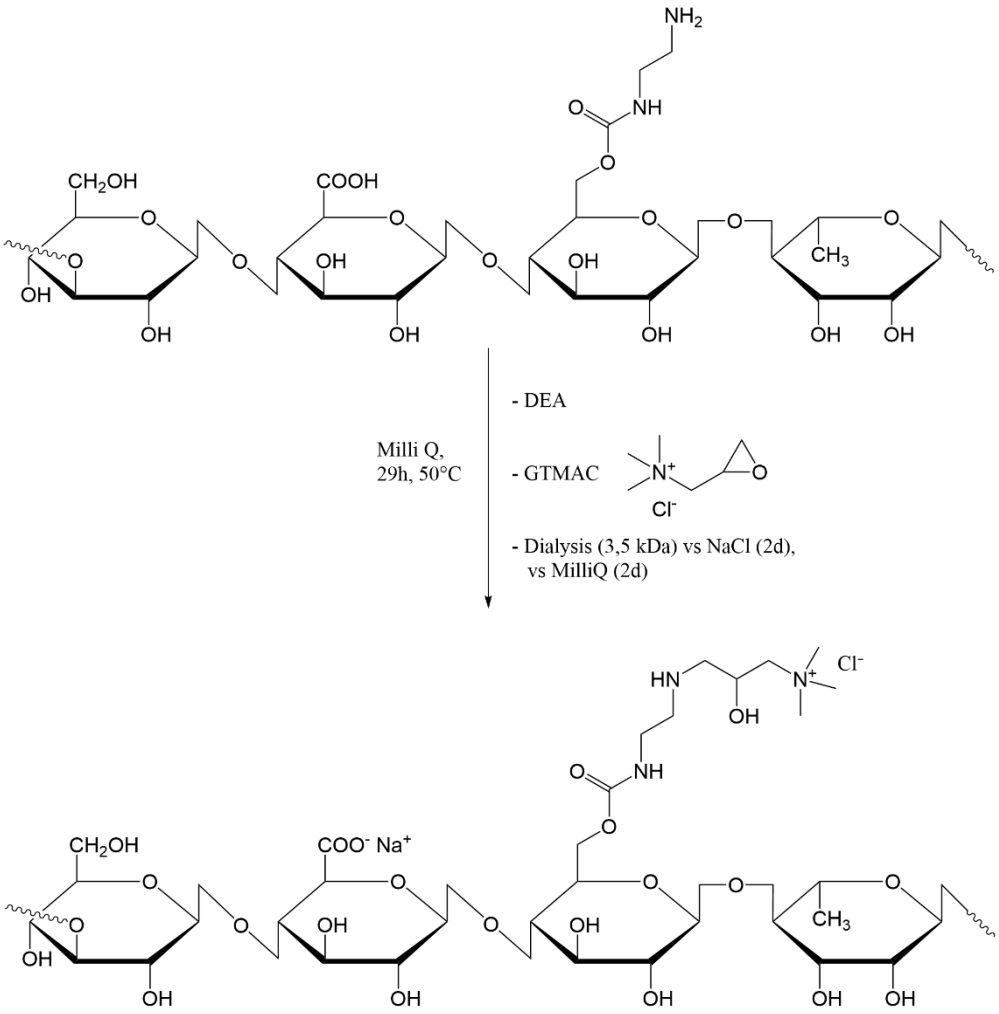

Figure 27. Scheme of synthesis of GG-EDA-GTMAC.

In particular, the reaction, which involves the opening of the epoxy ring of GTMAC by the nucleophilic amine groups of GG-EDA, was carried out by imposing a molar ratio between the GTMAC and the free amino groups of the starting polymer equal to 2, and a molar ratio between DEA and the GG-EDA itself equal to 1. The product, after dialysis purification, was isolated by freeze-drying with a yield by weight of 80.6 ± 1% and, then characterized by ^{1}H-NMR analysis and 2,4,6-trinitrobenzene sulphonic acid (TNBS) assay. As reported in Figure 28, comparing the spectra of the two biomaterials revealed the appearance of a peak, in the spectrum of the GG-EDA-GTMAC, at δ 3.2, related to the methyl groups bound to quaternary nitrogen (─N^{+}(**C**$\mathbf{H_3}$)$_3$) which allowed to confirm the functionalization of the GG-EDA backbone with GTMAC. Moreover, it enabled to calculate the derivatisation degree

(DD%), by comparing this peak with that at δ 1.30 attributable to the methyl groups of the α-l-rhamnose of the repeating units, which resulted in 20.7 ± 2.23%. To confirm this result, TNBS assay was carried out, showing a decrease in the concentration of the primary amino groups from GG-EDA to GG-EDA-GTMAC. This analysis highlighted a DD% of the latter of 22.12 ± 0.45%, thus corroborating the result obtained from ^{1}H-NMR.

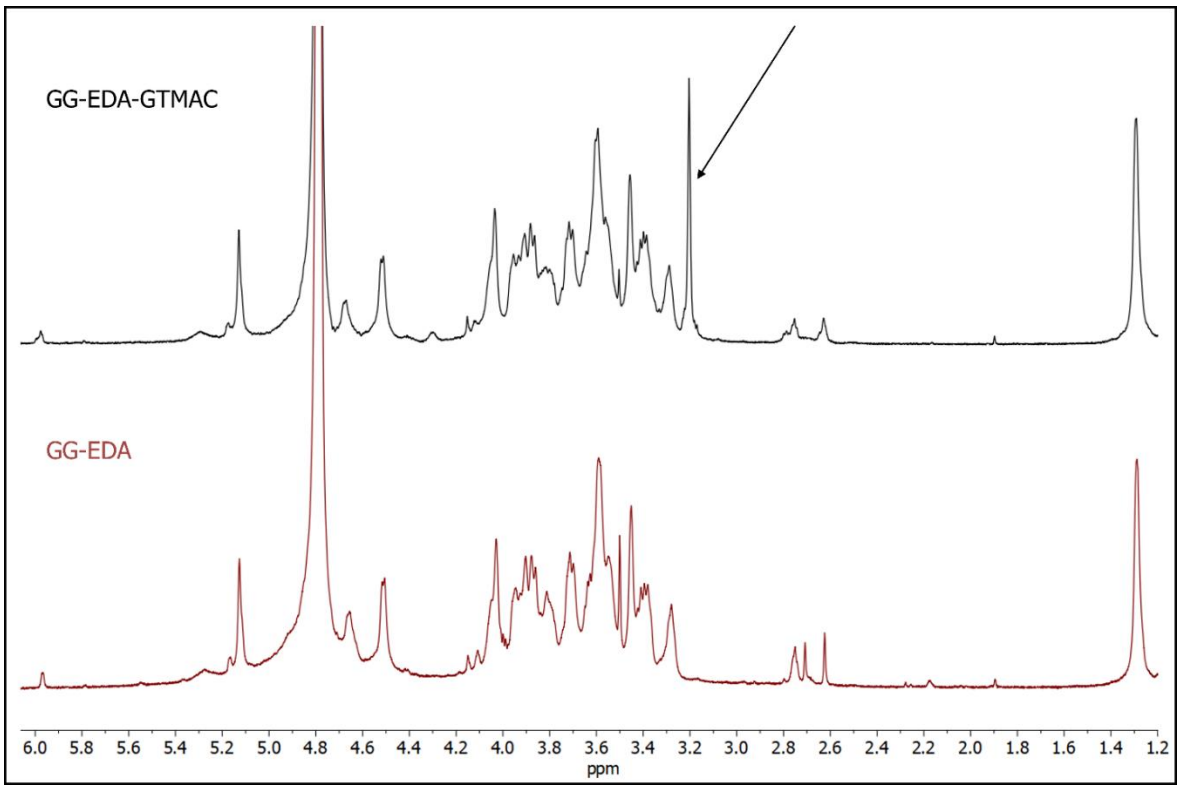

Figure 28. ^{1}H-NMR spectra of GG-EDA-GTMAC and GG-EDA.

3.2.2 Production and physicochemical characterization of nanocomposite hydrogels

In order to study the gelation properties of the cationic derivative, and, in particular, to investigate whether the insertion of quaternary ammonium groups could influence the thermotropic behaviour typical of both native GG and GG-EDA, a GG-EDA-GTMAC hydrogel was preliminarily produced, dissolving the polymer at a concentration of 3% w/v in MilliQ water at 70 °C.

Subsequently, the dispersion was cooled to room temperature, resulting in a stiff hydrogel (gelation was visually validated by the tube inversion test). This behaviour confirmed that aqueous dispersions of GG-EDA-GTMAC also undergo a temperature-induced gelation process; this means, as already described in the introduction, that the increase in temperature determines a conformational transition of polymer chains from double helix to random coil, allowing a complete solubilization. The subsequent decrease in the temperature results in a reorganisation into double helix structures and a *sol-gel* transition, enabling gelation without adding any gelling agents.

Concerning the production of the nanocomposite hydrogels (Figure 29), different amounts of an $AgNO_3$ solution (50 mM) were added to the GG-EDA-GTMAC *sol* in order to obtain hydrogels with different Ag^+ ions concentrations (Table 1).

Table 1. $AgNO_3$ final concentration in the nanocomposite hydrogels.

Sample	**H_0**	**$H_{0.5}$**	**H_1**	**$H_{1.5}$**	**H_2**	**$H_{2.5}$**	**H_5**
$AgNO_3$ (mM)	0	0.5	1	1.5	2	2.5	5

It is interesting to note that the addition of the salt solution did not result in immediate gelation of the system. This aspect is rather relevant considering the ionotropic gelling properties of this polysaccharide. Most likely, at the concentrations tested, the establishment of electrostatic interactions between the silver ions and carboxylate groups of the polymer backbone is not strong enough to induce an exhaustive *sol-gel* transition at high temperatures. However, it is plausible to assume that these interactions allow a homogeneous distribution of the ions in the polymeric *sol*. Complete gelation was achieved, as previously described, by decreasing the temperature, thus obtaining a physical hydrogel where the double helix structures are further stabilised by the presence of the Ag^+ ions.

The in situ production (within the hydrogels) of AgNPs was carried out by simply irradiating the hydrogels with UV light at 365 nm to achieve the reduction of Ag^{+} to Ag^{0}.

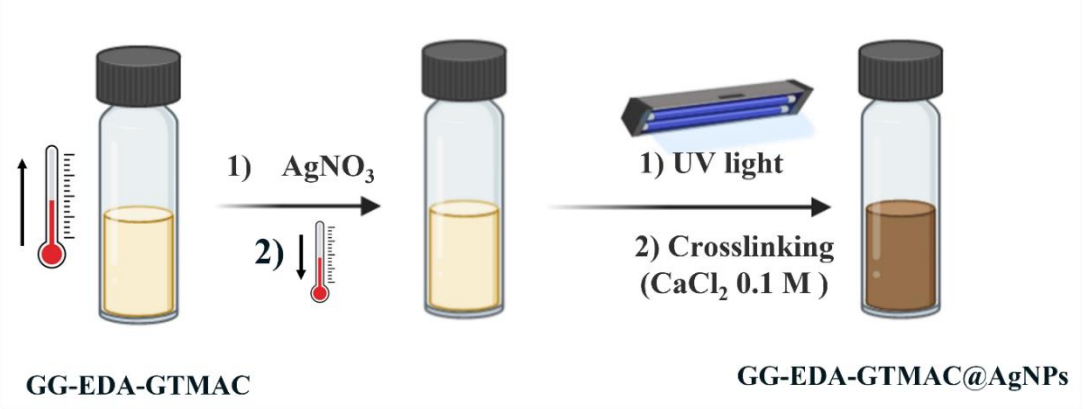

Figure 29. Schematic representation of the production of the nanocomposite hydrogels.

Macroscopic analysis of the samples formed in this way shows that, following the UV irradiation process, a colour change occurs, probably attributable to the formation of AgNPs. Furthermore, no dark aggregate formation has been observed within the hydrogels suggesting a uniform distribution of AgNPs. This result can also be attributed to the high fluidity of the GG-EDA-GTMAC *sol* and the stabilization of Ag^{+} ions, through electrostatic interactions, by the polymer backbone due to capping properties of polysaccharides[314,315,368] and the ability to complex and stabilize metal nanoparticles distinctive of biomaterials with a permanent positive charge[344,345].

Figure 30 shows the chromatic difference between H_0 and H_5 after UV irradiation.

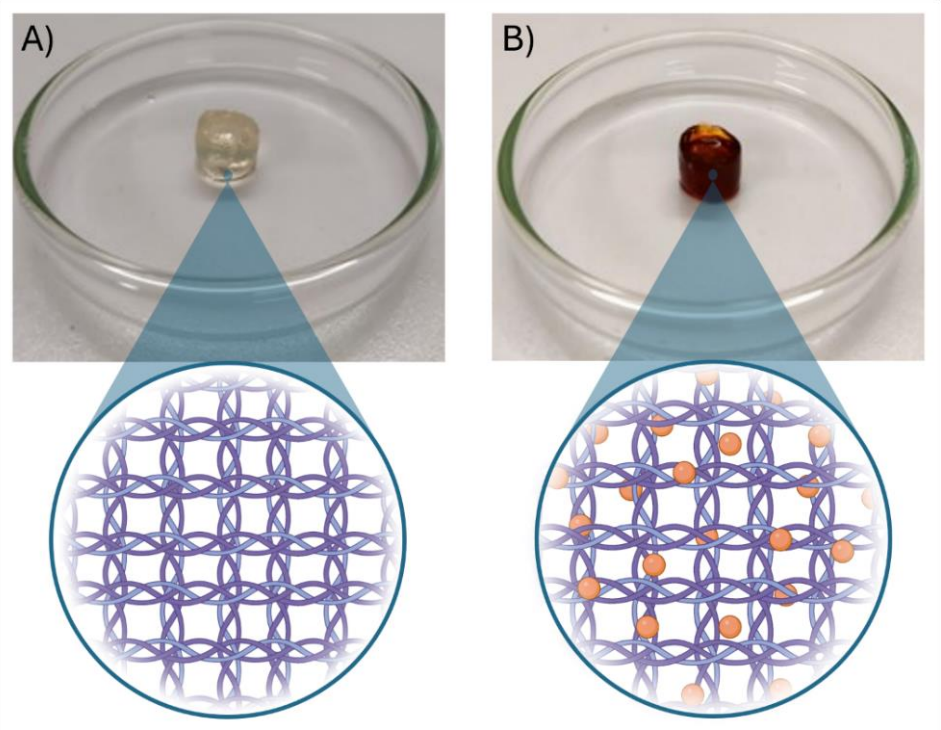

Figure 30. Macroscopic differences between H_0 and H_5 samples, correlated with a schematic representation of their network.

Regarding hydrogels' stiffness, all the samples, although visibly compact and capable of stably maintaining their shape, could flow upon the application of stress, demonstrating the typical behaviour of physical pseudoplastic hydrogels. This is the first macroscopic evidence of their possible injectability, which is further demonstrated. Furthermore, when treated with saline solution (DPBS or $CaCl_2$), the samples showed an increase in stiffness (not shown visually), indicating that the GG-EDA-GTMAC derivative still exhibits a pronounced sensitivity to ionic strength. Both these aspects were further investigated by rheological analysis.

The morphological characterization of the nanocomposite hydrogels was performed on freeze-dried samples, in particular on H_0 and H_5 samples, by scanning electron microscopy (SEM), which, firstly, revealed the porous structure of GG-EDA-GTMAC-based hydrogels and, also, the presence of AgNPs (H_5). Specifically, in order to assess the real contribution of quaternary ammonium groups on the stabilisation of AgNPs, a control nanocomposite

hydrogel (5 mM) was prepared using GG-EDA instead of GG-EDA-GTMAC at the same concentration (3% w/v). By means of this analysis, small sub-micrometric dots homogeneously distributed were observed in both samples, even though considerably smaller for GG-EDA-GTMAC-based samples. EDX analysis suggested that these structures could be attributable to AgNPs. Therefore, this would imply the greater effect of stabilisation of the nanosystems by the novel derivative (Figure 31).

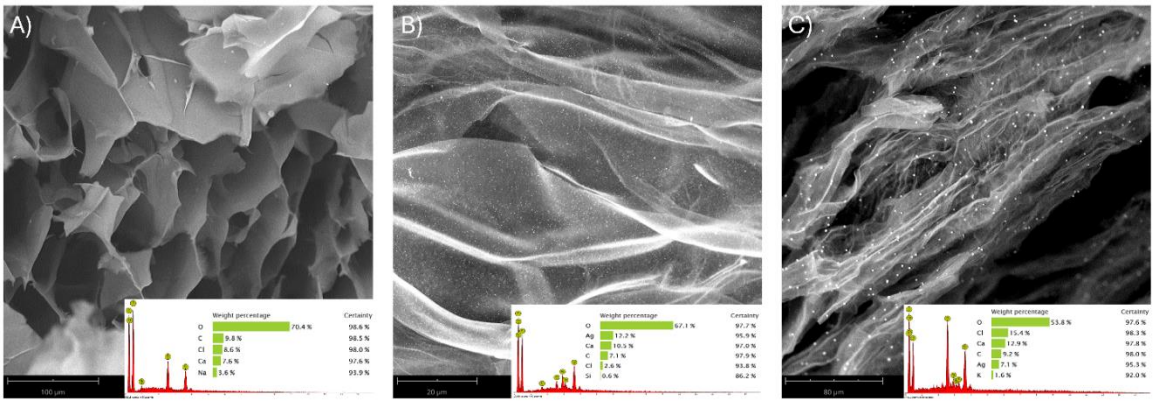

Figure 31. SEM images and EDX results for samples H_0 (A), H_5 (B) and GG-EDA 5 mM (C).

Further confirmation of the actual production of AgNPs within the hydrogels was obtained by UV-Vis spectrophotometric analysis of digested (by means of NaOH) samples. As reported in Figure 32A, the spectrum showed a typical peak (420 nm) relative to the plasmonic resonance of reduced silver Ag^0[369].

Finally, X-ray photoelectron spectroscopy (XPS) analyses were performed. By irradiating the sample with low-energy X-rays, it was possible to quali-quantitatively analyse the surface of the sample and determine, in particular, the state of oxidation of silver present in the sample. The analysis, performed on H_5, highlighted that silver was in its reduced state (Ag^0), thus, confirming the effectiveness of the reduction process. In detail, as shown in Figure 32B, the XPS spectrum presented two well-defined peaks at 368.18 eV and 374.18 eV, typical of metallic silver (Ag3d). The absence of further peaks attributable to different

species shows that all the silver in the sample is in the form of metal nanoparticles. This result confirmed the effectiveness of both the reduction and washing processes of the sample.

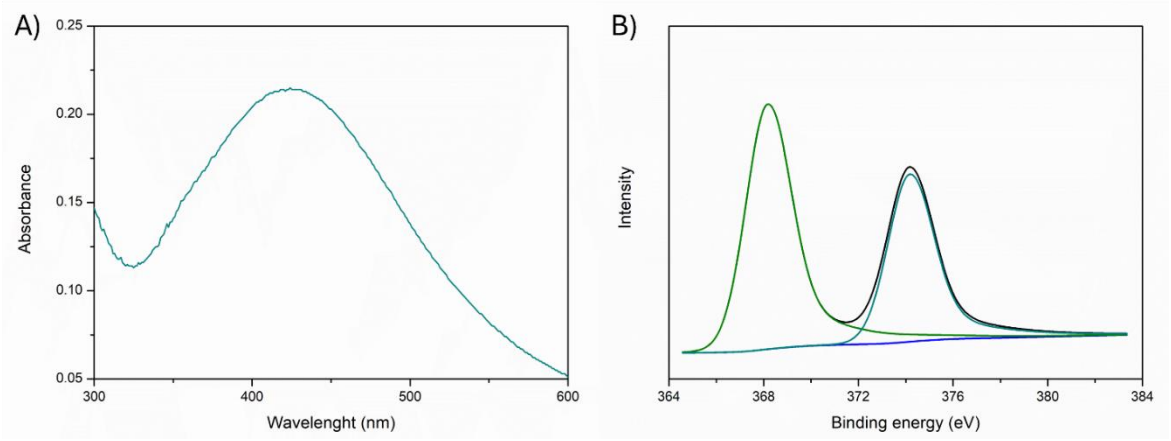

Figure 32. Results of UV-Vis (A) and XPS (B) analyses on the H_5 sample.

3.2.3 Hydrolytic degradation studies

To study the physicochemical properties of GG-EDA-GTMAC-based hydrogels, hydrolytic degradation studies were performed on H_0 and H_5 samples. These studies are important to understand the stability of the hydrogels in a physiological medium and to verify whether the degradation time is compatible with the wound healing timeline. For this reason, the xerogels were incubated in DPBS at 37 °C for 3, 7 and 14 days to observe any macroscopic erosion phenomena and to assess the weight loss over time. The results are reported in Figure 33. Both samples undergo a slight weight loss (maximum 30%) demonstrating their stability in a physiological medium, showing only slight differences.

Furthermore, this result is in line with the wound healing and treatment timeline. Indeed, a degradation of only about 30% after 14 days of incubation indicates that the system can remain at the wound site long enough to perform its function. This result means that, as the system is not rapidly washed away or degraded, it could potentially be applied for wound treatment.

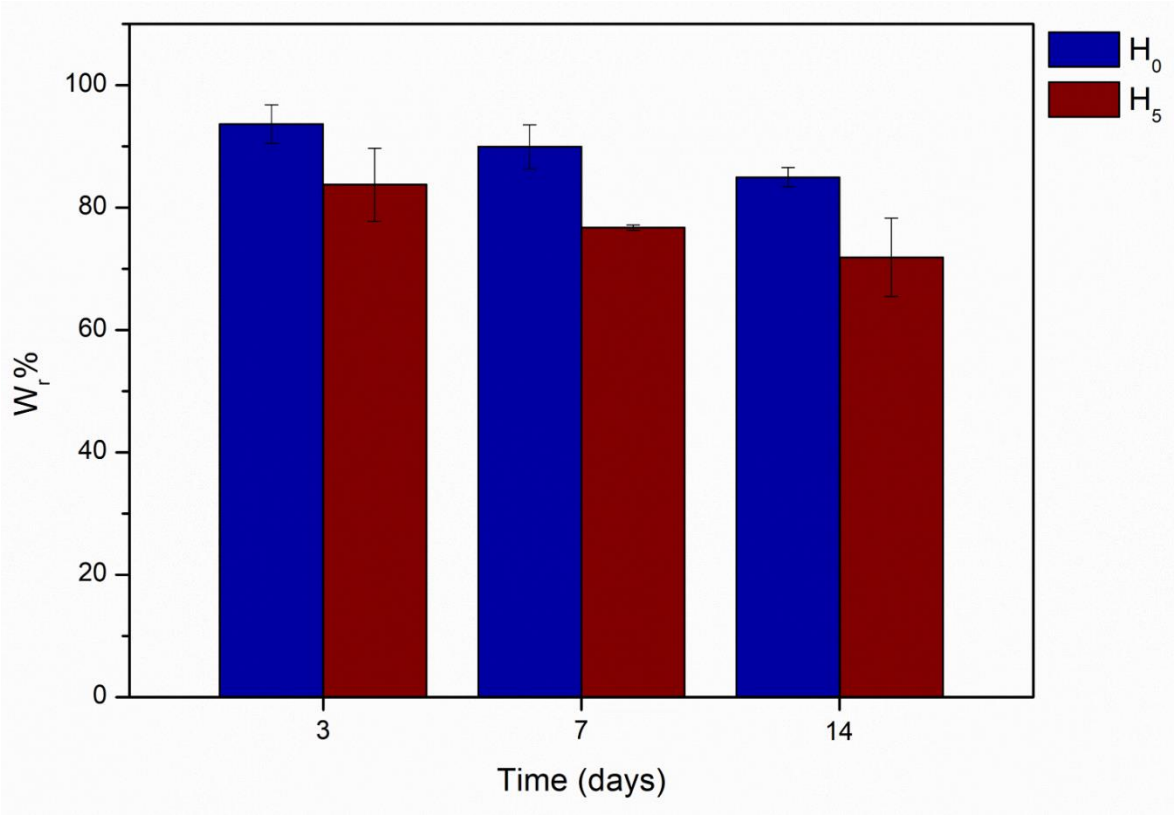

Figure 33. Degradation profile of H_0 and H_5 samples after 14 days of incubation in DPBS.

3.2.4 Rheological characterization

The rheological characterization of the nanocomposite hydrogels allowed to assess their viscoelastic properties as a function of the different starting concentrations of $AgNO_3$ and, thus, of AgNPs. In addition, their injectability was evaluated to assess the possibility of administering them in the wound bed via a minimally invasive technique. Since, as previously reported, nanocomposite hydrogels continued to exhibit macroscopically ionotropic behaviour, the rheological properties were also studied after treatment of the systems with a $CaCl_2$ 0.1M.

First, oscillation amplitude analyses were conducted in order to assess variation of G' and G'' moduli as a function of the deformation imposed on the system (applied strain%), thus, to study the elastic response (G') or the ability to dissipate energy by flow (G'') following mechanical stress or strain, respectively. Furthermore, this analysis provided information

about the influence of AgNPs (the analysis was carried out after UV irradiation) on the above-mentioned properties. As reported in Figure 34A-B, all samples exhibited viscoelastic behaviour depending on the applied strain. In particular, all the samples showed, for low strain %, G' values greater (about an order of magnitude) than G'', indicating that they therefore existed in a gel state. This result indicates that, for minor deformations, the hydrogels exhibited a solid-like behaviour, whereby the applied deformation induced predominantly an elastic response. This behaviour, as amply discussed, is mainly due to the presence of the numerous reversible bonds, in this case of a weak nature (dipole-dipole, hydrogen bonds, electrostatic interactions), which must be broken before allowing the system to flow. The magnitude of G' and G'' was comparable for all samples; no significant increase has been observed as the concentration of AgNPs in the system increased. However, it should be pointed out that the H_0 (without AgNPs) had a significantly lower G' than the H_5 (containing the highest amount of AgNPs). Probably the quantity of nanoparticles in the H_5 compared with the sample that is completely devoid (H_0) is such as to determine a greater number of interactions and thus make the system more structured. The above applies within the region of linear viscoelasticity (LVR), where G' and G'' are independent of strain. It is important to note that the width of this region is not the same for all the samples: in particular, it appears to shorten as the concentration of AgNPs increases. In all likelihood, a greater amount of AgNPs and, thus, of interactions within the hydrogel's network, makes the system more brittle and, therefore, its elastic response is reduced toward a plastic one (i.e. a deformation of the sample such that it flows). For strain % values above the LVR, there was a decrease in viscoelastic moduli as the applied strain increased, with a greater rate for G'. This effect led, graphically, to the intersection of the curves of G' and G'' at the cross point, beyond which G' is less than G'', indicating the *gel-sol* transition. This occurred at high

strain % values of approximately 200-300 % strain% increasing with the samples' AgNPs content.

Oscillation amplitude analyses were also conducted on $CaCl_2$-treated samples; the results are described in Figure 34C-D.

These studies showed the influence of ionotropic crosslinking induced by Ca^{2+} on viscoelastic moduli, resulting in an increase of G' and G'' values of about two orders of magnitude for all samples. This result is considerably relevant, especially, for hydrogels' use in 3D printing. In detail, as described in the introduction, it is often necessary, after the extrusion process, to stabilize the printed structure by crosslinking (ionotropically, enzymatically, or through photo-crosslinking), to allow it to maintain its shape over time. Therefore, such a high increase in G' and G'' following treatment with $CaCl_2$ suggests that the developed hydrogels may be applied in 3D printing stabilizing the printed constructs in this manner.

However, it is also worth noting that the LVR of all the hydrogels has been significantly reduced, suggesting that the greater degree of crosslinking of the systems, even though increases its 'rigidity', on the other hand, also makes it less capable of sustaining elastic-type responses and, therefore, of flowing or breaking under lesser stresses than the non-crosslinked one. Even though this could be considered a limit of the samples, the latter are developed for the treatment of infected wounds, which are usually exposed to low stress or strain.

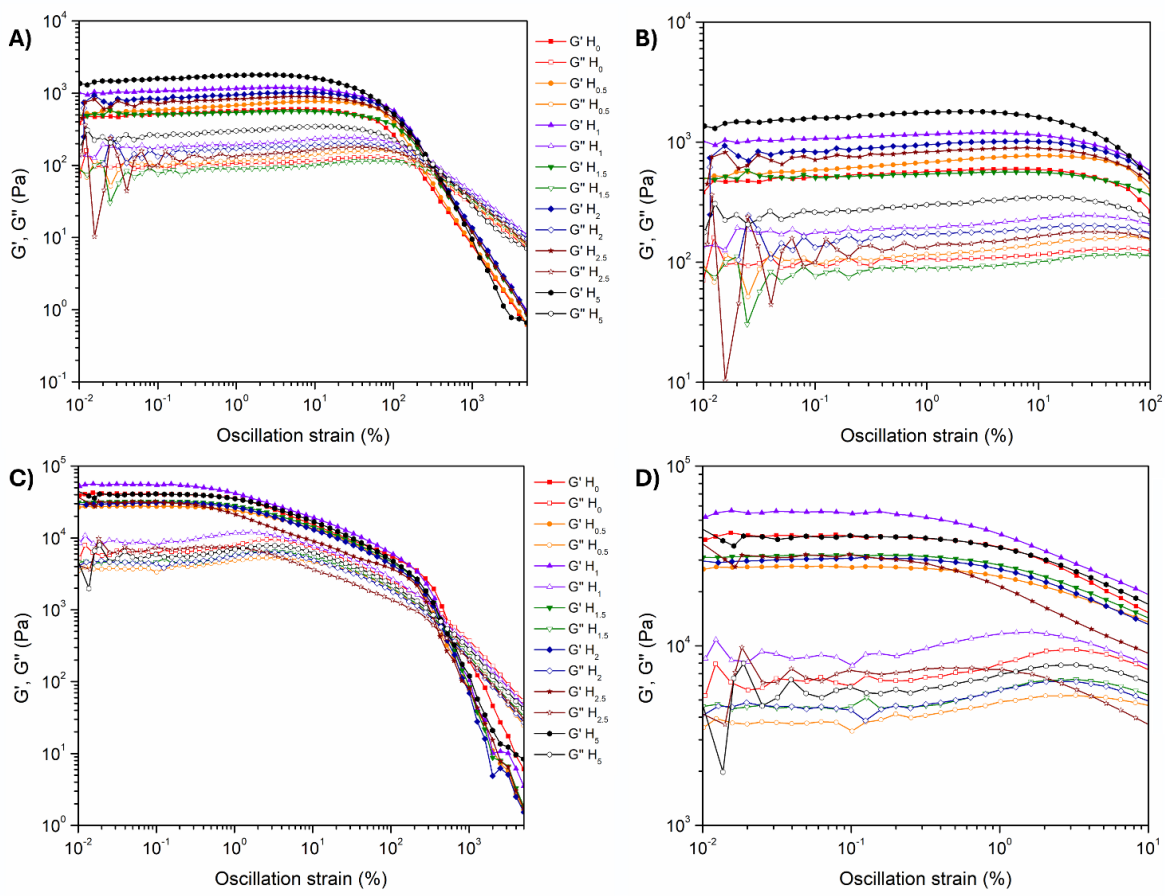

Figure 34. Results of oscillation amplitude tests before (A-B) and after (C-D) ionotropic crosslinking with $CaCl_2$. Figures A and C show the whole spectra, while B and D focus on the LVR.

It was also possible to investigate the shear-thinning properties of the hydrogels by means of flow sweep analyses (Figure 35), aimed at studying the variation of viscosity as a function of shear rate. The results demonstrated pseudoplastic behaviour, i.e. a decrease in viscosity of all systems as the applied shear rate increases. This behaviour can be traced back to the breaking of the intermolecular bonds between the polymer chains, which, as the applied shear rate increases, begin to align in the direction of the stress/strain. All hydrogels exhibited the same behaviour, although there were differences in viscosity at low shear rates, probably due to the different number of interactions between AgNPs and GG-EDA-GTMAC backbone.

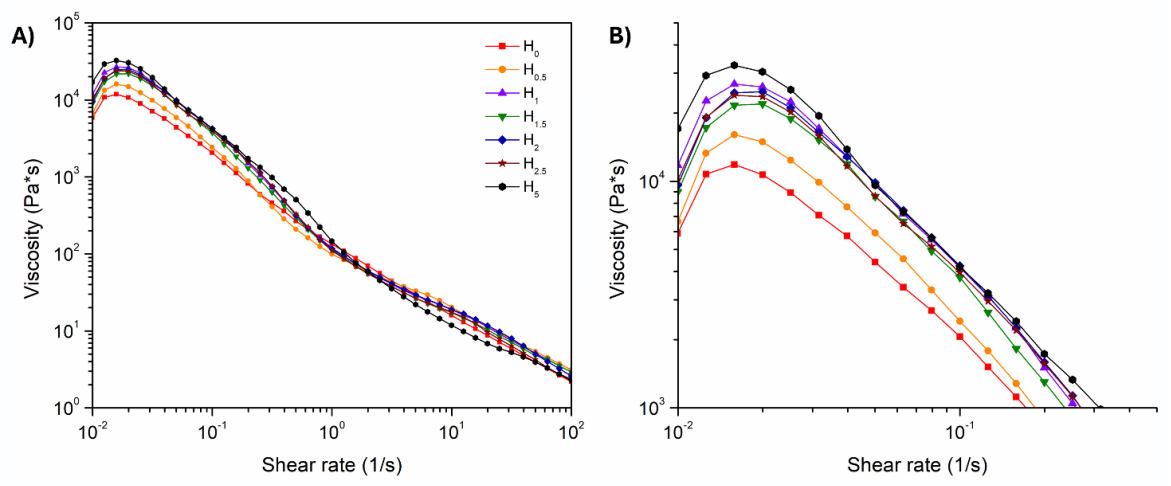

Figure 35. Results of flow sweep tests: whole graphs (A) and focus of the first part (shear rate 0.01-0.5) (B).

However, these differences became almost irrelevant for high shear rate values. Anyway, these results point to shear-thinning behaviour that is crucial for injectable and printable systems, as it indicates their capability to be extruded from a syringe needle.

The injectability of the samples under investigation was also assessed macroscopically by extruding the hydrogels through 21 G needles. As shown in Figure 36, the possibility of 'writing' by injecting the hydrogels using a syringe was a clear demonstration of the easy extrudability of the hydrogel (H_5), due to the presence of reversible interactions within the sample's network that can be broken upon the application of a stress/strain and subsequently reform once the same ceases to be applied.

Figure 36. Macroscopic demonstration on H_5 injectability, by writing with this hydrogel.

Finally, recovery time analyses were performed on the non-crosslinked samples by applying alternating cycles of high and low strain % to assess the recovery capacity of the viscoelastic properties of the systems and, thus, their self-healing behaviour. The results are reported in Figure 37: for better comprehension and, due to the absence of significant differences, the graphs show only H_0 and H_5 recovery properties. All systems recovered around 80 % of the G' and G'' starting values after the first cycle and this value reached almost 100 % in the successive cycles. These results validate the self-healing capabilities of the developed hydrogels and, also, highlight that the amount of AgNPs does not modify this behaviour.

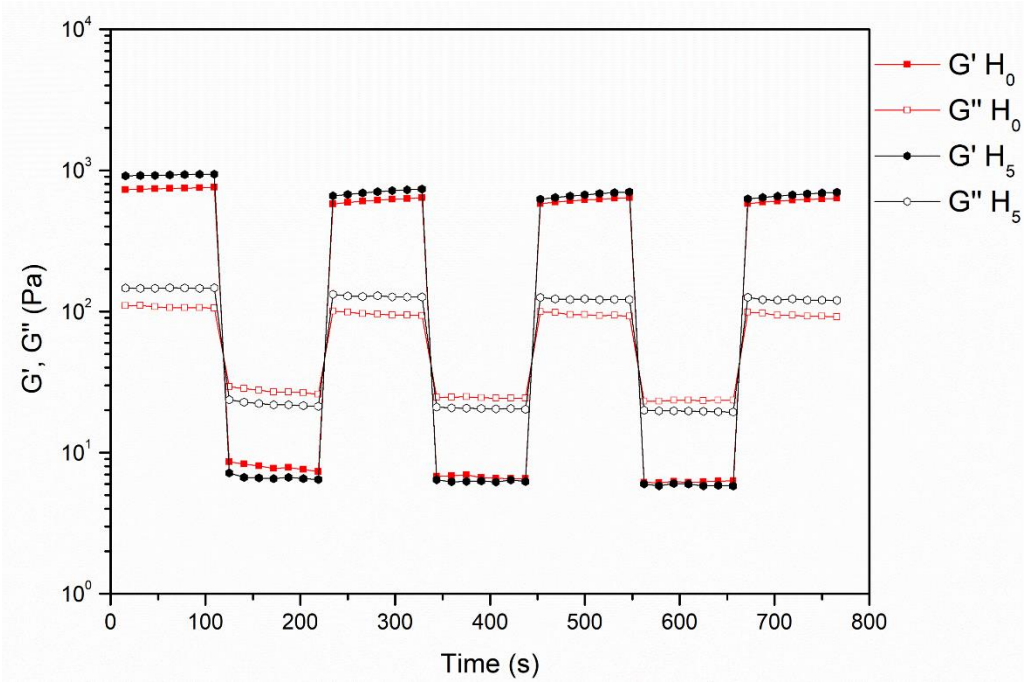

Figure 37. Results of the recovery time analyses performed on the samples H_0 and H_5.

3.2.5 Preliminary 3D printing tests

Once it had been demonstrated that the hydrogels were injectable and, at the same time, susceptible to ionic strength, such that they could be exploited for ionotropic crosslinking processes, 3D printing tests were carried out (Figure 38). H_0 and H_5 samples were taken as reference since rheological studies showed no significant differences between nanocomposite hydrogels with different amounts of AgNPs. In order to have a first proof of concept about the printability of the above-mentioned hydrogels, 15×15×1 mm grids with different mesh sizes were produced. No differences were found in the printing parameters of the two systems, nor in the resolution of the printed constructs.

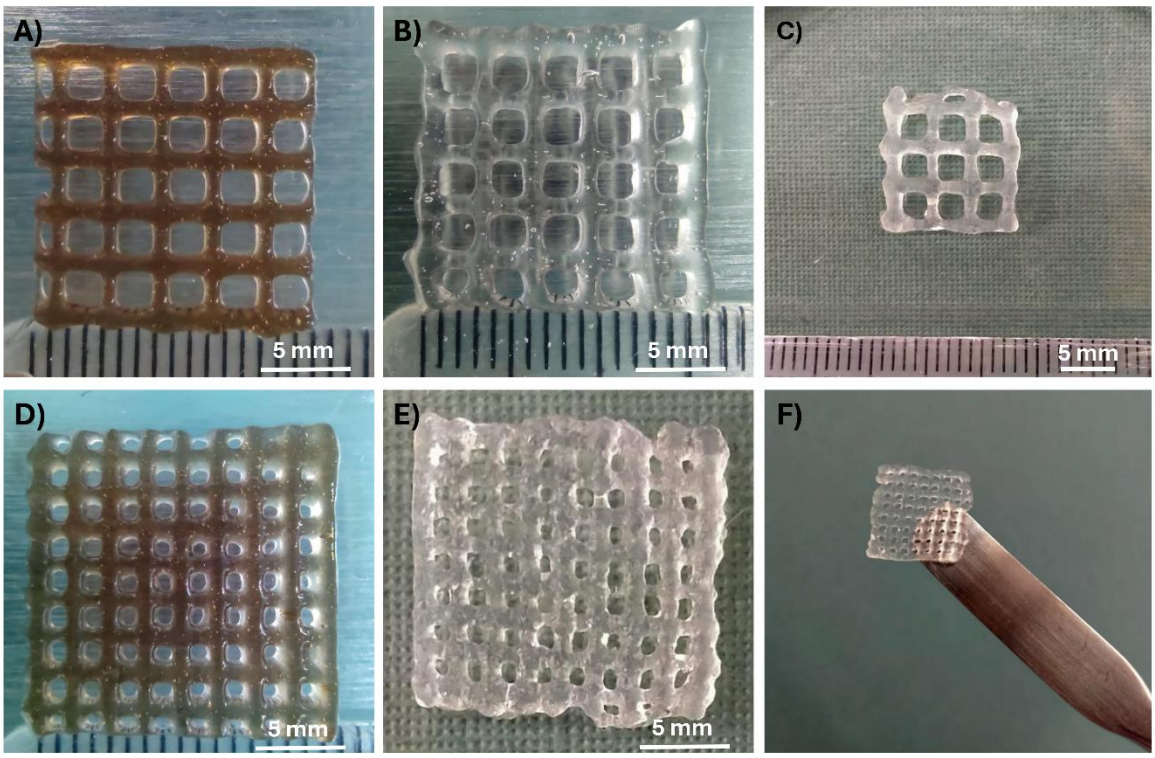

Figure 38. 3D printing preliminary tests performed on the H_0 and H_5 hydrogels realizing constructs with different infill %. H_5 10% of infill (A), H_0 10% of infill (B), H_0 5% of infill (C), H_5 of 15% infill (D), H_0 15% of infill (E) and macroscopic demonstration of handling of printed structures (H_0 15% of infill) after ionotropic crosslinking (F).

3.2.6 Cytocompatibility evaluation

Since the hydrogels were developed for biomedical applications, their cytocompatibility needed to be evaluated; for this reason, MTS assays (Figure 39) and Acridine Orange/Ethidium Bromide (AO/EB) staining were performed. Cell viability was carried out indirectly by placing the sample inside cell culture inserts, without direct contact with the cells (fetal dermal fibroblasts, FD-MSC) seeded at the base of the well. In this way, it was assessed whether any substances released from the samples could be cytotoxic. The MTS results highlighted that, after 24 h of incubation, the samples showed no significant differences (in terms of cell viability) compared to the control (cells cultured in the absence of samples), except for the H_5, whose viability % was approximately 60%. After 48 h, the

samples H_0, $H_{0.5}$, H_1, $H_{1.5}$, H_2, and $H_{2.5}$ showed a viability % of over 80% and can therefore be considered cytocompatible. The sample H_5, on the other hand, shows an increased viability %, albeit less than 80% (approx. 75%).

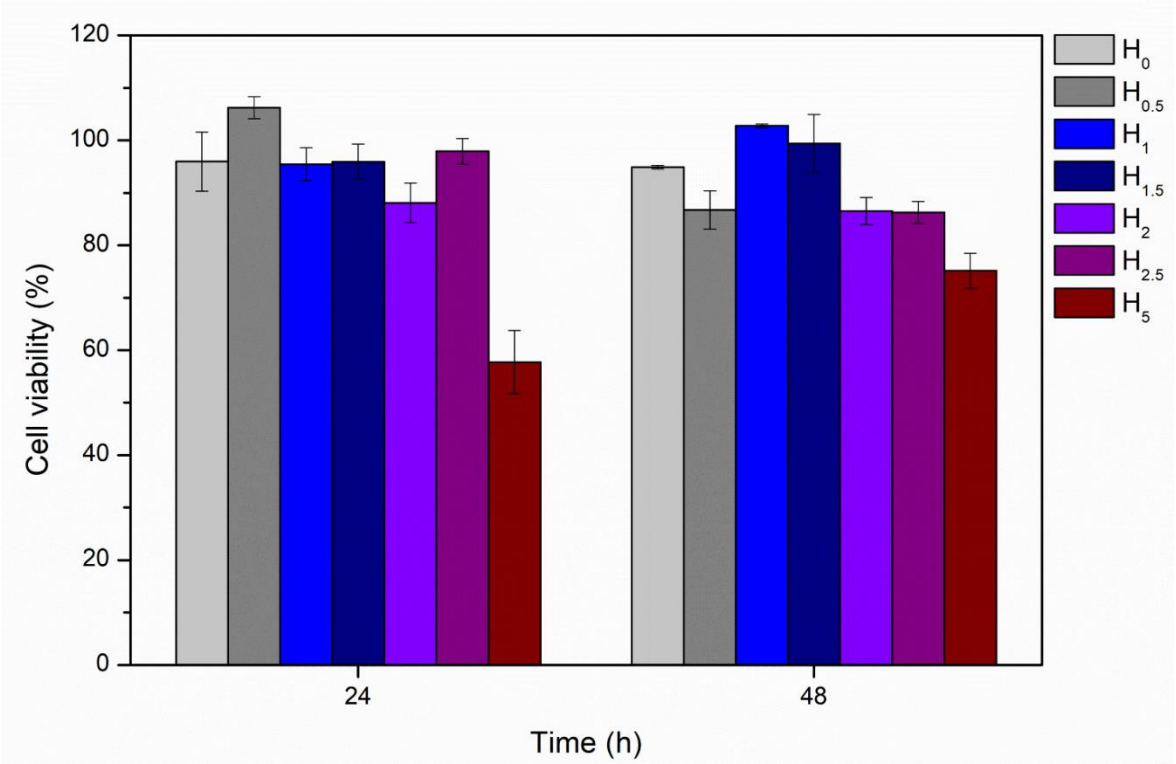

Figure 39. Results of MTS assay on GG-EDA-GTMAC-based hydrogels.

These results were confirmed by the AO/EB colourimetric assay. In detail, AO penetrating living cells emits a bright green fluorescence (if bound to double-stranded DNA, typically in the nucleus) or red fluorescence (if bound to single-stranded DNA or RNA, present in the cytosol), while EB binds to the DNA of cells with damaged membranes, such as dead cells, generating an intense red fluorescence at the nuclear level. As can be seen from Figure 40, the samples H_0, $H_{0.5}$, H_1, $H_{1.5}$, H_2, and $H_{2.5}$ did not affect cell viability and morphology, while the H_5 had significantly fewer live cells present, indicating that some cells died.

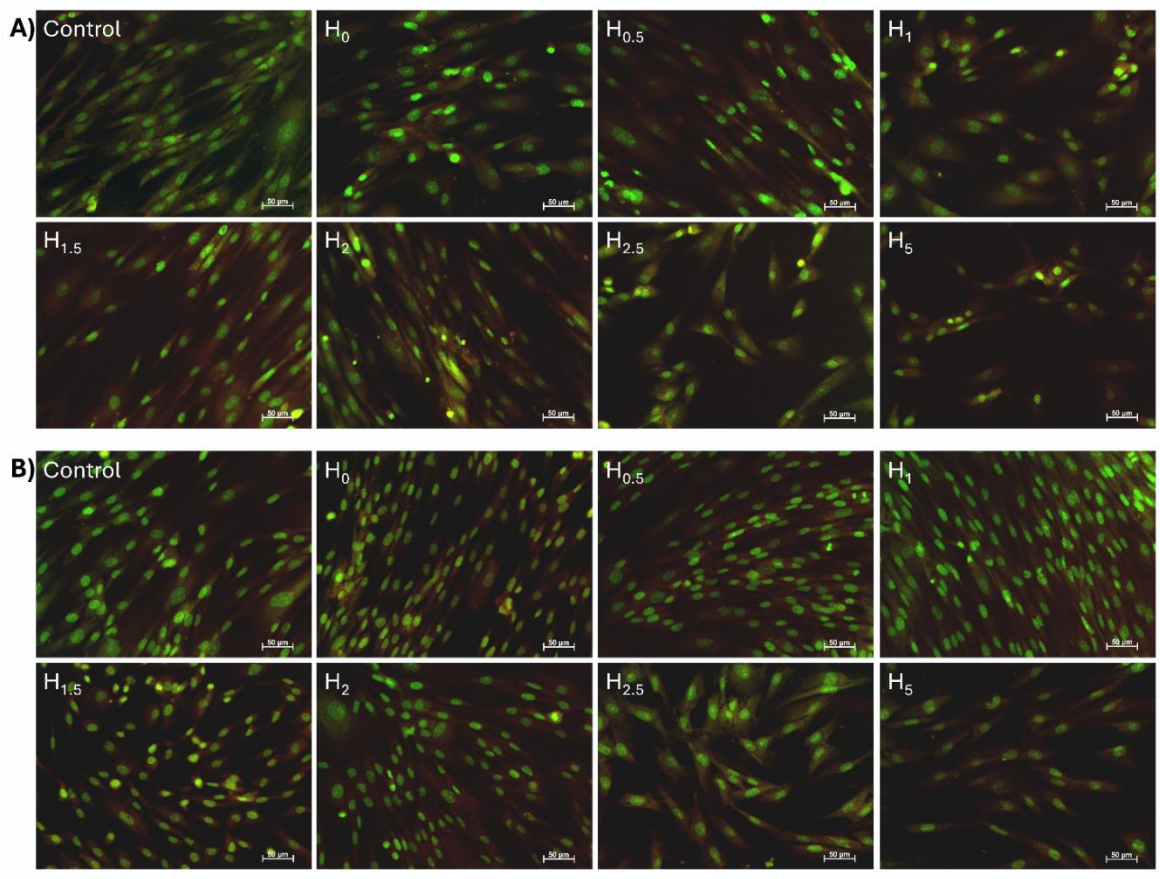

Figure 40. Results of AO/EB staining of FD-MSC incubated in the presence of the GG-EDA-GTMAC-based hydrogels after 24 h (A) and 48 h (B).

3.2.7 Hemocompatibility evaluation

Hemocompatibility is critical for wound dressing application as bleeding is common in wounds. Thus, a haemolysis test was performed to determine the hemocompatibility of the developed hydrogels.

The results, shown in Figure 41, highlighted that all hydrogels exhibited a low hemolytic index (less than 5%), which means favourable blood compatibility[370,371], except for H_5, which confirmed the trend observed in the previous assay. Macroscopically, the supernatants of the red blood cell suspensions treated with almost all samples were nearly transparent, indicating that no haemolysis had occurred.

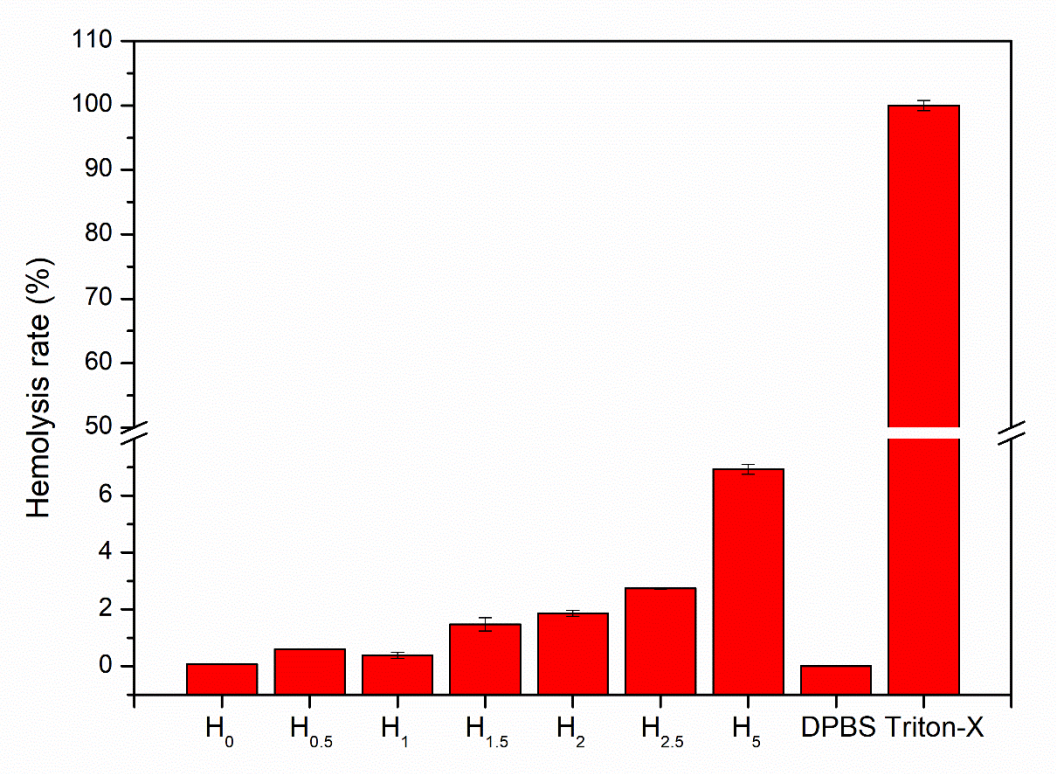

Figure 41. Results of hemolytic assay on GG-EDA-GTMAC-based hydrogels.

3.2.8 Antimicrobial activity

In order to assess the potential antimicrobial activity of the hydrogels, antimicrobial tests were performed against Gram-positive (*Staphylococcus aureus*) and Gram-negative (*Pseudomonas aeruginosa*) bacteria and also against protozoan parasites (*Leishmania infantum*).

3.2.8.1 Antibacterial activity

Inhibition of planktonic growth of the two pathogens (*S. aureus* and *P. aeruginosa*) was assessed through viable bacterial cell counts and expressed as colony-forming units (CFU/mL) after 24 h of incubation of the tested microorganisms in the presence of the produced hydrogels. The results (Figure 42) showed a gradual increase in the antimicrobial effect as the amount of AgNPs incorporated into the sample increased. In particular, the samples $H_{0.5}$ and H_1 show no antibacterial activity as they have CFU/mL values similar to those of H_0.

Likely, the amount of AgNPs in situ formed is not such that it will result in a significant death of these microorganisms. On the other hand, the samples H_1, $H_{1.5}$ and H_2 showed a significant logarithmic decrease (between 3 and 4), while H_5 resulted in a significant decrease (approximately 7 on a logarithmic scale) in viable counts. In this sense, these systems could have great potential for the eradication of bacteria from infected wounds and, consequently, in their regeneration.

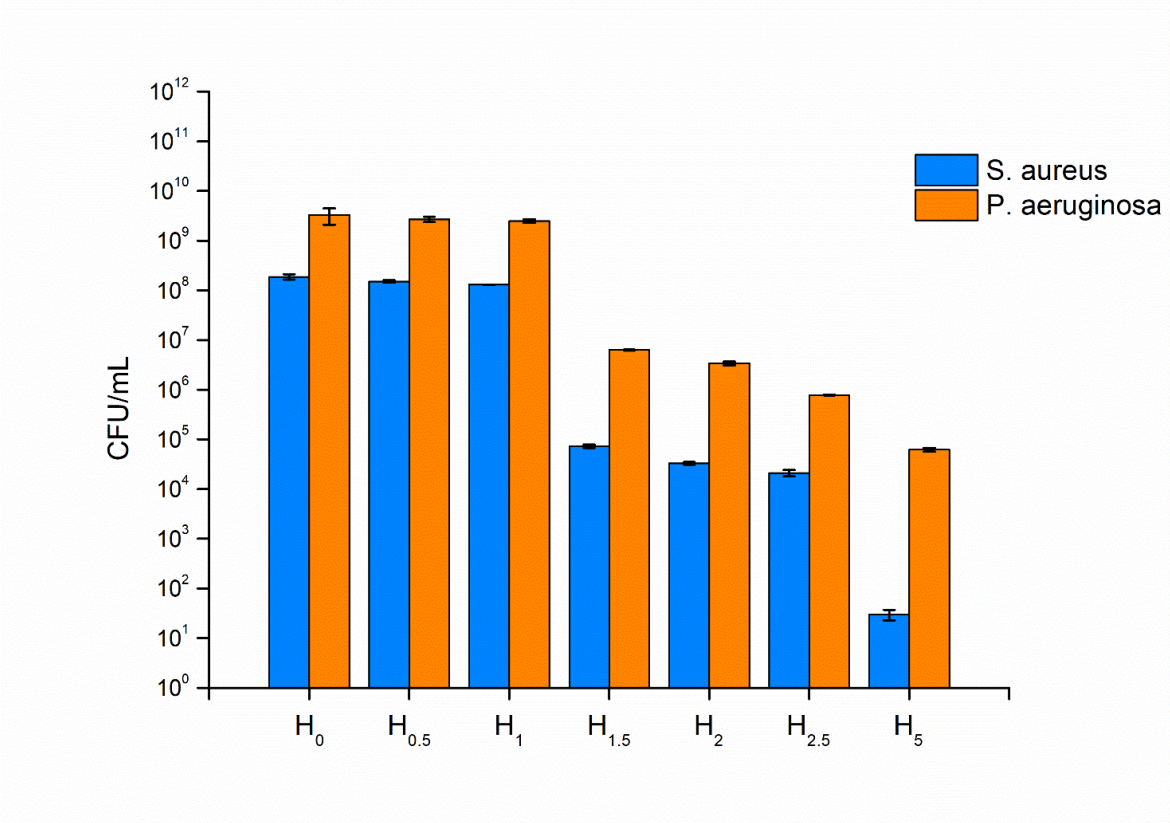

Figure 42. Antibacterial activity evaluation of GG-EDA-GTMAC-based hydrogels against *S. aureus* and *P. aeruginosa*.

3.2.8.2 Antiprotozoal activity

The antiprotozoal activity of GG-EDA-GTMAC@AgNPs hydrogels was evaluated on a strain of *Leishmania infantum*, aiming to determine the percentage of live protozoa compared to the non-AgNPs-loaded system (Figure 43). It was observed that there was no significant change in viability for protozoa treated with $H_{0.5}$. However, starting with the H_1

system, a decrease in protozoan concentration was observed. Therefore, the percentage of protozoa decreased significantly increasing the amount of AgNPs inside the systems. In particular, a significant reduction in *Leishmania* concentration is observed for samples $H_{1.5}$, H_2 and $H_{2.5}$; the latter, in detail, induced a complete eradication of the microorganism.

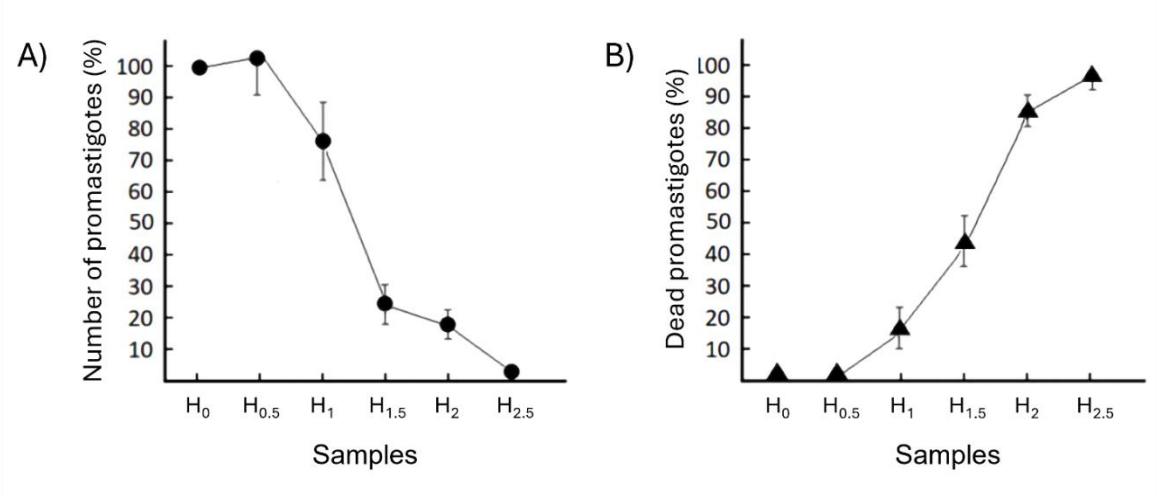

Figure 43. Results of antileishmanial activity evaluation of GG-EDA-GTMAC-based hydrogels.

Subsequently, the viability of the protozoa was assessed following incubation in the presence of these hydrogels; using fluorescence markers, AO/EB (Figure 44), the percentage of live protozoa out of 300 parasites was determined, expressing the results as dead protozoa %. This assay confirmed the previous one, which means that a significant reduction in cell viability was observed starting from $H_{1.5}$ (mortality of about 50 % of the protozoa was observed), whereas $H_{2.5}$ confirmed 100% mortality. The high activity of AgNPs and, thus, of the hydrogels, is probably due to *Leishmania*'s high sensitivity, especially at the mitochondrial level, to ROS, whose production is induced by AgNPs. These results are noteworthy since it was possible to completely eradicate the protozoan operating inside the cytocompatibility range. For this reason, the developed system could suggest an interesting therapeutic approach for the treatment of cutaneous infections.

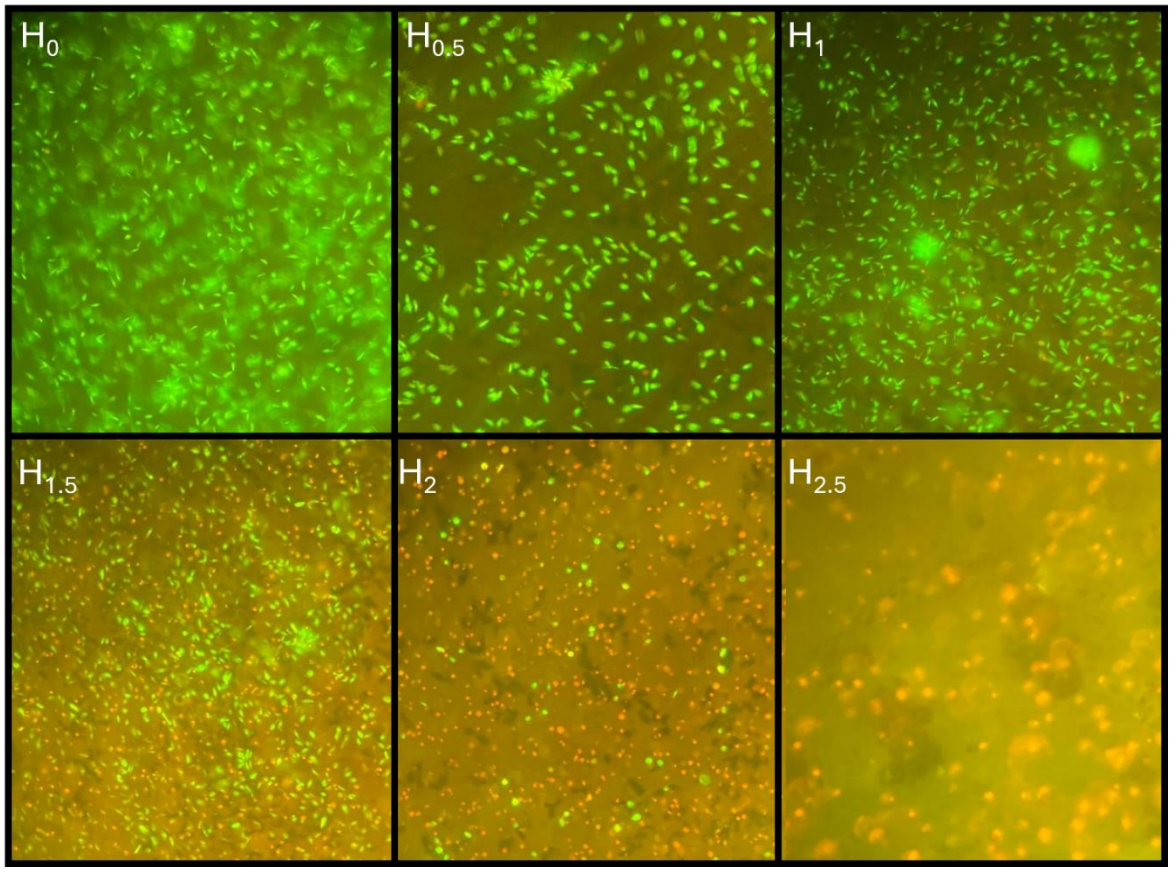

Figure 44. Results of AO/EB staining on *Leishmania infantum* incubated after 24 h of incubation with GG-EDA-GTMAC-based hydrogels. The images were acquired with a 100-X magnification.

3.2.9 Conclusions

In this work, injectable and 3D-printable nanocomposite hydrogels were developed for the treatment of infected wounds. In detail, a novel quaternized derivative of gellan gum was designed and synthesized and then, exploited to produce antimicrobial hydrogels, stabilizing in situ-produced silver nanoparticles.

These latter were obtained with a versatile and reproducible synthesis (by irradiation with UV light) directly within the hydrogels, without the need for additional reducing agents. UV-Vis, SEM-EDX and XPS analysis confirmed their formation and uniform distribution inside the hydrogels as well as the efficiency of the reduction process. Degradation studies

highlighted their high stability in physiological fluids and lower degradation independently of AgNPs content.

Rheological characterization confirmed hydrogels' ionotropic behaviour already macroscopically observed. Furthermore, pseudoplastic and self-healing behaviour was demonstrated, indicating good injectability and recovery of starting viscoelastic properties for all samples. The rheological results suggest the developed systems could be easily injected into the infected site, but they could be also suitable for 3D printing applications, as subsequently demonstrated. Cyto- and hemocompatibility were assessed for almost all samples. Lastly, the antimicrobial assays showed great activity against both bacteria (Gram-positive and negative) and protozoan (*Leishmania*), suggesting that a strong reduction of infecting microorganisms in chronic wounds could be obtained with the developed hydrogels, operating, at the same time, in biocompatible range. All these results suggest that the nanocomposite AgNPs-doped hydrogels could be potential candidates for the treatment of infected wounds overcoming current limitations.

3.3 3D-printed double-crosslinked polysaccharide/polyaminoacid hydrogels for bone regeneration

Bone defects are one of the main causes of disability worldwide[372]. Due to the limitations of autografting[373,374], the latest advances have been focused on tissue regeneration approaches that use injectable hydrogels or 3D-printed hydrogel-based constructs to refill appropriately small bone defects (like alveolar or maxillofacial bone fractures) without the need for external fixatives, leading to the regeneration of damaged tissue in the long term[335,375–377]. In this context, injectable hydrogels are extremely advantageous for this purpose, and, among them, double-crosslinkable hydrogels appear as ideal candidates, for direct injection and as inks for extrusion-based 3D printing. For this reason, in this work, injectable and printable double-crosslinked polysaccharide/polyaminoacid hydrogels were developed, by mixing oxidized xanthan gum (XGox) and methacrylate polyaspartylhydrazide (PAHy-MA) and incorporating hydroxyapatite nanoparticles (Hap)[378]. The hydrogels were designed by exploiting dynamic and covalent crosslinking and, specifically, hydrazone bond formation and photo-crosslinking, which allowed respectively instant gelation, self-healing, shear-thinning properties and increased stability and shape retention. Furthermore, the choice of PAHy-MA, with its dual functionalization (both hydrazine and methacrylic moieties), allowed this macromolecular crosslinker to spontaneously form dynamic bonds under physiological conditions and enabled controllable covalent crosslinking upon UV irradiation. This facilitated the development of a gelling system with a simple composition and a controllable crosslinking mechanism, permitting the adjustment of the viscoelastic properties of the resulting hydrogel. The interesting viscoelastic properties as well as their good printability suggested the suitability of the developed systems as injectable and printable materials. Furthermore, the absence of cytotoxicity and the early formation of a bone-like matrix when osteosarcoma-derived cells

(MG-63) were cultured in the scaffolds for 21 days, with an increased collagen I deposition, mineralization and the expression of characteristic osteogenic markers, suggested their application in bone regenerative medicine as a filling material for irregular small bone defects.

3.3.1 Synthesis and characterization of XGox

XGox was synthesized through oxidation by sodium (meta)periodate, as reported earlier[264] (Figure 45A). This reaction allows the formation of ring-opening dialdehyde products through selective cleavage of the C-C bond between the vicinal hydroxyl group of the anhydro-d-glucopyranose residues[131,379]. The success of the reaction was confirmed by FT-IR and ^{1}H-NMR analysis. The FT-IR spectrum (Figure 45B) showed the presence of a peak at 1723 cm^{-1} related to CHO groups (carbonyl stretching vibration), which was more pronounced than in the XG spectrum as reported elsewhere[129]. Moreover, the presence of aldehyde groups was confirmed by ^{1}H-NMR (Figure 45C), which exhibits its typical peak at around 9.35 ppm[360,380].

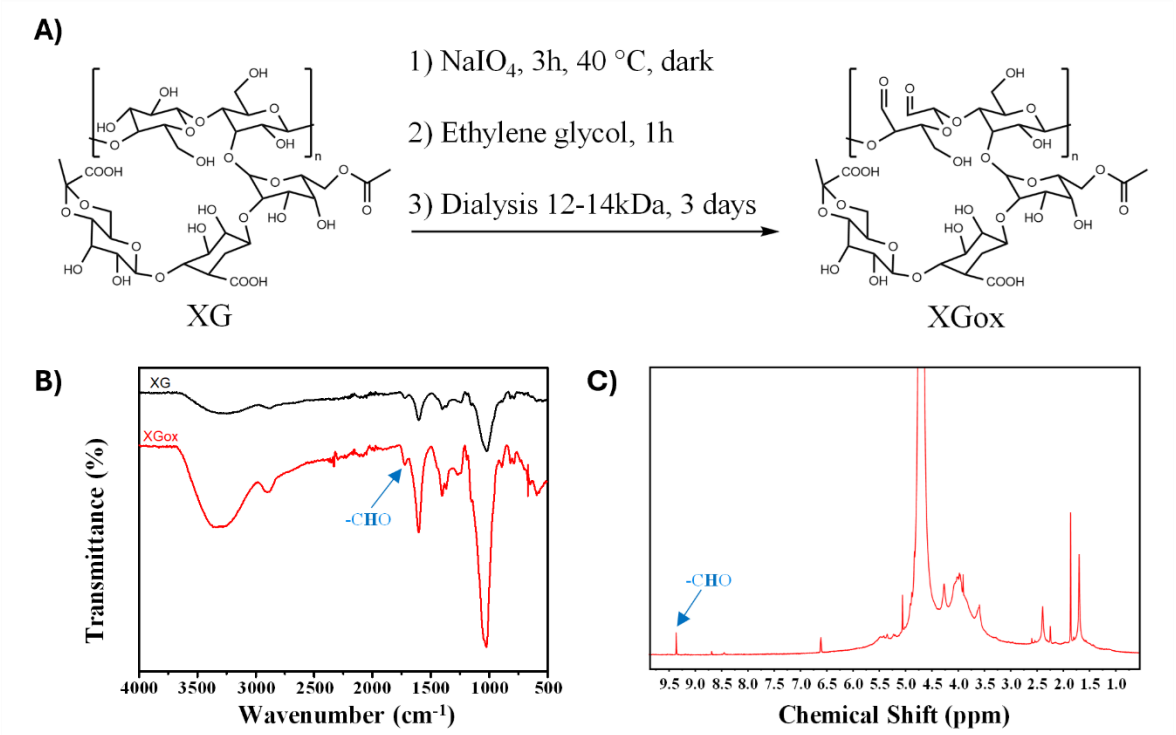

Figure 45. Schematic representation of XGox synthesis (A). FT-IR spectrum of XG (top, black) and XGox (bottom, red) (B). The spectra were normalized to the peak of carbonyl acetate stretching at 1021 cm^{-1}. ^{1}H-NMR spectrum of XGox (C).

3.3.2 Synthesis and characterization of PAHy-MA

Firstly, PAHy-MA was chosen due to the advantages of its precursor PAHy: synthesized for the first time by Giammona et al., in a facile and affordable manner through a reaction between a polysuccinimide (PSI) and hydrazine[381], α,β-polyaspartylhydrazide (PAHy) is a high water-soluble polymer, non-toxic and non-immunogenic, with a polyaminoacid-like backbone that can be easily functionalized with hydrophilic or hydrophobic moieties for different applications (hydrogels and nanoparticles for gene, protein and drug delivery)[382–388]. Furthermore, the presence of hydrazide moieties allows mixing with aldehyde-functionalized polymers (like oxidized polysaccharides) to form hydrazone-based networks[278,389].

PAHy was synthesized according to a procedure reported in the literature[381]. The methacrylation reaction was performed in carbonate-bicarbonate buffer (pH=9.4) with methacrylic anhydride and then the product was purified by dialysis (Figure 46A), following reaction conditions reported for the synthesis of methacrylated gelatin with some modifications[390]. Spectroscopic characterization of PAHy-MA by ^{1}H-NMR (Figure 46B) showed the presence of two peaks at δ 5.4-5.8 ppm, related to vinyl protons of the methacrylic moieties, not found in PAHy ^{1}H-NMR spectrum (Figure 46B, top). Comparing the area of the peak at δ 1.83 ppm, attributable to the methyl of the methacrylic group, with that of the peak around δ 2.5-3 ppm relative to methylene protons of the polyaspartamide chain, the derivation degree in methacrylic groups was approximated to be 36 mol% compared to PAHy repetitive units. This result was confirmed by 2,4,6-Trinitrobenzenesulphonic acid (TNBS) assay that showed a derivatization degree of 39 mol%.

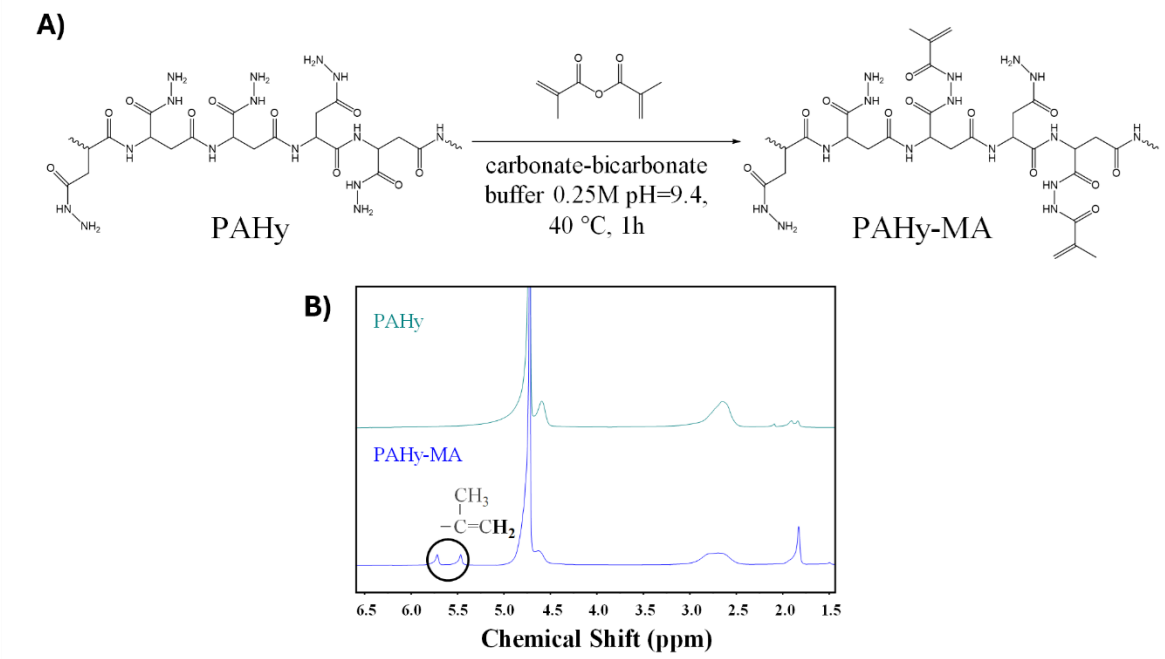

Figure 46. Schematic representation of PAHy-MA synthesis (A). ^{1}H-NMR spectra of PAHy (top, green) and PAHy-MA (bottom, blue) (B).

3.3.3 Production and physicochemical characterization of XGox/PAHy-MA-based hydrogels

The hydrogels were designed by exploiting the formation of hydrazone-based networks (Figure 47) and were produced by mixing XGox and PAHy-MA solutions, incorporating hydroxyapatite nanoparticles (Hap) when appropriate (Figure 48A).

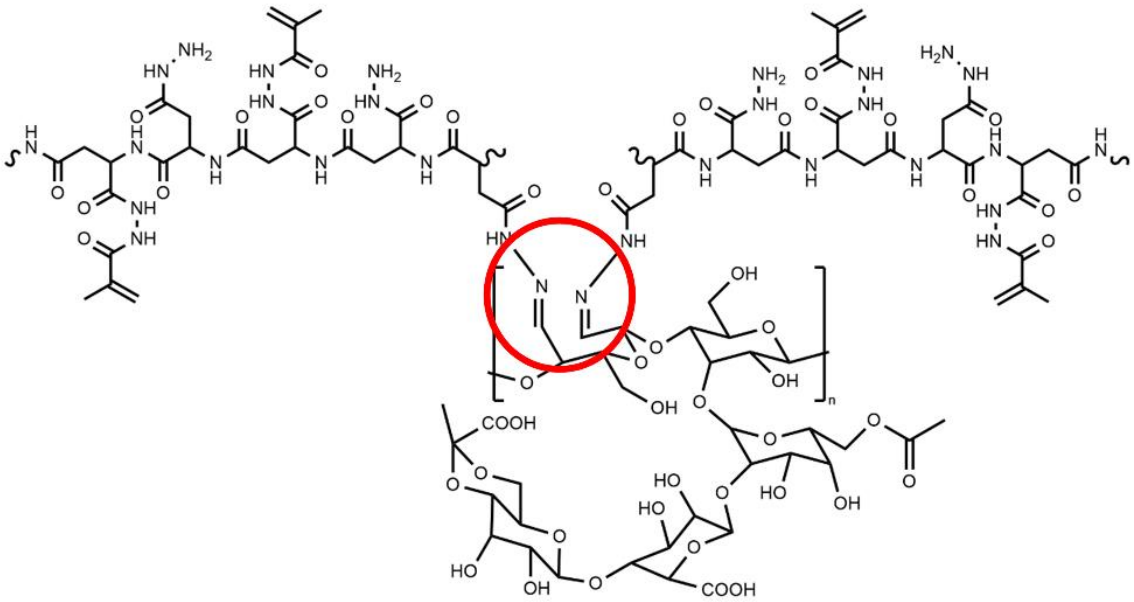

Figure 47. Schematic representation of hydrazone bond formation in XGox/PAHy-MA hydrogels.

With the aim of evaluating the influence of Hap on the viscoelastic and biological properties of the hydrogels, three different samples were produced with the same amount of XGox (1% w/v), PAHy-MA (2% w/v) and photoinitiator (PhI, 0.3% w/v) and different amounts of Hap (0%, 0.01%, 0.1% w/v) (Table 2).

Table 2. Final composition of XGox/PAHy-MA-based hydrogels.

Sample	XGox (%w/v)	PAHy-MA (%w/v)	Hap (%w/v)	PhI (%w/v)
A	1	2	0	0.3
B	1	2	0.01	0.3
C	1	2	0.1	0.3

The gelation process, by mixing the polymer solutions, was very quick and the hydrogels formed in a few seconds. All the obtained hydrogels showed macroscopic differences compared to XGox and PAHy-MA solutions at the same concentration: especially they had a higher viscosity, and gel behaviour as shown by their shape retention capability (Figure 48B). No macroscopic differences (except the colour) were observed between the hydrogels with and without Hap. On the other hand, photo-crosslinking caused an increase in stiffness that could be appreciated macroscopically. In this way, double-crosslinked systems were obtained: the formation of dynamic hydrazone bonds created a polymer network within the systems, allowing the gelation process after mixing the two polymer solutions, meanwhile, covalent photo-crosslinking, through UV irradiation, established another network, which increased the stability in physiological fluids and enhanced the viscoelastic moduli of the resulting systems, as further demonstrated.

In order to define the optimal viscoelastic properties for 3D printing, other weight ratios XGox/PAHy-MA were tested (1:4, 1:1 and 1:0.5). However, the viscoelastic properties of these samples were too stiff (1:4 XGox/PAHy-MA) or too fluid (1:1 and 1:0.5 XGox/PAHy-MA) to be extruded. Thus, hydrogels with an XGox/PAHy-MA weight ratio equal to 1:2 were designed (Figure 48B), showing the best combination of fluidity and stiffness for extrusion-based 3D printing.

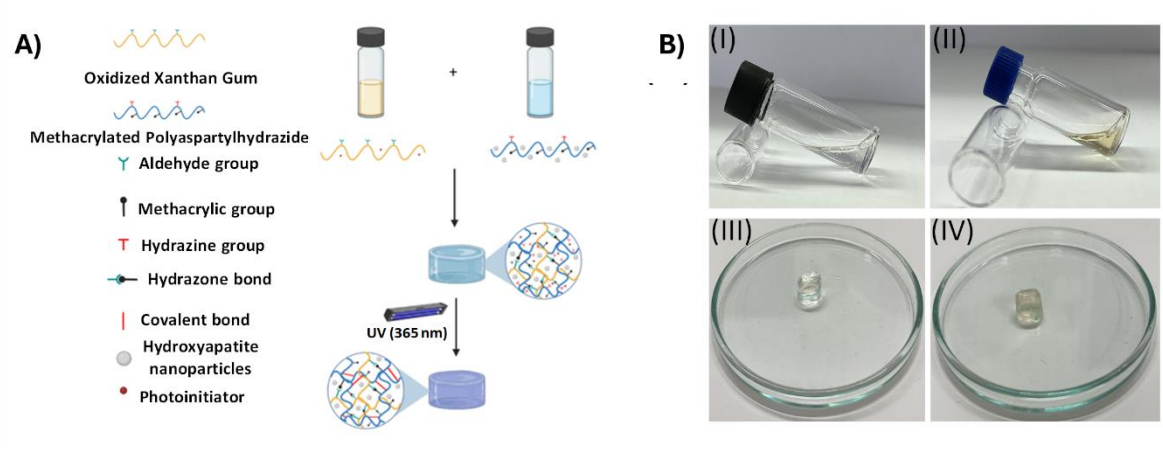

Figure 48. Schematic representation of hydrogel A preparation (A). Pictures of XGox dispersion (B, I), PAHy-MA dispersion (B, II), and hydrogel A before (B, III) and after (B, IV) the photo-crosslinking process.

FT-IR analysis (Figure 49A) confirmed the formation of the hydrazone bond as observed by the disappearance of the aldehyde band at 1723 cm^{-1} (stretching of carbonyl groups), even if it was not possible to appreciate the hydrazone band, as it overlapped with the characteristic bands of PAHy-MA. However, it has to be taken into account that the hydrazine moieties could also establish inter-polyelectrolyte interactions with oxidized polysaccharides that can contribute to the hydrogels' architecture, affecting their viscoelastic properties: indeed, depending on the pH, they could be protonated and, thus, establish electrostatic interactions with the carboxylate groups of XGox. However, they are not responsible for the gelation process, since, after mixing non-oxidized xanthan gum with PAHy-MA, no variations in the viscoelastic properties or the gelation process were observed. For this reason, it is possible to affirm that the main cause of gelation is the formation of a hydrazone-based network, which also provides to the system's self-healing properties; thus, this approach is often used to develop injectable hydrogels for different applications.

Furthermore, hydrazide moieties can be further exploited to introduce other functional moieties on PAHy. For example, in this case, the functionalization with methacrylic

anhydride gives the biomaterial the capability to undergo photo-crosslinking: in this way, it acts as a macromolecular crosslinker with double functionalisation, conferring good injectability and shape retention to the hydrogel.

Once the weight ratio of the main components of the hydrogels was established, their stability in physiological fluid (Figure 49B) was investigated. Double-crosslinked (covalent and dynamic) and single-crosslinked (dynamic crosslinking) hydrogels showed a different degradation profile over time. In particular, while the single-crosslinked hydrogels reached 61.29 ± 3.22 % of the initial weight after 21 days of incubation, the double-crosslinked ones suffered a lower initial weight loss (they maintained 81,95 ± 0.66 % of starting weight after 7 days of incubation) that remained constant over the next 14 days (77.77% ± 2,05% of the initial weight). This result confirmed the higher stability of the double-crosslinking hydrogels in physiological fluid; their longer degradation time, compared with the single-crosslinking ones, ensures longer stability in the physiological environment. These results suggest that the hydrogel could be injected and photo-crosslinked into the bone defect, allowing a longer permanence of the system in the damaged site.

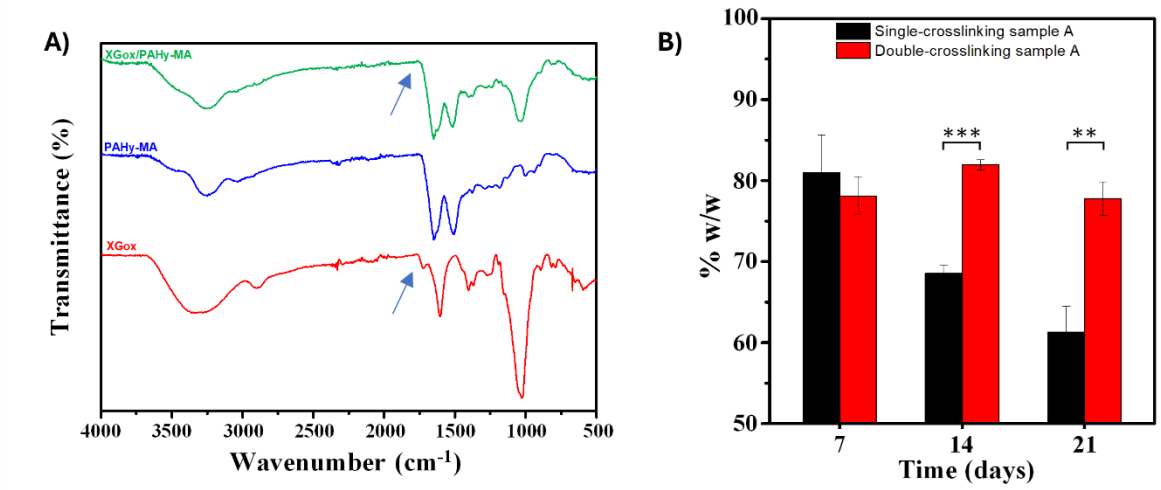

Figure 49. FT-IR spectra of sample A, PAHy-MA and XGox (A). Degradation studies of single-crosslinking and double-crosslinking hydrogels (B).

3.3.4 Rheological characterization

Rheological measurements were performed to evaluate the viscoelastic properties of double-crosslinked hydrogels. Specifically, the analyses aimed to validate the injectability of the systems, and, also to verify if they can be used as inks for 3D printing applications. In general, hydrogels with a storage modulus in the range of 10^2-10^4 Pa could be considered injectable and with good extrudability[93,240,329,391,392]. For this reason, pseudoplastic behaviour, self-healing properties and the viscoelastic modules of the hydrogels with different content of Hap were investigated.

Storage (G') and loss (G'') moduli were initially evaluated with oscillation amplitude analyses (Figure 50A-C). The results showed that the incorporation of Hap, at the concentration of 0.01% w/v (sample B), does not affect the viscoelastic moduli, which means that the Hap nanoparticles, in this case, do not interfere with the gelation process and with the formation of hydrazone network. However, by increasing the amount of Hap to 0.1% w/v (sample C), there is a small increase in the viscoelastic moduli before the photo-crosslinking. Regarding the latter, as expected, an increase of G' was observed after photo-crosslinking (Figure 50D-F): this is due to the formation of new intermolecular bonds, and thus, of another network, that led to the increase of viscoelastic modules. Furthermore, the capability of double-crosslinked hydrogels to recover after deformation was evaluated, as an indication of shape retention capability after the extrusion of a 3D printing process. A good recovery of the viscoelastic properties of samples before the photo-crosslinking process was evident (Figure 50G-I). After the first cycle, G' was about 45%, 60 % and 50 % of its starting value for samples A, B and C respectively. In the following cycles, the recovery of G' values (referred to the previous cycle) was about 92%, 95% and 90% for samples A, B and C, respectively. This property is due to the dynamic nature of the intermolecular interactions that provide a good recovery of viscoelastic moduli. This property allows a 3D printing

application of the hydrogel, being able to recover its viscoelastic properties and retain the shape after the extrusion process.

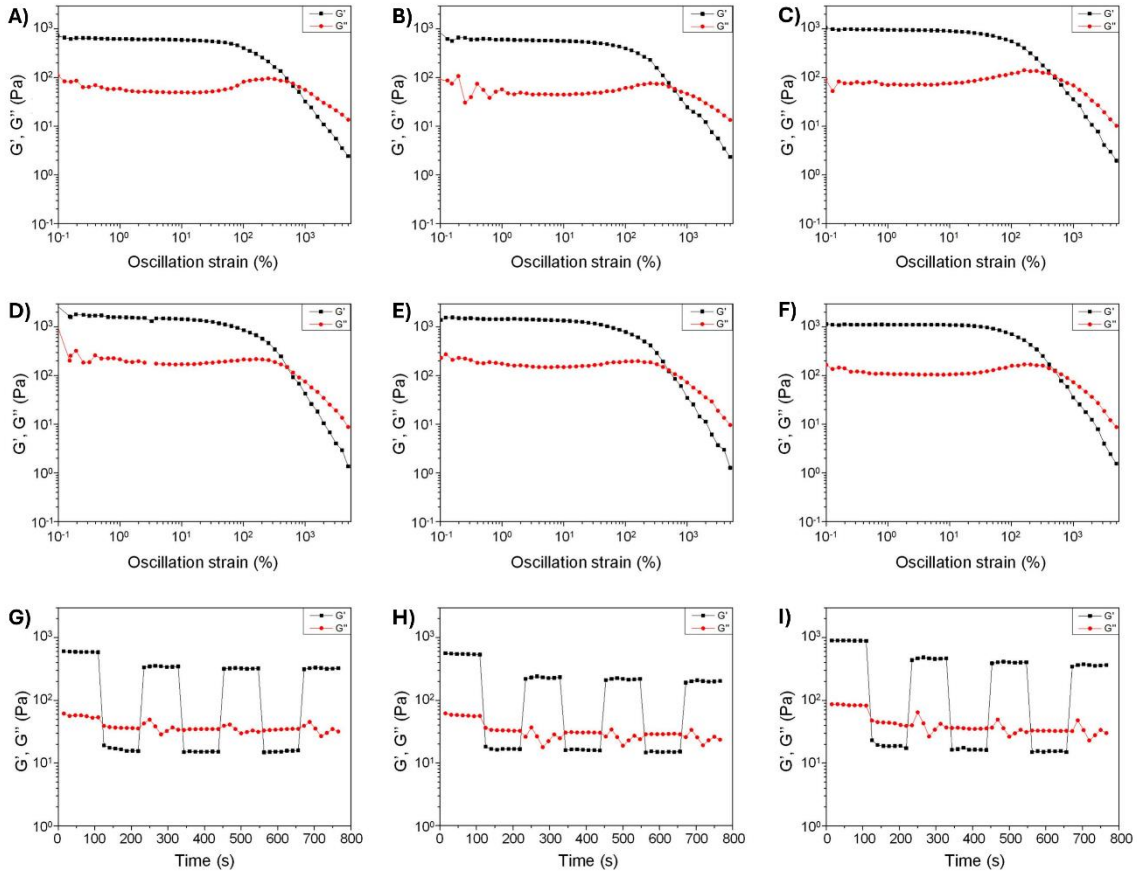

Figure 50. Rheological characterization of the hydrogels. Results of oscillation amplitude analysis for samples with 0% (sample A), 0.01% (sample B) and 0.1% w/v Hap (sample C) before photo-crosslinking (respectively A, B and C) and after UV irradiation (respectively D, E and F). Results of recovery time tests for samples A (G), B (H) and C (I) before photo-crosslinking.

Analysis of the viscosity of the samples under varying shear was carried out on sample A showing a pseudoplastic (or shear-thinning) behaviour (Figure 51A), with a decreasing viscosity with increasing shear rate. This result is probably due to the presence of hydrazone bonds in the polymer network that, due to their dynamic nature, provide the hydrogel with shear-thinning properties. Oscillation time and frequency sweep tests were carried out on

sample A in order to verify the variation of viscoelastic moduli over time and with the increase in frequency. Both the analyses (Figure 51B-C) showed that G' and G'' values, measured with a strain % on the linear viscoelastic region (LVR), are independent of time and frequency, thus suggesting the formation of a stable network structure after the gelation process.

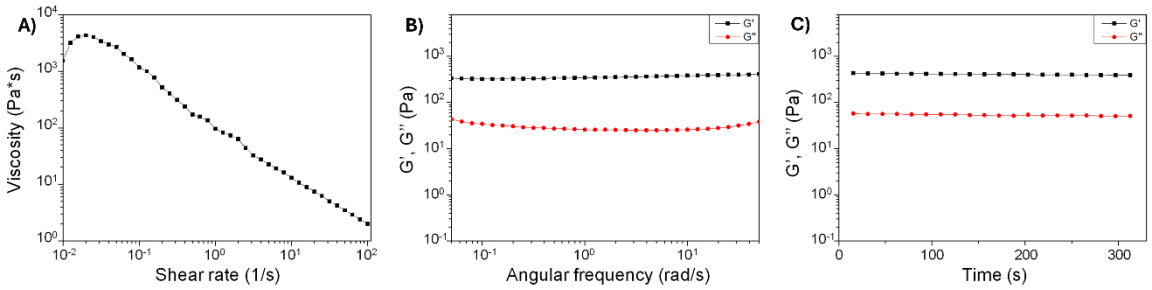

Figure 51. Results of shear sweep (A), frequency sweep (B) and time sweep tests (C) for sample A before photo-crosslinking.

3.3.5 3D Printing tests

After rheological characterization, the printability of the inks was investigated. All the inks were easily extruded through the tip of a printer cartridge, exhibiting shear-thinning properties, as expected considering the rheological characterization's results. More importantly, printed structures of all hydrogels retained the shape, especially after the photo-crosslinking process (Figure 52).

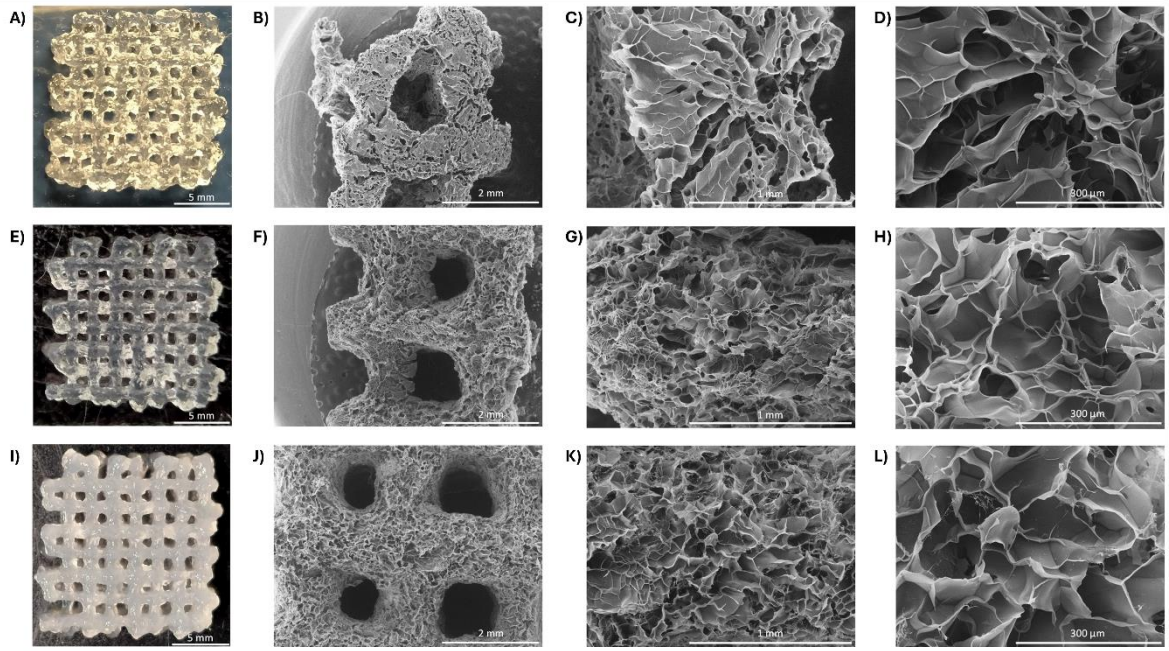

Figure 52. Printed structures of the different inks and SEM images with different magnifications of the scaffold: sample A (A-D), sample B (E-H) and sample C (I-L).

The printability was evaluated on wet and freeze-dried samples. Especially for the wet samples, the printability improved increasing the amount of Hap, according to the literature[393,394]. The calculated printability error (P_e) was 1.88 ± 0.25, 1.75 ± 0.20 and 1.30 ± 0.008 for samples A (0% Hap), B (0.01% Hap) and C (0.1% Hap), respectively. For the freeze-dried samples a P_e of 1.28 ± 0.17, 1.34 ± 0.12, 1.27 ± 0.07 for samples A (0% Hap), B (0.01% Hap) and C (0.1%) was calculated, respectively. No significant differences could be observed between the samples, although the values could be considered good for all of them and lower than other 3D-printable hydrogels reported in the literature[395,396]. After evaluating the printability and shape fidelity of the printing process, the printed structures were analysed by SEM (Figure 52). All the samples showed a porous structure with more defined pores in samples with higher concentrations of Hap. The obtained results suggest that double-crosslinking hydrogels, with a shear-thinning and self-healing behaviour, are promising candidates for 3D printing applications, due to their easy extrusion and shape retention and fidelity after the printing process.

3.3.6 Cytocompatibility tests

To evaluate the applicability of the formulated inks in bone tissue engineering, the cytocompatibility and capability to support cell growth of the biomaterial (XGox/PAHy-MA) were evaluated *in vitro* with MG-63 cells. After printing, the scaffolds were coated with elastin and then, the cells were seeded on these scaffolds. The elastin coating makes the scaffolds more attractive to cells. Although collagen is the most commonly used protein for this purpose, elastin is frequently reported in the literature for its ability to enhance cell adhesive properties[199,215,397,398]. Additionally, its high water solubility simplifies the coating process, and the lower cost of the raw material, along with the versatile and reproducible extraction process, further supported this choice.

Regarding the cytocompatibility assays, cells cultured on top of elastin-coated 3D-printed structures after 24h and 7 days of cultures remained viable (Figure 53A), with a calculated cell number of 49676.60 ± 9452.67 and 34982.31 ± 9272.90, respectively (no significant differences). Even if a small number of cells adhered to the surface of the scaffold (maybe because of the small cell density seeded), no reduction of their number over time was detected, indicating their viability and the absence of toxicity from the scaffold, as also highlighted by the following assay.

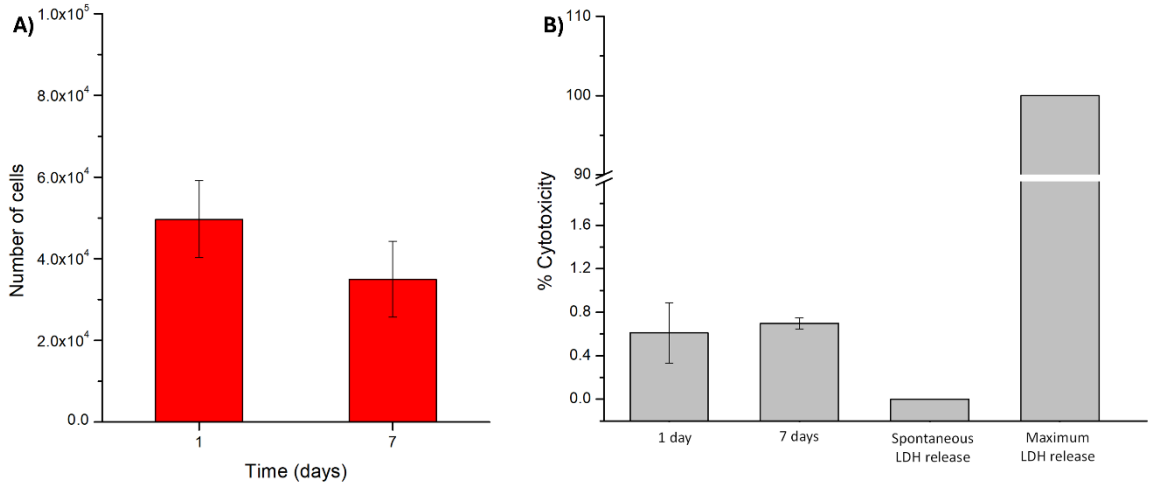

Figure 53. Number of cells (MG-63) on 3D-printed scaffolds of sample A after 24h and 7 days of culture (A). Cytotoxicity of 3D-printed sample A after 24h and 7 days of culture with MG-63 cells calculated from LDH release measurements (B).

The cytocompatibility of the materials, indeed, was evaluated through the amount of lactate dehydrogenase (LDH), an enzyme which is usually inside the cells and released into the culture medium when necrosis occurs. After 24h and 7 days of culture, a cytotoxicity of 0.610 ± 0.278 % and 0.698 ± 0.050 % was calculated, as compared to spontaneous LDH release controls and lysed cells (Figure 53B). This result suggests that the materials are cytocompatible and that the systems could be applied for tissue engineering applications and the regeneration of bone defects.

3.3.7 *In vitro* bone formation potential

To evaluate the capability of the scaffold to promote bone formation, cells were cultured on the 3D-printed structures for 14 and 21 days and their proliferation, gene expression and the deposition of bone-specific matrix were evaluated. Since the scaffolds were incubated in two different media (basal and differentiation media), the following abbreviations were used to refer to the results of these assays: A bm (sample A incubated in basal medium), B bm (sample B incubated in basal medium), C bm (sample C incubated in basal medium), A dm

(sample A incubated in differentiation medium), B dm (sample B incubated in differentiation medium), C dm (sample C incubated in differentiation medium).

Culture of MG-63 cells in basal medium on 3D-printed scaffolds confirmed their proliferation capability over time (Figure 54A), with 22618.25 ± 11786.12, 25723.4 ± 12943.77 and 37715.04 ± 13034.81 cells per scaffold in sample A, B and C, respectively, after 24 h of culture and 88845.90 ± 24098.52 (A bm), 168034.38 ± 67475.62 (B bm), 177594.42 ± 33981.58 (C bm), 74106.44 ± 7599.5 (A dm), 220110.83 ± 64312.70 (B dm), 126895.46 ± 65974.47 (C dm) after 21 days of culture.

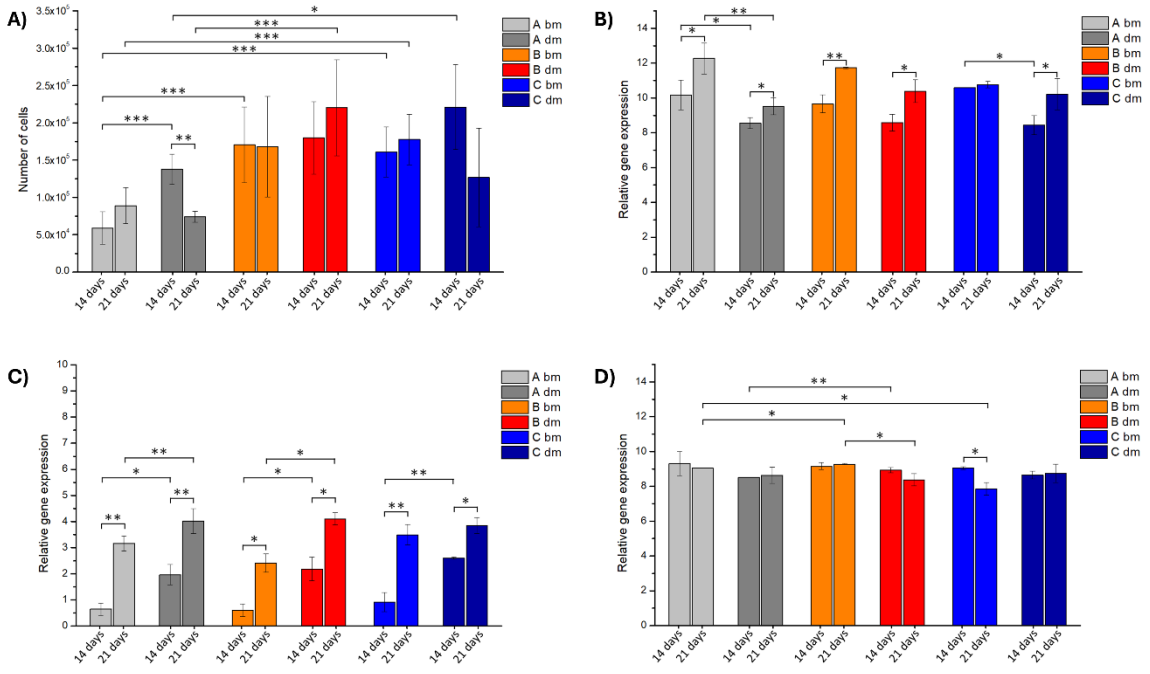

Figure 54. Number of cells (MG-63) on 3D-printed scaffolds of samples A, B and C after 14 and 21 days of culture in differentiation medium (dm) or basal medium (bm) (A). Relative expression of osteogenic genes BGLAP (B), COL1A1 (C) and RUNX2 (D) by MG-63 cells cultured on 3D-printed scaffolds of samples A, B and C and incubated in differentiation medium (dm) and basal medium (bm) after 14 and 21 days of culture.

Moreover, samples with Hap (B and C) cultured in basal medium showed a significant increase in the number of cells compared to sample A, especially after 14 days (58960.39 ±

21672.27 (A bm 14 days), 170422.48 ± 50533.75 (B bm 14 days), 160769.01 ± 33428.09 (C dm 14 days), 88845.90 ± 24098.52 (A bm 21 days), 168034.38 ± 67475.62 (B bm 21 days), 177594.42 ± 33981.58 (C bm 21 days)). Samples B and C (containing Hap) in differentiation medium, however, showed an apparent variation of the cell number (from 14 to 21 days), although not statistically significant (179731.31 ± 48729.67 and 220110.83 ± 64312.70 (B dm after 14 and 21 days) 220964.72 ± 56806.23 and 126895.46 ± 65974.47 (C dm 14 and 21 days). This might be a result of the activity of the cells, now focused on the differentiation process rather than on proliferation.

The gene expression of representative osteogenic markers (osteocalcin (BGLAP), collagen I and RunX2) was evaluated on MG-63 cells after 14 and 21 days of culture on 3D-printed scaffolds in both media (Figure 54B-D). A high relative expression of osteocalcin, a protein usually expressed by osteoblast, was found in all samples regardless of the medium condition, with no significant differences between the samples with different Hap concentrations (Figure 54B). Similarly, RunX2, a transcription factor involved in the osteoblastic differentiation process, was also highly expressed in cells cultured in all sample types (Figure 54C). In parallel, the genetic expression of collagen I was also significant for all samples, with a higher expression on cells cultured in differentiation medium and at the longer culture period of 21 days (Figure 54D). These data suggest that all samples, regardless of the Hap concentration, were able to retain an osteoblastic phenotype on seeded MG-63 cells, essential to induce bone formation at later stages.

Once the capability of XGox/PAHy-MA-based hydrogels to support cell growth and to retain an osteoblastic phenotype was validated, their ability to induce the deposition of a bone-like matrix was investigated. In particular, the formation of calcium deposits, very important in bone mineralization was evaluated by Alizarin Red staining (Figure 55).

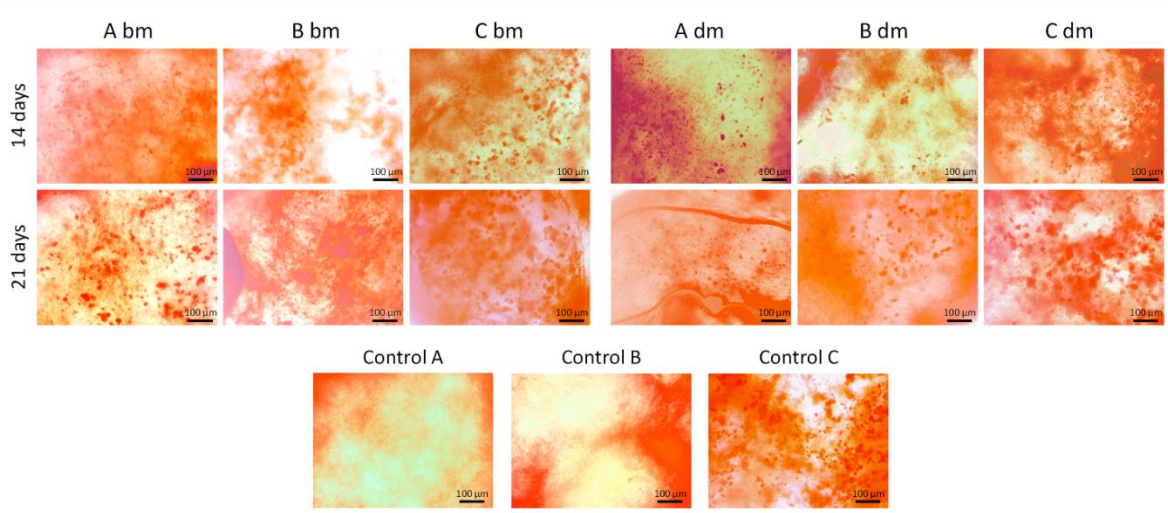

Figure 55. Results of Alizarin Red staining: mineralization of MG-63 cells cultured on 3D-printed scaffolds of samples A, B and C in differentiation medium (dm) or basal medium (bm) for 14 and 21 days. Controls A, B and C refer to the samples incubated without cells for 21 days (a). Scale bars are 100 µm.

The deposition of calcium was evidenced by the intense red-orange staining that took place on all the scaffolds, regardless of the Hap concentration. As a control, samples of XGox/PAHy-MA with the same amount of Hap were also analysed. The formation of a new matrix is more evident in samples A (A dm and A bm) because of the absence of Hap in the starting samples. The alizarin red staining results suggest that the XGox/PAHy-MA scaffolds promote the deposition of calcium and, hence, the mineralization process essential for bone formation.

Furthermore, the samples were analysed by immunofluorescence techniques to reveal the presence of cells on the scaffolds, the morphology of the cytoskeleton and the production of collagen I (Figure 56). The results show a clear presence of cells on the scaffolds, confirming the DNA assay results. After 14 days of culture, collagen I was visualized in the pericellular space in all samples in both, basal and differentiation medium conditions (Figure 56A). After 21 days of culture, a high deposition of fibrous collagen I is evident in all samples cultured

in differentiation medium (dm), regardless of the presence of Hap, while in samples cultured in basal medium (bm) conditions, collagen I appears to be only pericellular (Figure 56B). This is in line with the results of COL1A1 gene expression.

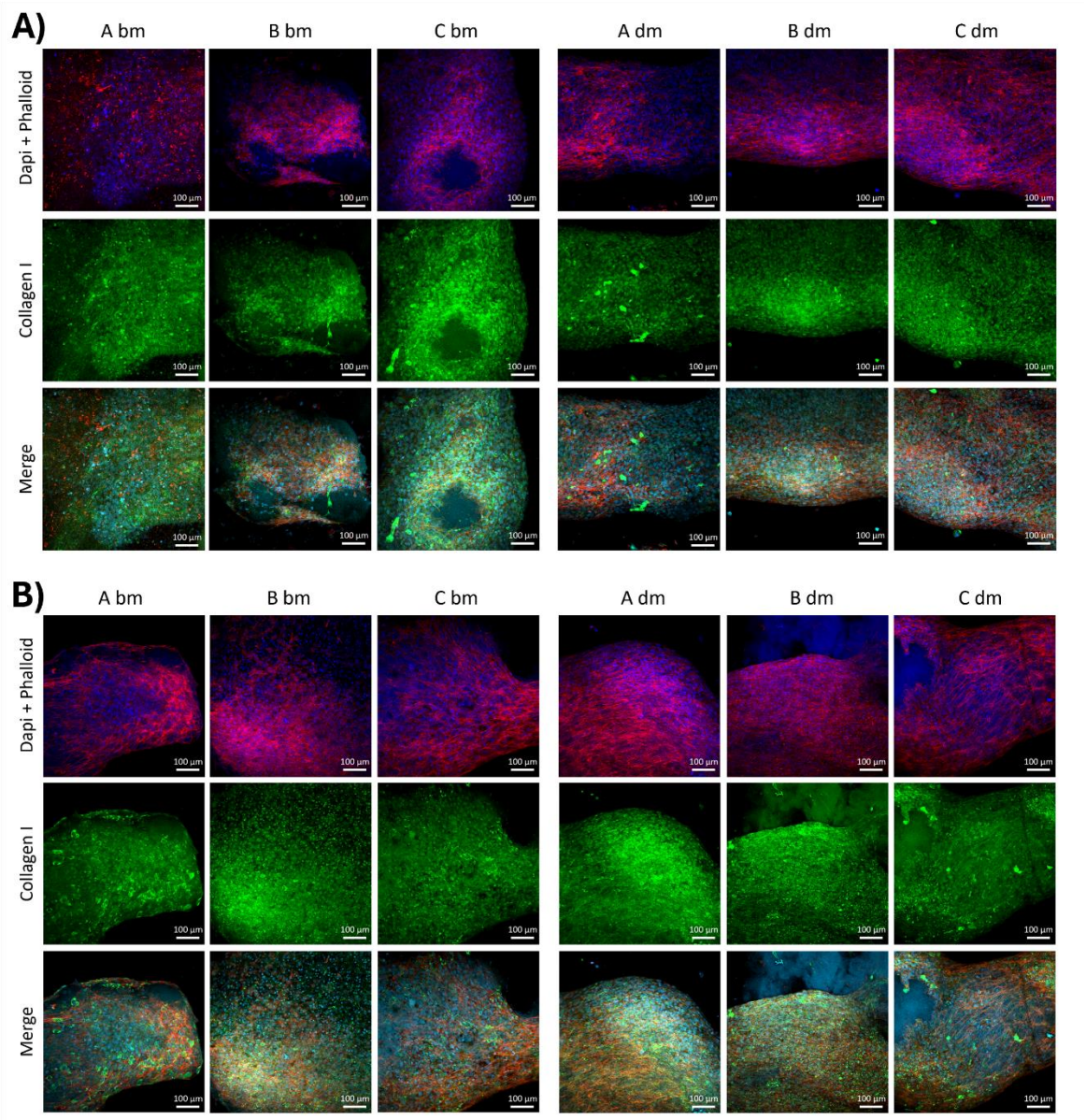

Figure 56. Immunofluorescence images of MG-63 cells cultured on 3D-printed scaffolds of samples A, B and C in differentiation (dm) and in basal medium (bm) after 14 (A) and 21 days of culture (B). Scale bars are 100 µm.

SEM images performed on the samples confirmed these results (Figure 57). In particular, the cell density increases from 14 days of culture to 21 days. The mineralization nuclei (visible as bright white dots on the surface of the cells) increase with the amount of Hap in the scaffolds. They are more evident in the sample at 14 days of culture because of the lower cell density on the scaffold surface. Furthermore, it was, also, possible to observe the formation of a fibrous matrix in the samples at both time points, with a more evident deposition in 14-day samples, again, due to lower cell density.

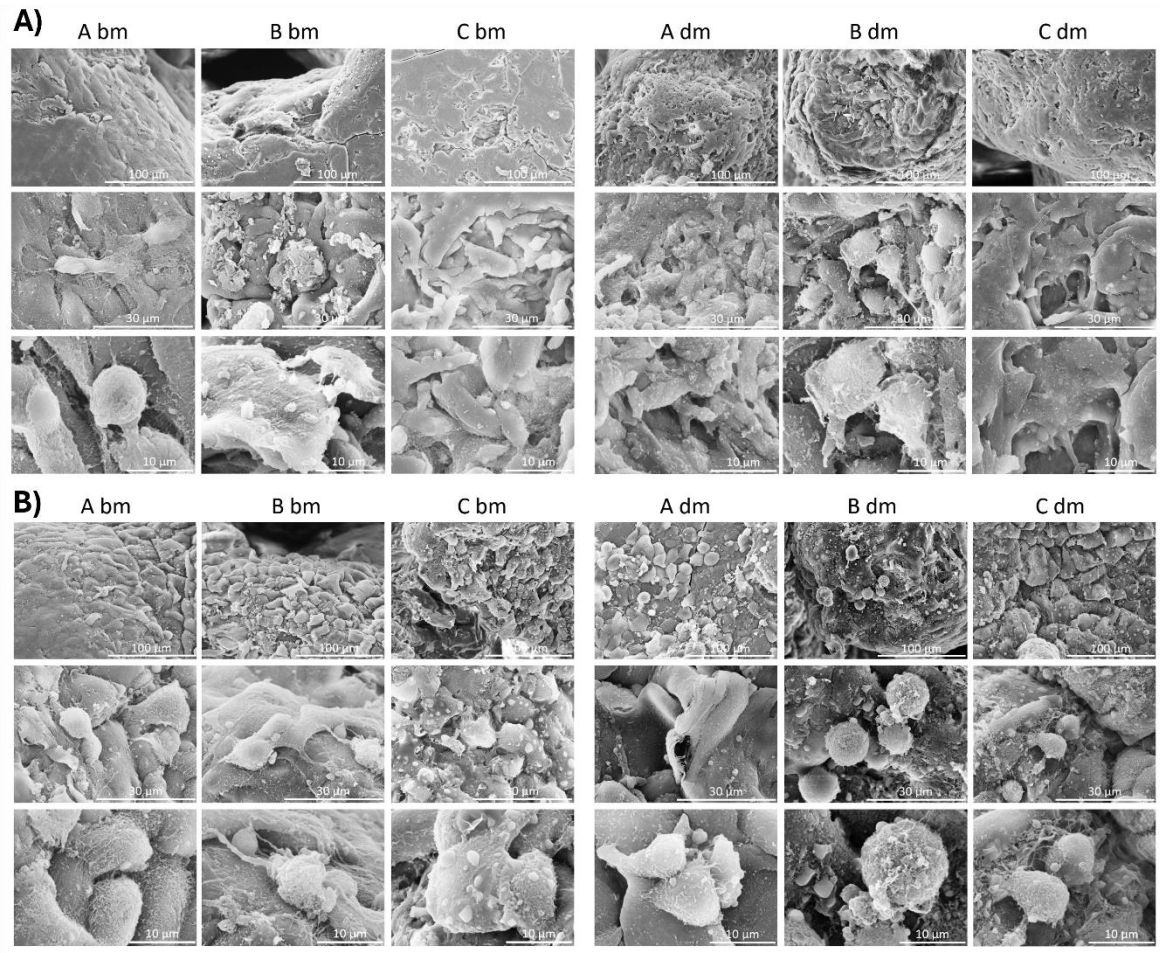

Figure 57. SEM images with different magnifications of MG-63 cells cultured on 3D-printed scaffolds of samples A, B and C incubated in differentiation medium (dm) or basal medium (bm) after 14 (A) and 21 days of culture (B). Scale bars are 100 µm (top), 30 µm (middle) and 10 µm (bottom) for both time points.

In this way, the presence of a fibrous matrix, collagen I deposition and expression as well as mineralization nuclei confirm the *in vitro* osteogenesis of the cells seeded on the surface of the scaffolds.

It is evident that, for a complete implementation of the systems, these preliminary results will need to be demonstrated *in vivo* to confirm both the real osteogenic properties of the scaffolds and their mechanical stability. Moreover, printing tests, considering the real shapes of the lesions, need to be carried out for further application of the systems.

3.3.8 Conclusions

In this work, double-crosslinking hydrogels incorporating hydroxyapatite nanoparticles were developed as injectable hydrogels and potential inks for bone regeneration. The hydrogels were formulated using a novel methacrylated polyaspartylhydrazide and an oxidized xanthan gum, exploiting a double crosslinking: a dynamic one through hydrazone bonds and a subsequent covalent one regulated by methacrylic groups activated via UV irradiation. The resulting hydrogels demonstrated good stability in physiological fluids and exhibited interesting rheological properties. Their viscoelastic and shear-thinning behaviour indicated good injectability, while their ability to maintain shape over time suggested good printability, which was confirmed by printing tests. The hydrogels were not cytotoxic and capable of stimulating bone tissue regeneration by increasing the expression of osteogenesis genes, calcium deposition and collagen fibre deposition. These findings suggest that the system could be applied as a potential scaffold for bone tissue engineering either as an injectable hydrogel or using extrusion-based 3D printing.

3.4 Injectable gellan gum/elastin-based nanocomposite hydrogels as fillers for irregular bone defects

Bone defects represent one of the most significant challenges for clinical treatment[372]. Furthermore, the regeneration of irregular bone defects poses a major challenge, because of their unpredictable size, shape, and depth. Although several bone grafts are often used, they do not allow a complete repair of the damaged area due to several limitations[373,374]. In this context, the development of injectable hydrogels represents a promising strategy, since they allow to completely fill the defective area, fitting its irregular morphology[128,279]. Moreover, by exploiting multiple crosslinking strategies, it is possible to obtain easy injection and in situ stabilisation. For this reason, in this work, polysaccharide/protein-based injectable hydrogels were designed and developed, starting from methacrylated derivatives of gellan gum and soluble elastin. Thanks to the advantages of both biomaterials (thermotropic and ionotropic properties of GG and cell adhesion capability of the elastin) shear-thinning, self-healing, cell-friendly and in situ photo-crosslinkable hydrogels were formulated. Likewise, by adding ZnO and β-TCP nanoparticles, osteoconductive and osteoinductive properties were potentially conferred to the developed systems. Comprehensively, this strategy allowed to obtain injectable hydrogels that could be easily administrated into the damaged irregular bone defects and, at the same time, could be crosslinked in situ thus increasing their stability and viscoelastic properties.

3.4.1 Synthesis and characterization of GG-AEMA

In order to formulate new injectable hydrogels that could be used as bone fillers and, in particular, for the filling and subsequent regeneration of small bone defects (e.g. maxillofacial, alveolar and cranial bones), various hydrogels were formulated, choosing a methacrylate derivative of gellan gum (named GG-AEMA) as the main biomaterial. Various other components were subsequently added to give the system suitable properties for bone

regeneration (ELMA, ZnO and β-TCP NPs). The choice of this polymer is primarily due to the above-mentioned advantageous properties of GG, such as ionotropic and thermotropic gelling. The functionalization of GG with 2-aminoethyl methacrylate (AEMA), on the other hand, made it possible to obtain a methacrylate derivative susceptible to photo-crosslinking and, therefore, capable of creating an additional network between the polysaccharide chains (within hydrogels), which could strengthen the structure. Furthermore, the chemical strategy of derivatization, i.e. the functionalisation of the primary hydroxyl groups of the GG, made it possible to maintain the carboxyl groups free and, thus, the ionotropic properties.

Moreover, the synthesis was carried out from a derivative with a lower molecular weight (approximately 39 kDa)[399], obtained by degrading the native polysaccharide in alkaline conditions; this made it possible to obtain aqueous dispersions that were less viscous than the starting polymer, which made them easier to process and prepare, but also less sensitive to ionic strength, making it possible to disperse the derivative in physiological solutions.

The synthesis of the polysaccharide derivative was conducted in two steps without isolating the intermediates; in detail, the reaction was carried out through the activation of the primary hydroxyl groups of the repeating units of GG-TBA with 4-NPBC, followed by nucleophilic substitution by AEMA in the presence of triethylamine (TEA) as a catalyst, leading to the formation of carbamide bonds, as shown in Figure 58.

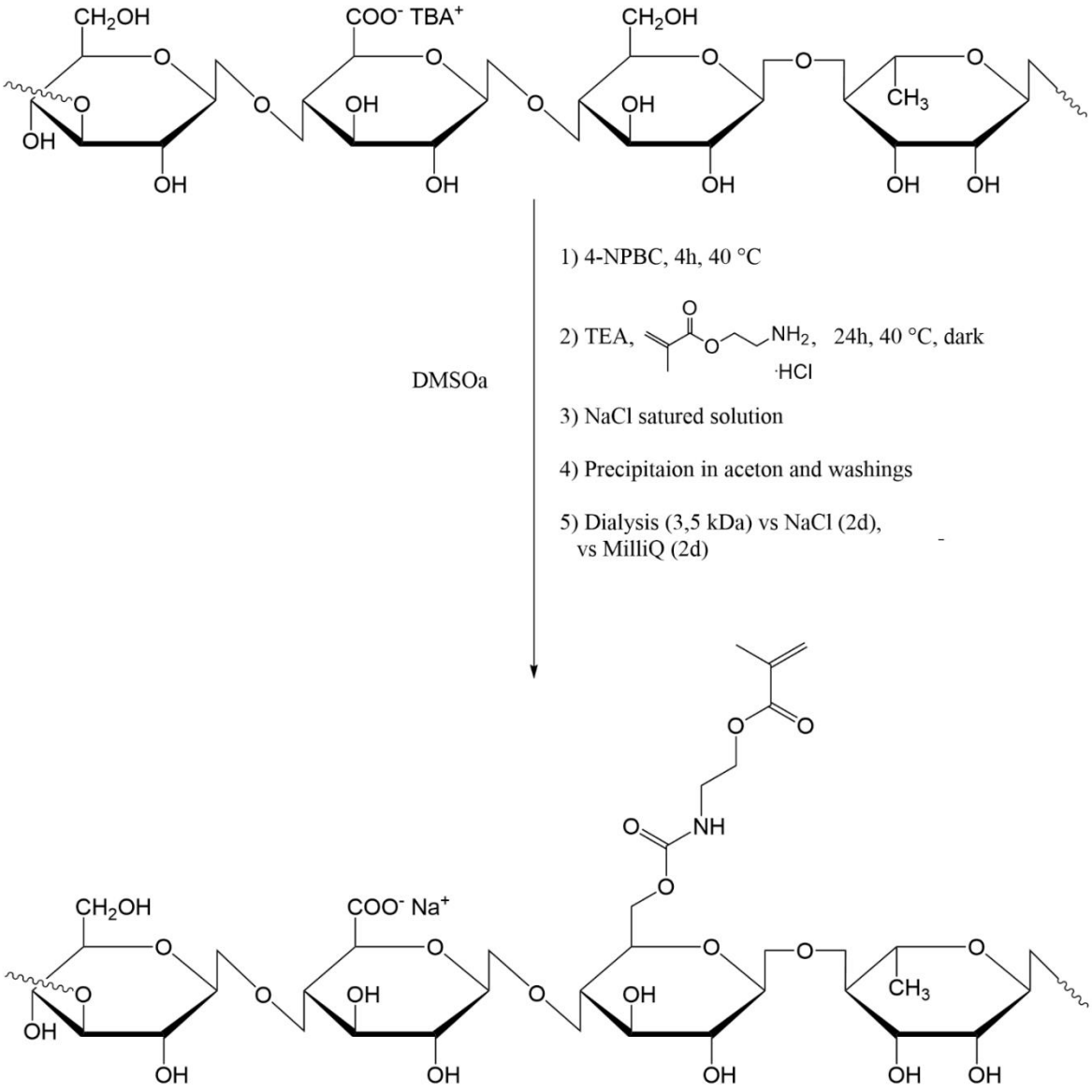

Figure 58. Scheme of synthesis of GG-AEMA.

After precipitation in acetone, washings and vacuum-drying, the product was dialyzed to completely purify the polymer, removing any traces of TEA. The product was isolated by freeze-drying with a yield by weight of about 70% and, then characterized by ^{1}H-NMR analysis, which confirmed the functionalization of GG.

As reported in Figure 59, comparing the spectra of GG-AEMA and GG revealed the appearance of characteristic peaks of methacrylic moieties. Indeed, the GG-AEMA spectrum showed two peaks around δ 5.5 attributable to the protons of the double bond of the methacrylic function (─C═C**H₂**) and a peak at δ 1.88 relating to the methyl protons of the

same function (─C**H**$_3$). The DD% in AEMA, calculated by comparing the integral of the peak at δ1.88 with that at δ 1.32 attributable to the methyl of the α-l-rhamnose residue of GG, was 15.68 ± 1.40 %.

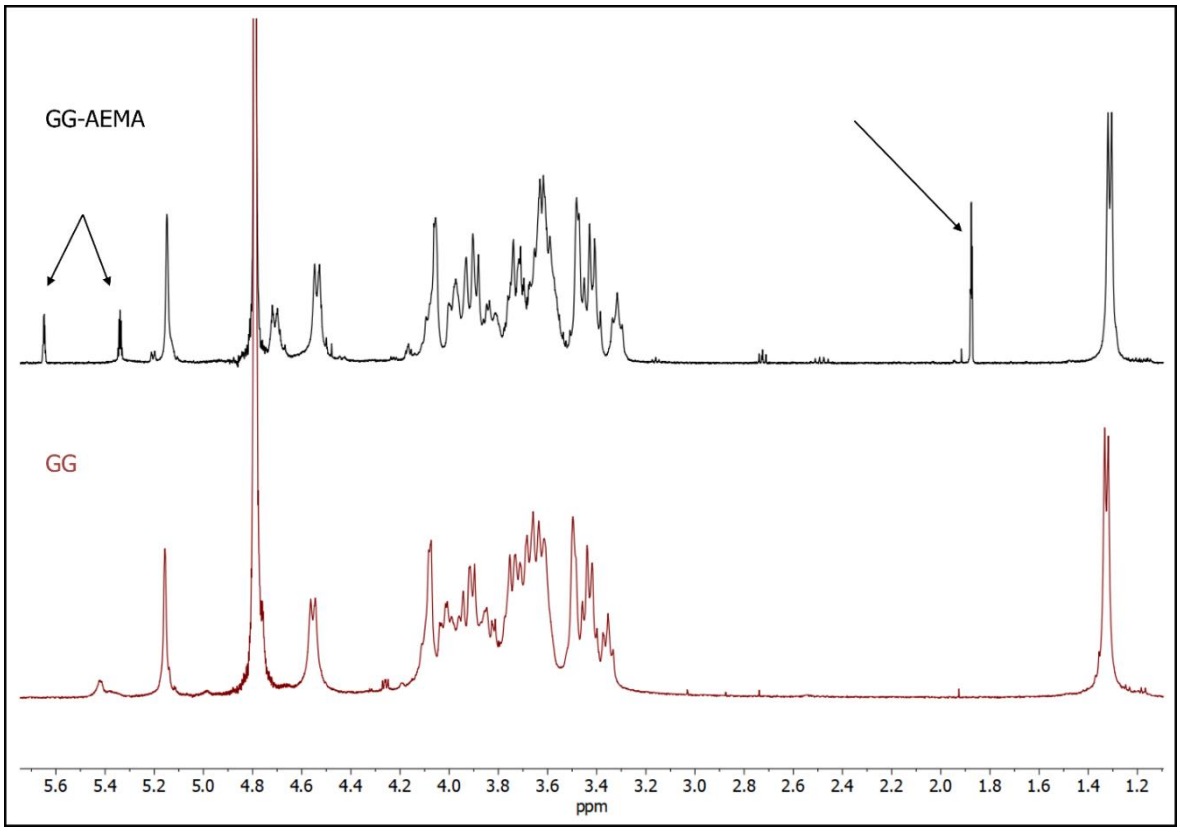

Figure 59. ^{1}H-NMR spectra of GG-AEMA and GG.

3.4.2 Synthesis and characterization of the ELMA

Since GG-AEMA, although improving (potentially) the physicochemical properties of native GG, does not possess cell adhesion properties, it was decided to mix it with elastin for its remarkable biological properties. Indeed, elastin is an essential component of the ECM of various organs and tissues like skin, lungs and arteries. Elastin fragments and elastin-derived peptides (EDPs) have demonstrated significant chemotactic capacity against several cell types involved in wound healing, the ability to enhance the angiogenic capacity of endothelial cells and, also bioadhesive properties towards cells through, interaction with specific cell receptors, such as integrin[199,398,400]. For these reasons, it was decided to

incorporate an elastin derivative in the polysaccharide-based hydrogels. Specifically, it was decided to use a soluble fraction of bovine elastin and functionalize it with methacrylic anhydride in order to make it susceptible to photo-crosslinking (like GG-AEMA). In detail, bovine neck ligament elastin (not soluble in aqueous media) was treated with boiling oxalic acid to extract the soluble fractions[401,402]. The resulting product, purified by dialysis and isolated by freeze-drying, was subsequently functionalised using methacrylic anhydride in the presence of TEA as a catalyst (Figure 60). The reaction was carried out in DMSO, given the high solubility of this protein in organic solvents, and purified by dialysis against the same solvent first and then against borate buffer at gradually decreasing concentrations, to eliminate the reaction by-products and, above all, to remove the DMSO gradually avoiding precipitation or coacervation of the functionalised protein.

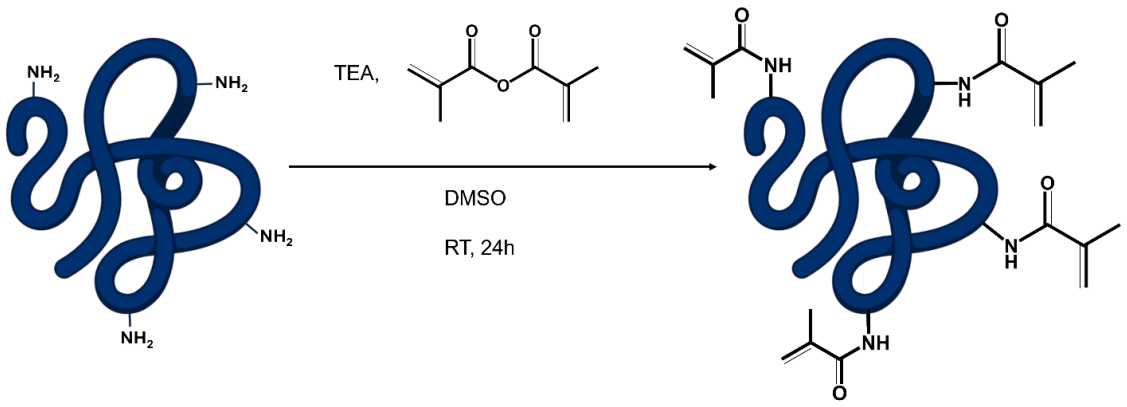

Figure 60. Schematic representation of the synthesis of ELMA.

The product, obtained with a weight yield of about 83%, was characterized by ^{1}H-NMR and TNBS analysis. The ^{1}H-NMR spectroscopy allowed to verify the success of the reaction, given the appearance of the same characteristic peaks of methacrylic groups already found in the GG-AEMA spectrum: the peak of the vinyl protons of the methacrylic moiety around δ 5.5 and that of the methyl protons of the same functional group at δ 1.92 (Figure 61). The efficiency of functionalisation was calculated indirectly by TNBS assay by quantifying free

primary amine groups of ELMA and relating this value to the non-functionalised elastin. This value was found to be 97.16 ± 3.11 %, indicating that almost all the amino groups were functionalized with methacrylic anhydride.

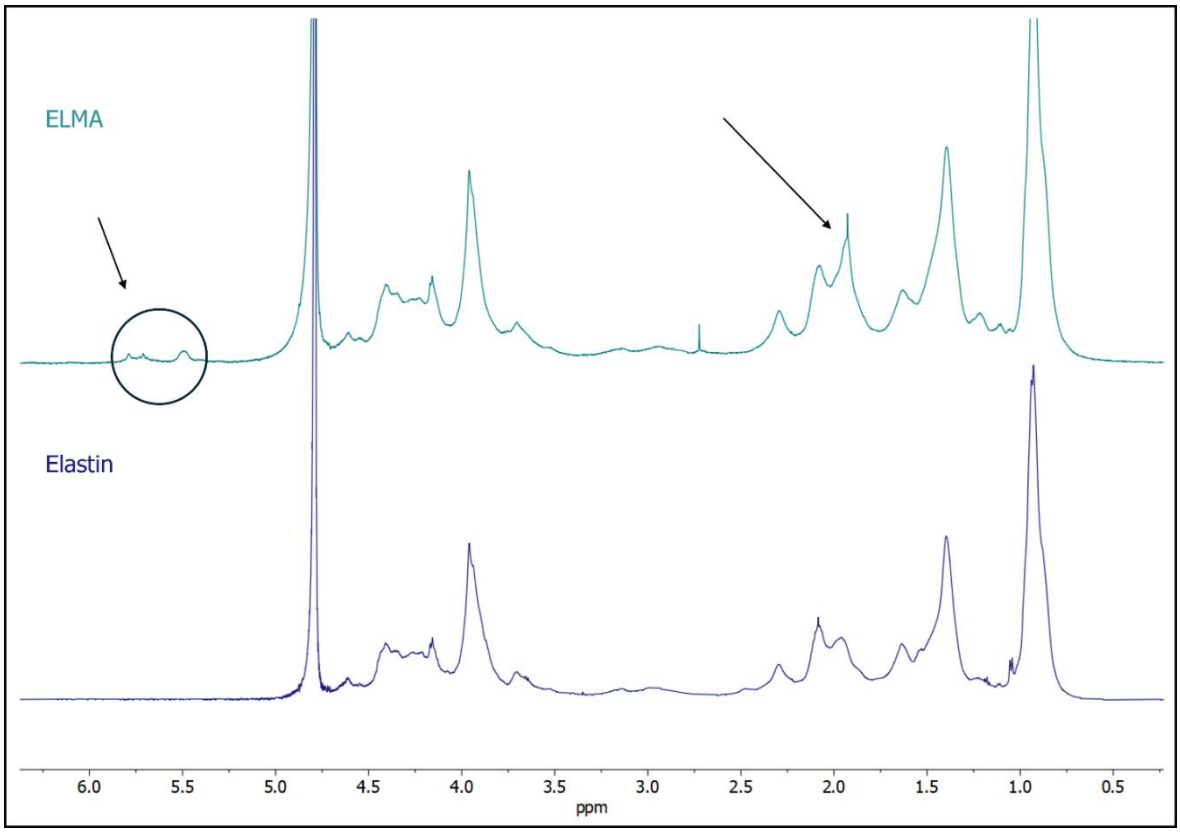

Figure 61. ^{1}H-NMR spectra of ELMA and elastin.

3.4.3 Production and characterization of base hydrogels

In order to obtain injectable hydrogels that could potentially be used for the regeneration of small bone defects as bone fillers, the two biomaterials were first mixed, combining the advantages of each one. Therefore, the base hydrogels were prepared by first mixing dispersions of GG-AEMA and ELMA in DPBS in the presence of a photoinitiator (PhI), according to the ratios shown in Table 3.

Table 3. Composition of GG-AEMA/ELMA-based hydrogels.

Sample	GG-AEMA (%w/v)	ELMA (%w/v)	PhI (%w/v)
H_A	4	0	0.3
H_B	4	2	0.3
H_C	4	4	0.3

Specifically, GG-AEMA was dispersed at 70°C in DPBS, in the presence of PhI, at a final concentration of 4% w/v. The dispersion, at this temperature, was in the state of *sol*. Following cooling to room temperature, thermotropic gelation of the system occurred: there was the formation of a physical hydrogel that can be easily spread by applying slight pressure (e.g. using a spatula). Furthermore, following UV irradiation, the system became macroscopically more compact, losing these flow properties. Indeed, in this case, following the application of stress, the hydrogel fragmented rather than flow, suggesting that static chemical bonds had formed. After the treatment with $CaCl_2$, this aspect was more evident, suggesting a further network formation.

This behaviour confirmed that aqueous dispersions of GG-AEMA, like those of GG, also undergo temperature-induced gelation. As already mentioned in the introduction, the increase in temperature causes a "double helix to random coil" transition, allowing a complete dispersion of the polymer and the formation of a *sol*. The subsequent decrease in temperature induces a reorganisation of the polymer chains into double helix structures and a subsequent *sol-gel* transition, which allows the formation of the hydrogel[224]. At the same time, the visually observed increase in stiffness made it possible to state, from a qualitative point of view, that the hydrogel and thus the above-mentioned derivative, were responsive to UV light and were able likely to undergo a photo-crosslinking process.

As far as the formation of hydrogels also containing ELMA is concerned, the choice of this polymer was due to the need to provide the polysaccharide derivative with adhesive properties, thus enabling it to be covalently incorporated into the network created by the UV irradiation process. In detail, such hydrogels were prepared by adding the protein derivative to the fluid dispersion of GG-AEMA. ELMA was initially added in different amounts (2%, 4% w/v) to define the most suitable concentration for cell adhesion. The polysaccharide/protein-based hydrogels also exhibited similar thermotropic and UV-responsive behaviour as the GG-AEMA-only hydrogel.

3.4.4 Cell adhesion studies

Cell adhesion studies were conducted to assess whether the developed samples exhibited adhesive properties towards FD-MSC cells. In particular, the studies were conducted in order to determine the optimal concentration of ELMA to obtain suitable biological properties. Light microscope images (Figure 62) showed that only for the H_C sample and the ELMA-based control, the cells adhered to the surface of the hydrogel, showing an elongated form, whereas the remaining samples did not show any elongated cells on them, but only rounded ones. This result was already visible after 2 h of incubation from the seeding of the cells on the hydrogels. After 4 h, it became more evident, leading to the choice of this composition as starting hydrogel.

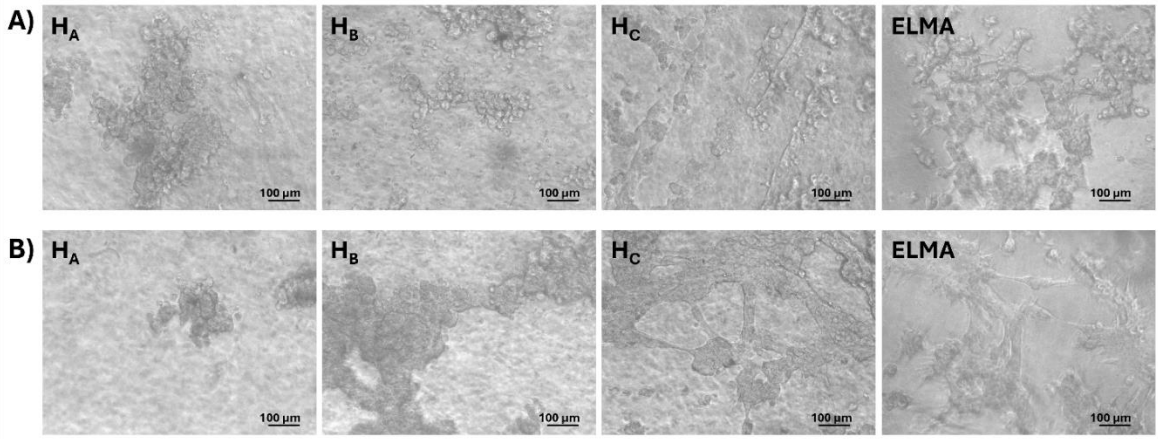

Figure 62. Images of the adhesion studies after 2h (A) and 4h (B) of incubation.

3.4.5 Rheological characterization of base hydrogels

The rheological analysis made it possible to obtain quantitative information about the viscoelastic properties of the hydrogels and the influence of photo- and ionotropic crosslinking processes as a function of the different ELMA content. Therefore, first of all, oscillation amplitude analyses were carried out, applying strain % increasing from 0.01% to 5000.0%, to study the viscoelastic behaviour of the hydrogels and, to identify the magnitude and trend of G' and G'' as a function of the applied strain.

As reported in Figure 63, for all samples, and at low strain values, the values of G' were about an order of magnitude higher than those of G'', indicating that the systems are in a gel state. This behaviour is mainly due to the large number of reversible non-covalent bonds such as dipole-dipole bonds and hydrogen bonds formed as a result of the thermotropic gelation described above. About the influence of the concentration of ELMA on the viscoelastic properties, a gradual increase in the values of G' and G'' was observed as the concentration of the protein derivative increased. This result can probably be explained by referring to the greater total polymer concentration in the hydrogel and thus to the higher number of interactions established between the two biomaterials, resulting in a greater degree of entanglement of the polymer chains.

Furthermore, it is also evident, at low values of % strain, the presence of a region of linear viscoelasticity (LVR) in which the G' and G'' are independent of the % strain applied; it should be noted that no significant differences were found in the extent of this region as the ELMA concentration varied.

For strain % values above the LVR, a decrease in viscoelastic moduli was observed as the applied strain increased. In particular, this effect led, graphically, to the intersection of the curves of G' and G'' at the cross point, beyond which G' is smaller than G'', thus indicating the transition of the system from gel to sol.

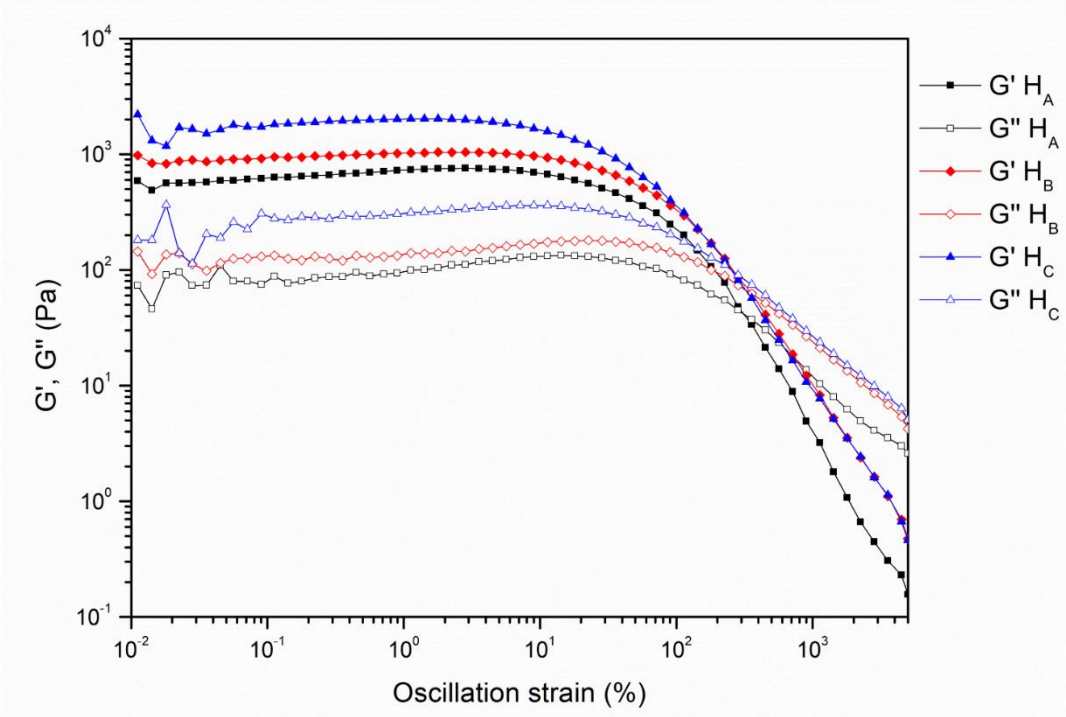

Figure 63. Oscillation amplitude results of GG-AEMA/ELMA hydrogels.

Once the viscoelastic properties of the systems have been determined, the responsiveness of the systems to UV light and cations was investigated by first assessing the degree of crosslinking under UV light. Photo-rheology analyses made it possible to study the variation of the G' and G'' during UV irradiation. As shown in Figure 64, there was a rapid increase in both modules by one logarithmic unit, and the values achieved are stably maintained over

time. In addition, no significant variations were observed between the various samples in terms of the increase in G' and G'', although it should be emphasised that after UV irradiation, no substantial differences were found between the various samples with different ELMA contents.

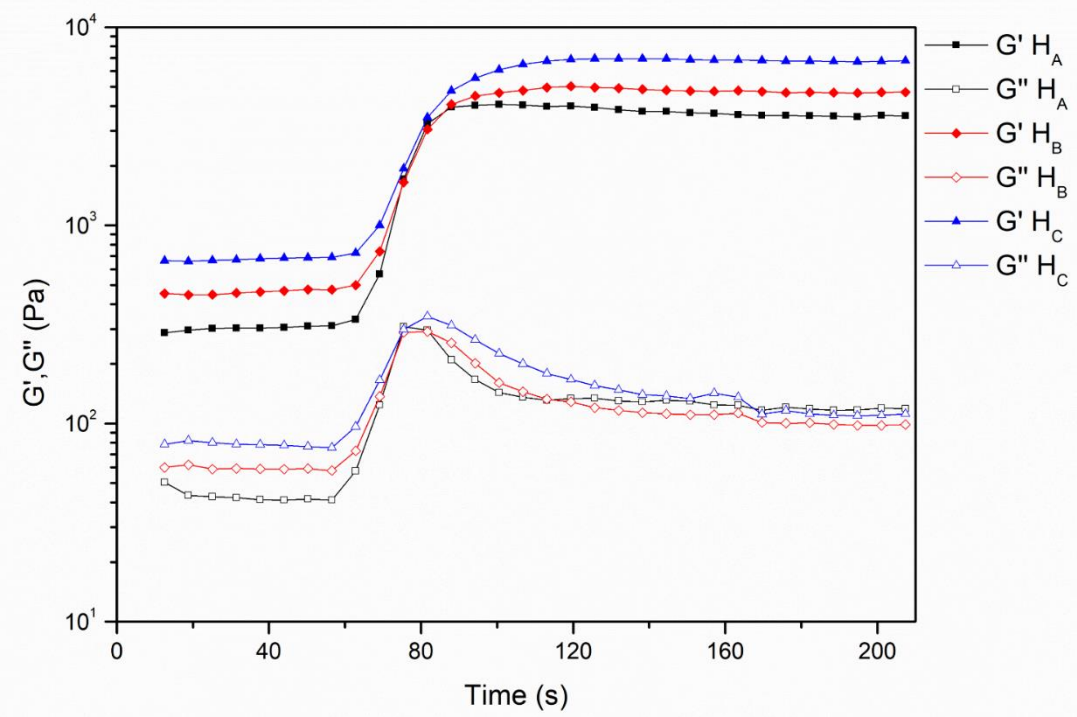

Figure 64. Results of photo-rheology analyses on GG-AEMA/ELMA hydrogels.

Since, as mentioned above, the hydrogels exhibited, macroscopically, ionotropic behaviour, the rheological properties were also studied after treatment of the samples with a $CaCl_2$ solution (0.1 M), after their photo-crosslinking. As reported in Figure 65, there was an increase in the G' and G'' moduli of more than one order of magnitude compared to the non-crosslinked samples; furthermore, the values of the aforementioned moduli were higher than those of the photo-crosslinked samples, indicating that the samples were susceptible to ionotropic crosslinking. Finally, it should be noted that no significant differences were found between the samples.

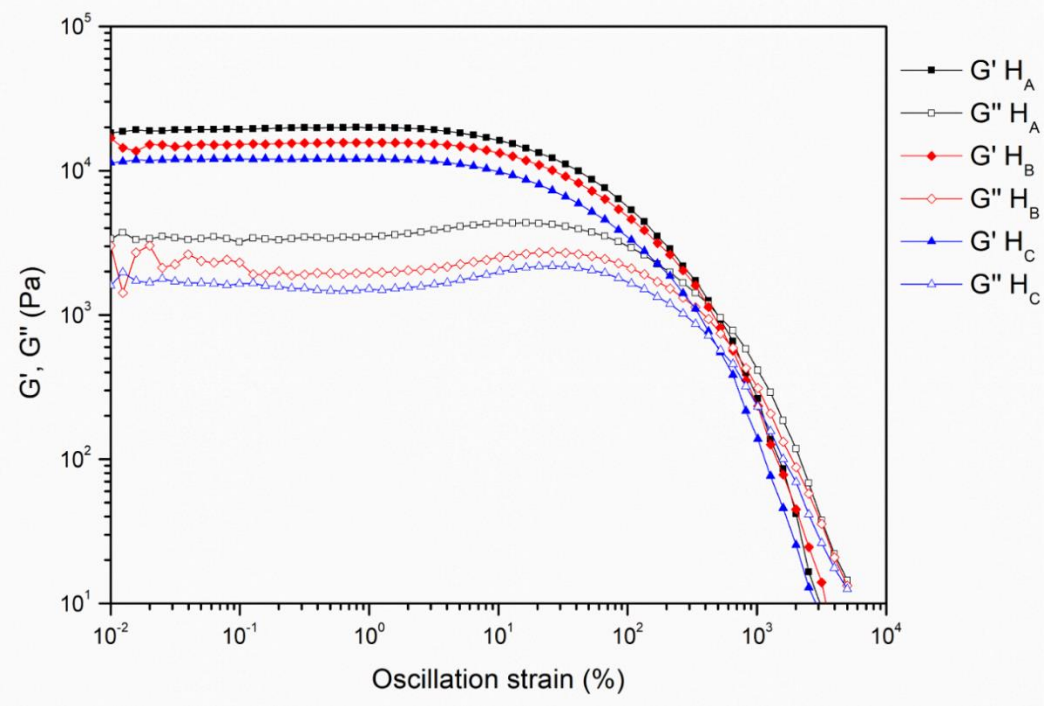

Figure 65. Results of oscillation amplitude analyses carried out on GG-AEMA/ELMA hydrogels after photo- and ionotropic crosslinking.

3.4.6 Production and rheological characterization of nanocomposite hydrogels

Once the optimal ELMA concentration was determined, different nanocomposite hydrogels were formulated by adding nanoparticles of ZnO and β-TCP to the selected base hydrogel (H_C) according to the ratios given in Table 4.

Table 4. Composition of the nanocomposite hydrogels.

Sample	GG-AEMA (%w/v)	ELMA (%w/v)	ZnO (%w/v)	β-TCP (%w/v)	PhI (%w/v)
$H_{nc}A$	4	4	0.1	0	0.3
$H_{nc}B$	4	4	0	5	0.3
$H_{nc}C$	4	4	0	20	0.3
$H_{nc}D$	4	4	0.1	5	0.3
$H_{nc}E$	4	4	0.1	20	0.3

The addition of these nanosystems, at the various concentrations tested, did not cause immediate gelation of the *sol* system nor did it modify the gelation properties of the previously described system. The nanocomposite hydrogels, indeed, also showed thermotropic (Figure 66) and photo-induced gelation. In addition, all the systems presented macroscopically a further slight structuring following treatment with $CaCl_2$, indicating the maintenance of the ionotropic properties despite the initial dispersion in a salt solution.

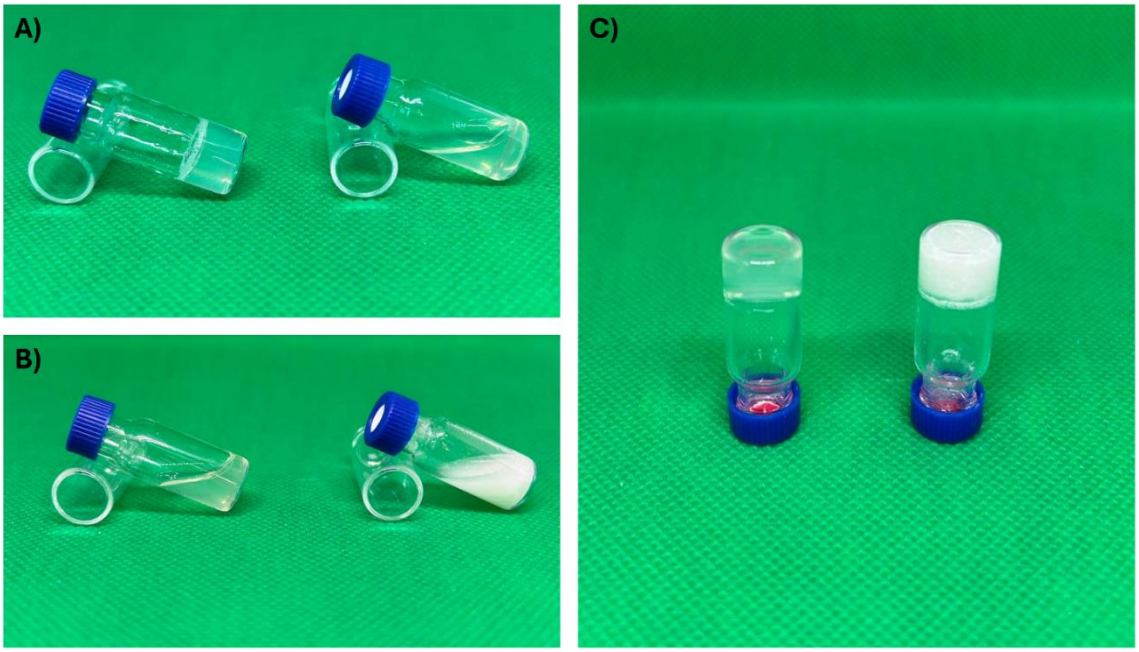

Figure 66. Inversion tube test for H_C and $H_{nc}E$. H_C at room temperature (left) and at 70 °C (right) (A). H_C (left) and $H_{nc}E$ (right) at 70 °C (B). H_C (left) and $H_{nc}E$ (right) at room temperature (C).

These properties were corroborated by rheological studies. In particular, they allowed to confirm the viscoelastic and ionotropic behaviour and responsivity to UV light of nanocomposite samples, as well as to assess the influence of nanoparticles on these properties. In addition, they made it possible to study the injectability and self-healing behaviour post-extrusion of the hydrogels produced, depending on the nanoparticle content.

First of all, oscillation amplitude analyses conducted on the nanocomposite samples confirmed a viscoelastic behaviour similar to that of the base sample (without nanoparticles), with no significant differences in the concentrations, amount and type of nanoparticles incorporated between the samples under investigation, as shown in Figure 67.

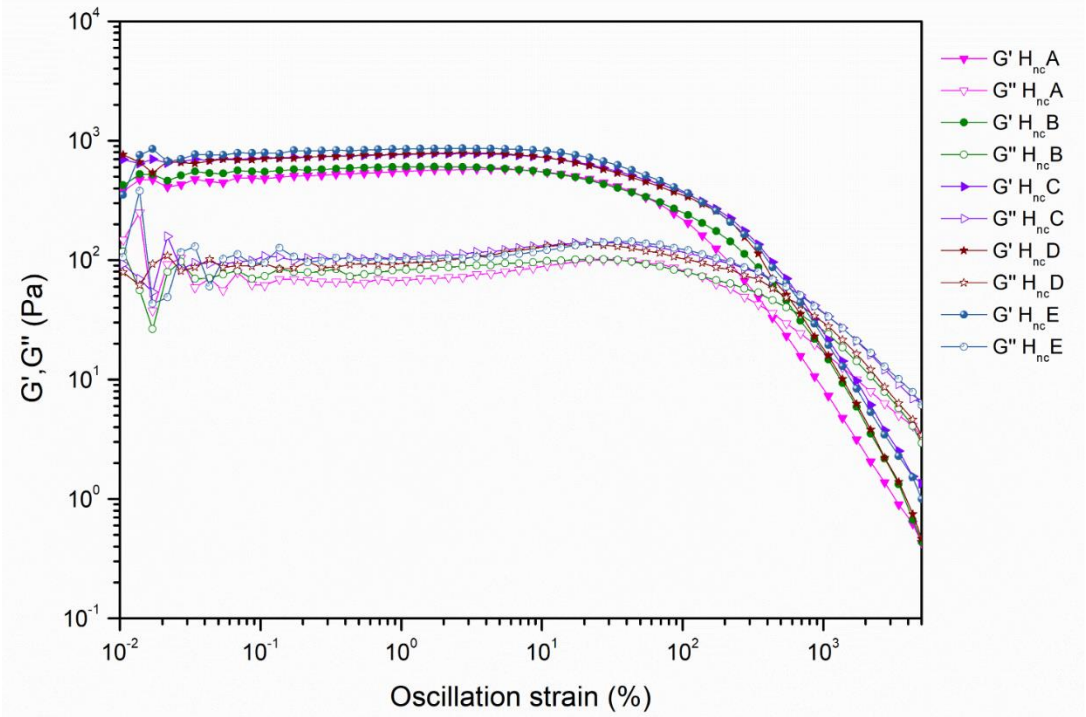

Figure 67. Oscillation amplitude results of nanocomposite hydrogels.

Flow sweep analyses, on the other hand, allowed to quantitatively study the injectability of the developed hydrogels, since they could be easily extruded using a syringe, as observed macroscopically. Specifically, the samples could be injected through the needle of a syringe even to the point of being able to write with them (Figure 68), giving a first and visual indication of their injectability and shear thinning properties.

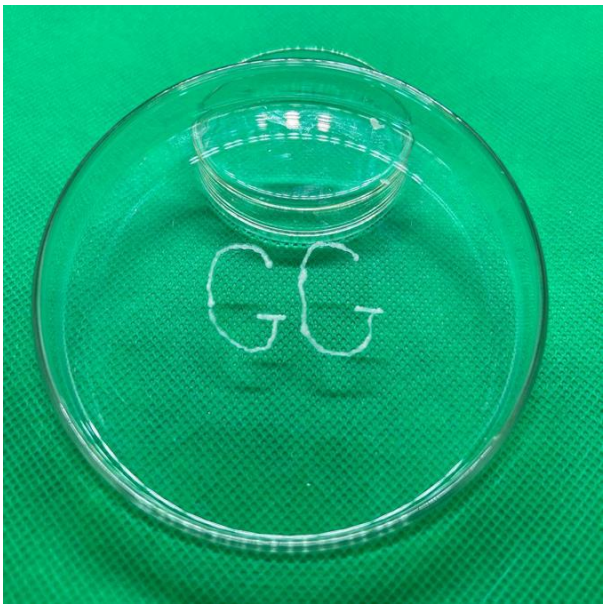

Figure 68. Macroscopic demonstration on $H_{nc}E$ injectability, by writing with this hydrogel.

Therefore, in order to corroborate this result and, thus, study their flow properties, flow sweep analyses were performed. These studies, in detail, allowed to evaluate the variation of viscosity as a function of the shear rate. This analysis is essential in the development of injectable hydrogels, as in this case, because as the pressure exerted on the syringe increases, the viscosity must decrease for the system to be extruded. Figure 69 shows a decrease in viscosity for all systems as the shear rate increases. This behaviour is due to the breaking of weak intermolecular bonds between the polymer chains, which, subjected to deformation at increasing rates, become ordered and aligned, thus allowing the sample to flow along the direction of the shear stress. All hydrogels showed similar behaviour with slight differences, suggesting that the concentration and type of particles only slightly influence the viscosity of the systems.

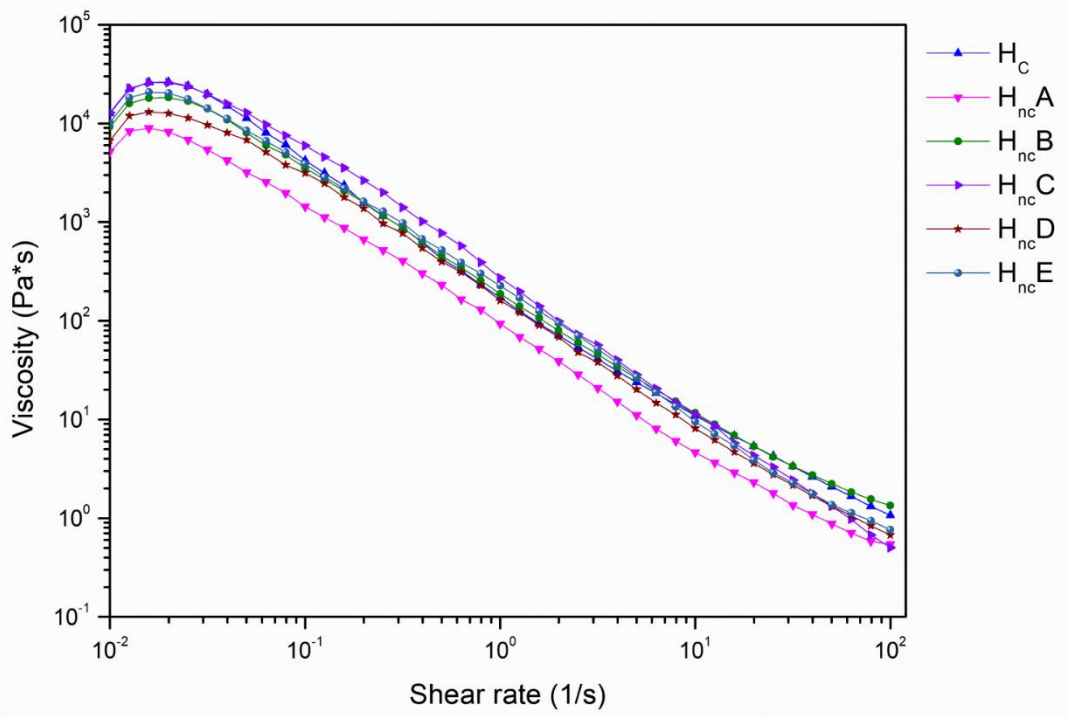

Figure 69. Flow sweep results of nanocomposite hydrogels.

Finally, recovery time analyses were performed on the non-crosslinked samples by applying alternating cycles of high and low strain % to assess the recovery capacity of the viscoelastic properties of the systems. The results (Figure 70) showed that all systems recovered more than 50 % of the G' and G'' starting values. Furthermore, it should be noted that this percentage increased as the amount of nanoparticles in the hydrogels decreased: indeed, the base system presented a recovery of over 80%, a value that progressively decreased until the samples containing 20% w/v of β-TCP. This result can be explained by referring to the fact that an increasing quantity of solid particles, increasing the solid-like behaviour of the samples, on the one hand, determines a greater structuring, while on the other hand hinders the recovery of the viscoelastic properties. It should be noted, however, that in subsequent cycles all samples show a recovery rate of around 100%.

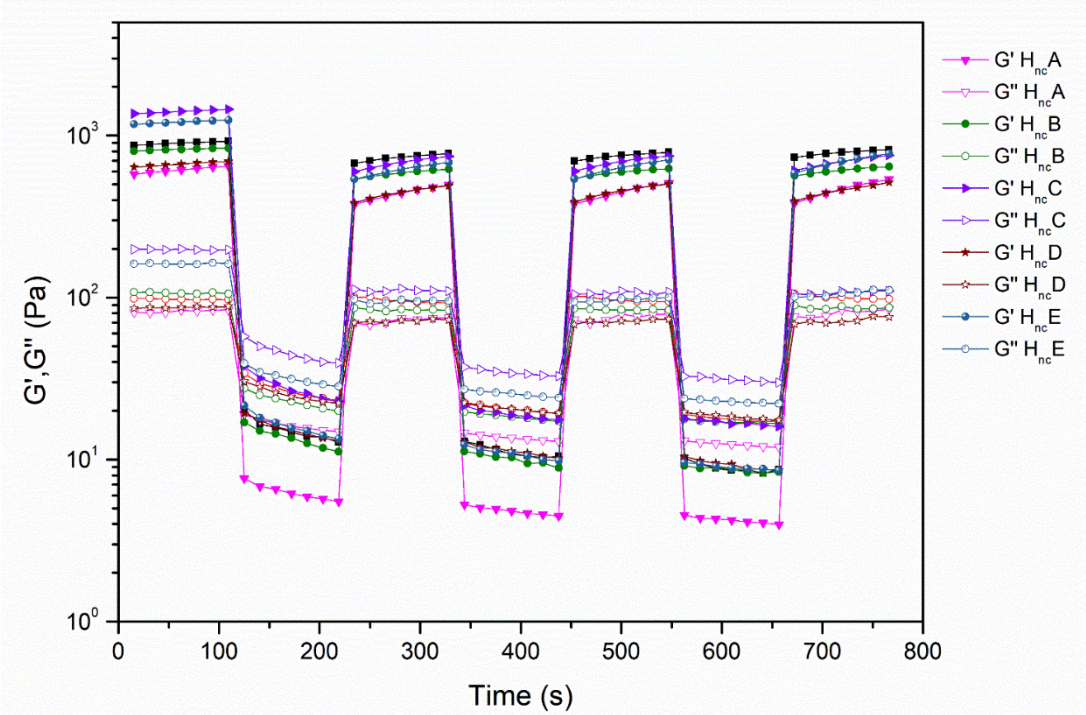

Figure 70. Results of the recovery time analyses performed on the nanocomposite hydrogels.

Since the viscoelastic, pseudoplastic and self-healing behaviour of the nanocomposite hydrogels was confirmed, their responsivity to UV light and ionotropic properties were investigated.

About the former, photo-rheological analysis highlighted an increase of approximately one order of magnitude of G' and G'' following UV irradiation, for all the samples, without observing any significant differences in the increment (Figure 71). The reported analysis confirmed that the incorporation of particles did not affect the ability of the two polymers and thus the hydrogels to crosslink when exposed to UV light in the presence of a photoinitiator.

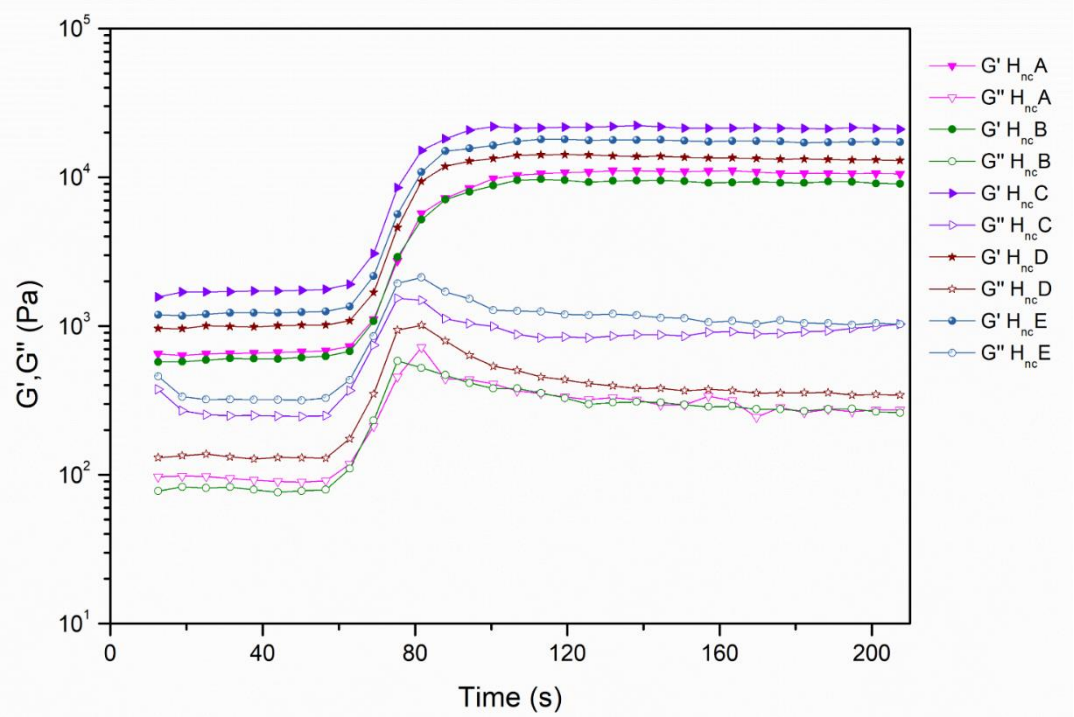

Figure 71. Results of photo-rheology analyses of the nanocomposite hydrogels.

On the other hand, concerning the oscillation amplitude analyses carried out on the photo- and ionotropic crosslinked samples (Figure 72), a similar behaviour of H_C was found. Thus, the ionotropic crosslinking on the samples was confirmed, even though with a less pronounced impact compared to the base hydrogels; only slight differences between the different samples (HncB is significantly less structured than the other samples, among which, by contrast, there are no significant differences).

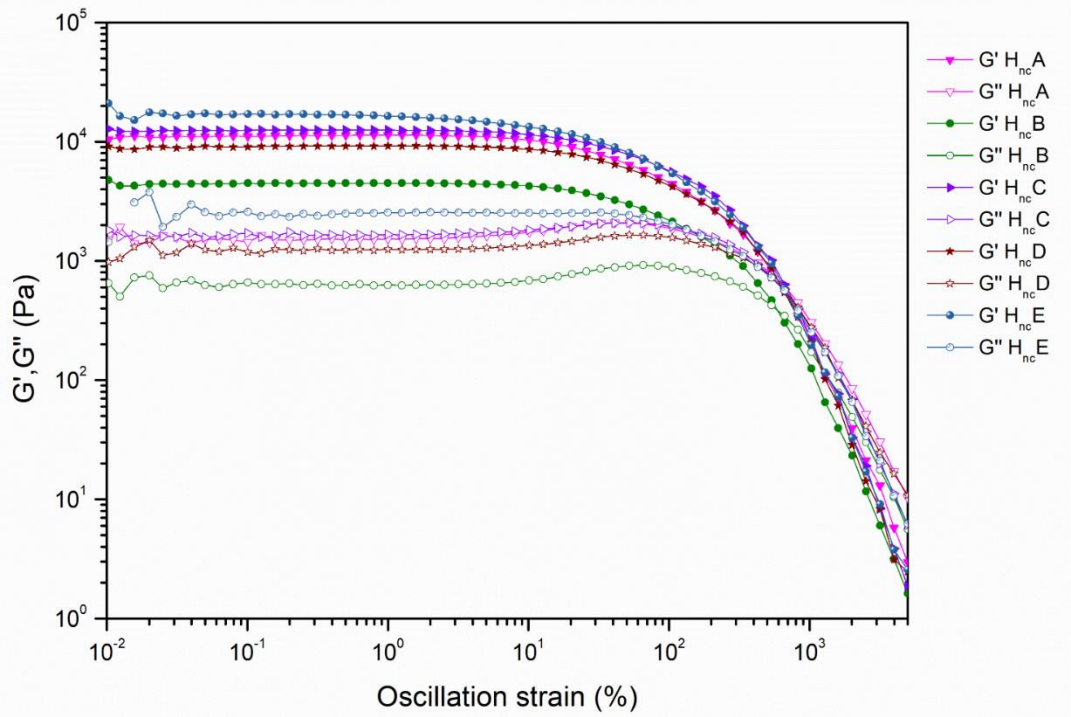

Figure 72. Results of oscillation amplitude analyses carried out on the nanocomposite hydrogels after photo- and ionotropic crosslinking.

3.4.7 Hydrolytic degradation studies

In order to characterise the physicochemical properties of hydrogels and study their hydrolytic resistance under physiological conditions, considering also the influence of the nanoparticles, degradation studies were performed on the samples. Furthermore, this study allowed to assess whether the degradation degree is compatible with the regeneration time of bone tissue. The study was performed on samples H_C, $H_{nc}D$ and $H_{nc}E$ as these represent the base control without nanoparticles and the two complete systems containing ZnO and the two different concentrations of β-TCP, respectively.

All samples showed a weight loss of about 20% after 7 days of incubation, maintaining their weight and structure for the remaining 21 days (Figure 73). Indeed, after the initial degradation, the weight of samples remains approximately constant over time. Furthermore, no significant differences were observed among the samples.

The results demonstrate that these systems can be used as a bone filler for small bone defects as they exhibit a degradation rate that could probably promote cell growth at the damaged site.

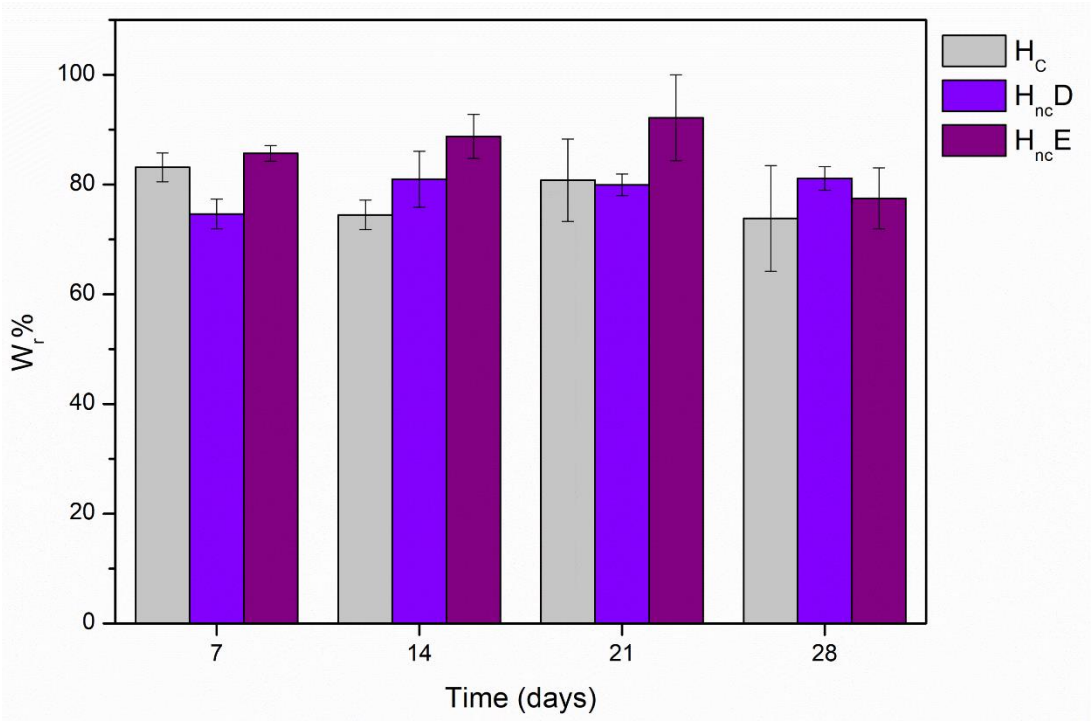

Figure 73. Degradation profile of H_C, $H_{nc}D$ and $H_{nc}E$ after 28 days of incubation in DPBS.

In this regard, qualitative tests were conducted on freeze-dried horse bones to evaluate macroscopically the stability of the hydrogels in contact with bone tissue. Specifically, the samples were injected into these bones as shown in Figure 74 and incubated for 28 days. The results suggest that the hydrogels not only can be injected into small bone fractures but also that they hold up over time (Figure 74).

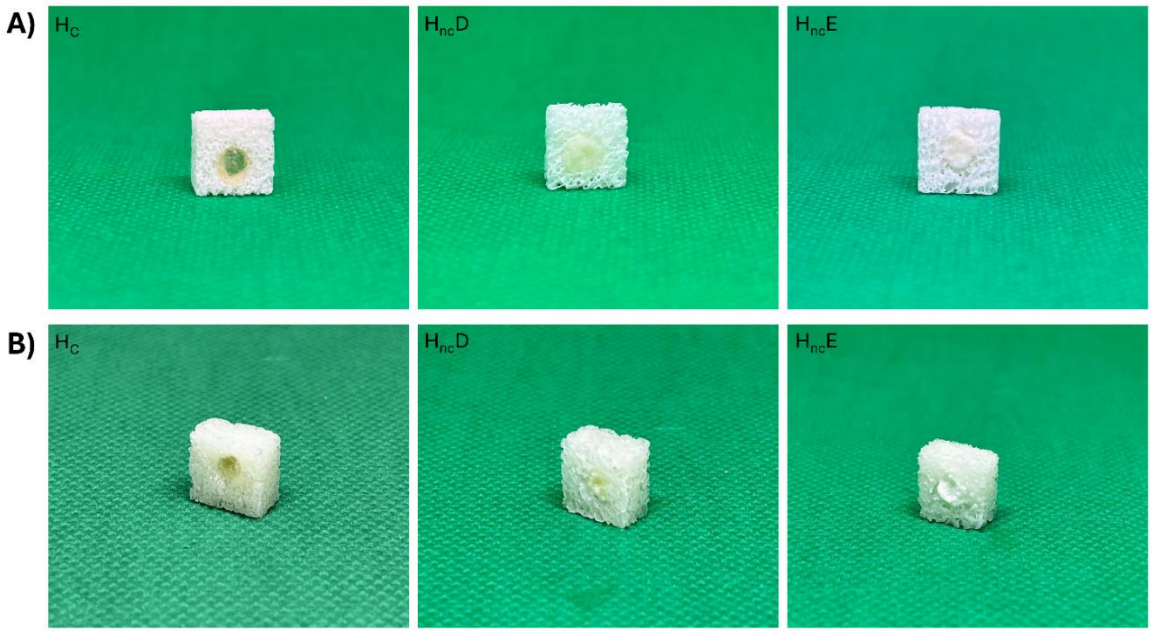

Figure 74. Degradation studies performed on horse bones: images at 0 days (A) and after 28 days of incubation (B).

Furthermore, once injected into perforated horse bones, the hydrogels filled the trabecular spaces of the bone proximal to the injection site. Micro-CT analyses, indeed, showed an integration of the injected system with the existing one (Figure 75). This is a clear demonstration of their possible application as bone fillers.

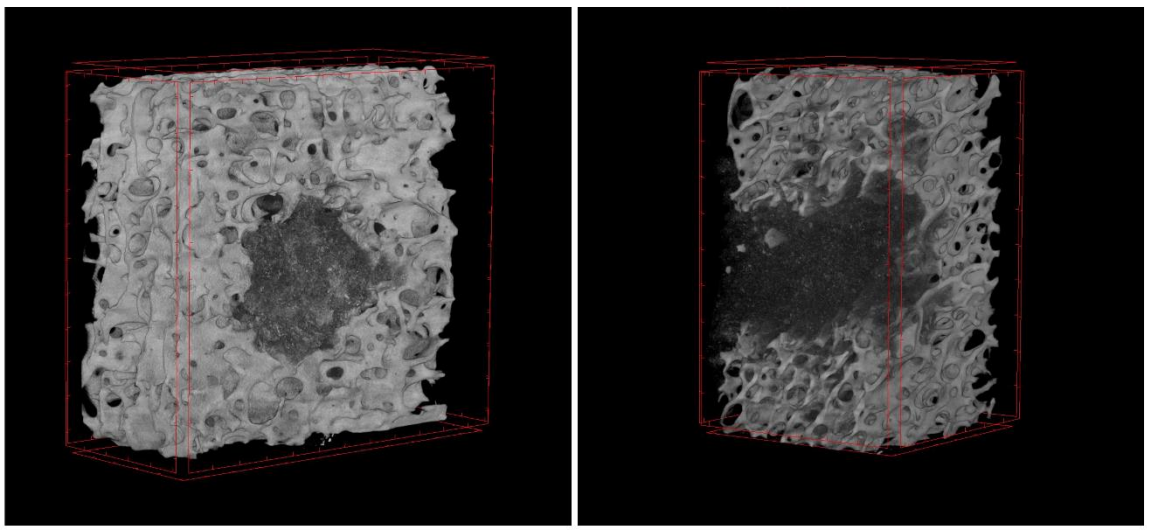

Figure 75. Micro-CT analysis of the sample $H_{nc}E$ carried out at time 0 (0 days, after injection).

3.4.8 Cytocompatibility evaluation of the hydrogels

The developed hydrogels were, also, subjected to biological studies to assess their cytocompatibility. Cell viability, in particular, was determined by means of the MTS assay and AO/EB staining. Analyses were performed by placing the sample in indirect contact (through cell culture inserts) with FD-MSC seeded at the base of a well. In this way, it has been possible to evaluate the toxicity of the sample caused by the possible release of substances from each tested sample. The MTS results (Figure 76) highlighted that, both after 24 h and after 48 h of incubation, the cells showed high viability (>90%) with no significant differences between the various samples tested.

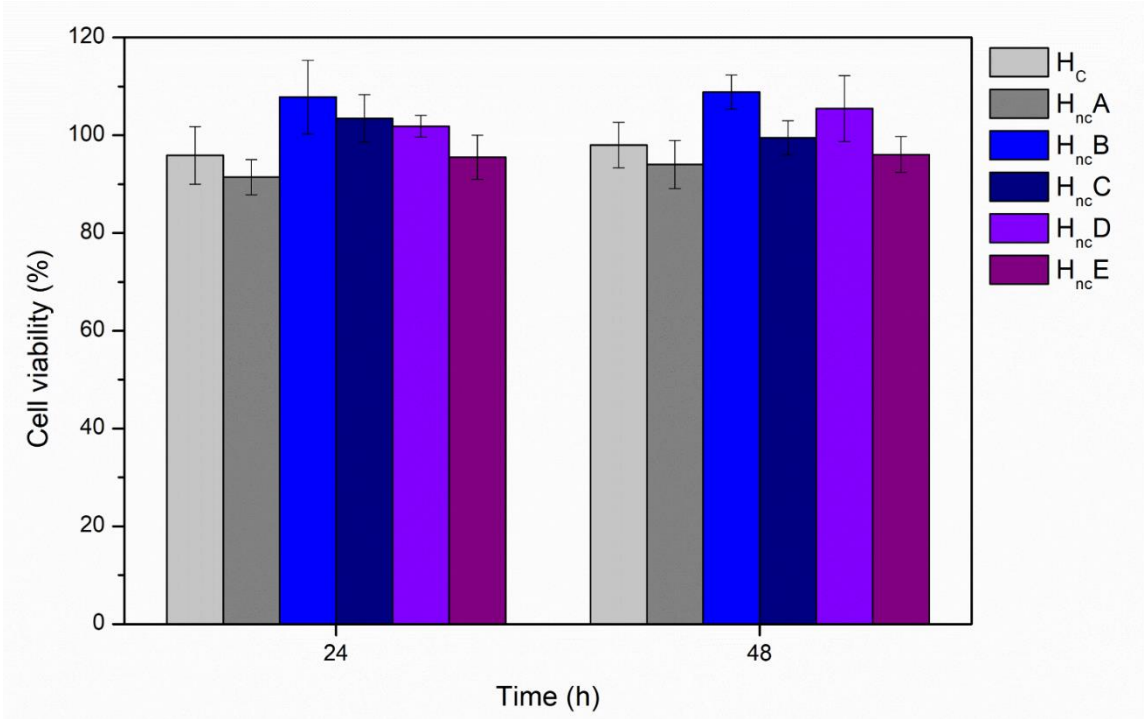

Figure 76. Results of MTS assay on nanocomposite hydrogels.

In addition, AO/EB staining was performed to qualitatively confirm the MTS colorimetric assay. As reported in Figure 77, all samples showed viable cells with similar morphology to the control, confirming the MTS results. In this way, it is possible to affirm that none of the samples affect cell viability.

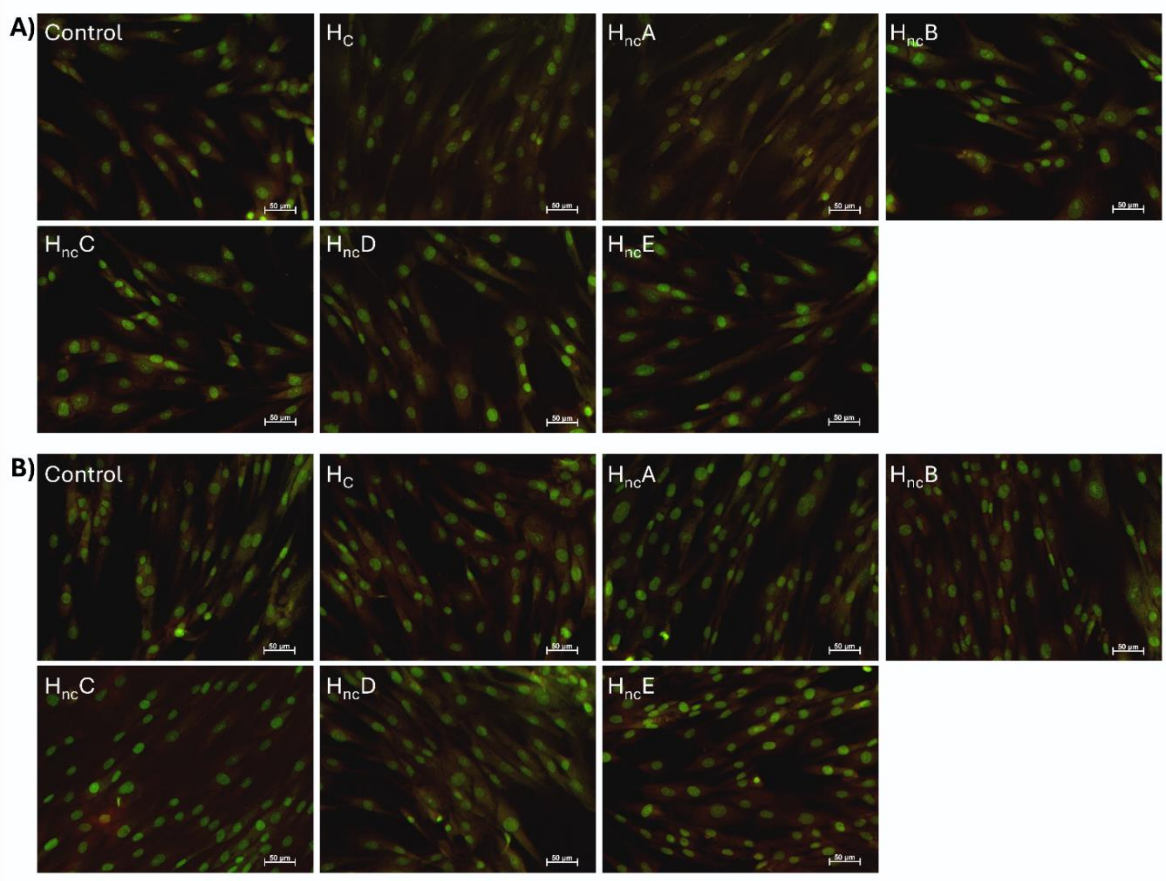

Figure 77. Results of AO/EB staining of FD-MSC incubated in the presence of the nanocomposite hydrogels after 24 h (A) and 48 h (B).

3.4.9 Conclusions

In this work, injectable gellan gum/elastin-based nanocomposite hydrogels were developed as filling materials for small bone defects. In detail, methacrylate derivatives of gellan gum and soluble elastin were designed and synthesized and then exploited for the production of photo-crosslinkable cell adhesive hydrogels. Physicochemical analyses on the derivatives confirmed the functionalisation.

Furthermore, the success of the reactions was corroborated by rheological studies, which showed an increase in hardness and thus viscoelastic properties of these hydrogels when irradiated with UV light. Also, rheological characterization highlighted the viscoelastic behaviour and the ionotropic properties of the samples.

After determining the optimal concentration of protein for good rheological and cell adhesion properties, ZnO and β-TCP, which can potentially stimulate bone tissue regeneration, were also added to the selected system.

The samples produced were studied in detail by means of physicochemical, rheological and biological analyses. First of all, it was demonstrated that the presence of the nanoparticles did not significantly alter the degradation of the systems, which moreover remained stable over time. Concerning rheological characterization, interesting results were obtained: the injectability and self-healing properties of the systems were demonstrated, as well as their higher stability following photo- and ionotropic crosslinking, confirming both the ionotropic behaviour of gellan gum derivative and the responsivity to UV light of the hydrogels. Furthermore, it was observed that the different content of introduced nanoparticles does not significantly affect the viscoelastic properties of the system. Lastly, biological studies showed the cytocompatibility of all the systems under study.

For these reasons, the developed hydrogels may be very promising in the regeneration of small bone defects and thus be used as bone filler in bone regenerative medicine, although more advanced biological tests demonstrating real osteoinductive properties are needed.

4. General conclusions

The development of hydrogels appears as an interesting strategy in regenerative medicine both for drug delivery and tissue engineering. In addition to the great advantages linked to the hydrogel's application, the use of injectable and printable hydrogels improves their potential since they allow to respectively fill irregular defects and create highly personalized implantable structures, thus increasing hydrogels' regeneration efficiency.

Furthermore, polysaccharide-based hydrogels and, among them, gellan gum and xanthan gum-based hydrogels, show very interesting properties, which could be very useful for this kind of application. The thermotropic and ionotropic behaviour of GG, as well as the mucoadhesive and rheological properties of XG make these biomaterials highly attractive for biomedical purposes and hydrogels formulation. In this thesis work, different derivatives of these polysaccharides were synthesized to develop injectable or printable hydrogels. For these reasons, different synthetic approaches and various crosslinking strategies have been used introducing various functionalities into the starting backbone and, thus, new properties useful for further hydrogels formulation.

In the first work, an XG-graft-pNIPAM biomaterial was synthesized and exploited for the production of injectable hydrogels for the delivery of a novel anti-candida peptide. The physical nature of the hydrogel allowed its shear-thinning behaviour, while the thermoresponsiveness given by pNIPAM as well as mucoadhesive properties of XG contributed to its retention in the application site. Furthermore, the incorporation of an antifungal peptide conferred anti-candida properties with a prolonged drug release.

On the other hand, GG too was employed in drug delivery and the treatment of infected wounds. In this case, designing multiple network hydrogels, the functionalization of GG-EDA with GTMAC helped the in situ production and stabilization of AgNPs, while GG viscoelastic properties were exploited for the easy preparation of the hydrogels, for their

printability and further shape maintenance. In this way, a personalized treatment of infected wounds could be possible, controlling printed constructs properties.

At the same time, both polysaccharides showed their potential in bone regeneration. In both cases, the technological ratio was the same: developing an injectable hydrogel that could be photo-crosslinked. However, this purpose was pursued in the first case by formulating double-crosslinking hydrogels, based on the hydrazone bond's formation and photo-crosslinking after the printing process, between XGox and PAHy-MA. In the second case, two different methacrylated polymers, GG and elastin derivatives, were mixed giving physical hydrogels, that could be stabilized once injected in situ through UV irradiation. Both systems showed suitable viscoelastic properties that allowed good injectability or extrudability and shape retention, demonstrating the potential of these approaches and their applications as 3D-printed constructs or as filling material for of small bone defects.

5. Materials and methods

5.1 Developing xanthan gum-based hydrogel with thermosensitive and mucoadhesive properties for the treatment of local candidiasis

5.1.1 Materials

Xanthan gum (VANZAN, viscosity of 1300-1700 mPa×s for 1% w/v dispersions), was purchased by Vanderbilt Minerals LLC.

Tetrabutylammonium hydroxide (TBA-OH), carboxylic acid terminated Poly(N-isopropyl acrylamide) 10000 Da (carboxyl-terminated pNIPAM), anhydrous Dimethyl sulfoxide (DMSOa), carbonyldiimidazole (CDI), Diethylamine (DEA), sodium chloride (NaCl), BCA Assay Kit, Dulbecco's Phosphate Buffered Saline (DPBS), porcine gastric mucin, Live/Dead Cell Double Staining Kit were purchased from Merck.

Dulbecco's Minimum Essential Medium (DMEM) was purchased from Euroclone.

CellTiter 96® AQueous One Solution Cell Proliferation Assay (MTS) was purchased from Promega. Sabouraud Dextrose (Dehydrated) and Agar Bacteriological were purchased from Thermo Scientific™ Oxoid™. For the antifungal tests *in vitro*, *Candida albicans* ATCC 10231, reference strains in official tests (UNI EN European Standard), was purchased from the Leibniz Institute DSMZ-German Collection of Microorganisms and Cell Cultures GmbH (Braunschweig, Germany). The tested peptide AMP14d (FHLVWRAGGTF**)** was purchased by a company (GenScript Biotech, Leiden, Netherlands), according to our design and suggestions. The peptide was synthesized using fluoreny-methyloxycarbonyl protecting group (Fmoc) solid phase technology. The quality and purity of the synthetic peptide (≈98%) were determined through mass spectrometry (MS) analyses and high-performance liquid chromatography. The powdered peptide was kept at –20 °C for storage.

5.1.2 Synthesis and characterization of XG-pNIPAM

XG tetrabutylammonium salt (XG-TBA) was produced using a procedure similar to those previously described for other polysaccharides[240,403,404]. Briefly, XG was dispersed in MilliQ water at 0.5% w/v at 37°C in an orbital shaker incubator overnight. The obtained dispersion was put in a dialysis bag (cut-off 12-14 kDa) against MilliQ water at pH 3 for 24 h then neutralised with TBA-OH, frozen at -20°C and freeze dried.

XG-pNIPAM was synthesized as follows: carboxyl-terminated pNIPAM (412 mg) was dissolved in 10 mL of anhydrous DMSO and activated with CDI (14 mg) at 40°C for 4 h (molar ratio between pNIPAM carboxyl groups and CDI equal to 2). The obtained solution was added dropwise to XG-TBA (200 mg) dissolved in 45 mL of anhydrous DMSO in the presence of DEA (molar ratio between DEA and pNIPAM carboxyl groups equal to 5). The molar ratio between pNIPAM and XG repetitive units was set to 0.1. The reaction was conducted for 72 h at 40°C, the product was purified by dialysis (cut-off 50kDa) against NaCl solution for 48 h and MilliQ water for further 5 days. The final product was isolated by freeze drying and characterized through ^{1}H-NMR and FT-IR analysis. ^{1}H-NMR spectra were obtained with a Bruker Avance II 400 MHz spectrometer. FT-IR spectra were obtained with Bruker Alpha in the wave number range of 400 and 4000 cm^{-1}.

5.1.3 Production of the hydrogel and incorporation of AMP14d

Hydrogels were prepared using XG-pNIPAM concentration of 5% (w/v) in H_2O MilliQ. Similarly, XG-pNIPAM-AMP14d hydrogels were prepared using the same polymer concentration (5% w/v), incorporating the peptide at a concentration of 0.234% (w/v). In this case, the AMP14d solution was mixed with XG-pNIPAM under mild agitation conditions to allow foam formation.

5.1.4 Hydrolytic degradation studies

For degradation studies, the hydrogels were prepared as described before and freeze-dried to obtain xerogels. The samples were accurately weighed, immersed in 2 mL of DPBS pH 7.4 and incubated at 37 °C in an orbital shaker (50 rpm). At scheduled times (4, 8, 24 h), samples were repeatedly washed with MilliQ water at 37 °C, then freeze-dried and re-weighed. The sample degradation was expressed as the percentage of recovered weight (W_r%), calculated by the following equation:

$$Wr\% = \frac{Wf}{Wi} \times 100 \quad (6)$$

where W_f is the weight of the recovered sample (final weight) at each time, and W_i represents the initial xerogel weight. Each experiment was performed in triplicate.

The stability of the XG-pNIPAM hydrogel was macroscopically investigated by assessing its ability to remain intact in DPBS pH 7.4 when adhered to porcine skin tissue (furnished from a local slaughter). 200 µL of the sample was placed on the surface of the skin at 25 °C and then, incubated in DPBS at 37 °C for 24 h in an orbital shaker (50 rpm), to evaluate whether the hydrogel could withstand on the skin surface without significant macroscopic degradation or fragmentation.

5.1.5 Rheological characterization

Rheological analyses were performed on XG-pNIPAM aqueous dispersion at 5% w/v using a DHR-2 TA Instrument oscillatory rheometer equipped with a 2.015° cone plate geometry of 40 mm in diameter and a self-heating Peltier plate. The dispersions were, firstly, analysed by performing oscillation amplitude tests applying a % strain between 0.1% and 1000% and a constant angular frequency of 1 Hz at 25 °C to study the storage (G') and loss (G'') modules, the linear viscoelastic region (LVR) and cross point between G' and G''. Temperature dependence of G' and G'' values was analysed by thermo-rheological

experiments which were performed heating the samples from 20 °C to 40 °C at a rate of 2 °C/min by applying a constant strain of 1% in the linear viscoelastic region and a frequency of 1 Hz. Furthermore, flow sweep tests were performed at two different temperatures (25 °C and 35 °C) increasing shear rate from 0.1 s^{-1} to 3000.0 s^{-1} All the experiments were performed in triplicate.

5.1.6 Mucoadhesive behaviour

Mucoadhesive properties of the formulations were evaluated by measuring the mucoadhesion force that is the force required to detach the formulations from a mucin film using a rheometer DHR-2 TA Instrument oscillatory rheometer equipped with a 2.015° cone plate geometry of 40 mm in diameter and a self-heating Peltier plate. Briefly, a 5% w/w porcine gastric mucin dispersion was previously prepared in water. Mucin films were prepared directly on the Peltier: the mucin dispersion (300 µL) was placed homogeneously on the Peltier, which was then firstly heated at 70 °C until a homogeneous dried film was formed and subsequently cooled for 3 min until 35 °C. Afterwards, 400 µL of dispersion (XG-pNIPAM or XG (5% w/v)) were spread onto the mucin film and the upper plate was lowered until reaching an axial force of 0.8N. After a contact of 3 min with the hydrogel, the upper plate was raised at a constant speed of 10 mm/min until the break-up of the film. The analyses were performed in triplicate for each sample. The same experiment was conducted using the hydrogel or XG dispersion without mucin[95,405]. The recorded force of detachment (mucoadhesion force) was measured and plotted.

5.1.7 *In vitro* cytocompatibility

NIH/3T3 cells were cultured in DMEM supplemented with 10% v/v FBS (10% v/v), glutamine (1% v/v), penicillin-streptomycin (1% v/v), and amphotericin B (0.1% v/v) at 37°C in a 5% CO_2 atmosphere, using an Eppendorf New Brunswik S41i incubator. *In vitro*

cytocompatibility studies involved assessing the viability of NIH/3T3 cells cultured in the presence of peptide-loaded hydrogels. The freeze-dried XG-pNIPAM was sterilised through UV irradiation (254 nm for 30 min with a 125 W UV lamp). The hydrogels were subsequently prepared as previously described using sterile MilliQ water. Hydrogels (100 µL) were pipetted in each well of a 24-well plate containing 2×10^4 cells, seeded 24 h earlier. After 24h of co-culture, cell viability was assessed using the MTS assay, following the manufacturer's instructions. UV measurements at 492 nm were performed using an Eppendorf AF2200 spectrophotometer. The results were expressed as a percentage of viability compared to control cells grown on the well of the plate without hydrogel. Each experiment and each measurement were performed in triplicate. Additionally, a live/dead staining was conducted according to the manufacturer's instructions. In this experiment, fluorescence images were acquired using the Zeiss AxioVert200 microscope.

5.1.8 Peptide release

The BCA assay was used for the peptide release study according to the procedure indicated by the provider. A peptide calibration curve was prepared with stock solutions of AMP14d at concentrations ranging from 100 to 1000 µg/mL. Aliquots were taken from these solutions and used in the BCA assay[406]. For the release experiment, 100 µL of each hydrogel was injected into 200 µL of DPBS pH 7.4 at 37 °C. The system was incubated in an orbital shaker at 37 °C and, at pre-established time intervals (0.5, 1, 2, 4, 6, 8 and 24 h), the medium was removed and replaced. The amount of peptide released over time was determined by the BCA assay. Briefly, the medium was brought to a volume of 1 mL with fresh DPBS pH 7.4, then 25 µL of this was mixed with 200 µL of BCA working solution and the absorbance at 570 nm was recorded using an Eppendorf AF2200 spectrophotometer. The experiments were performed in triplicate.

5.1.9 *In vitro* antifungal activity of the hydrogel

The antifungal activity against *C.albicans* ATCC 10231 of XG-pNIPAM-AMP14d hydrogels was assessed in terms of evaluation of inhibition of free-living fungal growth, using viable plate count method. Fungal suspension of *C.albicans* ATCC 10231 (turbidity 0.5 McFarland standard) was diluted 1:20 in NaCl 0.9% w/v to get the concentration of 10^6 colony forming unit (CFU)/mL, and 100 µL were added to 48-well plates containing XG-pNIPAM-AMP14d hydrogels in 1 mL of Sabouraud Dextrose medium. The plate was incubated at 37 °C under stationary conditions, using an Holity h28107 incubator, and non-peptide-loaded XG-pNIPAM hydrogel was used as control. Growth control wells containing microorganisms without hydrogels, and a negative control consisting of culture broth without microorganisms, were performed for comparison under the same experimental conditions. After 24 h of incubation, an aliquot of the fungal suspension was removed from each well and utilized for the viable cell count. Briefly, the fungal suspensions were added in test tubes with NaCl (0.9% w/v solution), five 10-fold dilutions were prepared, and 100 µL aliquots of each dilution were plated onto Sabouraud Dextrose plates, followed by incubation at 37 °C overnight. Each assay was performed in triplicate. To quantify the number of viable fungal cells, the value of CFU/mL was determined. Logarithmic (log) reduction was calculated by subtracting the difference between the log CFU/mL of the growth control (microorganisms without hydrogels) and the log CFU/mL of the XG-pNIPAM hydrogel or XG-pNIPAM-AMP14d hydrogel, after 24 h of incubation.

5.2 3D-printed quaternized gellan gum-based hydrogels doped with in situ synthesized silver nanoparticles for the treatment of infected wounds

5.2.1 Materials

GG (Gelrite®), DMSO, 4-NPBC, EDA, acetone, DEA, GTMAC, DPBS, TNBS, $CaCl_2$, AO/EB were purchased from Merck. DMEM was purchased by Euroclone. MTS was purchased from the company Promega. $AgNO_3$ was purchased by the company Prolabo. Bacteria strains of *Staphylococcus aureus* ATCC 25923 and *Pseudomonas aeruginosa* ATCC 15442 were used for antimicrobial experiments.

5.2.2 Synthesis of GG-EDA-GTMAC

The synthesis of GG-EDA was conducted as previously reported in the literature[122]. In particular, 500 mg GG were dispersed in 45 mL anhydrous DMSO to obtain a final concentration of 1% w/v and kept at 60 °C under magnetic stirring overnight. Subsequently, 4-NPBC (118.2 mg), previously dissolved in 5 mL of DMSO, was added dropwise and the reaction was conducted at 60 °C for 4 h. The molar ratio (X) between 4-NPBC and repeating units of GG was set to 0.5. After 4 h, a 10-fold molar excess of EDA (259.9 µL), to 4-NPBC, was added dropwise and under agitation to the dispersion and the reaction was conducted for a further 3 h at 60 °C. The product was isolated by precipitation in acetone and then washed several times with the same solvent. Lastly, GG-EDA was recovered by vacuum drying at room temperature with a yield of 98% of GG initial weight and subsequently characterized by ^{1}H-NMR and TNBS analysis.

The synthesis of the quaternary derivative GG-EDA-GTMAC was carried out under the following conditions: 500 mg of GG-EDA was dispersed in 50 mL of MilliQ water, to obtain a final concentration of 1% w/v, and the dispersion was placed under agitation in an oil bath at 50 °C for 30 min. Subsequently, considering a molar ratio (X') between DEA and amino groups of GG-EDA equal to 1, 21.6 µL of DEA was added dropwise to GG-EDA dispersion.

Therefore 56.2 µL of GTMAC were added dropwise and under magnetic stirring and the reaction was conducted for 29 h at 50°C. The molar ratio (Y') between GTMAC and repeating units of GG-EDA functionalized in EDA, was set equal to 2. The product was then purified by dialysis (cut-off 3.5 kDa) for 2 days against NaCl solution and for a further 2 days against MilliQ water. Finally, the product was isolated by freeze-drying and subsequently characterized by ^{1}H-NMR and TNBS assay.

^{1}H-NMR spectra were obtained with a Bruker Avance II 400 MHz spectrometer. Samples were prepared by at 2% w/v in D_2O.

TNBS assay was performed to calculate the percentage derivation degree (DD %) of GG-EDA and GG-EDA-GTMAC. Briefly, a solution of TNBS (5 % w/v), diluted in sodium borate buffer (0.1M, pH=9.3) 1:5, was added in a ratio of 1:19 to each polymer dispersion (25 µg/mL in sodium borate buffer) and incubated for 2 h at 37 °C. Meanwhile, serial dilutions of methoxy polyethylene glycol amine were prepared for the standard curve. Lastly, the absorbance at 492nm was measured using an Eppendorf AF2200 spectrophotometer. In particular, the DD % of GG-EDA-GTMAC was compared to that of GG-EDA with the following equation:

$$DD\ \% = \left[1 - \frac{n_{NH_2\ (GG-EDA)}}{n_{NH_2\ (GG-EDA-GTMAC)}}\right] \times 100 \quad (7)$$

Where *n NH_2 (GG-EDA-GTMAC)* and *n NH_2 GG-EDA* are the moles of amino groups of GG-EDA-GTMAC and GG-EDA respectively.

5.2.3 Production of nanocomposite hydrogels

Hydrogels were prepared by dispersing GG-EDA-GTMAC (3% w/v) in MilliQ water at 70 °C for 30 min. These hydrogels were indicated as H_0, as they were free of $AgNO_3$.

For the preparation of nanocomposite hydrogels, GG-EDA-GTMAC was dispersed in the same way to a concentration of just over 3% w/v and when fully dispersed, different aliquots

of a 50 mM $AgNO_3$, extemporaneously prepared, were added in order to obtain hydrogels with different Ag^+ ions concentration: 0.5 mM, 1 mM, 1.5 mM, 2 mM, 2.5 mM, 5 mM. The samples were named respectively as $H_{0.5}$, H_1, $H_{1.5}$, H_2, $H_{2.5}$ and H_5, as already indicated in Table 1. The hydrogels were, further, irradiated with UV light at 365 nm for 30 min in order to form silver nanoparticles (Ag NPs) by reduction of Ag^+ to Ag^0 and then crosslinked by immersing them in $CaCl_2$ 0.1M solution for 30 min. Finally, the samples were washed several times with MilliQ water to remove excess salt.

5.2.4 Characterization of the nanocomposite hydrogels

In order to determine the quali-quantitative formation of AgNPs within the hydrogels, as well as their morphology and stability, UV spectroscopy, XPS, SEM-EDX analyses and degradation studies were performed on the samples.

For UV spectroscopy analysis, H_5, prepared as indicated in the previous paragraph, was placed in a basic environment (for NaOH 1 M) at 100 °C until complete dispersion. It was then analysed using a Shimadzu UV-2401PC spectrophotometer.

For the analysis of XPS and SEM-EDX, the samples (H_5 (XPS), H_0 and H_5 (SEM-EDX)) were prepared as previously indicated and, then the analyses were performed on freeze-dried with a Phenom Pro X Desktop (SEM-EDX) and with a PHI 5000 VersaProbe II instrument (ULVAC-PHI, Inc., Kanagawa, Japan) with a source: Al Kα (1486.6 eV) and a 128-channel hemispherical analyzer, FAT mode (XPS).

Degradation studies were conducted on the samples H_0 and H_5 prepared as outlined in section 5.2.3 and freeze-dried, then weighed to determine the initial mass (about 12 mg). Subsequently, the scaffolds were immersed in 2 mL of DPBS pH 7.4 and incubated under gentle agitation at 37 °C in an orbital shaker. At scheduled times (3, 7 and 14 days), the samples were repeatedly washed with MilliQ water in order to remove residual DPBS salts, then freeze-dried and re-weighed. The sample degradation degree was expressed as the

percentage of recovered weight percentage ($W_r\%$), calculated by equation 6, which is here reported again for major comprehension:

$$W_r\% = \frac{W_f}{W_i} \times 100 \quad (6)$$

where W_f is the weight of the recovered sample (final weight) at each time, and W_i represents the initial weight. Each experiment was performed in triplicate.

5.2.5 Rheological characterization

Rheological studies were carried out in order to investigate the viscoelastic behaviour of the samples, injectability, self-recovery capability and the influence of ionotropic crosslinking on these parameters. For this reason, analyses were conducted on samples prepared as indicated in the previous section, both before and after treatment with $CaCl_2$ 0.1 M, using a DHR-2 TA Instrument rotational rheometer (TA Instruments – Waters S.p.A.) equipped with a flat geometry of 8 mm in diameter with grooves and a self-heating Peltier plate.

These studies were always carried out by loading 100 µL of each sample onto the lower geometry of the instrument and setting an analysis gap of 300 µm. The excess sample was carefully removed before the start of each experiment. All tests were performed in triplicate using the parallel flat plate geometry with grooves.

In particular, the G' and G'' values, the region of linear viscoelasticity and the cross-point between G' and G'' were assessed using oscillation amplitude analysis by applying increasing strain % values from 0.01% to 5000.0%, under constant temperature (25°C) and angular frequency (0.5 rad/s). The analysis was conducted before and after treatment of the samples with $CaCl_2$ 0.1 M in order to study the influence of ionotropic crosslinking.

In addition, flow sweep studies were carried out by subjecting the samples to increasing shear rates from 0.01 s^{-1} to 100.0 s^{-1}, under constant temperature (25°C) to assess the

hydrogels' variation in viscosity as a function of increasing shear rate and then to study hydrogels' shear-thinning properties.

Lastly, recovery time studies were conducted by alternating cycles of low (1.0 %) and high (1000.0 %) strain %, applied at a constant frequency (0.5 rad/s) and temperature (25°C), to study the self-healing properties of the hydrogels.

5.2.6 Preliminary 3D printing tests

In order to assess printability and, at the same time, determine the optimal printing parameters for hydrogels, preliminary printing tests were performed using a Dr. INVIVO 3D printer, Rokit Healthcare. The tests were carried out on samples H_0 and H_5, prepared as described previously. The shape selected was a grid of 15×15×1 mm with pores of different sizes, created with the NewCreatorK software.

The best parameters obtained, using a 24 G diameter needle, were the following: 500 mbar (air pressure), 6 mm/s (printing speed), 0.13 mm (height of each layer). At the end of the printing process, the constructs were crosslinked with $CaCl_2$ 0.1M.

5.2.7 Cell culture and cytocompatibility tests

In order to study the cytocompatibility of the hydrogels produced, the MTS assay and AO/EB staining were performed, assessing cell viability indirectly by placing the sample inside cell culture inserts, without direct contact with the cells. The studies were performed using FD-MSC, cultured in DMEM supplemented with FBS (10% v/v), penicillin/streptomycin (1% v/v), glutamine (1% v/v) and amphotericin B solution (0.1% v/v) and incubated at 37 °C in a humidified atmosphere containing 5% of CO_2, using an Eppendorf New Brunswik S41i incubator. To perform the experiments, after treatment with trypsin, cells were counted, resuspended in complete DMEM and seeded in a 24-well cell culture plate at a density of 4×10^4 cells/well, then incubated overnight to promote adhesion. Subsequently, the samples

(100 µL each), produced as described in section 5.2.3 and subsequently UV-sterilised at 254 nm for 30 min using a 125W UV lamp, were placed inside cell culture inserts in the aforementioned plate and immersed in 2 mL of complete DMEM. After 24 h and 48 h of incubation, cell viability was assessed by MTS and AO/EB staining. In detail, the inserts containing the hydrogels, and the culture medium were removed and lastly, the wells were washed with DPBS. Afterwards, the MTS assay was performed following the manufacturer's instructions. UV measurements at 492 nm were performed using an Eppendorf AF2200 spectrophotometer. The results were expressed as a percentage of viability compared to control cells grown on the well of the plate without hydrogel. Each experiment was performed in triplicate.

Regarding the AO/EB staining, at the set time intervals, after removing the insert containing the hydrogel, the culture medium and washing the wells with DPBS, the cells were fixed by formaldehyde (4% w/v), and the plate was incubated at 37 °C for 15 min. Subsequently, the wells were washed again with DPBS and incubated for 5 min in the presence of 200 µL of AO/EB solution. Finally, fluorescence images were acquired with an AxioVert200 microscope (Zeiss).

All analyses were performed in triplicate and cells seeded on plates incubated in the absence of a sample were used as controls for both assays.

5.2.8 Hemocompatibility evaluation

A hemolysis assay was performed to evaluate the hemocompatibility of the developed hydrogels. Healthy erythrocytes were collected by centrifuging 1 mL of fresh venous blood at 500× g for 10 min and then, by washing 3 times the pellet collected with DPBS (pH 7.4) until a colourless supernatant was observed. The pellet was recovered with PBS up to 1 mL and further diluted 50 times[407]. Then, 500 µL of diluted red blood cell suspension were incubated with the samples (100 µL) at 37◦C for 1 h Triton X-100 and DPBS were used,

respectively, as positive and negative control. After centrifugation at 500× g for 10 min, the amount of hemoglobin released was quantified by a UV spectrophotometer at 570 nm. The hemolysis rate was calculated by the following equation[408]:

$$Hemolysis\ rate = \frac{A_{sample} - A_{negative}}{A_{positive} - A_{negative}} \times 100 \quad (8)$$

Where A_{sample}, $A_{positive}$ and $A_{negative}$ represent respectively the absorbance of the experimental, positive control, and negative control groups.

5.2.9 Microbiological characterization

5.2.9.1 Antibacterial activity

The antimicrobial activity of the samples was assayed against two reference pathogenic bacterial strains:

- *Staphylococcus aureus* ATCC 25923
- *Pseudomonas aeruginosa* ATCC 15442

The bacterial strains were cultured in Tryptic Soy Agar (TSA) at 37 °C for 24 h. At the end of the incubation, a suspension in 0.9% NaCl containing approximately 10^5 CFU/mL was prepared for each bacterial strain. 200 µL of bacterial suspension of *S. aureus* and *P. aeruginosa*, were inoculated into the wells of a 24-well plate, each containing 2 mL of Mueller Hinton (MH) culture medium and a sterilized cylinder-shaped hydrogel (400 µL) of the samples (H_0, $H_{0.5}$, H_1, $H_{1.5}$, H_2, $H_{2.5}$ and H_5). The plates were incubated for 24 h at 37 °C. At the end of the incubation, vital counts were performed to determine antimicrobial activity by the decimal serial dilution method.

1 mL of bacterial culture of *S. Aureus* or *P. aeruginosa*, grown 24 h in the presence of the samples, was transferred into a tube containing 9 mL of saline. A series of decimal dilutions was made and 100µL of the diluted bacterial suspensions were transferred onto TSA culture medium and incubated 24h at 37 °C. At the end of the incubation bacterial colonies grown

on the culture medium were counted, and the results were expressed in terms of colony-forming units (CFU)/mL. The experiments were performed in duplicate.

5.2.9.2 Antiprotozoal activity

The culture of promastigotes of the MON1/IPT1 strain of *Leishmania infantum* was performed according to the protocol described by Sengupta et al.[409]. Briefly, promastigotes were maintained on Blood Agar Slants containing 1% glucose, 5.2% Brain Heart Infusion Agar and rabbit blood (6% v/v), with the addition of gentamicin at a concentration of 1-1.5 mg/mL medium, at 25 °C. The cells were collected and resuspended in RPMI medium, supplemented with 10% FBS, to obtain a culture density of 10^6 cells/mL. For the experiment, the protozoa were dispensed into a 24-well cell culture plate containing H_0, $H_{0.5}$, H_1, $H_{1.5}$, H_2, and $H_{2.5}$ sterile cylinder-shaped hydrogels (100 µL each), prepared as described in section 5.2.3, then incubated at 37 °C for 24 h. The number of parasites was determined after 24 h, using a Bürker chamber, and the results were expressed as a percentage of the control.

For the determination of protozoan viability, the parasites were treated with Acridine Orange (100 µg/mL) and Ethidium Bromide (100 µg/mL). After 24 h of treatment with the hydrogels, as described for the determination of parasite numbers, the parasite suspension was collected, centrifuged and the pellet resuspended in 25 µL of the dye mixture. Analysis was performed on 10 µL of each suspension using a Nikon Eclipse E200 fluorescence microscope. Live parasites were identified by absorption of Acridine Orange (green fluorescence) and exclusion of Ethidium Bromide (red fluorescence). Dead parasites were determined by the uptake of Ethidium Bromide. The percentage of parasite viability was determined after counting at least 300 parasites.

5.3 3D-printed double-crosslinked polysaccharide/polyaminoacid hydrogels for bone regeneration

5.3.1 Materials

Xanthan gum (VANZAN, viscosity of 1300-1700 mPa×s for 1% w/v dispersions), was purchased by Vanderbilt Minerals LLC. 2-Hydroxy-4′-(2-hydroxyethoxy)-2-methylpropiophenone 98% (photoinitiator, below referred to as PhI), hydroxyapatite nanopowder (Hap), N,N-dimethylformamide (DMF), hydrazine monohydrate, acetone, sodium carbonate anhydrous, sodium hydrogen carbonate >95%, sodium (meta)periodate ($NaIO_4$), ethylene glycol, elastin from bovine neck ligament, oxalic acid, DPBS, D_2O, Alizarin Red S have been purchased by Merck.

5.3.2 Synthesis and characterization of XGox

The oxidation of xanthan gum has been conducted as reported in the literature.[264] Briefly, 500 mg of xanthan gum (XG) were dissolved in MilliQ water at a concentration of 0.6% w/v by stirring overnight. Subsequently, an aqueous solution of $NaIO_4$ (0.8% w/w) was added dropwise and the reaction was carried out at 40 °C for 3h in the dark. The molar (X) ratio between the repetitive units of XG and $NaIO_4$ was set at 1:1.5. After 3 h, the reaction was quenched by adding 1.0415 mL of ethylene glycol, which reacted with excess $NaIO_4$. The dispersion was then purified by dialysis (cut-off 12-14kDa) against MilliQ water for 4 days. The obtained dispersion was then freeze-dried, and the product was characterized by FT-IR and ^{1}H-NMR analysis. ^{1}H-NMR spectra were obtained with a Bruker Avance II 400 MHz spectrometer. Samples were prepared by dissolution of 10 mg of samples in 500 µL of D_2O. FT-IR spectra were recorded with a Bruker Alpha in the wavenumber range of 400 and 4000 cm^{-1}.

The oxidation degree (OD) of XGox was calculated as follows by potentiometric titration of the NaOH/hydroxylamine hydrochloride solution[130]:

$$OD = \frac{n\,(NaOH) \times \Delta V}{\frac{m\,(XGox)}{M\,(XGox)}} \times \frac{1}{8} \times 100 \quad (9)$$

Where: *n(NaOH)* is 0.1 M, ΔV is the recorded NaOH consumed (L), *m* is the mass of XGox (g), and *M* is the molecular weight of the repeating unit XGox (993 g/mol). The oxidation degree of XGox was calculated to be 25.8% ± 0.2% according to the equation above.

5.3.3 Synthesis and characterization of PAHy-MA

PAHy-MA was synthesized in two different steps. Firstly PAHy was synthesized according to a procedure reported in the literature.[381] Briefly, 4.8 mL of hydrazine monohydrate in 5 mL of DMF were added dropwise and under continuous stirring, to a dispersion solution consisting of 3 g of PSI in 40 mL of DMF. The reaction temperature was maintained between 24-28 °C. After 4h, during which precipitate formation took place, the reaction mixture was filtered, and the product was washed with acetone until complete removal of the unreacted hydrazine (pH = 7). The obtained product was then vacuum dried, dispersed in MilliQ water to obtain a dispersion with a concentration of 5% w/v and further purified by dialysis against distilled water (cut-off 12-14kDa). The product was recovered by freeze-drying, with a yield of 94% w/w.

In a second step, PAHy-MA was synthesized following reaction conditions reported for the synthesis of methacrylated gelatin with some modifications[390]. Briefly, 500 mg of PAHy were dispersed in 5 mL of carbonate/bicarbonate buffer at pH 9.4 and then 288.66 µL of methacrylic anhydride were added dropwise to the obtained dispersion (molar ratio between methacrylic anhydride and PAHy repetitive units equal to 0.5). The reaction was conducted, under stirring, at 40 °C, in the dark for 1h, then stopped by the addition of HCl 1N until a pH = 7.4 was obtained. The dispersion was dialysed against MilliQ water (cut-off 3.5 kDa)

and the product was recovered by freeze-drying. The final yield was 70% w/w compared to the initial PAHy weight. Finally, the product was characterized by TNBS assay and ^{1}H-NMR analysis. The latter was carried out as reported for XG derivate.

TNBS assay was performed to calculate the percentage derivation degree (DD %) of PAHy-MA. Briefly, a solution of TNBS (5 % w/v), diluted in sodium borate buffer (0.1M, pH=9.3) 1:5, was added in a ratio of 1:19 to each polymer dispersion (PAHy and PAHy-MA, 25 µg/mL in sodium borate buffer) and incubated for 2 h at 37 °C. Meanwhile, serial dilutions of a tert-butyl carbazate (TBC) were prepared for the standard curve. Lastly, the absorbance at 492nm was measured using an Eppendorf AF2200 spectrophotometer. The DD % of PAHy-MA was calculated with the following equation:

$$DD\ \% = \left[1 - \frac{n_{NH_2}\ (PAHy-MA)}{n_{NH_2}\ (PAHy)}\right] \times 100 \qquad (10)$$

Where *n NH_2 (PAHy-MA)* and *n NH_2 PAHy* are the moles of hydrazine groups of PAHy-MA and PAHy respectively.

5.3.4 Formulation and characterization of XGox/PAHy-MA hydrogels

Hydrogels were produced by mixing aqueous solutions of XGox (1% w/v) and PAHy-MA (2% w/v). PhI (0.3% w/v) and different amounts of Hap (0%, 0.01%, 0.1% w/v) were also dispersed or dissolved in the gelling solution according to the precise weight ratios, as already reported in Table 3.

Photo-crosslinked hydrogels (500 µL) were prepared by irradiating samples for 1 min using a UV Rayonet system with a rotating carousel (365 nm, 100 W).

5.3.5 Hydrolytic degradation studies

Degradation studies of the materials were performed on freeze-dried hydrogels, prepared as described before (sample A). Scaffolds were accurately weighed (15mg), immersed in 2 mL

of DPBS pH 7.4 and incubated at 37 °C in an orbital shaker. At scheduled times (7, 14, 21 days), they were repeatedly washed with MilliQ water to remove the DPBS salts, then freeze-dried and re-weighed.

The sample degradation degree was expressed as the percentage of recovered weight percentage ($W_r\%$), calculated by equation 6, which is here reported again for major comprehension:

$$W_r\% = \frac{W_f}{W_i} \times 100 \quad (6)$$

where W_f is the weight of the recovered sample (final weight) at each time, and W_i represents the initial weight. Each experiment was performed in triplicate.

5.3.6 Rheological characterization

The rheological tests were conducted using a DHR-2 TA Instrument rotational rheometer (TA Instruments – Waters S.p.A.) equipped with a flat geometry of 8 mm in diameter with grooves and a self-heating Peltier plate. Hydrogels were first subjected to a variable amplitude of strain to study storage (G') and loss (G'') modules, the linear viscoelastic region (LVR) and the cross point between G' and G'' by applying % strain between 0.1% and 5×10^3%, under constant temperature (25°C) and at an angular frequency of 0.5 rad/s. Then, flow sweep experiments were carried out to assess the variation in viscosity at an increasing shear rate from 0.01 s^{-1} to 100.0 s^{-1}, under a constant temperature (25°C). To study the recovery and self-healing properties of the samples, recovery time tests were performed by subjecting hydrogels to 7 alternating cycles of 5% and 1.3×10^3 %, each for 100 s, applying a constant temperature of 25°C and an angular frequency of 0.5 rad/s. Moreover, frequency sweep tests were carried out at a constant temperature (25 °C), in a range of oscillation frequencies between 0.05 and 50 rad/s, applying a constant % strain of 5.0% (LVR). Lastly, oscillation time tests were carried out with a strain % of 5 %, angular frequency at 0.5 rad/s

and temperature at 25 °C for 300 s to evaluate variations of G' and G'' over time. Each analysis was carried out on 100 µL of sample. The measurement gap was set to 300 µm for all analyses performed and the excess sample was carefully removed before the start of each experiment. All tests were performed in triplicate.

5.3.7 3D printing tests

A REGEMAT3D Bio V1®bioprinter (3D Regemat, Spain) was used to print porous hydrogel scaffolds of 15 × 15 × 3 mm with a syringe of 5 mL and a 20 GA tip. The samples were printed with pores of 2 × 2 mm and a layer height of 0.30 mm. The infill and flow speeds were respectively in the range 5.5 - 6.5 mm/s and 3.5 - 4.5 mm/s. The printed structures were photo-crosslinked every two layers under UV light (1000 mW/cm^2 with a curing speed of 1 mm/s). Printability error (P_e) was evaluated using the following formula[395]:

$$Pe = \frac{filament\ diameter\ (d)}{Nozzle\ diameter\ (D)} \tag{11}$$

The measurements were performed using the ImageJ software on SEM images of freeze-dried samples. SEM analyses of the printed samples were performed by using a TM3030Plus SEM (Hitachi High-Technologies) apparatus; the surface of the samples was previously gold-coated using an SC7620 mini sputter coater/glow discharge system (Quorum).

5.3.8 Elastin extraction

The extraction of the water-soluble elastin from the elastin of the bovine neck ligament was performed as reported in the literature[199,397,401]. Briefly, 5 g of bovine elastin was suspended in 0.25 M oxalic acid solution and hydrolysed by sequential cycles of heating for 1 h in a water boiling bath. The supernatant was collected by centrifugation and the precipitate was treated in the same way until complete hydrolysis. The collected soluble fraction was dialyzed against water (3.5 kDa cut-off) and then freeze-dried.

5.3.9 Cell culture, scaffold seeding and cytocompatibility tests

An osteoblast cell line, MG-63 (ATCC CRL-1427), was expanded until passage 9 in monolayer culture in α-MEM supplemented with FBS (10% v/v) at 37 °C with 5% of CO_2 with a cell seeding density of 5000 cells/cm^2 until 80 % confluence. The culture medium was changed every 2–3 days.

For cell culture experiments on the scaffolds, XGox was sterilized by UV light (254nm for 40 min), while PAHy-MA and PhI were sterilized by filtration with a 0.2 µm pore mixed cellulose ester syringe filter prior to printing. After printing, the scaffolds were coated with elastin by covering them with an elastin solution at 500 µg/mL in PBS, followed by 1h incubation at 37°C and finally transferred to another plate. Cells at passage 9 were trypsinized, pelleted down by centrifugation at 500 rpm and resuspended to reach a density of 3.0×10^6/mL. 50 µL of the cell suspension were seeded on each scaffold to reach 1.5×10^5 cells/scaffold.

To study the cytocompatibility of the material, scaffolds of 6×15×3 mm (with pores of 2×2 mm) were printed in sterile conditions using a REGEMAT3D Bio V1®bioprinter for the composition A (1% XGox, 2% PAHy-MA, 0.3% PhI, 0% Hap). DNA assay and LDH evaluation were performed on the samples after 24 h and 7 days. All the experiments were performed in triplicate. The total DNA amount was measured with a CyQuant™ cell proliferation assay (Invitrogen), according to the manufacturer's instructions. A value of 6.6×10^{-6} µg of DNA was assumed for each cell to estimate the total cell numbers. At the different time points, the medium was removed, and the samples were washed with DPBS two times, then freeze-thawed three times and finally digested with 1 mg/mL Proteinase K (Fisher BioReagents™) in Tris/EDTA buffer at 56 °C overnight. Subsequently, a solution of RNAse A diluted in lysis buffer 1:500 was added in a ratio of 1:1 to each sample and incubated for 1 h at RT. Meanwhile, serial dilutions of a DNA standard were prepared for

the standard curve. Lastly, 100 µL of GR-dye solution (diluted 1:200 in lysis buffer) were added to the same volume of each sample in a black bottom microplate, incubated for 15 min at RT and then fluorescence was measured (480 nm excitation, 520 nm emission).

For the LDH, at the different time points, the samples' medium was collected and centrifuged at 500 rpm for 10 min to remove any cell, transferred into new tubes and stored at −80 °C until use. LDH content was measured following the manufacturer's instructions. (Cyquant LDH cytotoxicity assay, ThermoFisher).

5.3.10 Cell differentiation experiment

To evaluate the differentiation of cells seeded on the different scaffolds, samples of 4×4×3 mm (with a pore of 2×2mm) were printed in sterile conditions for all the compositions A, B, and C. After printing, the scaffolds were coated with the elastin extracted as described previously, and 2.0×10^5 cells were seeded on each scaffold. The scaffolds were incubated in basal medium (α-MEM supplemented with 10% v/v FBS) for 24 h and then this was substituted with the differentiation medium (α-MEM supplemented with 10% (v/v) FBS, 100 U/mL (1%) penicillin-streptomycin, 200 µM L-ascorbate-2-phohsphate (ASAP), 10 nM dexamethasone and 10 mM β-glycerophosphate). Samples incubated in the basal medium were used as a control. The medium was changed every 2-3 days and every week the samples were transferred to new plates. After 14 and 21 days, DNA assay, real-time PCR (RT-PCR), Alizarin Red S assay, immunostaining analyses and SEM were performed.

The following abbreviations were used to refer to the results of these assays: A bm (sample A incubated in basal medium), B bm (sample B incubated in basal medium), C bm (sample C incubated in basal medium), A dm (sample A incubated in differentiation medium), B dm (sample B incubated in differentiation medium), C dm (sample C incubated in differentiation medium).

5.3.10.1 Gene expression analysis: RNA isolation and purification, cDNA synthesis and quantitative Polymerase Chain Reaction (qPCR)

After 14 or 21 days of culture in basal and osteogenic media, the seeded scaffolds were rinsed with PBS three times. To lyse the cells, scaffolds were covered with 1 mL of TRIzol for 5 min at RT and freeze-thawed with liquid nitrogen three times. To eliminate proteoglycans from the extracts, which are powerful inhibitors of the Polymerase Chain Reaction, additional centrifugation at 12000×g for 5 min was done to precipitate them. The supernatant was mixed with 200 µL of $CHCl_3$ shaken vigorously for 15 seconds and incubated for 3 min at RT, followed by a centrifugation at 12000×g for 15 min. The upper colourless phase was mixed with 500 µL of isopropanol and incubated for 10 min at RT. After their centrifugation at 12000×g for 10 min at 4°C, the RNA formed a gel-like precipitate that was separated and mixed with an equal volume of ethanol. The extracted RNA was purified and eluted following the Invitrogen™ PureLink™ RNA Mini Kit protocol. The concentration of the extracted mRNA solutions was determined using an IMPLEN NanoPhotometer N60/N50 measuring the absorbance of the samples at 260 nm, and their purity grade checking the A260/A280 and A260/A230 absorbance ratios. To carry out the synthesis of complementary DNA, the Applied Biosystems™ High-Capacity RNA-to-cDNA™ Kit manufacturer's instructions were followed on a 20 µL reaction, setting a temperature program of 37°C for 60 min and 95°C for 5 min. To perform the qPCR experiment, 10 µL of reverse and forward primer 100 µM solutions were diluted in 980 µL of molecular grade H_2O. 8 µL of primer dilutions (*Col1a1*, *RunX2* and *BGLAP*) were mixed with 2 µL of cDNA solution and 10 µL of SyBR Green 2x in a 96-Well Clear Reaction Plate. A QuantStudio 1 thermocycler (Applied Biosystems) was used with a temperature set-up of a first step with 50°C for 2 min and 95°C for 2 min, and then 40 cycles with 95°C for 15 seconds and 60°C for 1 min. The primers used for qPCR experiments are shown in Table 5.

C_t values of each sample were determined and employed in the comparative C_T method to calculate the fold change of gene expression in the samples using GAPDH as the housekeeping gene.

Table 5. List of primers used for qPCR experiments.

Gene	Fw (5'-3')	Rv (5'-3')
GAPDH	ATG GGG AAG GTG AAG GTC G	TAA AAG CAG CCC TGG TGA CC
Col1a1	AGG GCC AAG ACG AAG ACA TC	AGA TCA CGT CAT CGC ACA ACA
Runx2	AGT GAT TTA GGG CGC ATT CCT	GGA GGG CCG TGG GTT CT
BGLAP	TGA GAG CCC TCA CAC TCC TC	CGC CTG GGT CTC TTC ACT AC

5.3.10.2 Alizarin Red S staining

For Alizarin Red S (ARS) staining, the samples were firstly fixed with paraformaldehyde (PFA) for 15 min, washed with PBS and then incubated with ARS staining solution (2% w/v) for 1.5 h. The samples were finally washed with MilliQ water and analysed with a Nikon Ts2 light microscope.

5.3.10.3 Immunostaining

Samples were fixed with PFA for 15 min and then permeabilized with TritonX-100 0.1% for 15 min followed by washing with PBS. Samples were then blocked with a solution of 3% BSA, 0.01% Triton X-100 in PBS for 1h and finally washed with a washing buffer (0.3% BSA, 0.001% Triton X-100 in PBS). Afterwards, the samples were stained with Anti-Collagen I Alexa Fluor-488 antibody (Abcam, ab275996, 1:100) for 2h, washed with WB, stained with Phalloidin Alexa Fluor 568 (Invitrogen, 1:100) for 2h, washed with Hoechst 33342 (1:500) for 15 min and lastly washed with PBS. The samples were kept in PBS at 4°C until imaging on a Nikon Eclipse Ti-2 inverted fluorescence microscope.

5.3.10.4 Scanning electron microscopy of cell-laden scaffolds

Samples were first fixed with PFA for 15 min and washed with PBS. After fixation, the samples were dehydrated, incubating at room temperature with solutions at increasing ethanol concentration in PBS (15 min for each one): 50%, 70%, 80%, 90%, 96% and 100% v/v. Then these samples were treated with hexamethyldisilazane (50% and 100% v/v in ethanol) and let dry completely overnight with airflow. SEM analyses were performed as described previously (section 5.3.7).

5.3.11 Statistical analysis

All results are reported with a media ± standard deviation and, when applicable the statistical analysis for significance was conducted with the Student's t-test, using the function t-test of Microsoft Excel, assuming the not homogenous variance at 2 samples and a dual tile distribution; values with $p < 0.05$ were considered statistically significant (*$p<0.05$; **$p<0.01$; ***$p<0.001$).

5.4 Injectable gellan gum/elastin-based nanocomposite hydrogels as fillers for irregular bone defects

5.4.1 Materials

GG (Gelrite®), NaOH, Dowex® 50WX8, TBA-OH, DMSO, 4-NPBC, TEA, AEMA, acetone, DPBS, TNBS, $CaCl_2$, 2-Hydroxy-4′-(2-hydroxyethoxy)-2-methylpropiophenone 98% (photoinitiator, below referred to as PhI), elastin from bovine neck ligament, oxalic acid, β-TCP, ZnO NPs, AO/EB were purchased from Merck. Methacrylic anhydride was purchased by the company Fluka. DMEM was purchased by Euroclone. MTS was purchased from the company Promega.

5.4.2 Synthesis and characterization of GG-AEMA

The synthesis of GG-AEMA started from a low molecular weight GG. For this reason, GG was, initially, hydrolysed under alkaline conditions as reported elsewhere[226,233]. Specifically, 5g of gellan gum were dispersed in a NaOH solution (0.1M) at a concentration of 1% (w/v) and the dispersion was kept under stirring at 50 °C for 24 h. Subsequently, HCl (1N) was added until neutralization and the dispersion was dialyzed (cut-off 25 kDa) against MilliQ. The resulting product, the sodium salt of degraded gellan gum, was transformed into its acid form using a Dowex® 50W-X8 hydrogen-exchange resin and the dispersion was neutralised with TBA-OH to obtain GG-TBA. The dispersion was freeze-dried and the product was used for the subsequent chemical modification.

The synthesis of the GG-AEMA was carried out as follows: 500 mg GG-TBA was dispersed in 40 mL anhydrous DMSO to obtain a final concentration of 1% (w/v) and the dispersion was stirred at 40°C for 30 min. Subsequently, 85.7 mg of 4-NPBC, previously solubilised in 5 mL anhydrous DMSO, were added dropwise and the reaction was conducted at 40°C for 4 h. The molar ratio (X) between 4-NPBC and the repeating units of GG-TBA was set equal to 0.5. After 4 h, 196 μL of TEA and 233.52 mg of AEMA, previously solubilised in 5 mL

of anhydrous DMSO, were added dropwise and under stirring to the polysaccharide's dispersion and the reaction was carried out for a further 24 h at 40°C. The molar ratio (Y) between AEMA and 4-NPBC was set equal to 5 while the molar ratio (Z) between TEA and AEMA was set equal to 1. The reaction was stopped by adding 500 µL of saturated NaCl solution and stirred for 30 min. Then, the product was isolated by precipitation in acetone and then purified by several washings with acetone/water mixture (8:2 v/v) and finally with acetone. The polymer was vacuum-dried at room temperature, dispersed in MilliQ water, and dialyzed (cut-off 3.5 kDa) against NaCl (2 days) and MilliQ water (2 days). Finally, the product was isolated by freeze-drying and subsequently characterized by ^{1}H-NMR analysis. ^{1}H-NMR spectra were obtained with a Bruker Avance II 400 MHz spectrometer. Samples were prepared at 2% w/v in D_2O.

5.4.3 Synthesis and characterization of ELMA

The soluble elastin fraction was extracted from bovine neck elastin using an oxalic acid extraction procedure[199,397,401]. Briefly, 5 g of bovine elastin were suspended in 0.25 M oxalic acid solution and hydrolysed by sequential cycles of heating for 1 h in a water boiling bath. The supernatant was collected by centrifugation and the precipitate was treated in the same way until complete hydrolysis. The collected soluble fraction was dialyzed against water (3.5 kDa cut-off) and then freeze-dried.

To obtain the ELMA, 1 g of degraded elastin was dispersed in 100 mL of anhydrous DMSO, then 250 µL TEA and 500 µL methacrylic anhydride were added dropwise at room temperature. The reaction was carried out for 24 h, at room temperature, under stirring and in the dark. The dispersion was then placed on membrane dialysis (cut-off 3.5 kDa) against DMSO. Gradually, DMSO was replaced with borate buffer pH 9 and MilliQ water in the following order: DMSO, borate buffer 0.1 M pH 9, borate buffer 0.05 M pH 9, borate buffer 0.01 M pH 9, MilliQ water. The product was recovered by freeze-drying with a yield of

about 90 % w/w and characterized by ^{1}H-NMR analysis and TNBS assay. The former was carried out as reported for GG derivate.

TNBS assay was performed as follows: a solution of TNBS (5 % w/v), diluted in sodium borate buffer (0.1M, pH=9.3) 1:5, was added in a ratio of 1:19 to each polymer (ELMA and soluble elastin) dispersion (25 µg/mL in sodium borate buffer) and incubated for 2 h at 37 °C. Meanwhile, serial dilutions of methoxy polyethylene glycol amine were prepared for the standard curve. Lastly, the absorbance at 492nm was measured using an Eppendorf AF2200 spectrophotometer. In particular, the efficiency of functionalisation of ELMA was calculated by comparing the amount of free amino groups of the two polymers with the following equation:

$$\text{Efficiency of functionalisation } \% = \left[1 - \frac{n_{NH_2}\ (ELMA)}{n_{NH_2}\ (soluble\ elastin)}\right] \times 100 \qquad (12)$$

Where *n NH_2 (ELMA)* and *n NH_2 (soluble elastin)* are the moles of amino groups of ELMA and soluble elastin respectively.

5.4.4 Production and characterization of base hydrogels

Initially, different hydrogels composed of GG-AEMA and ELMA were produced, with different contents of the latter polymer to assess the most suitable amount of the protein derivative to incorporate into the system. Specifically, the hydrogels were prepared by dispersing the GG-AEMA (4% w/v) in a solution of DPBS and PhI (0.3% w/v) at 70 °C, adding different amounts of ELMA, previously dispersed in the same solution, in order to obtain a final concentration of the protein derivative of 0%, 2% and 4% w/v.

Subsequently, the hydrogels were photo-crosslinked by UV light at 365 nm for 10 min, then ionotropically crosslinked by immersion in $CaCl_2$ (0.1 M) for 10 min and washed twice in MilliQ water to remove excess salt.

5.4.5 Cell adhesion studies

In order to study the biological properties of these hydrogels and to determine the optimal amount of ELMA, adhesion studies were conducted, thus assessing the possible ability of the systems to provide support for cell adhesion.

These studies were performed using FD-MSC, cultured in DMEM supplemented with 10% v/v FBS, 1% v/v penicillin/streptomycin, 1% v/v glutamine and 0.1% v/v amphotericin B solution and incubated at 37 °C in a humidified atmosphere containing 5% CO_2 using an Eppendorf New Brunswik S41i incubator. To perform adhesion experiments, after treatment with trypsin, the cells were counted, resuspended in complete DMEM and seeded onto the samples. These studies were performed on samples, prepared as indicated in section 5.4.4. Specifically, 300 μL of each sample (H_A, H_B, H_C, and control of ELMA alone (20% w/v) prepared in DPBS and PhI (0.3% w/v)) were injected into a 48-well plate in order to create a gel layer that evenly covered the well; then, the hydrogels were UV-sterilized at 254 nm, for 30 min, using a 125 W UV lamp. Subsequently, 4×10^4 cells were seeded onto each sample and incubated under the above conditions. Evaluation of cell adhesion on the surface of the hydrogels was performed by light microscopy using an AxioVert200 microscope (Zeiss).

5.4.6 Rheological characterization of base hydrogels

Rheological studies were carried out in order to investigate the viscoelastic behaviour of the samples and the influence of photo- and ionotropic crosslinking on the viscoelastic properties of the samples. For this reason, oscillation amplitude pre- and post-crosslinking (photo- and ionotropic crosslinking) and photo-rheology studies were conducted on the samples prepared as outlined in Section 5.4.4.

These studies were performed with a DHR-2 TA Instruments oscillatory rheometer, mainly using a parallel flat plate geometry with 8 mm diameter and grooves and a self-heating

Peltier plate (TA Instruments - Waters S.p.A.). Photo-rheology analyses were conducted using a parallel flat plate geometry with 20 mm diameter and a UV LED module (365 nm). The oscillation amplitude studies were performed by applying increasing percentage strain values from 0.01% to 5000.0%, keeping the temperature at 25°C and the angular frequency at 0.5 rad/s constant. These studies were conducted by loading 100 µL of each sample onto the lower geometry of the instrument and setting an analysis gap of 300 µm. Excess sample was carefully removed before the start of each experiment. All tests were performed in triplicate using the parallel flat plate geometry with grooves.

Photo-rheology tests, on the other hand, were carried out at constant strain % (1.0 %) and frequency (0.5 rad/s) by irradiating the sample with a UV power of 50 mW/cm^2 for 90 s after a time 60 s from the start of the analysis. These analyses were performed by loading 50 µL of each sample onto the lower geometry of the instrument and setting a gap of 100 µm.

5.4.7 Production of nanocomposite hydrogels

The nanocomposite hydrogels were formulated by incorporating 0.1% w/v ZnO and two different percentages of β-TCP (5% w/v and 20% w/v) into the selected hydrogel with 4% GG-AEMA and ELMA (H_C). Subsequently, the hydrogels were photo-crosslinked by UV light at 365 nm for 10 min, then ionotropically crosslinked by immersion in $CaCl_2$ (0.1 M) for 10 min and washed twice in MilliQ water to remove excess salt.

5.4.8 Rheological characterization of nanocomposite hydrogels

Rheological characterization was carried out also on the nanocomposite hydrogels: oscillation amplitude studies before and after the photo- and ionotropic crosslinking, flow sweep, recovery time and photo-rheology were conducted on all samples.

In particular, oscillation amplitude studies before and after photo-ion crosslinking and photo-rheology studies were carried out following the specifications indicated in section 5.4.6. The

flow sweep studies, on the other hand, were carried out by subjecting the samples to increasing shear rate from 0.01 s^{-1} to 100.0 s^{-1}, under constant temperature (25°C) to assess the hydrogels' variation in viscosity as a function of increasing shear rate and then to study hydrogels' shear-thinning properties.

Recovery time studies were conducted by alternating cycles of low (1.0 %) and high (1000.0 %) strain %, applied at a constant frequency (0.5 rad/s) and temperature (25°C). Both analyses were carried out with the same equipment for oscillation amplitude tests.

5.4.9 Hydrolytic degradation studies

Degradation studies were performed on 200 µL of samples H_C, $H_{nc}B$, $H_{nc}C$ prepared as described above. The samples were then freeze-dried and weighed to record the initial weight. Subsequently, the scaffolds were immersed in 2 mL of DPBS pH 7.4 and incubated under gentle agitation at 37 °C in an orbital shaker. The weight of the lyophilised scaffold was monitored after 7, 14, 21 and 28 days of incubation. At schedule times, the samples were washed repeatedly with MilliQ water in order to remove residual DPBS salts, then freeze-dried and re-weighed. The sample degradation degree was expressed as a percentage of weight recovered ($W_r\%$) calculated by equation 6, here reported again for major comprehension:

$$W_r\% = \frac{W_f}{W_i} \times 100 \quad (6)$$

where W_f is the weight of the recovered sample (final weight) at each time, and W_i represents the initial weight. Each experiment was performed in triplicate.

Furthermore, in order to macroscopically evaluate the degradation of the hydrogels under conditions as similar as possible to those *in vivo*, the hydrogels were injected into suitably perforated horse bone inserts and their adhesion to the tissue and degree of degradation was

evaluated. In detail, a time 0, a micro-CT analysis was performed of sample $H_{nc}C$ using a Microtac micro-CT Skyscan 1272 Bruker.

5.4.10 Cytocompatibility evaluation of the hydrogels

Finally, in order to assess the possible cytotoxicity of the developed hydrogels, cytocompatibility studies were carried out, through MTS assay and AO/EB staining, assessing cell viability indirectly by placing the sample inside cell culture inserts, without direct contact with the cells. These studies were performed using FD-MSC, cultured as outlined in section 5.4.5.

To perform the experiments, 4×10^4 cells were seeded in wells of a 24-well cell culture plate, then incubated overnight to promote adhesion. Subsequently, the samples (100 µL each), produced as outlined in section 5.5 and subsequently UV-sterilised (as for the adhesion assays), were placed inside cell culture inserts placed in the aforementioned plate and immersed in 2 mL of complete DMEM.

After 24 h and 48 h incubation, cell viability was assessed by MTS and AO/EB staining. In detail, the inserts containing the hydrogels, and the culture medium were removed and finally the wells were washed with DPBS. Afterwards, MTS assay was performed following the manufacturer's instructions UV measurements at 492 nm were performed using an Eppendorf AF2200 spectrophotometer. The results were expressed as a percentage of viability compared to control cells grown on the well of the plate without hydrogel. Each experiment was performed in triplicate. About the AO/EB staining, the cell's layers were fixed by 4% w/v formaldehyde (37°C for 15 min) and washed again with DPBS. Then, the samples were incubated for 5 min in the presence of 200 µL of AO/EB solution and finally, fluorescence images were acquired using an AxioVert200 microscope (Zeiss). All analyses were performed in triplicate and cells seeded on a plate, incubated in the absence of a sample, were used as controls for both assays.

6. References

[1] B. Lu, H. Cheng, L. Qu, Inorganic Hydrogel Based on Low-Dimensional Nanomaterials, ACS Nano. 18 (2024) 2730–2749. https://doi.org/10.1021/acsnano.3c11262.

[2] H. Cao, L. Duan, Y. Zhang, J. Cao, K. Zhang, Current hydrogel advances in physicochemical and biological response-driven biomedical application diversity, Signal Transduct. Target. Ther. 2021 61. 6 (2021) 1–31. https://doi.org/10.1038/s41392-021-00830-x.

[3] K.A. Uyanga, H. Zhao, X. Bo, W.A. Daoud, Advances and opportunities of hydrogels for metal-ion batteries, Energy Storage Mater. 72 (2024) 103707. https://doi.org/10.1016/j.ensm.2024.103707.

[4] S.J. Buwalda, T. Vermonden, W.E. Hennink, Hydrogels for Therapeutic Delivery: Current Developments and Future Directions, Biomacromolecules. 18 (2017) 316–330. https://doi.org/10.1021/acs.biomac.6b01604.

[5] B. Guo, J. Qu, X. Zhao, M. Zhang, Degradable conductive self-healing hydrogels based on dextran-graft-tetraaniline and N-carboxyethyl chitosan as injectable carriers for myoblast cell therapy and muscle regeneration, Acta Biomater. 84 (2019) 180–193. https://doi.org/10.1016/j.actbio.2018.12.008.

[6] H. Hong, Y.B. Seo, D.Y. Kim, J.S. Lee, Y.J. Lee, H. Lee, O. Ajiteru, M.T. Sultan, O.J. Lee, S.H. Kim, C.H. Park, Digital light processing 3D printed silk fibroin hydrogel for cartilage tissue engineering, Biomaterials. 232 (2020) 119679. https://doi.org/10.1016/j.biomaterials.2019.119679.

[7] B.M. Bakadia, A.A. Qaed Ahmed, L. Lamboni, Z. Shi, B. Mutu Mukole, R. Zheng, M. Pierre Mbang, B. Zhang, M. Gauthier, G. Yang, Engineering homologous platelet-rich plasma, platelet-rich plasma-derived exosomes, and mesenchymal stem cell-derived exosomes-based dual-crosslinked hydrogels as bioactive diabetic wound dressings, Bioact. Mater. 28 (2023) 74–94. https://doi.org/10.1016/j.bioactmat.2023.05.002.

[8] M. Isik, I. Vargel, E. Ozgur, S.B. Cam, P. Korkusuz, E. Emregul, S. Odabas, B. Derkus, Human periodontal ligament stem cells-derived exosomes-loaded hybrid hydrogel enhances the calvarial defect regeneration in middle-age rats, Mater. Today Commun. 36 (2023) 106869. https://doi.org/10.1016/j.mtcomm.2023.106869.

[9] Y. Wang, E.R. Zoneff, J.W. Thomas, N. Hong, L.L. Tan, D.J. McGillivray, A.W. Perriman, K.C.L. Law, L.H. Thompson, N. Moriarty, C.L. Parish, R.J. Williams, C.J. Jackson, D.R. Nisbet, Hydrogel oxygen reservoirs increase functional integration of neural stem cell grafts by meeting metabolic demands, Nat. Commun. 14 (2023) 1–11. https://doi.org/10.1038/s41467-023-36133-8.

[10] C.Y. Hsu, J. Lin, M.F. Wei, L.H. Chen, H.K.T. Liang, F.H. Lin, Local delivery of carboplatin-loaded hydrogel and calcium carbonate enables two-stage drug release for limited-dose

radiation to eliminate mouse malignant glioma, Biomaterials. 312 (2025) 122746. https://doi.org/10.1016/j.biomaterials.2024.122746.

[11] H. Ceylan, I.C. Yasa, O. Yasa, A.F. Tabak, J. Giltinan, M. Sitti, 3D-Printed Biodegradable Microswimmer for Theranostic Cargo Delivery and Release, ACS Nano. 13 (2019) 3353–3362. https://doi.org/10.1021/acsnano.8b09233.

[12] J. Xu, M. Tam, S. Samaei, S. Lerouge, J. Barralet, M.M. Stevenson, M. Cerruti, Mucoadhesive chitosan hydrogels as rectal drug delivery vessels to treat ulcerative colitis, Acta Biomater. 48 (2017) 247–257. https://doi.org/10.1016/j.actbio.2016.10.026.

[13] D.F. Argenta, B. da C. Bernardo, A.F. Chamorro, P.R. Matos, T. Caon, Thermosensitive hydrogels for vaginal delivery of secnidazole as an approach to overcome the systemic side-effects of oral preparations, Eur. J. Pharm. Sci. 159 (2021) 105722. https://doi.org/10.1016/j.ejps.2021.105722.

[14] H. Na, Y.W. Kang, C.S. Park, S. Jung, H.Y. Kim, J.Y. Sun, Hydrogel-based strong and fast actuators by electroosmotic turgor pressure, Science (80-.). 376 (2022) 301–307. https://doi.org/10.1126/science.abm7862.

[15] N. Leray, M. Talantikite, A. Villares, B. Cathala, Xyloglucan-cellulose nanocrystal-chitosan double network hydrogels for soft actuators, Carbohydr. Polym. 293 (2022) 119753. https://doi.org/10.1016/j.carbpol.2022.119753.

[16] K. Chen, Y. Hu, F. Wang, M. Liu, P. Liu, C. Li, Y. Yu, X. Xiao, Q. Feng, Ultra-stretchable, adhesive, and self-healing MXene/polyampholytes hydrogel as flexible and wearable epidermal sensors, Colloids Surfaces A Physicochem. Eng. Asp. 645 (2022) 128897. https://doi.org/10.1016/j.colsurfa.2022.128897.

[17] C. Li, H. Zhang, M. Liu, F.-F. Lang, J. Pang, X.-H. Bu, Recent progress in metal–organic frameworks (MOFs) for electrocatalysis, Ind. Chem. Mater. 1 (2023) 9–38. https://doi.org/10.1039/d2im00063f.

[18] C. Lei, J. Park, W. Guan, Y. Zhao, K.P. Johnston, G. Yu, Biomimetically Assembled Sponge-Like Hydrogels for Efficient Solar Water Purification, Adv. Funct. Mater. 33 (2023) 2303883. https://doi.org/10.1002/adfm.202303883.

[19] Z. Zhang, Y. Gao, Y. Gao, F. Jia, G. Gao, A self-adhesive, self-healing zwitterionic hydrogel electrolyte for high-voltage zinc-ion hybrid supercapacitors, Chem. Eng. J. 452 (2023) 139014. https://doi.org/10.1016/j.cej.2022.139014.

[20] C.L. Petrou, T.J. D'Ovidio, D.A. Bölükbas, S. Tas, R.D. Brown, A. Allawzi, S. Lindstedt, E. Nozik-Grayck, K.R. Stenmark, D.E. Wagner, C.M. Magin, Clickable decellularized extracellular matrix as a new tool for building hybrid-hydrogels to model chronic fibrotic diseases: In vitro, J. Mater. Chem. B. 8 (2020) 6814–6826. https://doi.org/10.1039/d0tb00613k.

[21] R.H. Dosh, N. Jordan-Mahy, C. Sammon, C.L. Le Maitre, Long-term in vitro 3D hydrogel

co-culture model of inflammatory bowel disease, Sci. Rep. 9 (2019) 1812. https://doi.org/10.1038/s41598-019-38524-8.

[22] S. Kim, J.H. Ahn, D.I. Jeong, M. Yang, J.H. Jeong, Y.E. Choi, H.J. Kim, Y. Han, M. Karmakar, H.J. Ko, H.J. Cho, Alum-tuned hyaluronic acid-based hydrogel with immune checkpoint inhibition for immunophoto therapy of cancer, J. Control. Release. 362 (2023) 1–18. https://doi.org/10.1016/j.jconrel.2023.08.027.

[23] A. Alioghli Ziaei, H. Erfan-Niya, M. Fathi, N. Amiryaghoubi, In situ forming alginate/gelatin hybrid hydrogels containing doxorubicin loaded chitosan/AuNPs nanogels for the local therapy of breast cancer, Int. J. Biol. Macromol. 246 (2023) 125640. https://doi.org/10.1016/j.ijbiomac.2023.125640.

[24] R.M. Wang, J.M. Mesfin, J. Hunter, P. Cattaneo, N. Guimarães-Camboa, R.L. Braden, C. Luo, R.C. Hill, M. Dzieciatkowska, K.C. Hansen, S. Evans, K.L. Christman, Myocardial matrix hydrogel acts as a reactive oxygen species scavenger and supports a proliferative microenvironment for cardiomyocytes, Acta Biomater. 152 (2022) 47–59. https://doi.org/10.1016/j.actbio.2022.08.050.

[25] T. Gong, Z. Zhang, X. Liu, Y. Wang, J. Zhou, S. Wang, X. Liu, H. Jin, Z. Zhao, Microstructurally and mechanically tunable acellular hydrogel scaffold using carboxymethyl cellulose for potential osteochondral tissue engineering, Int. J. Biol. Macromol. 253 (2023) 126658. https://doi.org/10.1016/j.ijbiomac.2023.126658.

[26] H. Zhao, Y. Zhang, C. Zhou, C. Zhang, B. Liu, Engineering pH responsive carboxyethyl chitosan and oxidized pectin -based hydrogels with self-healing, biodegradable and antibacterial properties for wound healing, Int. J. Biol. Macromol. 253 (2023) 127364. https://doi.org/10.1016/j.ijbiomac.2023.127364.

[27] S.Y. Wei, P.Y. Chen, C.C. Hsieh, Y.S. Chen, T.H. Chen, Y.S. Yu, M.C. Tsai, R.H. Xie, G.Y. Chen, G.C. Yin, J.M. Melero-Martin, Y.C. Chen, Engineering large and geometrically controlled vascularized nerve tissue in collagen hydrogels to restore large-sized volumetric muscle loss, Biomaterials. 303 (2023) 122402. https://doi.org/10.1016/j.biomaterials.2023.122402.

[28] C. Kwokdinata, V. Ramanujam, J. Chen, P.N. de Oliveira, M.H. Nai, W.H. Chooi, C.T. Lim, S.Y. Ng, L. David, S.Y. Chew, Encapsulation of Human Spinal Cord Progenitor Cells in Hyaluronan-Gelatin Hydrogel for Spinal Cord Injury Treatment, ACS Appl. Mater. Interfaces. 15 (2023) 50679–50692. https://doi.org/10.1021/acsami.3c07419.

[29] J. Chi, M. Lu, S. Wang, T. Xu, R. Ju, C. Liu, Z. Zhang, Z. Jiang, B. Han, Injectable hydrogels derived from marine polysaccharides as cell carriers for large corneal epithelial defects, Int. J. Biol. Macromol. 253 (2023) 127084. https://doi.org/10.1016/j.ijbiomac.2023.127084.

[30] W. Zhou, Z. Duan, J. Zhao, R. Fu, C. Zhu, D. Fan, Glucose and MMP-9 dual-responsive hydrogel with temperature sensitive self-adaptive shape and controlled drug release

accelerates diabetic wound healing, Bioact. Mater. 17 (2022) 1–17. https://doi.org/10.1016/j.bioactmat.2022.01.004.

[31] J.E. Won, T.I. Wi, C.M. Lee, J.H. Lee, T.H. Kang, J.W. Lee, B.C. Shin, Y.J. Lee, Y.M. Park, H.D. Han, NIR irradiation-controlled drug release utilizing injectable hydrogels containing gold-labeled liposomes for the treatment of melanoma cancer, Acta Biomater. 136 (2021) 508–518. https://doi.org/10.1016/j.actbio.2021.09.062.

[32] S.Y. Lee, S.I. Jeon, S.B. Sim, Y. Byun, C.H. Ahn, A supramolecular host-guest interaction-mediated injectable hydrogel system with enhanced stability and sustained protein release, Acta Biomater. 131 (2021) 286–301. https://doi.org/10.1016/j.actbio.2021.07.004.

[33] P. Lu, D. Ruan, M. Huang, M. Tian, K. Zhu, Z. Gan, Z. Xiao, Harnessing the potential of hydrogels for advanced therapeutic applications: current achievements and future directions, Signal Transduct. Target. Ther. 9 (2024) 1–66. https://doi.org/10.1038/s41392-024-01852-x.

[34] Y.S. Zhang, A. Khademhosseini, Advances in engineering hydrogels, Science. 356 (2017) eaaf3627. https://doi.org/10.1126/science.aaf3627.

[35] A. Chyzy, M.E. Plonska-Brzezinska, Hydrogel Properties and Their Impact on Regenerative Medicine and Tissue Engineering, Molecules. 25 (2020) 5795. https://doi.org/10.3390/molecules25245795.

[36] Y.C. Cho, H.T. Huang, W.C. Lan, M.S. Huang, T. Saito, B.H. Huang, C.H. Tsai, F.Y. Fan, K.L. Ou, The potential of a tailored biomimetic hydrogel for in vitro cell culture applications: Characterization and biocompatibility, Appl. Sci. 10 (2020) 1–13. https://doi.org/10.3390/app10249035.

[37] S. Naahidi, M. Jafari, M. Logan, Y. Wang, Y. Yuan, H. Bae, B. Dixon, P. Chen, Biocompatibility of hydrogel-based scaffolds for tissue engineering applications, Biotechnol. Adv. 35 (2017) 530–544. https://doi.org/10.1016/j.biotechadv.2017.05.006.

[38] M. He, B. Han, Z. Jiang, Y. Yang, Y. Peng, W. Liu, Synthesis of a chitosan-based photo-sensitive hydrogel and its biocompatibility and biodegradability, Carbohydr. Polym. 166 (2017) 228–235. https://doi.org/10.1016/j.carbpol.2017.02.072.

[39] N. Eslahi, A. Simchi, M. Mehrjoo, M.A. Shokrgozar, S. Bonakdar, Hybrid cross-linked hydrogels based on fibrous protein/block copolymers and layered silicate nanoparticles: Tunable thermosensitivity, biodegradability and mechanical durability, RSC Adv. 6 (2016) 62944–62957. https://doi.org/10.1039/c6ra08563f.

[40] D. Tang, R.S. Tare, L.Y. Yang, D.F. Williams, K.L. Ou, R.O.C. Oreffo, Biofabrication of bone tissue: approaches, challenges and translation for bone regeneration, Biomaterials. 83 (2016) 363–382. https://doi.org/10.1016/j.biomaterials.2016.01.024.

[41] T. Jayaramudu, H.U. Ko, H.C. Kim, J.W. Kim, J. Kim, Swelling Behavior of Polyacrylamide–Cellulose Nanocrystal Hydrogels: Swelling Kinetics, Temperature, and pH Effects, Materials. 12 (2019) 2080. https://doi.org/10.3390/ma12132080.

[42] H. Park, X. Guo, J.S. Temenoff, Y. Tabata, A.I. Caplan, F.K. Kasper, A.G. Mikos, Effect of swelling ratio of injectable hydrogel composites on chondrogenic differentiation of encapsulated rabbit marrow mesenchymal stem cells in vitro, Biomacromolecules. 10 (2009) 541–546. https://doi.org/10.1021/bm801197m.

[43] R.M.T. Staruch, G.E. Glass, R. Rickard, S.P. Hettiaratchy, P.E.M. Butler, Injectable Pore-Forming Hydrogel Scaffolds for Complex Wound Tissue Engineering: Designing and Controlling Their Porosity and Mechanical Properties, Tissue Eng. Part B Rev. 23 (2017) 183–198. https://doi.org/10.1089/ten.teb.2016.0305.

[44] N. Annabi, J.W. Nichol, X. Zhong, C. Ji, S. Koshy, A. Khademhosseini, F. Dehghani, Controlling the porosity and microarchitecture of hydrogels for tissue engineering, Tissue Eng. Part B Rev. 16 (2010) 371–383. https://doi.org/10.1089/ten.teb.2009.0639.

[45] T. Shi, D. Niu, J. You, S. Li, G. Li, K. Ren, S. Yan, G. Xu, J. Yin, Injectable macro-porous chitosan/polyethylene glycol-silicotungstic acid double-network hydrogels based on "smashed gels recombination" strategy for cartilage tissue engineering, Int. J. Biol. Macromol. 233 (2023) 123541. https://doi.org/10.1016/j.ijbiomac.2023.123541.

[46] K. Yan, W. Zhang, X. Feng, W. Zhao, L. Wu, Y. Deng, A high heat dissipation strategy based on a multi-scale porous hydrogel and heat sink exhibiting cooling capacity comparable to that of forced air convection but with zero energy consumption, Mater. Adv. 5 (2024) 3051–3057. https://doi.org/10.1039/d3ma00970j.

[47] C.W. Evans, D. Ho, P.K.H. Lee, A.D. Martin, I.L. Chin, Z. Wei, H. Li, R. Atkin, Y.S. Choi, M. Norret, P. Thordarson, K.S. Iyer, A dendronised polymer architecture breaks the conventional inverse relationship between porosity and mechanical properties of hydrogels, Chem. Commun. 57 (2021) 773–776. https://doi.org/10.1039/d0cc07115c.

[48] S.A. Jung, H. Malyaran, D.E. Demco, A. Manukanc, L.S. Häser, V. Kučikas, M. van Zandvoort, S. Neuss, A. Pich, Fibrin-Dextran Hydrogels with Tunable Porosity and Mechanical Properties, Biomacromolecules. 24 (2023) 3972–3984. https://doi.org/10.1021/acs.biomac.3C00269.

[49] Z. Guo, J. Xia, S. Mi, W. Sun, Mussel-Inspired Naturally Derived Double-Network Hydrogels and Their Application in 3D Printing: From Soft, Injectable Bioadhesives to Mechanically Strong Hydrogels, ACS Biomater. Sci. Eng. 6 (2020) 1798–1808. https://doi.org/10.1021/acsbiomaterials.9B01864.

[50] S.A. Bernal-Chávez, S. Alcalá-Alcalá, Y.S. Tapia-Guerrero, J.J. Magaña, M.L. Del Prado-Audelo, G. Leyva-Gómez, Cross-linked polyvinyl alcohol-xanthan gum hydrogel fabricated by freeze/thaw technique for potential application in soft tissue engineering, RSC Adv. 12 (2022) 21713–21724. https://doi.org/10.1039/d2ra02295h.

[51] Z. Zipei, W. Xu, Z. Weifeng, P. Xibo, Potential and advantages of metal organic frameworks-based hydrogel materials for repairing soft and hard tissues, Chinese J. Tissue Eng. Res. 28

(2024) 3583–3590. https://doi.org/10.12307/2024.526.

[52] X. Xue, Y. Hu, S. Wang, X. Chen, Y. Jiang, J. Su, Fabrication of physical and chemical crosslinked hydrogels for bone tissue engineering, Bioact. Mater. 12 (2022) 327–339. https://doi.org/10.1016/j.bioactmat.2021.10.029.

[53] X. Zhang, R. Zhang, S. Wu, Y. Sun, H. Yang, B. Lin, Physically and chemically dual-crosslinked hydrogels with superior mechanical properties and self-healing behavior, New J. Chem. 44 (2020) 9903–9911. https://doi.org/10.1039/donj00348d.

[54] X. Hu, L. Zhang, L. Yan, L. Tang, Recent Advances in Polysaccharide-Based Physical Hydrogels and Their Potential Applications for Biomedical and Wastewater Treatment, Macromol. Biosci. 22 (2022) 2200153. https://doi.org/10.1002/mabi.202200153.

[55] F. Liao, Z. Tian, X. Yang, H. Yang, X. Liu, H. Liao, L. Duan, Hydrophobic association: A facile approach to prepare physical cross-linked gelatin hydrogel with desirable thermal stability, flexibility and self-healing ability, Int. J. Biol. Macromol. 262 (2024) 130058. https://doi.org/10.1016/j.ijbiomac.2024.130058.

[56] M.L. Pita-López, G. Fletes-Vargas, H. Espinosa-Andrews, R. Rodríguez-Rodríguez, Physically cross-linked chitosan-based hydrogels for tissue engineering applications: A state-of-the-art review, Eur. Polym. J. 145 (2021) 110176. https://doi.org/10.1016/j.eurpolymj.2020.110176.

[57] Z. Qian, N. Zhao, S. Xu, W. Yuan, In situ injectable thermoresponsive nanocomposite hydrogel based on hydroxypropyl chitosan for precise synergistic calcium-overload, photodynamic and photothermal tumor therapy, Carbohydr. Polym. 324 (2024) 121487. https://doi.org/10.1016/j.carbpol.2023.121487.

[58] D. Nath, J. Ralhan, J.P. Joseph, C. Miglani, A. Pal, Thermoresponsive Injectable Hydrogel To Mimic the Heat- and Strain-Stiffening Behavior of Biopolymers toward Muscle Cell Proliferation, Biomacromolecules. 25 (2024) 853–863. https://doi.org/10.1021/acs.biomac.3c01018.

[59] B. Yin, M. Gosecka, M. Bodaghi, D. Crespy, G. Youssef, J.M. Dodda, S.H.D. Wong, A. Bin Imran, M. Gosecki, A. Jobdeedamrong, M. Afzali Naniz, A. Zolfagharian, Engineering multifunctional dynamic hydrogel for biomedical and tissue regenerative applications, Chem. Eng. J. 487 (2024) 150403. https://doi.org/10.1016/j.cej.2024.150403.

[60] P. Nezhad-Mokhtari, M. Ghorbani, L. Roshangar, J. Soleimani Rad, A review on the construction of hydrogel scaffolds by various chemically techniques for tissue engineering, Eur. Polym. J. 117 (2019) 64–76. https://doi.org/10.1016/j.eurpolymj.2019.05.004.

[61] W. He, K. Chen, W. Gao, R. Duan, Z. Li, B. Li, J. Xia, Y. Zhao, W. Liu, H. Zhou, X. Xiao, Q. Feng, Y. Yang, A sequential physical and chemical dual crosslinked multifunctional hydrogel with enhanced mechanical and osteogenic effects for vascularized bone tissue regeneration, Mater. Des. 237 (2024) 112563. https://doi.org/10.1016/j.matdes.2023.112563.

[62] D. Zhao, J. Huang, Y. Zhong, K. Li, L. Zhang, J. Cai, High-Strength and High-Toughness Double-Cross-Linked Cellulose Hydrogels: A New Strategy Using Sequential Chemical and Physical Cross-Linking, Adv. Funct. Mater. 26 (2016) 6279–6287. https://doi.org/10.1002/adfm.201601645.

[63] L. Rebers, R. Reichsöllner, S. Regett, G.E.M. Tovar, K. Borchers, S. Baudis, A. Southan, Differentiation of physical and chemical cross-linking in gelatin methacryloyl hydrogels, Sci. Rep. 11 (2021) 3256. https://doi.org/10.1038/s41598-021-82393-z.

[64] A.N. Tahneh, B. Dashtipour, A. Ghofrani, S.K. Nejad, Crosslinked natural hydrogels for drug delivery systems, J. Compos. Compd. 4 (2022) 109–123. https://doi.org/10.52547/jcc.4.2.6.

[65] H.M. El-Husseiny, E.A. Mady, L. Hamabe, A. Abugomaa, K. Shimada, T. Yoshida, T. Tanaka, A. Yokoi, M. Elbadawy, R. Tanaka, Smart/stimuli-responsive hydrogels: Cutting-edge platforms for tissue engineering and other biomedical applications, Mater. Today Bio. 13 (2022) 100186. https://doi.org/10.1016/j.mtbio.2021.100186.

[66] L. Liu, H. Liu, R. Wang, J. Zhou, L. Zhao, Q. Li, Z. Liu, Preparation and application of environmentally-responsive hydrogels in tissue engineering, Mater. Today Commun. 40 (2024) 109493. https://doi.org/10.1016/j.mtcomm.2024.109493.

[67] M. Inoue, T. Hayashi, S. Hikiri, M. Ikeguchi, M. Kinoshita, Mechanism of globule-to-coil transition of poly(N-isopropylacrylamide) in water: Relevance to cold denaturation of a protein, J. Mol. Liq. 292 (2019) 111374. https://doi.org/10.1016/j.molliq.2019.111374.

[68] M.J. Ansari, R.R. Rajendran, S. Mohanto, U. Agarwal, K. Panda, K. Dhotre, R. Manne, A. Deepak, A. Zafar, M. Yasir, S. Pramanik, Poly(N-isopropylacrylamide)-Based Hydrogels for Biomedical Applications: A Review of the State-of-the-Art, Gels. 8 (2022) 454. https://doi.org/10.3390/gels8070454.

[69] S. Kotova, S. Kostjuk, Y. Rochev, Y. Efremov, A. Frolova, P. Timashev, Phase transition and potential biomedical applications of thermoresponsive compositions based on polysaccharides, proteins and DNA: A review, Int. J. Biol. Macromol. 249 (2023) 126054. https://doi.org/10.1016/j.ijbiomac.2023.126054.

[70] J.A. Hunt, R. Chen, T. Van Veen, N. Bryan, Hydrogels for tissue engineering and regenerative medicine, J. Mater. Chem. B. 2 (2014) 5319–5338. https://doi.org/10.1039/c4tb00775a.

[71] S. Ohya, S. Kidoaki, T. Matsuda, Poly(N-isopropylacrylamide) (PNIPAM)-grafted gelatin hydrogel surfaces: Interrelationship between microscopic structure and mechanical property of surface regions and cell adhesiveness, Biomaterials. 26 (2005) 3105–3111. https://doi.org/10.1016/j.biomaterials.2004.08.006.

[72] O.A. Yeshchenko, N. V. Kutsevol, A. V. Tomchuk, P.S. Khort, Y.I. Kuziv, P. Hudhomme, O.M. Krupka, Dextran-graft-PNIPAM / Au nanoparticles / perylenediimide hybrid system as thermosensitive optical switches and fluorescent labels for potential use in nanophotonics and biomedical applications, Opt. Mater. (Amst). 131 (2022) 112753.

https://doi.org/10.1016/j.optmat.2022.112753.

[73] M.R. Dethe, P. A, H. Ahmed, M. Agrawal, U. Roy, A. Alexander, PCL-PEG copolymer based injectable thermosensitive hydrogels, J. Control. Release. 343 (2022) 217–236. https://doi.org/10.1016/j.jconrel.2022.01.035.

[74] T.T. Hoang Thi, L.H. Sinh, D.P. Huynh, D.H. Nguyen, C. Huynh, Self-Assemblable Polymer Smart-Blocks for Temperature-Induced Injectable Hydrogel in Biomedical Applications, Front. Chem. 8 (2020) 508305. https://doi.org/10.3389/fchem.2020.00019.

[75] J. Zhou, H. Wang, H. Chen, Y. Ling, Z. Xi, M. Lv, J. Chen, pH-responsive nanocomposite hydrogel for simultaneous prevention of postoperative adhesion and tumor recurrence, Acta Biomater. 158 (2023) 228–238. https://doi.org/10.1016/j.actbio.2022.12.025.

[76] Y. Liang, X. Zhao, P.X. Ma, B. Guo, Y. Du, X. Han, pH-responsive injectable hydrogels with mucosal adhesiveness based on chitosan-grafted-dihydrocaffeic acid and oxidized pullulan for localized drug delivery, J. Colloid Interface Sci. 536 (2019) 224–234. https://doi.org/10.1016/j.jcis.2018.10.056.

[77] C. Zhao, N.T. Qazvini, M. Sadati, Z. Zeng, S. Huang, A.L. De La Lastra, L. Zhang, Y. Feng, W. Liu, B. Huang, B. Zhang, Z. Dai, Y. Shen, X. Wang, W. Luo, B. Liu, Y. Lei, Z. Ye, L. Zhao, D. Cao, L. Yang, X. Chen, A. Athiviraham, M.J. Lee, J.M. Wolf, R.R. Reid, M. Tirrell, W. Huang, J.J. De Pablo, T.C. He, A pH-Triggered, Self-Assembled, and Bioprintable Hybrid Hydrogel Scaffold for Mesenchymal Stem Cell Based Bone Tissue Engineering, ACS Appl. Mater. Interfaces. 11 (2019) 8749–8762. https://doi.org/10.1021/acsami.8b19094.

[78] R. Luo, X. Xiang, Q. Jiao, H. Hua, Y. Chen, Photoresponsive Hydrogels for Tissue Engineering, ACS Biomater. Sci. Eng. 10 (2024) 3612–3630. https://doi.org/10.1021/acsbiomaterials.4c00314.

[79] P. Weis, S. Wu, Light-Switchable Azobenzene-Containing Macromolecules: From UV to Near Infrared, Macromol. Rapid Commun. 39 (2018) 1700220. https://doi.org/10.1002/marc.201700220.

[80] T.L. Rapp, C.A. DeForest, Visible Light-Responsive Dynamic Biomaterials: Going Deeper and Triggering More, Adv. Healthc. Mater. 9 (2020) 1901553. https://doi.org/10.1002/adhm.201901553.

[81] Q. Zhang, H.P. Bei, M. Zhao, Z. Dong, X. Zhao, Shedding light on 3D printing: Printing photo-crosslinkable constructs for tissue engineering, Biomaterials. 286 (2022) 121566. https://doi.org/10.1016/j.biomaterials.2022.121566.

[82] D.M. Catori, L.C.E. da Silva, M.F. de Oliveira, G.H. Nguyen, J.C. Moses, E.J. Brisbois, H. Handa, M.G. de Oliveira, In Situ Photo-crosslinkable Hyaluronic Acid/Gelatin Hydrogel for Local Nitric Oxide Delivery, ACS Appl. Mater. Interfaces. 15 (2023) 48930–48944. https://doi.org/10.1021/acsami.3c10030.

[83] H. Ding, B. Li, Y. Jiang, G. Liu, S. Pu, Y. Feng, D. Jia, Y. Zhou, pH-responsive UV

crosslinkable chitosan hydrogel via “thiol-ene” click chemistry for active modulating opposite drug release behaviors, Carbohydr. Polym. 251 (2021) 117101. https://doi.org/10.1016/j.carbpol.2020.117101.

[84] P. Hou, N. Zhang, R. Wu, W. Xu, Z. Hou, Photo-cross-linked biodegradable hydrogels based on n-arm-poly(ethylene glycol), poly(ε-caprolactone) and/or methacrylic acid for controlled drug release, J. Biomater. Appl. 32 (2017) 511–523. https://doi.org/10.1177/0885328217730465.

[85] I. Mironi-Harpaz, D.Y. Wang, S. Venkatraman, D. Seliktar, Photopolymerization of cell-encapsulating hydrogels: Crosslinking efficiency versus cytotoxicity, Acta Biomater. 8 (2012) 1838–1848. https://doi.org/10.1016/j.actbio.2011.12.034.

[86] X. Zhao, Q. Lang, L. Yildirimer, Z.Y. Lin, W. Cui, N. Annabi, K.W. Ng, M.R. Dokmeci, A.M. Ghaemmaghami, A. Khademhosseini, Photocrosslinkable Gelatin Hydrogel for Epidermal Tissue Engineering, Adv. Healthc. Mater. 5 (2016) 108–118. https://doi.org/10.1002/adhm.201500005.

[87] A. Darzi, Y. Munz, The impact of minimally invasive surgical techniques, Annu. Rev. Med. 55 (2004) 223–237. https://doi.org/10.1146/annurev.med.55.091902.105248.

[88] A. Washio, H. Teshima, K. Yokota, C. Kitamura, Y. Tabata, Preparation of gelatin hydrogel sponges incorporating bioactive glasses capable for the controlled release of fibroblast growth factor-2, J. Biomater. Sci. Polym. Ed. 30 (2019) 49–63. https://doi.org/10.1080/09205063.2018.1544474.

[89] B. Akin, B. Akgul, S. Tasdurmazli, E.S. Abamor, T. Ozbek, B. Ozcelik, E. Su, M.M. Ozmen, Tannic Acid Incorporated Antibacterial Polyethylene Glycol Based Hydrogel Sponges for Management of Wound Infections, Macromol. Biosci. 24 (2024) 2400101. https://doi.org/10.1002/mabi.202400101.

[90] Y. Sun, D. Nan, H. Jin, X. Qu, Recent advances of injectable hydrogels for drug delivery and tissue engineering applications, Polym. Test. 81 (2020) 106283. https://doi.org/10.1016/j.polymertesting.2019.106283.

[91] J.H. Lee, Injectable hydrogels delivering therapeutic agents for disease treatment and tissue engineering, Biomater. Res. 22 (2018) 1–14. https://doi.org/10.1186/s40824-018-0138-6.

[92] P. Bertsch, M. Diba, D.J. Mooney, S.C.G. Leeuwenburgh, Self-Healing Injectable Hydrogels for Tissue Regeneration, Chem. Rev. 123 (2023) 834–873. https://doi.org/10.1021/acs.chemrev.2c00179.

[93] X. Liu, Y. Zhang, Z. Hussain, P. Zheng, M. Xu, H. Zhao, Y. Liu, Y. Cao, I. Ullah, A. Osaka, R. Pei, Self-biomineralized in situ injectable CaSO4 nanorods-enriched collagen-hyaluronic acid composite hydrogels for biomimetic bone reconstruction in a minimally invasive manner, Appl. Mater. Today. 30 (2023) 101693. https://doi.org/10.1016/J.APMT.2022.101693.

[94] B. Vigani, S. Rossi, G. Sandri, M.C. Bonferoni, C.M. Caramella, F. Ferrari, Recent Advances in the Development of In Situ Gelling Drug Delivery Systems for Non-Parenteral Administration Routes, Pharmaceutics. 12 (2020) 859. https://doi.org/10.3390/pharmaceutics12090859.

[95] P.L. Destruel, N. Zeng, J. Seguin, S. Douat, F. Rosa, F. Brignole-Baudouin, S. Dufaÿ, A. Dufaÿ-Wojcicki, M. Maury, N. Mignet, V. Boudy, Novel in situ gelling ophthalmic drug delivery system based on gellan gum and hydroxyethylcellulose: Innovative rheological characterization, in vitro and in vivo evidence of a sustained precorneal retention time, Int. J. Pharm. 574 (2020) 118734. https://doi.org/10.1016/j.ijpharm.2019.118734.

[96] Z. Cai, H. Zhang, Y. Wei, M. Wu, A. Fu, Shear-thinning hyaluronan-based fluid hydrogels to modulate viscoelastic properties of osteoarthritis synovial fluids, Biomater. Sci. 7 (2019) 3143–3157. https://doi.org/10.1039/c9bm00298g.

[97] A.K. Podder, M.A. Mohamed, R.A. Seidman, G. Tseropoulos, J.J. Polanco, P. Lei, F.J. Sim, S.T. Andreadis, Injectable shear-thinning hydrogels promote oligodendrocyte progenitor cell survival and remyelination in the central nervous system, Sci. Adv. 10 (2024) adk9918. https://doi.org/10.1126/sciadv.adk9918.

[98] L. Zhang, T. Li, Y. Yu, K. Shi, Z. Bei, Y. Qian, Z. Qian, An injectable conductive hydrogel restores electrical transmission at myocardial infarct site to preserve cardiac function and enhance repair, Bioact. Mater. 20 (2023) 339–354. https://doi.org/10.1016/j.bioactmat.2022.06.001.

[99] S.S. Gharaie, S.M.H. Dabiri, M. Akbari, Smart shear-thinning hydrogels as injectable drug delivery systems, Polymers (Basel). 10 (2018) 1317. https://doi.org/10.3390/polym10121317.

[100] A. Daneshvar, M. Farokhi, S. Bonakdar, M. Vossoughi, Synthesis and characterization of injectable thermosensitive hydrogel based on Pluronic-grafted silk fibroin copolymer containing hydroxyapatite nanoparticles as potential for bone tissue engineering, Int. J. Biol. Macromol. 277 (2024) 134412. https://doi.org/10.1016/j.ijbiomac.2024.134412.

[101] H.S. Kim, C.J. Li, S.M. Park, K.W. Kim, J.H. Mo, G.Z. Jin, H.H. Lee, H.W. Kim, U.S. Shin, J.H. Lee, Development of an Injectable Biphasic Hyaluronic Acid-Based Hydrogel With Stress Relaxation Properties for Cartilage Regeneration, Adv. Healthc. Mater. 13 (2024) 2400043. https://doi.org/10.1002/adhm.202400043.

[102] S. Khattak, I. Ullah, H. Xie, X.D. Tao, H.T. Xu, J. Shen, Self-healing hydrogels as injectable implants: Advances in translational wound healing, Coord. Chem. Rev. 509 (2024) 215790. https://doi.org/10.1016/j.ccr.2024.215790.

[103] C. Loebel, C.B. Rodell, M.H. Chen, J.A. Burdick, Shear-thinning and self-healing hydrogels as injectable therapeutics and for 3D-printing, Nat. Protoc. 2017 128. 12 (2017) 1521–1541. https://doi.org/10.1038/nprot.2017.053.

[104] J. Manasi Esther, R. Solanki, M. Dhanka, P. Thareja, D. Bhatia, Self-healing, injectable chitosan-based hydrogels: structure, properties and biological applications, Mater. Adv. 5 (2024) 5365–5393. https://doi.org/10.1039/d4ma00131a.

[105] G.G.G. Perera, D.F. Argenta, T. Caon, The rheology of injectable hyaluronic acid hydrogels used as facial fillers: A review, Int. J. Biol. Macromol. 268 (2024) 131880. https://doi.org/10.1016/j.ijbiomac.2024.131880.

[106] M.H. Chen, L.L. Wang, J.J. Chung, Y.H. Kim, P. Atluri, J.A. Burdick, Methods to Assess Shear-Thinning Hydrogels for Application As Injectable Biomaterials, ACS Biomater. Sci. Eng. 3 (2017) 3146–3160. https://doi.org/10.1021/acsbiomaterials.7b00734.

[107] M. Guvendiren, H.D. Lu, J.A. Burdick, Shear-thinning hydrogels for biomedical applications, Soft Matter. 8 (2011) 260–272. https://doi.org/10.1039/c1sm06513k.

[108] M.J. Webber, M.W. Tibbitt, Dynamic and reconfigurable materials from reversible network interactions, Nat. Rev. Mater. 7 (2022) 541–556. https://doi.org/10.1038/s41578-021-00412-x.

[109] H. Wang, S.C. Heilshorn, Adaptable Hydrogel Networks with Reversible Linkages for Tissue Engineering, Adv. Mater. 27 (2015) 3717–3736. https://doi.org/10.1002/adma.201501558.

[110] J. Zhang, L. Chen, B. Shen, Y. Wang, P. Peng, F. Tang, J. Feng, Highly transparent, self-healing, injectable and self-adhesive chitosan/polyzwitterion-based double network hydrogel for potential 3D printing wearable strain sensor, Mater. Sci. Eng. C. 117 (2020) 111298. https://doi.org/10.1016/j.msec.2020.111298.

[111] C. Fiorica, G. Pitarresi, F.S. Palumbo, N. Mauro, S. Federico, G. Giammona, Production and physicochemical characterization of a new amine derivative of gellan gum and rheological study of derived hydrogels, Carbohydr. Polym. 236 (2020) 116033. https://doi.org/10.1016/j.carbpol.2020.116033.

[112] Y. Pang, H. Wang, Y. Yao, D. Chen, R. Yang, Z. Wang, J. Yang, Y. Li, W. Liu, An Injectable Self-Crosslinked Wholly Supramolecular Polyzwitterionic Hydrogel for Regulating Microenvironment to Boost Infected Diabetic Wound Healing, Adv. Funct. Mater. 33 (2023) 2303095. https://doi.org/10.1002/adfm.202303095.

[113] T.L. Sun, T. Kurokawa, S. Kuroda, A. Bin Ihsan, T. Akasaki, K. Sato, M.A. Haque, T. Nakajima, J.P. Gong, Physical hydrogels composed of polyampholytes demonstrate high toughness and viscoelasticity, Nat. Mater. 12 (2013) 932–937. https://doi.org/10.1038/nmat3713.

[114] X. Fan, T. Wang, W. Miao, The preparation of pH-sensitive hydrogel based on host-guest and electrostatic interactions and its drug release studies in vitro, J. Polym. Res. 25 (2018) 215. https://doi.org/10.1007/s10965-018-1608-1.

[115] D.C. Tuncaboylu, A. Argun, M. Sahin, M. Sari, O. Okay, Structure optimization of self-healing hydrogels formed via hydrophobic interactions, Polymer. 53 (2012) 5513–5522.

https://doi.org/10.1016/j.polymer.2012.10.015.

[116] Y. Sugioka, J. Nakamura, C. Ohtsuki, A. Sugawara-narutaki, Thixotropic Hydrogels Composed of Self-Assembled Nanofibers of Double-Hydrophobic Elastin-Like Block Polypeptides, Int. J. Mol. Sci. 22 (2021) 4104. https://doi.org/10.3390/ijms22084104.

[117] C.B. Rodell, A.L. Kaminski, J.A. Burdick, Rational design of network properties in guest-host assembled and shear-thinning hyaluronic acid hydrogels, Biomacromolecules. 14 (2013) 4125–4134. https://doi.org/10.1021/bm401280z.

[118] G. Chen, M. Jiang, Cyclodextrin-based inclusion complexation bridging supramolecular chemistry and macromolecular self-assembly, Chem. Soc. Rev. 40 (2011) 2254–2266. https://doi.org/10.1039/c0cs00153h.

[119] L. Voorhaar, B. De Meyer, F. Du Prez, R. Hoogenboom, One-Pot Automated Synthesis of Quasi Triblock Copolymers for Self-Healing Physically Crosslinked Hydrogels, Macromol. Rapid Commun. 37 (2016) 1682–1688. https://doi.org/10.1002/marc.201600380.

[120] Y. Liang, X. Zhao, T. Hu, B. Chen, Z. Yin, P.X. Ma, B. Guo, Adhesive Hemostatic Conducting Injectable Composite Hydrogels with Sustained Drug Release and Photothermal Antibacterial Activity to Promote Full-Thickness Skin Regeneration During Wound Healing, Small. 15 (2019) 1900046. https://doi.org/10.1002/smll.201900046.

[121] Y. Liu, S.H. Hsu, Synthesis and biomedical applications of self-healing hydrogels, Front. Chem. 6 (2018) 449. https://doi.org/10.3389/fchem.2018.00449.

[122] L. Tomasello, C. Fiorica, R. Mauceri, A. Martorana, F.S. Palumbo, G. Pitarresi, G. Pizzolanti, G. Campisi, C. Giordano, G. Cavallaro, Bioactive Scaffolds Based on Amine-Functionalized Gellan Gum for the Osteogenic Differentiation of Gingival Mesenchymal Stem Cells, ACS Appl. Polym. Mater. 4 (2022) 1805–1815. https://doi.org/10.1021/acsapm.1c01586.

[123] P. Ghaderinejad, N. Najmoddin, Z. Bagher, M. Saeed, S. Karimi, S. Simorgh, M. Pezeshki-Modaress, An injectable anisotropic alginate hydrogel containing oriented fibers for nerve tissue engineering, Chem. Eng. J. 420 (2021) 130465. https://doi.org/10.1016/j.cej.2021.130465.

[124] M.J. Harrington, A. Masic, N. Holten-Andersen, J.H. Waite, P. Fratzl, Iron-clad fibers: A metal-based biological strategy for hard flexible coatings, Science (80-.). 328 (2010) 216–220. https://doi.org/10.1126/science.1181044.

[125] R.J. Sundberg, Interactions of histidine and other imidazole derivatives with transition metal ions in chemical and biological systems, Chem. Rev. 74 (1974) 471–517. https://doi.org/10.1021/cr60290a003.

[126] L. Shi, P. Ding, Y. Wang, Y. Zhang, D. Ossipov, J. Hilborn, Self-Healing Polymeric Hydrogel Formed by Metal–Ligand Coordination Assembly: Design, Fabrication, and Biomedical Applications, Macromol. Rapid Commun. 40 (2019) 1800837. https://doi.org/10.1002/marc.201800837.

[127] C. Mo, L. Xiang, Y. Chen, Advances in Injectable and Self-healing Polysaccharide Hydrogel Based on the Schiff Base Reaction, Macromol. Rapid Commun. 42 (2021) 2100025. https://doi.org/10.1002/marc.202100025.

[128] S. Lü, X. Bai, H. Liu, P. Ning, Z. Wang, C. Gao, B. Ni, M. Liu, An injectable and self-healing hydrogel with covalent cross-linking in vivo for cranial bone repair, J. Mater. Chem. B. 5 (2017) 3739–3748. https://doi.org/10.1039/c7tb00776k.

[129] F.A. Ngwabebhoh, O. Zandraa, R. Patwa, N. Saha, Z. Capáková, P. Saha, Self-crosslinked chitosan/dialdehyde xanthan gum blended hypromellose hydrogel for the controlled delivery of ampicillin, minocycline and rifampicin, Int. J. Biol. Macromol. 167 (2021) 1468–1478. https://doi.org/10.1016/j.ijbiomac.2020.11.100.

[130] J. Guo, L. Ge, X. Li, C. Mu, D. Li, Periodate oxidation of xanthan gum and its crosslinking effects on gelatin-based edible films, Food Hydrocoll. 39 (2014) 243–250. https://doi.org/10.1016/j.foodhyd.2014.01.026.

[131] S. Das, G. Dalei, In situ forming dialdehyde xanthan gum-gelatin Schiff-base hydrogels as potent controlled release fertilizers, Sci. Total Environ. 875 (2023) 162660. https://doi.org/10.1016/j.scitotenv.2023.162660.

[132] Y.C. Chen, W.Y. Su, S.H. Yang, A. Gefen, F.H. Lin, In situ forming hydrogels composed of oxidized high molecular weight hyaluronic acid and gelatin for nucleus pulposus regeneration, Acta Biomater. 9 (2013) 5181–5193. https://doi.org/10.1016/j.actbio.2012.09.039.

[133] B. Guo, J. Qu, X. Zhao, M. Zhang, Degradable conductive self-healing hydrogels based on dextran-graft-tetraaniline and N-carboxyethyl chitosan as injectable carriers for myoblast cell therapy and muscle regeneration, Acta Biomater. 84 (2019) 180–193. https://doi.org/10.1016/j.actbio.2018.12.008.

[134] G. Xiao, Y. Wang, H. Zhang, L. Chen, S. Fu, Facile strategy to construct a self-healing and biocompatible cellulose nanocomposite hydrogel via reversible acylhydrazone, Carbohydr. Polym. 218 (2019) 68–77. https://doi.org/10.1016/j.carbpol.2019.04.080.

[135] C.M. Nimmo, S.C. Owen, M.S. Shoichet, Diels-alder click cross-linked hyaluronic acid hydrogels for tissue engineering, Biomacromolecules. 12 (2011) 824–830. https://doi.org/10.1021/bm101446k.

[136] S.L. Banerjee, N.K. Singha, A new class of dual responsive self-healable hydrogels based on a core crosslinked ionic block copolymer micelle prepared via RAFT polymerization and Diels–Alder “click” chemistry, Soft Matter. 13 (2017) 9024–9035. https://doi.org/10.1039/c7sm01906h.

[137] C. Shao, M. Wang, H. Chang, F. Xu, J. Yang, A Self-Healing Cellulose Nanocrystal-Poly(ethylene glycol) Nanocomposite Hydrogel via Diels-Alder Click Reaction, ACS Sustain. Chem. Eng. 5 (2017) 6167–6174. https://doi.org/10.1021/acssuschemeng.7b01060.

[138] Z. Wei, J.H. Yang, X.J. Du, F. Xu, M. Zrinyi, Y. Osada, F. Li, Y.M. Chen, Dextran-Based Self-Healing Hydrogels Formed by Reversible Diels–Alder Reaction under Physiological Conditions, Macromol. Rapid Commun. 34 (2013) 1464–1470. https://doi.org/10.1002/marc.201300494.

[139] J.M. Jung, S.H. Kim, V.H. Giang Phan, T. Thambi, D.S. Lee, Therapeutic effects of boronate ester cross-linked injectable hydrogels for the treatment of hepatocellular carcinoma, Biomater. Sci. 9 (2021) 7275–7286. https://doi.org/10.1039/d1bm00881a.

[140] B. Liu, J. Li, Z. Zhang, J.D. Roland, B.P. Lee, pH responsive antibacterial hydrogel utilizing catechol–boronate complexation chemistry, Chem. Eng. J. 441 (2022) 135808. https://doi.org/10.1016/j.cej.2022.135808.

[141] W. Shi, B. Hass, M.A. Kuss, H. Zhang, S. Ryu, D. Zhang, T. Li, Y. long Li, B. Duan, Fabrication of versatile dynamic hyaluronic acid-based hydrogels, Carbohydr. Polym. 233 (2020) 115803. https://doi.org/10.1016/j.carbpol.2019.115803.

[142] R. Yang, X. Liu, Y. Ren, W. Xue, S. Liu, P. Wang, M. Zhao, H. Xu, B. Chi, Injectable adaptive self-healing hyaluronic acid/poly (γ-glutamic acid) hydrogel for cutaneous wound healing, Acta Biomater. 127 (2021) 102–115. https://doi.org/10.1016/j.actbio.2021.03.057.

[143] H. Yu, Y. Wang, H. Yang, K. Peng, X. Zhang, Injectable self-healing hydrogels formed via thiol/disulfide exchange of thiol functionalized F127 and dithiolane modified PEG, J. Mater. Chem. B. 5 (2017) 4121–4127. https://doi.org/10.1039/c7tb00746a.

[144] P. Nagy, Kinetics and Mechanisms of Thiol–Disulfide Exchange Covering Direct Substitution and Thiol Oxidation-Mediated Pathways, Https://Home.Liebertpub.Com/Ars. 18 (2013) 1623–1641. https://doi.org/10.1089/ars.2012.4973.

[145] X. Zhang, S. Jiang, T. Yan, X. Fan, F. Li, X. Yang, B. Ren, J. Xu, J. Liu, Injectable and fast self-healing protein hydrogels, Soft Matter. 15 (2019) 7583–7589. https://doi.org/10.1039/c9sm01543d.

[146] S. Zhu, J. Wang, H. Yan, Y. Wang, Y. Zhao, B. Feng, K. Duan, J. Weng, An injectable supramolecular self-healing bio-hydrogel with high stretchability, extensibility and ductility, and a high swelling ratio, J. Mater. Chem. B. 5 (2017) 7021–7034. https://doi.org/10.1039/c7tb01183k.

[147] C.B. Rodell, N.N. Dusaj, C.B. Highley, J.A. Burdick, Injectable and Cytocompatible Tough Double-Network Hydrogels through Tandem Supramolecular and Covalent Crosslinking, Adv. Mater. 28 (2016) 8419–8424. https://doi.org/10.1002/adma.201602268.

[148] L. Meng, C. Shao, C. Cui, F. Xu, J. Lei, J. Yang, Autonomous Self-Healing Silk Fibroin Injectable Hydrogels Formed via Surfactant-Free Hydrophobic Association, ACS Appl. Mater. Interfaces. 12 (2020) 1628–1639. https://doi.org/10.1021/acsami.9b19415.

[149] H. Guo, S. Huang, X. Yang, J. Wu, T.B. Kirk, J. Xu, A. Xu, W. Xue, Injectable and Self-Healing Hydrogels with Double-Dynamic Bond Tunable Mechanical, Gel-Sol Transition and

Drug Delivery Properties for Promoting Periodontium Regeneration in Periodontitis, ACS Appl. Mater. Interfaces. 13 (2021) 61638–61652. https://doi.org/10.1021/acsami.1c18701.

[150] Y. Liang, Z. Li, Y. Huang, R. Yu, B. Guo, Dual-Dynamic-Bond Cross-Linked Antibacterial Adhesive Hydrogel Sealants with On-Demand Removability for Post-Wound-Closure and Infected Wound Healing, ACS Nano. 15 (2021) 7078–7093. https://doi.org/10.1021/acsnano.1c00204.

[151] L. Wang, F. Deng, W. Wang, A. Li, C. Lu, H. Chen, G. Wu, K. Nan, L. Li, Construction of Injectable Self-Healing Macroporous Hydrogels via a Template-Free Method for Tissue Engineering and Drug Delivery, ACS Appl. Mater. Interfaces. 10 (2018) 36721–36732. https://doi.org/10.1021/acsami.8b13077.

[152] H. Wang, D. Zhu, A. Paul, L. Cai, A. Enejder, F. Yang, S.C. Heilshorn, Covalently Adaptable Elastin-Like Protein–Hyaluronic Acid (ELP–HA) Hybrid Hydrogels with Secondary Thermoresponsive Crosslinking for Injectable Stem Cell Delivery, Adv. Funct. Mater. 27 (2017) 1605609. https://doi.org/10.1002/adfm.201605609.

[153] X. Ding, Y. Wang, J. Liu, P. Zhang, G. Li, T. Sun, C. Xiao, Injectable in Situ Forming Double-Network Hydrogel to Enhance Transplanted Cell Viability and Retention, Chem. Mater. 33 (2021) 5885–5895. https://doi.org/10.1021/acs.chemmater.1c00635.

[154] X. Zhao, Y. Liang, Y. Huang, J. He, Y. Han, B. Guo, Physical Double-Network Hydrogel Adhesives with Rapid Shape Adaptability, Fast Self-Healing, Antioxidant and NIR/pH Stimulus-Responsiveness for Multidrug-Resistant Bacterial Infection and Removable Wound Dressing, Adv. Funct. Mater. 30 (2020) 1910748. https://doi.org/10.1002/adfm.201910748.

[155] Y. Yin, Q. Gu, X. Liu, F. Liu, D.J. McClements, Double network hydrogels: Design, fabrication, and application in biomedicines and foods, Adv. Colloid Interface Sci. 320 (2023) 102999. https://doi.org/10.1016/j.cis.2023.102999.

[156] A.A. Aldana, F.L.C. Morgan, S. Houben, L.M. Pitet, L. Moroni, M.B. Baker, Biomimetic double network hydrogels: Combining dynamic and static crosslinks to enable biofabrication and control cell-matrix interactions, J. Polym. Sci. 59 (2021) 2832–2843. https://doi.org/10.1002/POL.20210554.

[157] F.L.C. Morgan, L. Moroni, M.B. Baker, Dynamic Bioinks to Advance Bioprinting, Adv. Healthc. Mater. 9 (2020) 1901798. https://doi.org/10.1002/adhm.201901798.

[158] Z. Gu, K. Huang, Y. Luo, L. Zhang, T. Kuang, Z. Chen, G. Liao, Double network hydrogel for tissue engineering, Wiley Interdiscip. Rev. Nanomedicine Nanobiotechnology. 10 (2018) e1520. https://doi.org/10.1002/wnan.1520.

[159] A.A. Aldana, S. Houben, L. Moroni, M.B. Baker, L.M. Pitet, Trends in Double Networks as Bioprintable and Injectable Hydrogel Scaffolds for Tissue Regeneration, ACS Biomater. Sci. Eng. 7 (2021) 4077–4101. https://doi.org/doi.org/10.1021/acsbiomaterials.0c01749.

[160] S. Vanaei, M.S. Parizi, S. Vanaei, F. Salemizadehparizi, H.R. Vanaei, An Overview on

Materials and Techniques in 3D Bioprinting Toward Biomedical Application, Eng. Regen. 2 (2021) 1–18. https://doi.org/10.1016/j.engreg.2020.12.001.

[161] M. Deptuła, M. Zawrzykraj, J. Sawicka, A. Banach-Kopeć, R. Tylingo, M. Pikuła, Application of 3D- printed hydrogels in wound healing and regenerative medicine, Biomed. Pharmacother. 167 (2023) 115416. https://doi.org/10.1016/j.biopha.2023.115416.

[162] Q. Yu, Q. Wang, L. Zhang, W. Deng, X. Cao, Z. Wang, X. Sun, J. Yu, X. Xu, The applications of 3D printing in wound healing: The external delivery of stem cells and antibiosis, Adv. Drug Deliv. Rev. 197 (2023) 114823. https://doi.org/10.1016/j.addr.2023.114823.

[163] J. Wang, Y. Zhang, N.H. Aghda, A.R. Pillai, R. Thakkar, A. Nokhodchi, M. Maniruzzaman, Emerging 3D printing technologies for drug delivery devices: Current status and future perspective, Adv. Drug Deliv. Rev. 174 (2021) 294–316. https://doi.org/10.1016/j.addr.2021.04.019.

[164] Z. Wang, Y. Wang, J. Yan, K. Zhang, F. Lin, L. Xiang, L. Deng, Z. Guan, W. Cui, H. Zhang, Pharmaceutical electrospinning and 3D printing scaffold design for bone regeneration, Adv. Drug Deliv. Rev. 174 (2021) 504–534. https://doi.org/10.1016/j.addr.2021.05.007.

[165] S. V. Murphy, A. Atala, 3D bioprinting of tissues and organs, Nat. Biotechnol. 32 (2014) 773–785. https://doi.org/10.1038/nbt.2958.

[166] Z. Yue, X. Liu, P.T. Coates, G.G. Wallace, Advances in printing biomaterials and living cells: Implications for islet cell transplantation, Curr. Opin. Organ Transplant. 21 (2016) 467–475. https://doi.org/10.1097/mot.0000000000000346.

[167] S. Kumar, Synthetic polymer-derived single-network inks/bioinks for extrusion-based 3D printing towards bioapplications, Mater. Adv. 2 (2021) 6928–6941. https://doi.org/10.1039/d1ma00525a.

[168] M.E. Prendergast, J.A. Burdick, Recent Advances in Enabling Technologies in 3D Printing for Precision Medicine, Adv. Mater. 32 (2020) 1902516. https://doi.org/10.1002/adma.201902516.

[169] Y. Kang, P. Datta, S. Shanmughapriya, I.T. Ozbolat, 3D Bioprinting of Tumor Models for Cancer Research, ACS Appl. Bio Mater. 3 (2020) 5552–5573. https://doi.org/10.1021/acsabm.0c00791.

[170] V. Mironov, Printing technology to produce living tissue, Expert Opin. Biol. Ther. 3 (2003) 701–704. https://doi.org/10.1517/14712598.3.5.701.

[171] J. Li, C. Wu, P.K. Chu, M. Gelinsky, 3D printing of hydrogels: Rational design strategies and emerging biomedical applications, Mater. Sci. Eng. R Reports. 140 (2020) 100543. https://doi.org/10.1016/j.mser.2020.100543.

[172] F.C. Godoi, S. Prakash, B.R. Bhandari, 3d printing technologies applied for food design: Status and prospects, J. Food Eng. 179 (2016) 44–54. https://doi.org/10.1016/j.jfoodeng.2016.01.025.

[173] T. Almela, S. Al-Sahaf, I.M. Brook, K. Khoshroo, M. Rasoulianboroujeni, F. Fahimipour, M. Tahriri, E. Dashtimoghadam, R. Bolt, L. Tayebi, K. Moharamzadeh, 3D printed tissue engineered model for bone invasion of oral cancer, Tissue Cell. 52 (2018) 71–77. https://doi.org/10.1016/j.tice.2018.03.009.

[174] A.J.R. Barcena, K. Dhal, P. Patel, P. Ravi, S. Kundu, K. Tappa, Current Biomedical Applications of 3D-Printed Hydrogels, Gels. 10 (2023) 8. https://doi.org/10.3390/gels10010008.

[175] D. Chimene, K.K. Lennox, R.R. Kaunas, A.K. Gaharwar, Advanced Bioinks for 3D Printing: A Materials Science Perspective, Ann. Biomed. Eng. 44 (2016) 2090–2102. https://doi.org/10.1007/s10439-016-1638-y.

[176] J. Groll, J.A. Burdick, D.W. Cho, B. Derby, M. Gelinsky, S.C. Heilshorn, T. Jüngst, J. Malda, V.A. Mironov, K. Nakayama, A. Ovsianikov, W. Sun, S. Takeuchi, J.J. Yoo, T.B.F. Woodfield, A definition of bioinks and their distinction from biomaterial inks, Biofabrication. 11 (2019) 013001. https://doi.org/10.1088/1758-5090/aaec52.

[177] P.A. Amorim, M.A. D'Ávila, R. Anand, P. Moldenaers, P. Van Puyvelde, V. Bloemen, Insights on shear rheology of inks for extrusion-based 3D bioprinting, Bioprinting. 22 (2021) e00129. https://doi.org/10.1016/j.bprint.2021.e00129.

[178] T. Gao, G.J. Gillispie, J.S. Copus, A.P.R. Kumar, Y.J. Seol, A. Atala, J.J. Yoo, S.J. Lee, Optimization of gelatin-alginate composite bioink printability using rheological parameters: A systematic approach, Biofabrication. 10 (2018) 034106. https://doi.org/10.1088/1758-5090/aacdc7.

[179] L.L. Wang, C.B. Highley, Y.C. Yeh, J.H. Galarraga, S. Uman, J.A. Burdick, Three-dimensional extrusion bioprinting of single- and double-network hydrogels containing dynamic covalent crosslinks, J. Biomed. Mater. Res. A. 106 (2018) 865–875. https://doi.org/10.1002/jbm.a.36323.

[180] M.E. Cooke, D.H. Rosenzweig, The rheology of direct and suspended extrusion bioprinting, APL Bioeng. 5 (2021) 1–20. https://doi.org/10.1063/5.0031475.

[181] S.A. Wilson, L.M. Cross, C.W. Peak, A.K. Gaharwar, Shear-Thinning and Thermo-Reversible Nanoengineered Inks for 3D Bioprinting, ACS Appl. Mater. Interfaces. 9 (2017) 43449–43458. https://doi.org/10.1021/acsami.7b13602.

[182] Y. Wu, A. Wenger, H. Golzar, X. (Shirley) Tang, 3D bioprinting of bicellular liver lobule-mimetic structures via microextrusion of cellulose nanocrystal-incorporated shear-thinning bioink, Sci. Rep. 10 (2020) 20648. https://doi.org/10.1038/s41598-020-77146-3.

[183] A. Hernández-Sosa, R.A. Ramírez-Jiménez, L. Rojo, F. Boulmedais, M.R. Aguilar, M. Criado-Gonzalez, R. Hernández, Optimization of the Rheological Properties of Self-Assembled Tripeptide/Alginate/Cellulose Hydrogels for 3D Printing, Polymers (Basel). 14 (2022) 2229. https://doi.org/10.3390/polym14112229.

[184] V.H.M. Mouser, F.P.W. Melchels, J. Visser, W.J.A. Dhert, D. Gawlitta, J. Malda, Yield stress determines bioprintability of hydrogels based on gelatin-methacryloyl and gellan gum for cartilage bioprinting, Biofabrication. 8 (2016) 035003. https://doi.org/10.1088/1758-5090/8/3/035003.

[185] S. Bom, R. Ribeiro, H.M. Ribeiro, C. Santos, J. Marto, On the progress of hydrogel-based 3D printing: Correlating rheological properties with printing behaviour, Int. J. Pharm. 615 (2022) 121506. https://doi.org/10.1016/j.ijpharm.2022.121506.

[186] H. Jafari, H. Alimoradi, C. Delporte, K. V. Bernaerts, R. Heidari, D. Podstawczyk, S.V. Niknezhad, A. Shavandi, An injectable, self-healing, 3D printable, double network co-enzymatically crosslinked hydrogel using marine poly- and oligo-saccharides for wound healing application, Appl. Mater. Today. 29 (2022) 101581. https://doi.org/10.1016/j.apmt.2022.101581.

[187] A.R. Osi, H. Zhang, J. Chen, Y. Zhou, R. Wang, J. Fu, P. Müller-Buschbaum, Q. Zhong, Three-Dimensional-Printable Thermo/Photo-Cross-Linked Methacrylated Chitosan-Gelatin Hydrogel Composites for Tissue Engineering, ACS Appl. Mater. Interfaces. 13 (2021) 22902–22913. https://doi.org/10.1021/acsami.1c01321.

[188] Y. Wang, Y. Chen, J. Zheng, L. Liu, Q. Zhang, Three-Dimensional Printing Self-Healing Dynamic/Photocrosslinking Gelatin-Hyaluronic Acid Double-Network Hydrogel for Tissue Engineering, ACS Omega. 7 (2022) 12076–12088. https://doi.org/10.1021/acsomega.2c00335.

[189] S.C. Lee, G. Gillispie, P. Prim, S.J. Lee, Physical and Chemical Factors Influencing the Printability of Hydrogel-based Extrusion Bioinks, Chem. Rev. 120 (2020) 10834–10886. https://doi.org/10.1021/acs.chemrev.0c00015.

[190] N. Soltan, L. Ning, F. Mohabatpour, P. Papagerakis, X. Chen, Printability and Cell Viability in Bioprinting Alginate Dialdehyde-Gelatin Scaffolds, ACS Biomater. Sci. Eng. 5 (2019) 2976–2987. https://doi.org/10.1021/acsbiomaterials.9b00167.

[191] F.-F. Cai, S. Heid, A.R. Boccaccini, Potential of Laponite® incorporated oxidized alginate–gelatin (ADA-GEL) composite hydrogels for extrusion-based 3D printing, J. Biomed. Mater. Res. Part B Appl. Biomater. 109 (2021) 1090–1104. https://doi.org/10.1002/jbm.b.34771.

[192] L. Ouyang, R. Yao, Y. Zhao, W. Sun, Effect of bioink properties on printability and cell viability for 3D bioplotting of embryonic stem cells, Biofabrication. 8 (2016) 035020. https://doi.org/10.1088/1758-5090/8/3/035020.

[193] K.H. Kang, L.A. Hockaday, J.T. Butcher, Quantitative optimization of solid freeform deposition of aqueous hydrogels, Biofabrication. 5 (2013) 035001. https://doi.org/10.1088/1758-5082/5/3/035001.

[194] Y. He, F. Yang, H. Zhao, Q. Gao, B. Xia, J. Fu, Research on the printability of hydrogels in 3D bioprinting, Sci. Rep. 6 (2016) 1–13. https://doi.org/10.1038/srep29977.

[195] G. Gillispie, P. Prim, J. Copus, J. Fisher, A.G. Mikos, J.J. Yoo, A. Atala, S.J. Lee, Assessment methodologies for extrusion-based bioink printability, Biofabrication. 12 (2020) 022003. https://doi.org/10.1088/1758-5090/ab6f0d.

[196] B. Webb, B.J. Doyle, Parameter optimization for 3D bioprinting of hydrogels, Bioprinting. 8 (2017) 8–12. https://doi.org/10.1016/j.bprint.2017.09.001.

[197] G.B. Ramírez Rodríguez, T.M.F. Patrício, J.M. Delgado López, Natural polymers for bone repair, Bone Repair Biomater. Regen. Clin. Appl. Second Ed. (2019) 199–232. https://doi.org/10.1016/b978-0-08-102451-5.00008-1.

[198] C. Fu, Y. Fan, G. Liu, W. Li, J. Ma, J. Xiao, One-step fabrication of an injectable antibacterial collagen hydrogel with in situ synthesized silver nanoparticles for accelerated diabetic wound healing, Chem. Eng. J. 480 (2024) 148288. https://doi.org/10.1016/j.cej.2023.148288.

[199] D.M. Tian, H.H. Wan, J.R. Chen, Y. Bin Ye, Y. He, Y. Liu, L.Y. Tang, Z.Y. He, K.Z. Liu, C.J. Gao, S.L. Li, Q. Xu, Z. Yang, C. Lai, X.J. Xu, C.S. Ruan, Y.S. Xu, C. Zhang, L. Luo, L.P. Yan, In-situ formed elastin-based hydrogels enhance wound healing via promoting innate immune cells recruitment and angiogenesis, Mater. Today Bio. 15 (2022) 100300. https://doi.org/10.1016/j.mtbio.2022.100300.

[200] D. Hua, S. Gao, M. Zhang, W. Ma, C. Huang, A novel xanthan gum-based conductive hydrogel with excellent mechanical, biocompatible, and self-healing performances, Carbohydr. Polym. 247 (2020). https://doi.org/10.1016/j.carbpol.2020.116743.

[201] P.K. Byram, K.C. Sunka, A. Barik, M. Kaushal, S. Dhara, N. Chakravorty, Biomimetic silk fibroin and xanthan gum blended hydrogels for connective tissue regeneration, Int. J. Biol. Macromol. 165 (2020) 874–882. https://doi.org/10.1016/j.ijbiomac.2020.09.231.

[202] B. De Zheng, L. Gan, L.Y. Tian, G.H. Chen, Protein/polysaccharide-based hydrogels loaded probiotic-mediated therapeutic systems: A review, Int. J. Biol. Macromol. 253 (2023) 126841. https://doi.org/10.1016/j.ijbiomac.2023.126841.

[203] S.A. Meenach, J.Z. Hilt, K.W. Anderson, Poly(ethylene glycol)-based magnetic hydrogel nanocomposites for hyperthermia cancer therapy, Acta Biomater. 6 (2010) 1039–1046. https://doi.org/10.1016/j.actbio.2009.10.017.

[204] J. Kodavaty, Poly (vinyl alcohol) and hyaluronic acid hydrogels as potential biomaterial systems - A comprehensive review, J. Drug Deliv. Sci. Technol. 71 (2022) 103298. https://doi.org/10.1016/j.jddst.2022.103298.

[205] N. Davari, N. Bakhtiary, M. Khajehmohammadi, S. Sarkari, H. Tolabi, F. Ghorbani, B. Ghalandari, Protein-Based Hydrogels: Promising Materials for Tissue Engineering, Polymers (Basel). 14 (2022) 986. https://doi.org/10.3390/polym14050986.

[206] L. Ye, F. Yao, J. Li, Peptide and protein-based hydrogels, in: Sustain. Hydrogels Synth. Prop. Appl., Elsevier, 2023: pp. 137–173. https://doi.org/10.1016/b978-0-323-91753-7.00018-1.

[207] I. Gholamali, Stimuli-Responsive Polysaccharide Hydrogels for Biomedical Applications: a

Review, Regen. Eng. Transl. Med. 7 (2021) 91–114. https://doi.org/10.1007/s40883-019-00134-1.

[208] B. De Zheng, M.T. Xiao, Polysaccharide-based hydrogel with photothermal effect for accelerating wound healing, Carbohydr. Polym. 299 (2023) 120228. https://doi.org/10.1016/j.carbpol.2022.120228.

[209] C. Xu, Q. Ban, W. Wang, J. Hou, Z. Jiang, Novel nano-encapsulated probiotic agents: Encapsulate materials, delivery, and encapsulation systems, J. Control. Release. 349 (2022) 184–205. https://doi.org/10.1016/j.jconrel.2022.06.061.

[210] K. Yue, G. Trujillo-de Santiago, M.M. Alvarez, A. Tamayol, N. Annabi, A. Khademhosseini, Synthesis, properties, and biomedical applications of gelatin methacryloyl (GelMA) hydrogels, Biomaterials. 73 (2015) 254–271. https://doi.org/10.1016/j.biomaterials.2015.08.045.

[211] E.Y. Chuang, Y.C. Lin, Y.M. Huang, C.H. Chen, Y.Y. Yeh, L. Rethi, Y.J. Chou, P.R. Jheng, J.M. Lai, C.J. Chiang, C.C. Wong, Biofunctionalized hydrogel composed of genipin-crosslinked gelatin/hyaluronic acid incorporated with lyophilized platelet-rich fibrin for segmental bone defect repair, Carbohydr. Polym. 339 (2024) 122174. https://doi.org/10.1016/j.carbpol.2024.122174.

[212] Y.T. Shih, K.C. Cheng, Y.J. Ko, C.Y. Lin, M.C. Wang, C.I. Lee, P.L. Lee, R. Qi, J.J. Chiu, S. hui Hsu, 3D-Printed proangiogenic patches of photo-crosslinked gelatin and polyurethane hydrogels laden with vascular cells for treating vascular ischemic diseases, Biomaterials. 309 (2024) 122600. https://doi.org/10.1016/j.biomaterials.2024.122600.

[213] J. Ciriza, A. Rodríguez-Romano, I. Nogueroles, G. Gallego-Ferrer, R.M. Cabezuelo, J.L. Pedraz, P. Rico, Borax-loaded injectable alginate hydrogels promote muscle regeneration in vivo after an injury, Mater. Sci. Eng. C. 123 (2021) 112003. https://doi.org/10.1016/j.msec.2021.112003.

[214] Z. Fang, G. Liu, B. Wang, H. Meng, A. Bahatibieke, J.F. Li, M. Ma, J. Peng, Y. Zheng, An injectable self-healing alginate hydrogel with desirable mechanical and degradation properties for enhancing osteochondral regeneration, Carbohydr. Polym. 343 (2024) 122424. https://doi.org/10.1016/j.carbpol.2024.122424.

[215] C. Fiorica, F.S. Palumbo, G. Pitarresi, M. Allegra, R. Puleio, G. Giammona, Hyaluronic acid and α-elastin based hydrogel for three dimensional culture of vascular endothelial cells, J. Drug Deliv. Sci. Technol. 46 (2018) 28–33. https://doi.org/10.1016/j.jddst.2018.04.017.

[216] W. Duan, X. Jin, Y. Zhao, S. Martin-Saldaña, S. Li, L. Qiao, L. Shao, B. Zhu, S. Hu, F. Li, L. Feng, Y. Ma, B. Du, L. Zhang, Y. Bu, Engineering injectable hyaluronic acid-based adhesive hydrogels with anchored PRP to pattern the micro-environment to accelerate diabetic wound healing, Carbohydr. Polym. 337 (2024) 122146. https://doi.org/10.1016/j.carbpol.2024.122146.

[217] S. Wang, Y. Yao, T. Zhou, J. Xie, J. Ding, W. Cao, L. Shen, Y. Zhu, C. Gao, Preservation of cardiac functions post myocardial infarction in vivo by a phenylboric acid-grafted hyaluronic hydrogel with anti-oxidation and accelerated degradation under oxidative microenvironment, Compos. Part B Eng. 238 (2022) 109941. https://doi.org/10.1016/j.compositesb.2022.109941.

[218] H. Cui, B. Cui, H. Chen, X. Geng, X. Geng, Z. Li, S. Cao, J. Shen, J. Li, A chitosan-based self-healing hydrogel for accelerating infected wound healing, Biomater. Sci. 11 (2023) 4226–4237. https://doi.org/10.1039/d3bm00061c.

[219] Y. Su, Y. Liu, X. Hu, Y. Lu, J. Zhang, W. Jin, W. Liu, Y. Shu, Y.Y. Cheng, W. Li, Y. Nie, B. Pan, K. Song, Caffeic acid-grafted chitosan/sodium alginate/nanoclay-based multifunctional 3D-printed hybrid scaffolds for local drug release therapy after breast cancer surgery, Carbohydr. Polym. 324 (2024) 121441. https://doi.org/10.1016/j.carbpol.2023.121441.

[220] P. Ding, X. Ding, X. Liu, Y. Lu, Y. Zhao, Y. Chu, L. Fan, L. Nie, Injectable, self-healing, antibacterial hydrogel dressing based on oxidized dextran and sialic acid substituted chitosan with incorporation of tannic acid, Eur. Polym. J. 216 (2024) 113297. https://doi.org/10.1016/j.eurpolymj.2024.113297.

[221] T. Osmałek, A. Froelich, S. Tasarek, Application of gellan gum in pharmacy and medicine, Int. J. Pharm. 466 (2014) 328–340. https://doi.org/10.1016/j.ijpharm.2014.03.038.

[222] L.R. Stevens, K.J. Gilmore, G.G. Wallace, M. In het Panhuis, Tissue engineering with gellan gum, Biomater. Sci. 4 (2016) 1276–1290. https://doi.org/10.1039/c6bm00322b.

[223] V.D. Prajapati, G.K. Jani, B.S. Zala, T.A. Khutliwala, An insight into the emerging exopolysaccharide gellan gum as a novel polymer, Carbohydr. Polym. 93 (2013) 670–678. https://doi.org/10.1016/j.carbpol.2013.01.030.

[224] F.S. Palumbo, S. Federico, G. Pitarresi, C. Fiorica, Gellan gum-based delivery systems of therapeutic agents and cells, Carbohydr. Polym. 229 (2020) 115430. https://doi.org/10.1016/j.carbpol.2019.115430.

[225] E.R. Morris, K. Nishinari, M. Rinaudo, Gelation of gellan - A review, Food Hydrocoll. 28 (2012) 373–411. https://doi.org/10.1016/j.foodhyd.2012.01.004.

[226] Y. Nitta, R. Takahashi, K. Nishinari, Viscoelasticity and phase separation of aqueous Na-type gellan solution, Biomacromolecules. 11 (2010) 187–191. https://doi.org/10.1021/bm901063k.

[227] M.S. Kuo, A.J. Mort, A. Dell, Identification and location of l-glycerate, an unusual acyl substituent in gellan gum, Carbohydr. Res. 156 (1986) 173–187. https://doi.org/10.1016/s0008-6215(00)90109-5.

[228] A.J. Jay, I.J. Colquhoun, M.J. Ridout, G.J. Brownsey, V.J. Morris, A.M. Fialho, J.H. Leitão, I. Sá-Correia, Analysis of structure and function of gellans with different substitution patterns,

Carbohydr. Polym. 35 (1998) 179–188. https://doi.org/10.1016/s0144-8617(97)00241-5.

[229] D.M. Kirchmajer, B. Steinhoff, H. Warren, R. Clark, M. In Het Panhuis, Enhanced gelation properties of purified gellan gum, Carbohydr. Res. 388 (2014) 125–129. https://doi.org/10.1016/j.carres.2014.02.018.

[230] H. Moritaka, H. Fukuba, K. Kumeno, N. Nakahama, K. Nishinari, Effect of monovalent and divalent cations on the rheological properties of gellan gels, Top. Catal. 4 (1991) 495–507. https://doi.org/10.1016/s0268-005x(09)80200-2.

[231] C.S.F. Picone, R.L. Cunha, Influence of pH on formation and properties of gellan gels, Carbohydr. Polym. 84 (2011) 662–668. https://doi.org/10.1016/j.carbpol.2010.12.045.

[232] Y. Gong, C. Wang, R.C. Lai, K. Su, F. Zhang, D.A. Wang, An improved injectable polysaccharide hydrogel: Modified gellan gum for long-term cartilage regeneration in vitro, J. Mater. Chem. 19 (2009) 1968–1977. https://doi.org/10.1039/b818090c.

[233] S. Agnello, F.S. Palumbo, G. Pitarresi, C. Fiorica, G. Giammona, Synthesis and evaluation of thermo-rheological behaviour and ionotropic crosslinking of new gellan gum-alkyl derivatives, Carbohydr. Polym. 185 (2018) 73–84. https://doi.org/10.1016/j.carbpol.2018.01.021.

[234] J. Silva-Correia, B. Zavan, V. Vindigni, T.H. Silva, J.M. Oliveira, G. Abatangelo, R.L. Reis, Biocompatibility evaluation of ionic- and photo-crosslinked methacrylated gellan gum hydrogels: In vitro and in vivo study, Adv. Healthc. Mater. 2 (2013) 568–575. https://doi.org/10.1002/adhm.201200256.

[235] G. Pitarresi, A. Martorana, F.S. Palumbo, C. Fiorica, G. Giammona, New gellan gum-graft-poly(D,L-lactide-co-glycolide) copolymers as promising bioinks: Synthesis and characterization, Int. J. Biol. Macromol. 162 (2020) 1653–1667. https://doi.org/10.1016/j.ijbiomac.2020.07.254.

[236] Z. Xu, Z. Li, S. Jiang, K.M. Bratlie, Chemically Modified Gellan Gum Hydrogels with Tunable Properties for Use as Tissue Engineering Scaffolds, ACS Omega. 3 (2018) 6998–7007. https://doi.org/10.1021/acsomega.8B00683.

[237] D.F. Coutinho, S. V. Sant, H. Shin, J.T. Oliveira, M.E. Gomes, N.M. Neves, A. Khademhosseini, R.L. Reis, Modified Gellan Gum hydrogels with tunable physical and mechanical properties, Biomaterials. 31 (2010) 7494–7502. https://doi.org/10.1016/j.biomaterials.2010.06.035.

[238] S. Vieira, A. da Silva Morais, E. Garet, J. Silva-Correia, R.L. Reis, Á. González-Fernández, J. Miguel Oliveira, Self-mineralizing Ca-enriched methacrylated gellan gum beads for bone tissue engineering, Acta Biomater. 93 (2019) 74–85. https://doi.org/10.1016/j.actbio.2019.01.053.

[239] H. Jongprasitkul, S. Turunen, V.S. Parihar, M. Kellomäki, Two-step crosslinking to enhance the printability of methacrylated gellan gum biomaterial ink for extrusion-based 3D

bioprinting, Bioprinting. 25 (2022) e00185. https://doi.org/10.1016/j.bprint.2021.e00185.

[240] G. Pitarresi, F.S. Palumbo, C. Fiorica, F. Bongiovì, A. Martorana, S. Federico, C.M. Chinnici, G. Giammona, Composite Hydrogels of Alkyl Functionalized Gellan Gum Derivative and Hydroxyapatite/Tricalcium Phosphate Nanoparticles as Injectable Scaffolds for bone Regeneration, Macromol. Biosci. 22 (2022) 2100290. https://doi.org/10.1002/mabi.202100290.

[241] A.H. Bacelar, J. Silva-Correia, J.M. Oliveira, R.L. Reis, Recent progress in gellan gum hydrogels provided by functionalization strategies, J. Mater. Chem. B. 4 (2016) 6164–6174. https://doi.org/10.1039/c6tb01488g.

[242] C.J. Ferris, L.R. Stevens, K.J. Gilmore, E. Mume, I. Greguric, D.M. Kirchmajer, G.G. Wallace, M. In Het Panhuis, Peptide modification of purified gellan gum, J. Mater. Chem. B. 3 (2015) 1106–1115. https://doi.org/10.1039/c4tb01727g.

[243] C. Wang, Y. Gong, Y. Lin, J. Shen, D.A. Wang, A novel gellan gel-based microcarrier for anchorage-dependent cell delivery, Acta Biomater. 4 (2008) 1226–1234. https://doi.org/10.1016/j.actbio.2008.03.008.

[244] O. Alheib, L.P. da Silva, A. da Silva Morais, K.A. Mesquita, R.P. Pirraco, R.L. Reis, V.M. Correlo, Injectable laminin-biofunctionalized gellan gum hydrogels loaded with myoblasts for skeletal muscle regeneration, Acta Biomater. 143 (2022) 282–294. https://doi.org/10.1016/j.actbio.2022.03.008.

[245] M. Chen, H. Tan, W. Xu, Z. Wang, J. Zhang, S. Li, T. Zhou, J. Li, X. Niu, A self-healing, magnetic and injectable biopolymer hydrogel generated by dual cross-linking for drug delivery and bone repair, Acta Biomater. 153 (2022) 159–177. https://doi.org/10.1016/j.actbio.2022.09.036.

[246] J.H. Choi, A. Park, W. Lee, J. Youn, M.A. Rim, W. Kim, N. Kim, J.E. Song, G. Khang, Preparation and characterization of an injectable dexamethasone-cyclodextrin complexes-loaded gellan gum hydrogel for cartilage tissue engineering, J. Control. Release. 327 (2020) 747–765. https://doi.org/10.1016/j.jconrel.2020.08.049.

[247] G. Biscari, G. Pitarresi, C. Fiorica, D. Schillaci, V. Catania, F. Salvatore Palumbo, G. Giammona, Near-infrared light-responsive and antibacterial injectable hydrogels with antioxidant activity based on a Dopamine-functionalized Gellan Gum for wound healing, Int. J. Pharm. 627 (2022) 122257. https://doi.org/10.1016/j.ijpharm.2022.122257.

[248] E.M. Nsengiyumva, P. Alexandridis, Xanthan gum in aqueous solutions: Fundamentals and applications, Int. J. Biol. Macromol. 216 (2022) 583–604. https://doi.org/10.1016/j.ijbiomac.2022.06.189.

[249] A.L. Miranda, S.S. Costa, D. de J. Assis, C.S. de Jesus, A.G. Guimarães, J.I. Druzian, Influence of strain and fermentation time on the production, composition, and properties of xanthan gum, J. Appl. Polym. Sci. 137 (2020) 48557. https://doi.org/10.1002/app.48557.

[250] C.E. Brunchi, S. Morariu, M. Bercea, Intrinsic viscosity and conformational parameters of xanthan in aqueous solutions: Salt addition effect, Colloids Surfaces B Biointerfaces. 122 (2014) 512–519. https://doi.org/10.1016/j.colsurfb.2014.07.023.

[251] K.P. Shatwell, I.W. Sutherland, I.C.M. Dea, S.B. Ross-Murphy, The influence of acetyl and pyruvate substituents on the helix-coil transition behaviour of xanthan, Carbohydr. Res. 206 (1990) 87–103. https://doi.org/10.1016/0008-6215(90)84009-j.

[252] D.F.S. Petri, Xanthan gum: A versatile biopolymer for biomedical and technological applications, J. Appl. Polym. Sci. 132 (2015). https://doi.org/10.1002/app.42035.

[253] R. Moorhouse, M.D. Walkinshaw, S. Arnott, Xanthan Gum—Molecular Conformation and Interactions, in: 1977: pp. 90–102. https://doi.org/10.1021/bk-1977-0045.ch007.

[254] A. Kumar, K.M. Rao, S.S. Han, Application of xanthan gum as polysaccharide in tissue engineering: A review, Carbohydr. Polym. 180 (2018) 128–144. https://doi.org/10.1016/j.carbpol.2017.10.009.

[255] B.T. Stokke, B.E. Christensen, Release of disordered xanthan oligomers upon partial acid hydrolysis of double-stranded xanthan, Food Hydrocoll. 10 (1996) 83–89. https://doi.org/10.1016/s0268-005x(96)80058-0.

[256] P. Banerjee, I. Mukherjee, S. Bhattacharya, S. Datta, S.P. Moulik, D. Sarkar, Sorption of water vapor, hydration, and viscosity of carboxymethylhydroxypropyl guar, diutan, and xanthan gums, and their molecular association with and without salts (NaCl, CaCl2, HCOOK, CH3COONa, (NH4)2SO4 and MgSO4) in aqueous solution, Langmuir. 25 (2009) 11647–11656. https://doi.org/10.1021/la901259e.

[257] H.A. Khouryieh, T.J. Herald, F. Aramouni, S. Alavi, Intrinsic viscosity and viscoelastic properties of xanthan/guar mixtures in dilute solutions: Effect of salt concentration on the polymer interactions, Food Res. Int. 40 (2007) 883–893. https://doi.org/10.1016/j.foodres.2007.03.001.

[258] L. Zhong, M. Oostrom, M.J. Truex, V.R. Vermeul, J.E. Szecsody, Rheological behavior of xanthan gum solution related to shear thinning fluid delivery for subsurface remediation, J. Hazard. Mater. 244–245 (2013) 160–170. https://doi.org/10.1016/j.jhazmat.2012.11.028.

[259] C.E. Brunchi, M. Avadanei, M. Bercea, S. Morariu, Chain conformation of xanthan in solution as influenced by temperature and salt addition, J. Mol. Liq. 287 (2019) 111008. https://doi.org/10.1016/j.molliq.2019.111008.

[260] L. Su, W.K. Ji, W.Z. Lan, X.Q. Dong, Chemical modification of xanthan gum to increase dissolution rate, Carbohydr. Polym. 53 (2003) 497–499. https://doi.org/10.1016/s0144-8617(02)00287-4.

[261] D.A.Z. Wever, F. Picchioni, A.A. Broekhuis, Polymers for enhanced oil recovery: A paradigm for structure-property relationship in aqueous solution, Prog. Polym. Sci. 36 (2011) 1558–1628. https://doi.org/10.1016/j.progpolymsci.2011.05.006.

[262] V.B. Bueno, R. Bentini, L.H. Catalani, D.F.S. Petri, Synthesis and swelling behavior of xanthan-based hydrogels, Carbohydr. Polym. 92 (2013) 1091–1099. https://doi.org/10.1016/j.carbpol.2012.10.062.

[263] C.R. Soccol, A. Pandey, C. Larroche, Fermentation processes engineering in the food industry, CRC Press, 2013. https://doi.org/10.1201/b14070.

[264] J. Huang, Y. Deng, J. Ren, G. Chen, G. Wang, F. Wang, X. Wu, Novel in situ forming hydrogel based on xanthan and chitosan re-gelifying in liquids for local drug delivery, Carbohydr. Polym. 186 (2018) 54–63. https://doi.org/10.1016/j.carbpol.2018.01.025.

[265] M.A.S.P. Nur Hazirah, M.I.N. Isa, N.M. Sarbon, Effect of xanthan gum on the physical and mechanical properties of gelatin-carboxymethyl cellulose film blends, Food Packag. Shelf Life. 9 (2016) 55–63. https://doi.org/10.1016/j.fpsl.2016.05.008.

[266] A. Palaniraj, V. Jayaraman, Production, recovery and applications of xanthan gum by Xanthomonas campestris, J. Food Eng. 106 (2011) 1–12. https://doi.org/10.1016/j.jfoodeng.2011.03.035.

[267] H. Mittal, V. Kumar, Saruchi, S.S. Ray, Adsorption of methyl violet from aqueous solution using gum xanthan/Fe3O4 based nanocomposite hydrogel, Int. J. Biol. Macromol. 89 (2016) 1–11. https://doi.org/10.1016/j.ijbiomac.2016.04.050.

[268] S. Signorini, A. Delledonne, S. Pescina, A. Bianchera, C. Sissa, M. Vivero-Lopez, C. Alvarez-Lorenzo, P. Santi, C. Padula, S. Nicoli, A sterilizable platform based on crosslinked xanthan gum for controlled-release of polymeric micelles: Ocular application for the delivery of neuroprotective compounds to the posterior eye segment, Int. J. Pharm. 657 (2024) 124141. https://doi.org/10.1016/j.ijpharm.2024.124141.

[269] R.R. Shiledar, A.A. Tagalpallewar, C.R. Kokare, Formulation and in vitro evaluation of xanthan gum-based bilayered mucoadhesive buccal patches of zolmitriptan, Carbohydr. Polym. 101 (2014) 1234–1242. https://doi.org/10.1016/j.carbpol.2013.10.072.

[270] M. Ahmad, C. Ritzoulis, J. Chen, H. Meigui, R. Bushra, Y. Jin, H. Xiao, Xanthan gum − mucin complexation: Molecular interactions, thermodynamics, and rheological analysis, Food Hydrocoll. 114 (2021) 106579. https://doi.org/10.1016/j.foodhyd.2020.106579.

[271] S. Maity, B. Sa, Ca-carboxymethyl xanthan gum mini-matrices: Swelling, erosion and their impact on drug release mechanism, Int. J. Biol. Macromol. 68 (2014) 78–85. https://doi.org/10.1016/j.ijbiomac.2014.04.036.

[272] J. Patel, S. Maiti, N.S.H.N. Moorthy, Repaglinide-laden hydrogel particles of xanthan gum derivatives for the management of diabetes, Carbohydr. Polym. 287 (2022) 119354. https://doi.org/10.1016/j.carbpol.2022.119354.

[273] X. Wang, H. Xin, Y. Zhu, W. Chen, E. Tang, J. Zhang, Y. Tan, Synthesis and characterization of modified xanthan gum using poly(maleic anhydride/1-octadecene), Colloid Polym. Sci. 294 (2016) 1333–1341. https://doi.org/10.1007/s00396-016-3898-3.

[274] M. Jadav, R. Solanki, S. Patel, D. Pooja, H. Kulhari, Development of thiolated xanthan gum-stearylamine conjugate based mucoadhesive system for the delivery of biochanin-A to melanoma cells, Int. J. Biol. Macromol. 257 (2024) 128693. https://doi.org/10.1016/j.ijbiomac.2023.128693.

[275] L. Zhang, Z. Bei, T. Li, Z. Qian, An injectable conductive hydrogel with dual responsive release of rosmarinic acid improves cardiac function and promotes repair after myocardial infarction, Bioact. Mater. 29 (2023) 132–150. https://doi.org/10.1016/j.bioactmat.2023.07.007.

[276] K. Chen, J. Huang, Z. Li, J. Zhang, S. Li, C. Chen, Y. Liu, G. Qu, Y. Teng, R. Ma, Z. Li, Y. Jiang, K. Wang, J. Chen, X. Wu, J. Ren, In situ bioprinting of double network anti-digestive xanthan gum derived hydrogel scaffolds for the treatment of enterocutaneous fistulas, Carbohydr. Polym. 326 (2024) 121508. https://doi.org/10.1016/j.carbpol.2023.121508.

[277] A.M. Namazi, M.S. Aghajanzadeh, R. Imani, Optimizing a self-healing gelatin/aldehyde-modified xanthan gum hydrogel for extrusion-based 3D printing in biomedical applications, Mater. Today Chem. 40 (2024) 102208. https://doi.org/10.1016/j.mtchem.2024.102208.

[278] P.K. Sharma, S. Taneja, Y. Singh, Hydrazone-Linkage-Based Self-Healing and Injectable Xanthan-Poly(ethylene glycol) Hydrogels for Controlled Drug Release and 3D Cell Culture, ACS Appl. Mater. Interfaces. 10 (2018) 30936–30945. https://doi.org/10.1021/acsami.8b07310.

[279] R. Singhal, M.K. Sarangi, G. Rath, Injectable Hydrogels: A Paradigm Tailored with Design, Characterization, and Multifaceted Approaches, Macromol. Biosci. 24 (2024) 2400049. https://doi.org/10.1002/mabi.202400049.

[280] T.N. Pham, C.F. Su, C.C. Huang, J.S. Jan, Biomimetic hydrogels based on L-Dopa conjugated gelatin as pH-responsive drug carriers and antimicrobial agents, Colloids Surfaces B Biointerfaces. 196 (2020) 111316. https://doi.org/10.1016/j.colsurfb.2020.111316.

[281] H. Suo, M. Hussain, H. Wang, N. Zhou, J. Tao, H. Jiang, J. Zhu, Injectable and pH-Sensitive Hyaluronic Acid-Based Hydrogels with On-Demand Release of Antimicrobial Peptides for Infected Wound Healing, Biomacromolecules. 22 (2021) 3049–3059. https://doi.org/10.1021/acs.biomac.1c00502.

[282] D.T. Pham, K. Navesit, L. Wiwatkunupakarn, P. Chomchalao, W. Tiyaboonchai, Nanoparticles-hydrogel composites: A promising innovative system for local antimicrobial applications, J. Drug Deliv. Sci. Technol. 89 (2023) 105055. https://doi.org/10.1016/j.jddst.2023.105055.

[283] C. Mattar, S. Edwards, E. Baraldi, J. Hood, An overview of the global antimicrobial resistance research and development hub and the current landscape, Curr. Opin. Microbiol. 57 (2020) 56–61. https://doi.org/10.1016/j.mib.2020.06.009.

[284] M. Woolhouse, C. Waugh, M.R. Perry, H. Nair, Global disease burden due to antibiotic

resistance - State of the evidence, J. Glob. Health. 6 (2016) 010306. https://doi.org/10.7189/jogh.06.010306.

[285] J. Murugaiyan, P. Anand Kumar, G.S. Rao, K. Iskandar, S. Hawser, J.P. Hays, Y. Mohsen, S. Adukkadukkam, W.A. Awuah, R.A.M. Jose, N. Sylvia, E.P. Nansubuga, B. Tilocca, P. Roncada, N. Roson-Calero, J. Moreno-Morales, R. Amin, B. Krishna Kumar, A. Kumar, A.R. Toufik, T.N. Zaw, O.O. Akinwotu, M.P. Satyaseela, M.B.M. van Dongen, Progress in Alternative Strategies to Combat Antimicrobial Resistance: Focus on Antibiotics, Antibiotics. 11 (2022) 200. https://doi.org/10.3390/antibiotics11020200.

[286] B.D. Brooks, A.E. Brooks, Therapeutic strategies to combat antibiotic resistance, Adv. Drug Deliv. Rev. 78 (2014) 14–27. https://doi.org/10.1016/j.addr.2014.10.027.

[287] K. Kannan, M. Govindaraj, B. Rajeswari, K. Vijayakumar, Green synthesis silver nanoparticles using medicinal plant and antimicrobial activity against human pathogens, Mater. Today Proc. 69 (2022) 1346–1350. https://doi.org/10.1016/j.matpr.2022.08.506.

[288] L. Luo, W. Huang, J. Zhang, Y. Yu, T. Sun, Metal-Based Nanoparticles as Antimicrobial Agents: A Review, ACS Appl. Nano Mater. 7 (2024) 2529–2545. https://doi.org/10.1021/acsanm.3c05615.

[289] I.W. Hamley, Small Bioactive Peptides for Biomaterials Design and Therapeutics, Chem. Rev. 117 (2017) 14015–14041. https://doi.org/10.1021/acs.chemrev.7b00522.

[290] M. Muttenthaler, G.F. King, D.J. Adams, P.F. Alewood, Trends in peptide drug discovery, Nat. Rev. Drug Discov. 2021 204. 20 (2021) 309–325. https://doi.org/10.1038/s41573-020-00135-8.

[291] N. Ahmad, S.N.A. Bukhari, M.A. Hussain, H. Ejaz, M.U. Munir, M.W. Amjad, Nanoparticles incorporated hydrogels for delivery of antimicrobial agents: developments and trends, RSC Adv. 14 (2024) 13535–13564. https://doi.org/10.1039/d4ra00631c.

[292] N. Nassar, S. Kasapis, Fundamental advances in hydrogels for the development of the next generation of smart delivery systems as biopharmaceuticals, Int. J. Pharm. 633 (2023) 122634. https://doi.org/10.1016/j.ijpharm.2023.122634.

[293] B. De Zheng, J. Ye, Y.C. Yang, Y.Y. Huang, M.T. Xiao, Self-healing polysaccharide-based injectable hydrogels with antibacterial activity for wound healing, Carbohydr. Polym. 275 (2022) 118770. https://doi.org/10.1016/j.carbpol.2021.118770.

[294] J.M. Abdo, N.A. Sopko, S.M. Milner, The applied anatomy of human skin: A model for regeneration, Wound Med. 28 (2020) 100179. https://doi.org/10.1016/j.wndm.2020.100179.

[295] B.K. Sun, Z. Siprashvili, P.A. Khavari, Advances in skin grafting and treatment of cutaneous wounds, Science (80-.). 346 (2014) 941–945. https://doi.org/10.1126/science.1253836.

[296] W. Fu, S. Sun, Y. Cheng, J. Ma, Y. Hu, Z. Yang, H. Yao, Z. Zhang, Opportunities and challenges of nanomaterials in wound healing: Advances, mechanisms, and perspectives, Chem. Eng. J. 495 (2024) 153640. https://doi.org/10.1016/j.cej.2024.153640.

[297] J. Larouche, S. Sheoran, K. Maruyama, M.M. Martino, Immune regulation of skin wound healing: Mechanisms and novel therapeutic targets, Adv. Wound Care. 7 (2018) 209–231. https://doi.org/10.1089/wound.2017.0761.

[298] M. Falcone, B. De Angelis, F. Pea, A. Scalise, S. Stefani, R. Tasinato, O. Zanetti, L. Dalla Paola, Challenges in the management of chronic wound infections, J. Glob. Antimicrob. Resist. 26 (2021) 140–147. https://doi.org/10.1016/j.jgar.2021.05.010.

[299] S. Shahabudin, N.S. Azmi, M.N. Lani, M. Mukhtar, M.S. Hossain, Candida albicans skin infection in diabetic patients: An updated review of pathogenesis and management, Mycoses. 67 (2024) e13753. https://doi.org/10.1111/myc.13753.

[300] L. Guenin-Macé, R. Oldenburg, F. Chrétien, C. Demangel, Pathogenesis of skin ulcers: Lessons from the Mycobacterium ulcerans and Leishmania spp. pathogens, Cell. Mol. Life Sci. 71 (2014) 2443–2450. https://doi.org/10.1007/s00018-014-1561-z.

[301] C. Bergonzi, A. Bianchera, G. Remaggi, M.C. Ossiprandi, R. Bettini, L. Elviri, 3D Printed Chitosan/Alginate Hydrogels for the Controlled Release of Silver Sulfadiazine in Wound Healing Applications: Design, Characterization and Antimicrobial Activity, Micromachines. 14 (2023) 137. https://doi.org/10.3390/mi14010137.

[302] X. Wang, J. Qi, W. Zhang, Y. Pu, R. Yang, P. Wang, S. Liu, X. Tan, B. Chi, 3D-printed antioxidant antibacterial carboxymethyl cellulose/ε-polylysine hydrogel promoted skin wound repair, Int. J. Biol. Macromol. 187 (2021) 91–104. https://doi.org/10.1016/j.ijbiomac.2021.07.115.

[303] Y. Tang, R. Zhao, M. Yi, Z. Ge, D. Wang, G. Wang, X. Deng, Multifunctional Hydrogel Enhances Inflammatory Control, Antimicrobial Activity, and Oxygenation to Promote Healing in Infectious Wounds, Biomacromolecules. 25 (2024) 2423–2437. https://doi.org/10.1021/acs.biomac.3c01386.

[304] Y. Wei, J. Fu, E. Liu, J. Gao, Y. Lv, Z. Li, Injectable hydrogels doped with PDA nanoparticles for photothermal bacterial inhibition and rapid wound healing in vitro, RSC Adv. 14 (2024) 2778–2791. https://doi.org/10.1039/d3ra08219a.

[305] E. Chaparro, P.I. da Silva, Lacrain: the first antimicrobial peptide from the body extract of the Brazilian centipede Scolopendra viridicornis, Int. J. Antimicrob. Agents. 48 (2016) 277–285. https://doi.org/10.1016/j.ijantimicag.2016.05.015.

[306] F. Rivero-Pino, M.J. Leon, M.C. Millan-Linares, S. Montserrat-de la Paz, Antimicrobial plant-derived peptides obtained by enzymatic hydrolysis and fermentation as components to improve current food systems, Trends Food Sci. Technol. 135 (2023) 32–42. https://doi.org/10.1016/j.tifs.2023.03.005.

[307] J.R. Morones, J.L. Elechiguerra, A. Camacho, K. Holt, J.B. Kouri, J.T. Ramírez, M.J. Yacaman, The bactericidal effect of silver nanoparticles, Nanotechnology. 16 (2005) 2346–2353. https://doi.org/10.1088/0957-4484/16/10/059.

[308] J.S. Kim, E. Kuk, K.N. Yu, J.H. Kim, S.J. Park, H.J. Lee, S.H. Kim, Y.K. Park, Y.H. Park, C.Y. Hwang, Y.K. Kim, Y.S. Lee, D.H. Jeong, M.H. Cho, Antimicrobial effects of silver nanoparticles, Nanomedicine. 3 (2007) 95–101. https://doi.org/10.1016/j.nano.2006.12.001.

[309] I. Sondi, B. Salopek-Sondi, Silver nanoparticles as antimicrobial agent: a case study on E. coli as a model for Gram-negative bacteria, J. Colloid Interface Sci. 275 (2004) 177–182. https://doi.org/10.1016/j.jcis.2004.02.012.

[310] G. Wyszogrodzka, B. Marszałek, B. Gil, P. Dorozyński, Metal-organic frameworks: mechanisms of antibacterial action and potential applications, Drug Discov. Today. 21 (2016) 1009–1018. https://doi.org/10.1016/j.drudis.2016.04.009.

[311] M. Lopez-Carrizales, E. Mendoza-Mendoza, R.D. Peralta-Rodriguez, M.A. Pérez-Díaz, D. Portales-Pérez, M. Magaña-Aquino, A. Aragón-Piña, R. Infante-Martínez, E.D. Barriga-Castro, R. Sánchez-Sánchez, G.A. Martinez-Castañon, F. Martinez-Gutierrez, Characterization, antibiofilm and biocompatibility properties of chitosan hydrogels loaded with silver nanoparticles and ampicillin: an alternative protection to central venous catheters, Colloids Surfaces B Biointerfaces. 196 (2020) 111292. https://doi.org/10.1016/j.colsurfb.2020.111292.

[312] A. Le Yang, S. Bin Sun, L.Y. Qu, X.Y. Li, J.L. Liu, F. Zhou, Y.J. Xu, Polysaccharide hydrogel containing silver nanoparticle@catechol microspheres with photothermal, antibacterial and anti-inflammatory activities for infected-wounds repair, Int. J. Biol. Macromol. 265 (2024) 130898. https://doi.org/10.1016/j.ijbiomac.2024.130898.

[313] S. Wang, W. Li, G. Cheng, S. Wang, X. Liu, Q. Huang, One–step synthesis of silver nanoparticles by lignocellulose nanofibrils to obtain antimicrobial hydrogels with accelerated wound healing, Mater. Today Commun. 39 (2024) 108663. https://doi.org/10.1016/j.mtcomm.2024.108663.

[314] S. Sanyasi, R.K. Majhi, S. Kumar, M. Mishra, A. Ghosh, M. Suar, P.V. Satyam, H. Mohapatra, C. Goswami, L. Goswami, Polysaccharide-capped silver Nanoparticles inhibit biofilm formation and eliminate multi-drug-resistant bacteria by disrupting bacterial cytoskeleton with reduced cytotoxicity towards mammalian cells, Sci. Rep. 6 (2016) 1–16. https://doi.org/10.1038/srep24929.

[315] B. Chakraborty, M.P. Bhat, D.S. Basavarajappa, M. Rudrappa, S. Nayaka, R.S. Kumar, A.I. Almansour, K. Perumal, Biosynthesis and characterization of polysaccharide-capped silver nanoparticles from Acalypha indica L. and evaluation of their biological activities, Environ. Res. 225 (2023) 115614. https://doi.org/10.1016/j.envres.2023.115614.

[316] X. Ke, Z. Dong, S. Tang, W. Chu, X. Zheng, L. Zhen, X. Chen, C. Ding, J. Luo, J. Li, A natural polymer based bioadhesive with self-healing behavior and improved antibacterial properties, Biomater. Sci. 8 (2020) 4346–4357. https://doi.org/10.1039/d0bm00624f.

[317] M.R. Reithofer, A. Lakshmanan, A.T.K. Ping, J.M. Chin, C.A.E. Hauser, In situ synthesis of

size-controlled, stable silver nanoparticles within ultrashort peptide hydrogels and their anti-bacterial properties, Biomaterials. 35 (2014) 7535–7542. https://doi.org/10.1016/j.biomaterials.2014.04.102.

[318] J.R. Fanti, F. Tomiotto-Pellissier, M.M. Miranda-Sapla, A.H.D. Cataneo, C.G.T. de J. Andrade, C. Panis, J.H. da S. Rodrigues, P.F. Wowk, D. Kuczera, I.N. Costa, C.V. Nakamura, G. Nakazato, N. Durán, W.R. Pavanelli, I. Conchon-Costa, Biogenic silver nanoparticles inducing Leishmania amazonensis promastigote and amastigote death in vitro, Acta Trop. 178 (2018) 46–54. https://doi.org/10.1016/j.actatropica.2017.10.027.

[319] A.B. Alves, B.T. da Silva Bortoleti, F. Tomiotto-Pellissier, A.F.M. Ganaza, M.D. Gonçalves, A.C.M. Carloto, A.C.J. Rodrigues, T.F. Silva, G. Nakazato, R.K.T. Kobayashi, D. Lazarin-Bidóia, M.M. Miranda-Sapla, I.N. Costa, W.R. Pavanelli, I. Conchon-Costa, Synergistic Antileishmanial Effect of Oregano Essential Oil and Silver Nanoparticles: Mechanisms of Action on Leishmania amazonensis, Pathogens. 12 (2023). https://doi.org/10.3390/pathogens12050660.

[320] T.M. Koushik, C.M. Miller, E. Antunes, Bone Tissue Engineering Scaffolds: Function of Multi-Material Hierarchically Structured Scaffolds, Adv. Healthc. Mater. 12 (2023) 2202766. https://doi.org/10.1002/adhm.202202766.

[321] S.H. Ralston, Bone structure and metabolism, Medicine. 49 (2021) 567–571. https://doi.org/10.1016/j.mpmed.2021.06.009.

[322] A. Salhotra, H.N. Shah, B. Levi, M.T. Longaker, Mechanisms of bone development and repair, Nat. Rev. Mol. Cell Biol. 21 (2020) 696–711. https://doi.org/10.1038/s41580-020-00279-w.

[323] L. Claes, P. Augat, G. Suger, H.J. Wilke, Influence of size and stability of the osteotomy gap on the success of fracture healing, J. Orthop. Res. 15 (1997) 577–584. https://doi.org/10.1002/jor.1100150414.

[324] N. Amiryaghoubi, M. Fathi, J. Barar, Y. Omidi, Hydrogel-based scaffolds for bone and cartilage tissue engineering and regeneration, React. Funct. Polym. 177 (2022) 105313. https://doi.org/10.1016/j.reactfunctpolym.2022.105313.

[325] R. Langer, J.P. Vacanti, Tissue engineering, Science. 260 (1993) 920–926. https://doi.org/10.1126/science.8493529.

[326] F.J. O'Brien, Biomaterials & scaffolds for tissue engineering, Mater. Today. 14 (2011) 88–95. https://doi.org/10.1016/S1369-7021(11)70058-X.

[327] P. Bajaj, R.M. Schweller, A. Khademhosseini, J.L. West, R. Bashir, 3D Biofabrication Strategies for Tissue Engineering and Regenerative Medicine, Annu. Rev. Biomed. Eng. 16 (2014) 247–276. https://doi.org/10.1146/annurev-bioeng-071813-105155.

[328] B. Wang, C. Feng, Y. Liu, F. Mi, J. Dong, Recent advances in biofunctional guided bone regeneration materials for repairing defective alveolar and maxillofacial bone: A review, Jpn.

Dent. Sci. Rev. 58 (2022) 233–248. https://doi.org/10.1016/j.jdsr.2022.07.002.

[329] Y. Pan, Y. Zhao, R. Kuang, H. Liu, D. Sun, T. Mao, K. Jiang, X. Yang, N. Watanabe, K.H. Mayo, Q. Lin, J. Li, Injectable hydrogel-loaded nano-hydroxyapatite that improves bone regeneration and alveolar ridge promotion, Mater. Sci. Eng. C. 116 (2020) 111158. https://doi.org/10.1016/j.msec.2020.111158.

[330] A. Sivashanmugam, P. Charoenlarp, S. Deepthi, A. Rajendran, S. V. Nair, S. Iseki, R. Jayakumar, Injectable Shear-Thinning CaSO4/FGF-18-Incorporated Chitin-PLGA Hydrogel Enhances Bone Regeneration in Mice Cranial Bone Defect Model, ACS Appl. Mater. Interfaces. 9 (2017) 42639–42652. https://doi.org/10.1021/acsami.7b15845.

[331] N. Amiryaghoubi, N. Noroozi Pesyan, M. Fathi, Y. Omidi, Injectable thermosensitive hybrid hydrogel containing graphene oxide and chitosan as dental pulp stem cells scaffold for bone tissue engineering, Int. J. Biol. Macromol. 162 (2020) 1338–1357. https://doi.org/10.1016/j.ijbiomac.2020.06.138.

[332] X. yang Chu, K. Yang, X. He, K. tao Yu, Y. yi Luan, Q. bing He, Z. lu Li, Y. lan Xiang, H. Chen, Y. Zeng, Y.Z. Li, D. liang Zhang, Cross-linking N-succinyl chitosan-oxidated hyaluronic acid-based hydrogel loaded with bone marrow mesenchymal stem cell-derived exosomes induce bone regeneration in cranial defects, Mater. Des. 241 (2024) 112969. https://doi.org/10.1016/j.matdes.2024.112969.

[333] Y. Ma, Y. Ji, T. Zhong, W. Wan, Q. Yang, A. Li, X. Zhang, M. Lin, Bioprinting-Based PDLSC-ECM Screening for in Vivo Repair of Alveolar Bone Defect Using Cell-Laden, Injectable and Photocrosslinkable Hydrogels, ACS Biomater. Sci. Eng. 3 (2017) 3534–3545. https://doi.org/10.1021/acsbiomaterials.7b00601.

[334] X. Yuan, W. Zhu, Z. Yang, N. He, F. Chen, X. Han, K. Zhou, Recent Advances in 3D Printing of Smart Scaffolds for Bone Tissue Engineering and Regeneration, Adv. Mater. 36 (2024) 2403641. https://doi.org/10.1002/adma.202403641.

[335] M. Monavari, S. Homaeigohar, M. Fuentes-Chandía, Q. Nawaz, M. Monavari, A. Venkatraman, A.R. Boccaccini, 3D printing of alginate dialdehyde-gelatin (ADA-GEL) hydrogels incorporating phytotherapeutic icariin loaded mesoporous SiO2-CaO nanoparticles for bone tissue engineering, Mater. Sci. Eng. C. 131 (2021) 112470. https://doi.org/10.1016/j.msec.2021.112470.

[336] W. Wang, K.W.K. Yeung, Bone grafts and biomaterials substitutes for bone defect repair: A review, Bioact. Mater. 2 (2017) 224–247. https://doi.org/10.1016/j.bioactmat.2017.05.007.

[337] D. Arcos, M. Vallet-Regí, Substituted hydroxyapatite coatings of bone implants, J. Mater. Chem. B. 8 (2020) 1781–1800. https://doi.org/10.1039/c9tb02710f.

[338] M. Du, J. Chen, K. Liu, H. Xing, C. Song, Recent advances in biomedical engineering of nano-hydroxyapatite including dentistry, cancer treatment and bone repair, Compos. Part B Eng. 215 (2021) 108790. https://doi.org/10.1016/j.compositesb.2021.108790.

[339] K. Maji, S. Dasgupta, K. Pramanik, A. Bissoyi, Preparation and characterization of gelatin-chitosan-nanoβ-TCP based scaffold for orthopaedic application, Mater. Sci. Eng. C. 86 (2018) 83–94. https://doi.org/10.1016/j.msec.2018.02.001.

[340] P. Zhuang, X. Wu, H. Dai, Y. Yao, T. Qiu, Y. Han, S. Li, Nano β-tricalcium phosphate/hydrogel encapsulated scaffolds promote osteogenic differentiation of bone marrow stromal cells through ATP metabolism, Mater. Des. 208 (2021) 109881. https://doi.org/10.1016/j.matdes.2021.109881.

[341] Y. Tang, P. Rajendran, V.P. Veeraraghavan, S. Hussain, J.P. Balakrishna, A. Chinnathambi, S.A. Alharbi, T.A. Alahmadi, T. Rengarajan, S.K. Mohan, Osteogenic differentiation and mineralization potential of zinc oxide nanoparticles from Scutellaria baicalensis on human osteoblast-like MG-63 cells, Mater. Sci. Eng. C. 119 (2021) 111656. https://doi.org/10.1016/j.msec.2020.111656.

[342] P.N. Christy, S.K. Basha, V.S. Kumari, Nano zinc oxide and nano bioactive glass reinforced chitosan/poly(vinyl alcohol) scaffolds for bone tissue engineering application, Mater. Today Commun. 31 (2022) 103429. https://doi.org/10.1016/j.mtcomm.2022.103429.

[343] S. Kandasamy, V. Narayanan, S. Sumathi, Zinc and manganese substituted hydroxyapatite/CMC/PVP electrospun composite for bone repair applications, Int. J. Biol. Macromol. 145 (2020) 1018–1030. https://doi.org/10.1016/j.ijbiomac.2019.09.193.

[344] B. Liu, X. Li, C. Zheng, X. Wang, R. Sun, Facile and green synthesis of silver nanoparticles in quaternized carboxymethyl chitosan solution, Nanotechnology. 24 (2013) 235601. https://doi.org/10.1088/0957-4484/24/23/235601.

[345] Y. Zhang, H. Peng, W. Huang, Y. Zhou, X. Zhang, D. Yan, Hyperbranched poly(amidoamine) as the stabilizer and reductant to prepare colloid silver nanoparticles in situ and their antibacterial activity, J. Phys. Chem. C. 112 (2008) 2330–2336. https://doi.org/10.1021/jp075436g.

[346] R. Li, X. Wang, K. Yin, Q. Xu, S. Ren, X. Wang, Z. Wang, Y. Yi, Fatty acid modification of antimicrobial peptide CGA-N9 and the combats against Candida albicans infection, Biochem. Pharmacol. 211 (2023) 115535. https://doi.org/10.1016/j.bcp.2023.115535.

[347] T. Demirci, M.E. Hasköylü, M.S. Eroğlu, J. Hemberger, E. Toksoy Öner, Levan-based hydrogels for controlled release of Amphotericin B for dermal local antifungal therapy of Candidiasis, Eur. J. Pharm. Sci. 145 (2020) 105255. https://doi.org/10.1016/j.ejps.2020.105255.

[348] J. Kanchanapiboon, U. Kongsa, D. Pattamadilok, S. Kamponchaidet, D. Wachisunthon, S. Poonsatha, S. Tuntoaw, Boesenbergia rotunda extract inhibits Candida albicans biofilm formation by pinostrobin and pinocembrin, J. Ethnopharmacol. 261 (2020) 113193. https://doi.org/10.1016/j.jep.2020.113193.

[349] J.D. Sobel, R. Sobel, Current treatment options for vulvovaginal candidiasis caused by azole-

resistant Candida species, Expert Opin. Pharmacother. 19 (2018) 971–977. https://doi.org/10.1080/14656566.2018.1476490.

[350] X. Hou, K.R. Healey, E. Shor, M. Kordalewska, C.J. Ortigosa, P. Paderu, M. Xiao, H. Wang, Y. Zhao, L.Y. Lin, Y.H. Zhang, Y.Z. Li, Y.C. Xu, D.S. Perlin, Y. Zhao, Novel FKS1 and FKS2 modifications in a high-level echinocandin resistant clinical isolate of Candida glabrata, Emerg. Microbes Infect. 8 (2019) 1619–1625. https://doi.org/10.1080/22221751.2019.1684209.

[351] S.E. Murphy, T. Bicanic, Drug Resistance and Novel Therapeutic Approaches in Invasive Candidiasis, Front. Cell. Infect. Microbiol. 11 (2021) 759408. https://doi.org/10.3389/fcimb.2021.759408.

[352] D. Punginelli, V. Catania, G. Abruscato, C. Luparello, M. Vazzana, M. Mauro, V. Cunsolo, R. Saletti, A. Di Francesco, V. Arizza, D. Schillaci, New Bioactive Peptides from the Mediterranean Seagrass Posidonia oceanica (L.) Delile and Their Impact on Antimicrobial Activity and Apoptosis of Human Cancer Cells, Int. J. Mol. Sci. 2023, Vol. 24, Page 5650. 24 (2023) 5650. https://doi.org/10.3390/ijms24065650.

[353] M. Zasloff, Antimicrobial peptides of multicellular organisms, Nat. 2002 4156870. 415 (2002) 389–395. https://doi.org/10.1038/415389a.

[354] D. Punginelli, V. Catania, M. Vazzana, M. Mauro, A. Spinello, G. Barone, G. Barberi, C. Fiorica, M. Vitale, V. Cunsolo, R. Saletti, A. Di Francesco, V. Arizza, D. Schillaci, A Novel Peptide with Antifungal Activity from Red Swamp Crayfish Procambarus clarkii, Antibiotics. 11 (2022). https://doi.org/10.3390/antibiotics11121792.

[355] G. Barberi, G. Biscari, V. Catania, D. Punginelli, C. Scialabba, C. Fiorica, D. Schillaci, G. Cavallaro, Thermosensitive and mucoadhesive Xanthan gum-based hydrogel for local release of anti-Candida peptide, J. Drug Deliv. Sci. Technol. 100 (2024). https://doi.org/10.1016/j.jddst.2024.106054.

[356] M. Hamcerencu, J. Desbrieres, A. Khoukh, M. Popa, G. Riess, Thermodynamic investigation of thermoresponsive xanthan-poly (N-isopropylacrylamide) hydrogels, Polym. Int. 60 (2011) 1527–1534. https://doi.org/10.1002/pi.3113.

[357] M. Said, B. Haq, D. Al Shehri, M.M. Rahman, N.S. Muhammed, M. Mahmoud, Modification of xanthan gum for a high-temperature and high-salinity reservoir, Polymers (Basel). 13 (2021) 4212. https://doi.org/10.3390/polym13234212/S1.

[358] R. Elashnikov, P. Slepička, S. Rimpelova, P. Ulbrich, V. Švorčík, O. Lyutakov, Temperature-responsive PLLA/PNIPAM nanofibers for switchable release, Mater. Sci. Eng. C. 72 (2017) 293–300. https://doi.org/10.1016/j.msec.2016.11.028.

[359] Y. Shi, C. Ma, L. Peng, G. Yu, Conductive “Smart” Hybrid Hydrogels with PNIPAM and Nanostructured Conductive Polymers, Adv. Funct. Mater. 25 (2015) 1219–1225. https://doi.org/10.1002/adfm.201404247.

[360] D. Paiva, C. Gonçalves, I. Vale, M.M.S.M. Bastos, F.D. Magalhães, Oxidized Xanthan Gum and Chitosan as Natural Adhesives for Cork, Polymers (Basel). 8 (2016) 259. https://doi.org/10.3390/polym8070259.

[361] S.A. Jadhav, V. Brunella, I. Miletto, G. Berlier, D. Scalarone, Synthesis of poly(N-isopropylacrylamide) by distillation precipitation polymerization and quantitative grafting on mesoporous silica, J. Appl. Polym. Sci. 133 (2016) 44181. https://doi.org/10.1002/app.44181.

[362] Y. Tang, D. Dubbeldam, S. Tanase, Water-Ethanol and Methanol-Ethanol Separations Using in Situ Confined Polymer Chains in a Metal-Organic Framework, ACS Appl. Mater. Interfaces. 11 (2019) 41383–41393. https://doi.org/10.1021/acsami.9b14367.

[363] A. Skender, A. Hadj-Ziane-Zafour, E. Flahaut, Chemical functionalization of Xanthan gum for the dispersion of double-walled carbon nanotubes in water, Carbon N. Y. 62 (2013) 149–156. https://doi.org/10.1016/j.carbon.2013.06.006.

[364] L. Yang, X. Fan, J. Zhang, J. Ju, Preparation and Characterization of Thermoresponsive Poly(N-Isopropylacrylamide) for Cell Culture Applications, Polym. 2020, Vol. 12, Page 389. 12 (2020) 389. https://doi.org/10.3390/polym12020389.

[365] D. Pranantyo, C.K. Yeo, Y. Wu, C. Fan, X. Xu, Y.S. Yip, M.I.G. Vos, S.H. Mahadevegowda, P.L.K. Lim, L. Yang, P.T. Hammond, D.I. Leavesley, N.S. Tan, M.B. Chan-Park, Hydrogel dressings with intrinsic antibiofilm and antioxidative dual functionalities accelerate infected diabetic wound healing, Nat. Commun. 2024 151. 15 (2024) 1–19. https://doi.org/10.1038/s41467-024-44968-y.

[366] C.G.A. Das, V.G. Kumar, T.S. Dhas, V. Karthick, K. Govindaraju, J.M. Joselin, J. Baalamurugan, Antibacterial activity of silver nanoparticles (biosynthesis): A short review on recent advances, Biocatal. Agric. Biotechnol. 27 (2020) 101593. https://doi.org/10.1016/j.bcab.2020.101593.

[367] K. Kannan, M. Govindaraj, B. Rajeswari, K. Vijayakumar, Green synthesis silver nanoparticles using medicinal plant and antimicrobial activity against human pathogens, Mater. Today Proc. 69 (2022) 1346–1350. https://doi.org/10.1016/j.matpr.2022.08.506.

[368] A. Shavandi, P. Saeedi, M.A. Ali, E. Jalalvandi, Green synthesis of polysaccharide-based inorganic nanoparticles and biomedical aspects, Funct. Polysaccharides Biomed. Appl. (2019) 267–304. https://doi.org/10.1016/b978-0-08-102555-0.00008-x.

[369] M. Sastry, K.S. Mayya, K. Bandyopadhyay, pH Dependent changes in the optical properties of carboxylic acid derivatized silver colloidal particles, Colloids Surfaces A Physicochem. Eng. Asp. 127 (1997) 221–228. https://doi.org/10.1016/s0927-7757(97)00087-3.

[370] A.I. Raafat, N.M. El-Sawy, N.A. Badawy, E.A. Mousa, A.M. Mohamed, Radiation fabrication of Xanthan-based wound dressing hydrogels embedded ZnO nanoparticles: In vitro evaluation, Int. J. Biol. Macromol. 118 (2018) 1892–1902. https://doi.org/10.1016/j.ijbiomac.2018.07.031.

[371] G. Peng, J. Hu, J. Guo, J. Dong, Y. Zhao, T. Ye, F. Xiao, Z. Meng, H. Gan, R. Gu, P. Han, W. Sun, G. Dou, Y. Sun, S. Liu, Injectable exosome-loaded quaternized chitosan/oxidized sodium alginate hydrogel with self-healing, bioadhesive, and antibacterial properties for treating combined radiation-wound injury, Chem. Eng. J. 494 (2024) 152933. https://doi.org/10.1016/j.cej.2024.152933.

[372] K.E. Ensrud, Epidemiology of fracture risk with advancing age, J. Gerontol. A. Biol. Sci. Med. Sci. 68 (2013) 1236–1242. https://doi.org/10.1093/gerona/glt092.

[373] C.R. Dosier, B.A. Uhrig, N.J. Willett, L. Krishnan, M.T.A. Li, H.Y. Stevens, Z. Schwartz, B.D. Boyan, R.E. Guldberg, Effect of cell origin and timing of delivery for stem cell-based bone tissue engineering using biologically functionalized hydrogels, Tissue Eng. Part A. 21 (2015) 156–165. https://doi.org/10.1089/ten.tea.2014.0057.

[374] M. Liu, X. Zeng, C. Ma, H. Yi, Z. Ali, X. Mou, S. Li, Y. Deng, N. He, Injectable hydrogels for cartilage and bone tissue engineering, Bone Res. 5 (2017) 1–20. https://doi.org/10.1038/boneres.2017.14.

[375] C. Wang, W. Huang, Y. Zhou, L. He, Z. He, Z. Chen, X. He, S. Tian, J. Liao, B. Lu, Y. Wei, M. Wang, 3D printing of bone tissue engineering scaffolds, Bioact. Mater. 5 (2020) 82–91. https://doi.org/10.1016/j.bioactmat.2020.01.004.

[376] H.S. Budi, M.F. Jameel Al-azzawi, F. Al-Dolaimy, M.M. Alahmari, S.S. Abullais, S. Ebrahimi, I.H. Khlewee, A.H.R. Alawady, A.H. Alsaalamy, F.K. Shayan, Injectable and 3D-printed hydrogels: State-of-the-art platform for bone regeneration in dentistry, Inorg. Chem. Commun. 161 (2024) 112026. https://doi.org/10.1016/j.inoche.2024.112026.

[377] Z. Cao, X. Bai, C. Wang, L. Ren, D. Ma, A simple polysaccharide based injectable hydrogel compositing nano-hydroxyapatite for bone tissue engineering, Mater. Lett. 293 (2021) 129755. https://doi.org/10.1016/j.matlet.2021.129755.

[378] G. Barberi, S. Ramos-Díez, C. Fiorica, F.S. Palumbo, S. Camarero-Espinosa, G. Pitarresi, Developing double-crosslinking 3D printed hydrogels for bone tissue engineering, React. Funct. Polym. 203 (2024). https://doi.org/10.1016/j.reactfunctpolym.2024.106016.

[379] W. Wang, M.Y. Liu, M. Shafiq, H.Y. Li, R. Hashim, M. EL-Newehy, H. EL-Hamshary, Y. Morsi, X. Mo, Synthesis of oxidized sodium alginate and its electrospun bio-hybrids with zinc oxide nanoparticles to promote wound healing, Int. J. Biol. Macromol. 232 (2023) 123480. https://doi.org/10.1016/j.ijbiomac.2023.123480.

[380] M. Hu, X. Peng, S. Shi, C. Wan, C. Cheng, X. Yu, Dialdehyde xanthan gum and curcumin synergistically crosslinked bioprosthetic valve leaflets with anti-thrombotic, anti-inflammatory and anti-calcification properties, Carbohydr. Polym. 310 (2023) 120724. https://doi.org/10.1016/j.carbpol.2023.120724.

[381] G. Giammona, B. Carlisi, G. Cavallaro, G. Pitarresi, S. Spampinato, A new water-soluble synthetic polymer, α,β-polyasparthydrazide, as potential plasma expander and drug carrier, J.

Control. Release. 29 (1994) 63–72. https://doi.org/10.1016/0168-3659(94)90122-8.

[382] R.S. Wu, J. Lin, Y.M. Xing, Z.L. Dai, L.W. Wang, X.P. Zhang, pH-Sensitive Black Phosphorous–Incorporated Hydrogel as Novel Implant for Cancer Treatment, J. Pharm. Sci. 108 (2019) 2542–2551. https://doi.org/10.1016/j.xphs.2019.03.003.

[383] K. Yang, X. Zhao, W. Wei, C.X. Lin, L. Sun, Z. Wei, Q. Huang, X. Ge, M. Zrínyi, Y.M. Chen, A novel injectable and self-biodegradable poly(aspartic acid) hydrogel, Mater. Des. 226 (2023) 111662. https://doi.org/10.1016/j.matdes.2023.111662.

[384] G. Pitarresi, G. Cavallaro, G. Giammona, G. De Guidi, M.G. Salemi, S. Sortino, New hydrogel matrices containing an anti-inflammatory agent. Evaluation of in vitro release and photoprotective activity, Biomaterials. 23 (2002) 537–550. https://doi.org/10.1016/S0142-9612(01)00136-3.

[385] G. Giammona, G. Cavallaro, L. Maniscalco, E.F. Craparo, G. Pitarresi, Synthesis and characterisation of novel chemical conjugates based on α,β-polyaspartylhydrazide and β-cyclodextrins, Eur. Polym. J. 42 (2006) 2715–2729. https://doi.org/10.1016/j.eurpolymj.2006.05.005.

[386] M. Licciardi, G. Cavallaro, M. Di Stefano, G. Pitarresi, C. Fiorica, G. Giammona, New self-assembling polyaspartylhydrazide copolymer micelles for anticancer drug delivery, Int. J. Pharm. 396 (2010) 219–228. https://doi.org/10.1016/j.ijpharm.2010.06.021.

[387] E. Pedone, G. Cavallaro, S.C.W. Richardson, R. Duncan, G. Giammona, α,β-poly(asparthylhydrazide)–glycidyltrimethylammonium chloride copolymers (PAHy–GTA): novel polymers with potential for DNA delivery, J. Control. Release. 77 (2001) 139–153. https://doi.org/10.1016/S0168-3659(01)00459-X.

[388] R. Zhang, Z. Huang, M. Xue, J. Yang, T. Tan, Detailed characterization of an injectable hyaluronic acid-polyaspartylhydrazide hydrogel for protein delivery, Carbohydr. Polym. 85 (2011) 717–725. https://doi.org/10.1016/j.carbpol.2011.02.014.

[389] T. Wu, C. Cui, Y. Huang, Y. Liu, C. Fan, X. Han, Y. Yang, Z. Xu, B. Liu, G. Fan, W. Liu, Coadministration of an Adhesive Conductive Hydrogel Patch and an Injectable Hydrogel to Treat Myocardial Infarction, ACS Appl. Mater. Interfaces. 12 (2020) 2039–2048. https://doi.org/10.1021/acsami.9b17907.

[390] M. Zhu, Y. Wang, G. Ferracci, J. Zheng, N.J. Cho, B.H. Lee, Gelatin methacryloyl and its hydrogels with an exceptional degree of controllability and batch-to-batch consistency, Sci. Reports 2019 91. 9 (2019) 1–13. https://doi.org/10.1038/s41598-019-42186-x.

[391] S.D. Dutta, K. Ganguly, A. Randhawa, T. V. Patil, D.K. Patel, K.T. Lim, Electrically stimulated 3D bioprinting of gelatin-polypyrrole hydrogel with dynamic semi-IPN network induces osteogenesis via collective signaling and immunopolarization, Biomaterials. 294 (2023) 121999. https://doi.org/10.1016/j.biomaterials.2023.121999.

[392] W. Ma, M. Yang, C. Wu, S. Wang, M. Du, Bioinspired self-healing injectable nanocomposite

hydrogels based on oxidized dextran and gelatin for growth-factor-free bone regeneration, Int. J. Biol. Macromol. 251 (2023) 126145. https://doi.org/10.1016/j.ijbiomac.2023.126145.

[393] E. Ojeda, Á. García-Barrientos, N. Martínez de Cestafe, J.M. Alonso, R. Pérez-González, V. Sáez-Martínez, Nanometric Hydroxyapatite Particles as Active Ingredient for Bioinks: A Review, Macromol. 2 (2022) 20–29. https://doi.org/10.3390/macromol2010002.

[394] P. Comeau, T. Willett, Printability of Methacrylated Gelatin upon Inclusion of a Chloride Salt and Hydroxyapatite Nano-Particles, Macromol. Mater. Eng. 304 (2019) 1900142. https://doi.org/10.1002/mame.201900142.

[395] D.K. Patel, T. V. Patil, K. Ganguly, S.D. Dutta, K.T. Lim, Nanocellulose-assisted 3D-printable, transparent, bio-adhesive, conductive, and biocompatible hydrogels as sensors and moist electric generators, Carbohydr. Polym. 315 (2023) 120963. https://doi.org/10.1016/j.carbpol.2023.120963.

[396] S.D. Dutta, J. Hexiu, D.K. Patel, K. Ganguly, K.T. Lim, 3D-printed bioactive and biodegradable hydrogel scaffolds of alginate/gelatin/cellulose nanocrystals for tissue engineering, Int. J. Biol. Macromol. 167 (2021) 644–658. https://doi.org/10.1016/j.ijbiomac.2020.12.011.

[397] F.S. Palumbo, G. Pitarresi, C. Fiorica, S. Rigogliuso, G. Ghersi, G. Giammona, Chemical hydrogels based on a hyaluronic acid-graft-α-elastin derivative as potential scaffolds for tissue engineering, Mater. Sci. Eng. C. 33 (2013) 2541–2549. https://doi.org/10.1016/j.msec.2013.02.015.

[398] X. Wang, Z. Bai, K. Li, J. Dong, H. Zhang, X. Liu, W. Han, Q. Li, Bioinspired PLCL/Elastin Nanofibrous Vascular Tissue Engineering Scaffold Enhances Endothelial Cells and Inhibits Smooth Muscle Cells, Biomacromolecules. 24 (2023) 2741–2754. https://doi.org/10.1021/acs.biomac.3c00175.

[399] C. Fiorica, G. Biscari, F.S. Palumbo, G. Pitarresi, A. Martorana, G. Giammona, Physicochemical and Rheological Characterization of Different Low Molecular Weight Gellan Gum Products and Derived Ionotropic Crosslinked Hydrogels, Gels. 7 (2021). https://doi.org/10.3390/gels7020062.

[400] S. Hollingshead, J.C. Liu, pH-Sensitive Mechanical Properties of Elastin-Based Hydrogels, Macromol. Biosci. 20 (2020) 1900369. https://doi.org/10.1002/mabi.201900369.

[401] S.M. PARTRIDGE, H.F. DAVIS, G.S. ADAIR, The chemistry of connective tissues. 2. Soluble proteins derived from partial hydrolysis of elastin, Biochem. J. 61 (1955) 11–21. https://doi.org/10.1042/bj0610011.

[402] M. Davril, K. -K Han, M. -H Loucheux-Lefebvre, Study by circular dichroism of soluble fragments of elastin from porcine and normal and pathological human aortas, Biopolymers. 18 (1979) 2195–2211. https://doi.org/10.1002/bip.1979.360180909.

[403] G. Biscari, M. Malkoch, C. Fiorica, Y. Fan, F.S. Palumbo, S. Indelicato, D. Bongiorno, G.

Pitarresi, Gellan gum-dopamine mediated in situ synthesis of silver nanoparticles and development of nano/micro-composite injectable hydrogel with antimicrobial activity, Int. J. Biol. Macromol. 258 (2024) 128766. https://doi.org/10.1016/j.ijbiomac.2023.128766.

[404] C. Fiorica, F.S. Palumbo, G. Pitarresi, F. Bongiovì, G. Giammona, Hyaluronic acid and beta cyclodextrins films for the release of corneal epithelial cells and dexamethasone, Carbohydr. Polym. 166 (2017) 281–290. https://doi.org/10.1016/j.carbpol.2017.02.071.

[405] B. Gyarmati, G. Stankovits, B.Á. Szilágyi, D.L. Galata, P. Gordon, A. Szilágyi, A robust mucin-containing poly(vinyl alcohol) hydrogel model for the in vitro characterization of mucoadhesion of solid dosage forms, Colloids Surfaces B Biointerfaces. 213 (2022) 112406. https://doi.org/10.1016/j.colseurfb.2022.112406.

[406] B.J.S.C. Olson, J. Markwell, Assays for Determination of Protein Concentration, Curr. Protoc. Protein Sci. 48 (2007) 3.4.1-3.4.29. https://doi.org/10.1002/0471140864.ps0304s48.

[407] G. Giammona, S.E. Drago, G. Calabrese, P. Varvarà, M.G. Rizzo, N. Mauro, G. Nicotra, S. Conoci, G. Pitarresi, Galactosylated Polymer/Gold Nanorods Nanocomposites for Sustained and Pulsed Chemo-Photothermal Treatments of Hepatocarcinoma, Pharmaceutics. 14 (2022) 2503. https://doi.org/10.3390/pharmaceutics14112503.

[408] T. Li, J. Zhao, Y. Yue, B. Han, W. Wang, H. Zhang, Z. Liu, Z. Chen, X. Tian, Preparation of nano-silver containing black phosphorus based on quaternized chitosan hydrogel and evaluating its effect on skin wound healing, Int. J. Biol. Macromol. 268 (2024) 131950. https://doi.org/10.1016/j.ijbiomac.2024.131950.

[409] S. Sengupta, J. Tripathi, R. Tandon, M. Raje, R.P. Roy, S.K. Basu, A. Mukhopadhyay, Hemoglobin Endocytosis in Leishmania Is Mediated through a 46-kDa Protein Located in the Flagellar Pocket, J. Biol. Chem. 274 (1999) 2758–2765. https://doi.org/10.1074/jbc.274.5.2758.